MAGMATIC DIFFERENTIATION AND GROWTH OF A LARGE MAFIC INTRUSION IN THE LOWER CRUST: INSIGHTS FROM VARYING SCALES

by

ANDREW B. MAENDEL

(Under the Direction of Mattia Pistone)

ABSTRACT

Magmatic processes in the roots of transcrustal magmatic systems that feed volcanoes are not fully constrained. The lower crustal Mafic Complex of the Ivrea-Verbano Zone (Alps, Italy), part of a transcrustal magmatic system which fed volcanism during the Permian, has been studied extensively for five decades. Studies have provided an exceptional history of the growth and evolution of this magmatic system, yet questions remain. Textural, *in-situ* geochemical, and bulk rock analyses of a suite of ultramafic to mafic rocks from the Upper Mafic Complex show that *in-situ* magmatic differentiation can explain the heterogeneous nature of these rocks. Statistical analysis of bulk rock data from the Mafic Complex shows an overall tholeiitic trend of differentiation and the presence of large-scale yet discrete magmatic differentiation at higher stratigraphic levels, contrasting recent ideas that propose pervasive reactive melt flow during the growth of the complex.

INDEX WORDS: Ivrea-Verbano Zone, Sesia Magmatic System, Magmatic Differentiation, Layered Mafic Intrusions, Petrology

MAGMATIC DIFFERENTIATION AND GROWTH OF A LARGE MAFIC INTRUSION IN THE LOWER CRUST: INSIGHTS FROM VARYING SCALES

by

ANDREW B. MAENDEL

BS, State University of New York College at Cortland, 2021

A Thesis Submitted to the Graduate Faculty of The University of Georgia in Partial Fulfillment of the Requirements for the Degree

MASTER OF SCIENCE

ATHENS, GEORGIA

2023

MAGMATIC DIFFERENTIATION AND GROWTH OF A LARGE MAFIC INTRUSION IN THE LOWER CRUST: INSIGHTS FROM VARYING SCALES

by

ANDREW B. MAENDEL

Major Professor:	Mattia Pistone
Committee:	Othmar Müntener
	Douglas Crowe

Electronic Version Approved:

Ron Walcott
Vice Provost for Graduate Education and Dean of the Graduate School
The University of Georgia
December 2023

ACKNOWLEDGEMENTS

The support of many people in my life made this work possible. Firstly, I would like to thank Mattia Pistone for his continuous support. His availability for questions and support helped me through times when I was preparing to throw in the towel. His mentorship, excitement, and optimism will leave a lasting impact on me, as will my preference for Valsesian food and fine Italian “Digestivo” acquired through the weeks of fieldwork in the Ivrea.

Although I cannot mention them all, I am also appreciative of the many friends in Athens, Georgia, who provided balance in my life (Tommy, Bailey). The Magma Mia lab group members made working in the lab something to look forward to. And thank you to those close to me (Roger, Riley) for moral support during long days and nights of writing.

I also thank Othmar Müntener as well as many other faculty members at University of Lausanne, Switzerland for bulk rock preparation and analysis in summer 2021. I cannot thank Lorenzo Tavazzani, Adrianna Virmond, Olivier Bachmann, and many other faculty at the IGP at ETH Zurich, enough for the incredible research opportunities I could experience in Switzerland in summer 2022. I am indebted to Matt Loocke for the incredible EPMA data from Louisiana State University and his insightful comments. And lastly, thank you to Steve Holland for introducing me to data analysis and R software programming.

This work was made financially possible through a SNSF Ambizione Fellowship awarded to Mattia Pistone, the University of Georgia Department of Geology Watts-Wheeler Grant, the Science Office at the Embassy of Switzerland ThinkSwiss Research Scholarship, and the Institute of Geochemistry and Petrology at ETH Zurich, Switzerland.

TABLE OF CONTENTS

Page

LIST OF TABLES

Page

LIST OF FIGURES

Page

CHAPTER 1

INTRODUCTION

Magma reaches the surface in many different tectonic settings, from convergent plate boundaries to extensional mid-ocean ridge systems (Winter, 2014). Eruption of these magmas on the surface, in the form of volcanoes, and the style and frequency of eruptions have impact on human societies. Volcanic eruption style and frequency are largely controlled by composition and state of the intruding magma below volcanoes. However, the processes controlling the geochemical evolution and transport of these magmas from their source in the mantle to the surface are not directly observable. Therefore, experimental work, geophysics, modeling, and studies of the petrological and geochemical characteristics of exposed fossilized magmatic systems are employed.

In recent years, the concept of transcrustal magmatic systems, encompassing the entirety of magma transport and differentiation from the base of the crust to the upper crust, even to volcanoes, has been recently changed from single and chemically zoned crustal magma reservoirs to open and vertically extended plumbing systems (Cashman and Giordano, 2014; Solano *et al.*, 2014; Cashman *et al.*, 2017; Jackson *et al.*, 2018; Sparks *et al.*, 2019). In the transcrustal perspective (Fig. 1), the connection of processes occurring in the lower crust are connected to magmatic processes in the shallow crust that may lead to eruption (Cashman *et al.*, 2017). Magmas are divided into crystal-poor, eruptible magmas and porous, supersolidus crystal mushes that are rigid, rheological immobile, and compose the bone structure of the transcrustal plumbing system (e.g., Bachmann and Bergantz, 2004; 2008). A few models have proposed how

large magma reservoirs are formed in the crust that feed volcanoes and cool to form plutonic igneous rocks, and the processes modeled may all act simultaneously. One model is the idea of incremental emplacement, in which magma is emplaced in the crust over a protracted period of time; early sills emplaced completely solidify, but over a longer timeframe, and the ambient temperature may result in the formation of magma reservoir (magma and mush) (e.g., Annen *et al.*, 2006; Annen, 2011; Caricchi *et al.*, 2014). The remobilization model is similar in that intrusion of new magma below may raise temperatures above the solidus, thus remobilizing the magma (Sparks *et al.*, 2019). Lastly, the reactive melt segregation model, as developed by Jackson *et al.* (2018), proposes that melt-rich layers may develop in a magma reservoir and their remobilization occurs through changes in composition of the percolating melt fraction through the mush and does not require an increase of temperature.

The one-dimensional model of Jackson *et al.* (2018) simulating melt flow reactivation during magma emplacement lends itself well to testable geochemical and structural hypotheses as applied to the Mafic Complex of the Ivrea-Verbano Zone (Western Alps, Italy). In this model (Fig. 2 and 3), sills are emplaced at a depth controlled by buoyancy of the intruding magma and the host rock at a rate of 5 mm/yr. The first sills emplaced solidify quickly, but later intrusions raise the geothermal gradient. The sills allow for chemical differentiation before cooling, leading to depleted cumulates at the base of the sill and more-evolved melt at the top (Jackson *et al.*, 2018). Successive intrusions raise the geothermal gradient to where melt fractions increase continuously between successive injections of new magma, ending the incubation phase. However, unlike the classical magma chamber concept, the resulting magmatic body is a mush rather than a liquid magma. As time progresses, melts migrate upwards and form a high melt fraction body; counterintuitively, this high melt fraction body has lower temperature than where

the sills are intruded because the local composition of this layer will have evolved to a eutectic composition (Jackson *et al.*, 2018). The reactive melts percolating through the compacting crystal mush react with the earlier-formed crystals, and therefore change the local bulk composition and decrease the sharp contrasts between the sills emplaced earlier. Also, the model predicts that intrusion of new sills will occur progressively deeper over time (Jackson *et al.*, 2018). In the high melt fraction layer, convection may occur. Buoyant magmas of mafic or felsic chemistry can then escape the system (Jackson *et al.*, 2018), feeding volcanoes and therefore complete the transcrustal magmatic system.

To study the composition and architecture of transcrustal magmatic systems and infer their dynamics that drives magmatism and volcanism on Earth, we need to apply *a posteriori* petrological investigation of sub-volcanic processes using exposed crust–mantle sections (Rudnick and Presper, 1990; Percival *et al.*, 1992). Studies of exposed crustal sections are important for estimating the Earth's crust composition, geophysical structure, and dynamics through time. Consequently, these cross-sections offer rare opportunities to determine the time-integrated evolution of the structure of the generally inaccessible Earth's deep crust, information that cannot be obtained by xenolith investigations alone. Thus, magma petrogenesis, differentiation, and crustal assimilation processes occurring in the deep crust and their effect on upper crustal processes and volcanic eruption dynamics require the observation of exposed sections, but many of these sections around the world are incomplete (Salisbury and Fountain, 1981; Pistone *et al.*, 2020).

The past five decades have yielded numerous models of emplacement for the Mafic Complex of the Ivrea-Verbano Zone, a Permian-age, intact, lower crustal mafic pluton. Most of these models developed since the 1990s invoke, to some degree, the repetitious intrusion of

basaltic melts, the downward flow of cumulate mush and partially digested and depleted metapelitic septa, and in the model of Jackson *et al.* (2018), pervasive reactive melt flow and remobilization. These models are based on structural, geochemical, and isotopic data. However, newer models do not seem to fully account for the petrological variability that is stratigraphically controlled. Using a high-resolution petrological and geochemical study of a mafic suite of rocks from the Upper Zone of the Mafic Complex, I test the hypothesis that the olivine gabbros of this suite formed from *in-situ* differentiation. Secondly, through statistical analysis of a large compilation of bulk rock compositions of the Mafic Complex, I test the hypothesis that the Mafic Complex, particularly the Upper Mafic Complex, grew from multiple injections of magma at different levels, which differentiated somewhat independently.

CHAPTER 2

GEOLOGY

The Ivrea-Verbano Zone

The Ivrea-Verbano Zone (Western Alps, Italy) is the most complete crustal cross section among many identified crustal cross sections in the world (e.g., Prince Rupert, British Columbia, Canada; Doubtful Sound, Fiordland, New Zealand; Kohistan, Pakistan; Talkeetna, Alaska, USA; Sierra de Famatina, Argentina). The Ivrea-Verbano Zone shows only minor tectonic attenuation during the post-Permian exhumation and minor lithospheric thinning that have not removed significant rock sequences along the section (Schmid *et al.*, 1987; Handy and Zingg, 1991; Schmid, 1993; Demarchi *et al.*, 1998; Petri *et al.*, 2019). Thus, the Ivrea-Verbano Zone (IVZ) (Fig. 4) provides a unique opportunity to evaluate the evolution of the continental crust structure and composition through time.

The discovery that the IVZ is an exposed crustal section in the 1960s initiated a period of intense research activity (Schweizerische Mineralogische und Petrographische Mitteilungen, v. 48, no. 1, 1968; Berckhemer, 1969) that continues today. Essentially, the IVZ is made of upper and middle crustal rocks exposed in the Serie dei Laghi / Strona Ceneri Zone, and lower crustal rocks exposed in the IVZ *sensu stricto* (Fig. 4), in which metamorphic grade increase from amphibolite (~0.4 GPa) to granulite facies grade (~0.9 GPa) towards the Insubric Line (Fig. 4) (Zingg, 1983; Henk *et al.*, 1997; Demarchi *et al.*, 1998; Petri *et al.*, 2019).

The IVZ and Serie dei Laghi / Strona Ceneri Zone are two lithostratigraphic terranes composed of metamorphosed sedimentary and plutonic rocks that abut the rocks of the Austro-

Alpine domain and are separated by the Alpine-age (<30 Ma) Insubric Line to the west and northwest (Schmid *et al.*, 1987; Quick *et al.*, 2003). The Serie dei Laghi, to the east, is separated from the IVZ by the Pogallo Line and the Cossato-Mergozzo-Brissago (CMB) Line (Zingg, 1983; Boriani *et al.*, 1990). The IVZ and Serie dei Laghi / Strona Ceneri Zone represent the lower and the middle to upper crust, respectively, with the Insubric Line at the base of the exposed section. Granulite-facies metasediments, metabasites intercalated with plutonic mafic lithologies, and slivers of mantle peridotite bodies are found at the base of the IVZ (Zingg, 1990; Quick *et al.*, 1995) (Fig. 4). In the southern IVZ, compositional layering and foliation are presently subvertical, and isobars are approximately parallel the Insubric Line, which is the tectonic boundary between Eurasian and African plate (Demarchi *et al.*, 1998). On geological maps, the IVZ can therefore be seen as a vertical cross section through the pre-Alpine crust, tilted by ~90° along an axis that strikes N-NE (Quick *et al.*, 2003) (Fig. 4).

The most ancient rocks of the IVZ are pre-Permian metapelitic sequences composing the Paleozoic basement of the IVZ crustal section recording a protracted, complex tectonic history. The upper crust of Serie dei Laghi / Strona Ceneri Zone compose the Orobic Basement, which displays greenschist facies rocks (Schnetger, 1994; Bea and Montero, 1999). These are pelitic rocks of the Serie dei Laghi and arenaceous rocks with abundant clay, intruded by Ordovician intrusions leading to the granitization of the metasediments (including the anatectic melting in paragneisses) composing the upper crust of the IVZ around 466 Ma (Hunziker and Zingg, 1980; Boriani *et al.*, 1990). In the lower crustal portion, the metapelitic sequences are amphibolite- and granulite-facies rocks that compose the Kinzigite Formation (garnet, biotite, plagioclase, quartz, sillimanite ± muscovite schist and migmatitic gneiss) and Stronalite Formation (garnet, K-feldspar, and sillimanite schistose to migmatitic gneiss), respectively. Both formations display a

complete prograde metamorphic sequence of metapelites (*sensu lato*, specifically quartz-bearing peraluminous metasediments) with minor intercalations of metabasites, quartzites, and marbles ranging from middle amphibolite to granulite facies (Bertolani, 1968; Schmid and Wood, 1976; Zingg, 1980; 1983). These metapelites are from Proterozoic metasediments juxtaposed during accretionary wedge formation and underplating above the Rheic subducted oceanic crust of the IVZ during the Late Proterozoic to Early Paleozoic period (Schmid, 1993). Later, during the Variscan orogeny (320-350 Ma) crustal thickening and decoupling between lower crust (IVZ) and upper crustal levels (Serie dei Laghi / Strona Ceneri) was accompanied by sedimentation of metasediments in an accretionary prism, including their burial, incorporation into the continental lower crust, and prograde metamorphism (Schmid and Wood, 1976; Schmid, 1993; Redler *et al.*, 2012; Wyatt *et al.*, 2022). The pre-Permian metapelites in the IVZ were accreted to the base of a Variscan magmatic arc system about 10 Ma prior to the onset of Lower Permian crustal thinning and magmatism induced by upper mantle decompression melting (Wyatt *et al.*, 2022).

During the Carboniferous (300-320 Ma), peridotite bodies representing slivers of the Earth's mantle (Balmuccia, Baldissero, Premosello bodies) were exhumed and emplaced in granulite-facies metapelites of the lower crust of IVZ (Rivalenti *et al.*, 1975; Handy *et al.*, 1999; Decarlis *et al.*, 2023). The final mantle peridotite exhumation occurred ~316-275 Ma (Klötzli *et al.*, 2014; Peressini *et al.*, 2007) during the initial period of magmatic underplating (Voshage *et al.*, 1990) producing magmas derived from a hydrous mantle source (Berno *et al.*, 2020).

The Mafic Complex

Following crustal amalgamation and accretion during the Devonian to Carboniferous (von Raumer *et al.*, 2013), the IVZ experienced a stratigraphic and chemical change during the early Permian (270-290 Ma), when transextensional processes formed new continental crust

reaching a thickness of 30–35 km (Handy *et al.*, 1999; Petri *et al.*, 2019). During this period, a large body of ultramafic to evolved mafic magmas formed an intrusive plutonic assembly in the IVZ lower crust, the "Basischer Hauptzug" or Mafic Formation or Mafic Complex (Rivalenti *et al.*, 1975; Zing, 1983; Quick *et al.*, 1995; 2003) (Fig. 5). In this extensional tectonic regime, mantle-derived magmas intruded and underplated the lower crust by forming the Mafic Complex forming the roots of the Lower Permian Sesia Magmatic System (Rivalenti *et al.*, 1984; Sinigoi *et al.*, 1994; 2010; 2011; Pin and Sills, 1986; Peressini *et al.*, 2007; Karakas *et al.*, 2019) (Fig. 5).

The Mafic Complex (>240 km^2 exposure, composed of a ~50 km wide and ~8 to ~12 km thick pluton, measured from the quadrangle map of Quick *et al.*, 2003), intruded in the Paleozoic metasedimentary rocks of the IVZ lower crust, provides an excellent example of the lower roots of a transcrustal magmatic system connected to granitic plutons in the upper crust and feeding the Sesia volcano producing caldera-forming eruptions in the early Permian (Quick *et al.*, 2009; Sinigoi *et al.*, 2010; Karakas *et al.*, 2019). Mineral geothermobarometry has shown that the roof of the Mafic Complex can roughly be considered and isopleth at ~15 km in depth and that pressures increase progressively westward towards the Insubric Line at about 0.036 GPa/km (Demarchi *et al.*, 1998; Petri *et al.*, 2019). Additionally, emplacement of the Mafic Complex did not induce the granulite facies metamorphism observed in the metapelitic country rocks found in the Kinzigite Formation (Barboza *et al.*, 1999; Barboza and Bergantz, 2000). Recent zircon U-Pb petrochronology has shown that the Sesia Magmatic System developed from the base in the lower crust (Mafic Complex) to its eruptions over a ~4 Ma time frame, with a peak of 2.1-Ma-long activity between 284.7 and 282.6 Ma (Karakas *et al.*, 2019).

The Mafic Complex is composed dominantly of gabbroic rocks and diorites at the roof, with minor coeval ultramafic bodies, granitoid bodies, and restitic paragneiss septa (or "felsic

granulites"; Rivalenti *et al.*, 1975) (e.g., Quick *et al.*, 2003). The Mafic Complex is an intruded stratiform body that mostly preserved its original igneous textures (layering, intrusive contacts, magma mingling) and geochemical signature (Rivalenti *et al.*, 1975) while also preserving evidence of synmagmatic deformation (Quick *et al.*, 1992).

Rivalenti *et al.* (1975) proposed one of the earlier divisions of the Mafic Complex along Val Sesia (Fig. 6), which became the primary transect across the Mafic Complex to study the development and construction of transcrustal systems in continental settings. Specifically, using recent geological mapping (Quick *et al.*, 1994; Snoke *et al.*, 1999; Quick *et al.*, 2009) supporting pioneering observations (Rivalenti *et al.*, 1975; 1984), the Val Sesia transect displays the Mafic Complex as an enormous magma system that grew from continuous input of new magma through mantle uplift and associated partial melting via mantle decompression. Over the last three decades, models have pointed to large-scale ductile deformation of the Mafic Complex and transport of cumulates downward from the forming pluton, located at the roof of the complex, due to extensional tectonics (Quick *et al.*, 1992). Val Sesia roughly corresponds with the major axis of the Mafic Complex and, therefore, exhibits the most complete stratigraphic section, excluding the Lower Mafic Complex.

The rock groups identified from west to east (corresponding to bottom to top; Fig. 6) in Val Sesia are the following: the Lower Layered Group (Rivalenti *et al.*, 1975; 1981a; 1981b; 1984), the Paragneiss-bearing Belt (Sinigoi *et al.*, 1996), the Upper Layered Group (Rivalenti *et al.*, 1975) or the Upper Zone (Rivalenti *et al.*, 1984), the Main Gabbro (Rivalenti *et al.*, 1984), and the Diorite Group (Rivalenti *et al.*, 1984; Sinigoi *et al.*, 1996; 2011; 2016) composing the Upper Mafic Complex (Sinigoi *et al.*, 1996). The Lower Layered Group is composed primarily of a layered series of cumulate rocks such as dunites, harzburgites, norites, gabbros with rare

lherzolites, pyroxenites, and anorthosites, and the Upper Layered Group is composed of gabbroic rocks with common olivine-bearing gabbros as well as apatite and Fe-Ti oxide cumulates and rare pyroxenites (Rivalenti *et al.*, 1975; Mazzucchelli, 1983). The Paragneiss-bearing Belt is a stratigraphic level of the Mafic Complex that separates the Lower and Upper Mafic Complex. The Paragneiss-bearing Belt contains a sequence of metasedimentary horizons (septa) and lenses of the Kinzigite Formation, made of highly depleted granulite-facies mineral assemblages (quartz, antiperthitic plagioclase, garnet, mesoperthite ± sillimanite ± corundum ± rutile ± graphite) and associated charnockitic lenses and layers (quartz, mesoperthite ± opx ± garnet) derived from crystallised anatectic melts (Sinigoi *et al.*, 1996; 2011; 2016). The Main Gabbro is considered as a relatively homogeneous gabbroic unit consisting of hornblende-bearing norite and gabbronorite (Rivalenti *et al.*, 1984). The Diorite Group (termed *Diorites* in this study) is composed of gabbroic to dioritic rocks containing biotite accompanied by monzonitic or even granitic (leuco-charnockites) rocks (Fig. 6) (Sinigoi *et al.*, 1996; 2011; 2016).

Slow, isobaric cooling induced re-equilibration of primary igneous phases, and this caused coronitic and granoblastic textures, as well as unmixing in low- and high-Ca pyroxenes (orthopyroxene and clinopyroxene in this study). Re-equilibration pressures have been estimated to vary between 0.8 and 0.5 GPa from bottom to roof in the region south of Val Sesia and slightly higher (0.8 to 0.9 GPa) in the lower units of Val Sesia (Demarchi *et al.*, 1998).

The compilation of bulk rock compositions and representative mineral chemical compositions (e.g., Rivalenti *et al.*, 1975, 1981, 1984; Voshage *et al.*, 1990; Sinigoi *et al.*, 1994, 1996, 2011, 2016; Tribuzio *et al.*, 2023) indicate, overall, that: i) the first gabbroic layers and most of the first ultramafic layers of the Lower Layered Group display a MORB-type trace element signature with Sr and Nd isotope compositions compatible with their derivation from a

depleted mantle source; ii) variably enriched trace element patterns and isotope signatures are recorded in the upper portion of the Lower Layered Group, iii) variable and, in places, extreme incompatible element enrichment and high $\delta^{18}O$, $^{87}Sr/^{86}Sr$, and $^{143}Nd/^{144}Nd$ signatures accompanied by marked Eu, Sr, and Ba enrichments in bulk rocks and minerals in the Upper Layered Group (Sinigoi *et al.* 1994; Voshage *et al.* 1990), iv) modest geochemical variability (positive Eu anomalies and enrichment in LREE) with isotopes that remain enriched and constant in the Main Gabbro, and v) dramatically enriched rocks (similar to the rocks of the Upper Layered Group / Upper Zone) forming the transition to the Diorite Group, which displays pervasively enriched characteristics. All these geochemical signatures might be explained by a combination of processes that include assimilation and fractional crystallization processes in the lower portions of the Mafic Complex, and melting, assimilation, storage, hybridization, refilling, tapping, and fractionation in the Main Gabbro and upper units of the Mafic Complex.

Metapelites were affected by episodic heating with background conductive cooling punctuated by pulses of magmatism and heating, which occurred throughout the Permian and Jurassic (Fig. 3). Thermochronological constraints, based on the U–Pb dating of high-temperature accessory minerals such as rutile and zircon, offer lower crustal peak metamorphic conditions and, thus, the maximum temperatures at specific times of the IVZ thermal history (Fig. 3). Thermo-kinematic modelling combining 1-D thermal modelling with depth-dependent thinning (Royden and Keen, 1980; Kusznir and Karner, 2007; Huismans and Beaumont, 2008; 2014) via pure shear extension of the IVZ lithosphere during Tethyan rifting (Smye *et al.*, 2019) help constrain the prograde heating and how the cumulative effects of short-term advective heat addition and long-term conductive heat transport from the mantle can control the IVZ thermal structure. In this model, lateral heat transport and related temperature gradients through the

lithosphere are subordinate to vertical gradients. In contrast, the 2-D petrological-thermomechanical model of the closure of the Rheic Ocean and subsequent Variscan continental collision (Gonzales *et al.*, 2020) shows how localized gravitational collapse linked to extensional thinning of the lower crust favors partial melting of mechanically mixed metasediments prior to upwelling and decompression melting of asthenospheric mantle. This model explains the tholeiitic character of the underplated Mafic Complex as well as the geochemical and isotopic signatures of the alkaline pipes and their associated Ni-Cu-Co-PGE deposits (Holwell *et al.*, 2022; Gonzales *et al.*, 2020). This model can explain the asthenospheric thermal energy required to promote partial melting of the metasomatized lithospheric mantle during the Variscan orogenic collapse, the Mafic Complex construction, and the formation of Ni-Cu-Co-PGE sulfides in the lowermost portion of the IVZ lower crust (Locmelis *et al.*, 2016; Gonzales *et al.*, 2020).

CHAPTER 3

METHODS

Fieldwork

A previous field campaign in 2017 was conducted in 36 sites in the Mastallone, Sesia, and Sessera valleys across the exposed crustal section through the Lower Mafic Complex, Paragneiss Bearing Belt and Upper Mafic Complex (Fig. 6). These samples were collected as 2 cm rock cores for a comprehensive evaluation of the development and evolution of the Mafic Complex through high-resolution X-ray tomography and bulk rock analyses, the latter of which was completed in this work.

Fieldwork consisted of sampling representative rocks of the Mafic Complex with a focus on the rock outcrops at the hamlet of Saliceto, Cravagliana municipality in the Mastallone valley (Val Mastallone), as well as outcrop-scale mapping the extent of the rock units and boundaries in an area of ~0.1 km^2 (Fig 7).

The gabbroic to ultramafic rock suite, the focus of this work, is found in a roadcut outcrop of Strada Provinciale 9 and in a river outcrop at Saliceto, Italy (Fig. 7). In total, ~30 samples were collected. Samples were collected during two field missions conducted in 2021 and 2022. The first mission aimed to sample the olivine gabbro and adjacent suites, and the second mission was designed to sample for zircon U/Pb geochronology. In the first mission, sampling primarily targeted the olivine gabbros and surrounding gabbro-norites within 100 meters of the ultramafic layer. The second mission targeted rocks that contained a wide range of crystallization and thus potential for finding zircon, guided by elevated amounts of Zr from bulk analyses of the

rocks collected in 2021. Additional samples (AM_VM22_3a, AM_VM22_3b) were taken from a gabbroic rock outcropping 1.5 km to the north at Ferrera, with the intent of zircon U/Pb dating. Mapping of the field area was conducted along the road outcrop and in the riverbed. Weathering, plants and metal grating challenged comprehensive mapping efforts along the road outcrop (Fig. 8), but river outcrops below the road showed better the lithologies and contacts, despite their weathered appearance.

Thin Sections and Petrography

In total, 53 thin sections were created from the Saliceto samples, of which 42 were polished to 50 – 70 micrometers in thickness for in-situ analyses and petrography, and 11 were polished to 30 micrometers. These latter 11 thin sections include 8 covered sections for petrographic characterization only, and 3 polished for SEM and EPMA analyses. Additionally, more than 100 thin sections from the 2017 field mission were available for petrographic analysis, including billets of the same samples prepared for bulk rock analysis.

Thin sections were characterized in terms of mineralogy, microstructures and suitability for geochemical analyses using a Nikon Eclipse LV100N POL petrographic microscope at the Department of Geology of the University of Georgia. High-resolution full thin section scans in plane-polarized and cross-polarized light were captured with a Keyence VHX-S650E digital microscope and a Keyence VHX-7000 digital microscope for use in geochemical analysis planning and data processing, petrography, and point counting.

To calculate modal abundances of phases for key samples, point counting was performed on full thin section scans. Point counting was conducted using JMicroVision v1.3.4 software, and >500 points were identified on a random grid for each thin section. The random grid was generated by the software. Mineral identification in thin section scans was corroborated with

optical observation under a petrographic microscope, because some minerals, particularly orthopyroxene and clinopyroxene, were challenging to differentiate on the thin section scans (plane-polarized light). Due to difficulty distinguishing minerals from full thin section scans, point counting was also performed using a Leica DM750P petrographic microscope fitted with a point counting stage. A 1 by 1 μm point counting grid was used for most thin sections, and a 0.4 by 1 mm grid was used for to point count the 10 mm by 20 mm melanocratic portion of thin section 14D (AM-VM22-14D). Between 600 and 1500 points were counted for each thin section using this method.

SEM

Scanning electron microscopy (SEM) was performed on seven Saliceto thin sections for microstructural analysis and semi-quantitative geochemical analysis of minerals. A Thermo Fischer Scientific (FEI) Teneo field emission scanning electron microscope (FESEM) at Georgia Electron Microscopy Center of the University of Georgia was used at 15 kV and 1 nA to acquire backscattered electron (BSE) images to identify rock microstructures and minerals. The Oxford large area windowless energy-dispersive X-ray spectrometer (EDS) allowed semi-quantitative major and minor element composition of minerals and X-ray distribution elemental maps of major elements, which served as a guide for mineral identification and for generating navigation maps for the successive in-situ quantitative analysis via EPMA and LA-ICP-MS.

EPMA

For quantitative major and minor element analysis of minerals in Saliceto samples, electron probe microanalysis (EPMA) was performed on polished thin sections. A JEOL JXA-8230 EPMA with EDS detector and three wavelength-dispersive spectrometers (WDS) was utilized at Louisiana State University facilities for major and minor element analysis of minerals

in gabbro-norite (sample AM-IVZ-VM017, thin section A17), garnet olivine gabbro (sample AM-IVZ-VM009, thin section A9), and plagioclase-bearing, olivine-bearing pyroxenite (sample AM-IVZ-VM008, thin section B5). The goal of this EPMA session was to analyze all major and accessory phases present, with a focus on oxide minerals. EDS was used for mineral recognition, and BSE images were captured of key textures and microstructures. The following crystals were used for element detection: TAP for Si Kα, Al Kα, Mg Kα, Na Kα, F Kα, P Kα; LIFH for Ti Kα, Ba Lα, Zn Kα, V Kα; LIF for Fe Kα, Mn Kα, Cr Kα, Ni Kα, Co Kα, Cu Kα; PETH for Ca Kα, K Kα, Pb Mα, Cl Kα; PETJ for Cl Kα, Ca Kα, Sr Lα, S Kα. Combined acquisition of Cl from PETJ and PETH was used for amphibole, pyroxene, and oxide minerals. On sulfides LIFH was used for Ni Kα. A beam current of 20 nA and 15 kV acceleration voltage was used for all the mineral analyses. Different beam diameters (spot sizes) were used depending on the mineral to analyze: 10 µm for apatite, 5 µm for pyroxene, amphibole, epidote and plagioclase, and 1 µm for all other minerals. The following Astimex Standards Ltd. (mineral standards mount MINM25-53) were used: diopside (Si, Mg, Ca), rutile (Ti), chromite (Cr), rhodonite (Mn), Al_2O_3 (Al), albite (Na), tugtupite (Cl), fluorite (F), plagioclase, celestite (Sr), barite (Ba), olivine (Si, Mg), almandine, sphalerite (Zn), galena (Pb), pyrite (Fe, S), cobaltite (Co), pentlandite (Ni), chalcopyrite (Cu), and apatite (P). The standard Ni-diopside from the University of Oregon (Eugene, OR) was used for NiO in olivine. MAC standards used included Al_2O_3 (Al), V_2O_5 (V), $MgAl_2O_4$ (Al), NiO (Ni), titanite (Ti), andradite (Fe), spessartine (Mn). Other standards from the National Museum of Natural History (NMNH) of the Smithsonian Institution (Washington, DC) include: Kakanui (Otago, New Zealand) hornblende (NMNH 143965; Al and Fe), microcline (NMNH 143966; K), Great Sitkin Island (Alaska, USA) anorthite (NMNH 137041; Al and Ca), Rockport (Massachusetts, USA) fayalite (NMNH 85276; Fe), Ilmen Mountains (Russia) ilmenite (NMNH

96189; Ti and Mn), and Borborema Province (Brazil) gahnite (NMNH 145883; Zn). The counting time on the peak and background positions for pyroxenes was 30 s and 20 s for Ti Kα, Cr kα, Fe Kα, Mn Kα, K Kα, Cl Kα, F Kα, and Si Kα, Al Kα, Mg Kα, Ca Kα, Na Kα. For plagioclase, the counting time on the peak and background positions was 40 and 20 s for Ti Kα, 30 and 15 for Fe Kα, Mn Kα, Mg Kα, Ba Lα, Sr Lα, K Kα, and 20 and 10 s for Si Kα, Al Kα, Ca Kα, Na Kα. For sulfide minerals, the counting time on the peak and background positions was 60 and 30 s for Pb Mα, 40 and 20 s for Co Kα, Cu Kα, P Kα, 30 and 15 s for Zn Kα, Fe Kα, Ni Kα, and 20 and 10 s for Si Kα, Al Kα, Mg Kα, Na Kα, S Kα. For olivine, the counting time on the peak and background positions was 60 and 30 s for Al Kα, Ca Kα, 40 and 20 s for Cr Kα, 30 and 15 s for Ni Kα, Mn Kα, and 20 and 10 s for Si Kα, Fe Kα, Mg Kα. Garnet analyses had the counting time on the peak and background positions of 40 and 20 s for Ti Kα, Cr Kα, 30 and 15 s for F Kα, 20 and 10 s for Fe Kα, Mn Kα, Mg Kα, Ca Kα, and 10 and 5 s for Si Kα, Al Kα. For apatite analyses, the counting time on the peak and background positions was 60 and 30 s for Sr Lα, 40 and 20 s for Pb Mα, Y Lα, 30 and 15 s for Fe Kα, Mn Kα, Mg Kα, Cl Kα, F Kα, and 20 and 10 s for Si Kα, Al Kα, Ca Kα, Na Kα, P Kα. Oxygen was calculated by stoichiometry, and data were corrected for the ZAF (atomic number. [Z], absorption [A], and fluorescence excitation [F]) effects (Armstrong, 1988).

Similarly, a JEOL JXA-8230 EPMA with five WDS detectors was used to measure major elements in phases from three Saliceto samples: gabbro-norite (AM-IVZ-VM-017), garnet olivine gabbro (AM-VM22-6c) and pyroxenite (AM-IVZ-VM-007) at the Department of Earth Sciences at ETH Zurich (Switzerland). Some minerals from the gabbro-norite sample analyzed at Louisiana State University were re-analyzed to test data reproducibility. Beam current was 20 nA and 15 kV acceleration voltage. The following crystals were used for element detection: LIFH

for Fe Kα, Mn Kα, Ni Kα, PETL for Cr Kα, Ti Kα, PETJ for Ca Kα, K Kα, PETL for Cr Kα, Ti Kα, TAP for Al Kα, Si Kα TAPH for Na Kα, Mg Kα, and TAP for Al Kα, Si Kα. The counting time was 20 s for Fe Kα, Mn Kα, Ni Kα, and 30 s for K Kα, Ti Kα, Cr Kα, Si Kα, Al Kα, Na Kα, Mg Kα, Ca Kα. The same set of elements was used for all analyses. The following in-house synthetic and natural standards were used: D015 - Rutile for Ti Kα, D023 - Pyrolusite for Mn Kα, D028 - Chromite for Cr Kα, D042 - Bunsenite for Ni Kα, H021 - Albite for Na Kα, Si Kα, H083 - Forsterite for Mg Kα, H103 - Anorthite for Al Kα, Ca Kα, H116 - Fayalite for Fe Kα, and SM MCL - Microcline for K Kα. For apatite analyses, P_2O_5 EDS data was used due to machine constraints preventing the addition of a P_2O_5 standard; moreover, apatite analysis was also not exclusively performed on correctly oriented apatite. Oxygen was calculated by stoichiometry, and data were corrected with the ZAF method (Armstrong, 1988). The in-house standard Arenal hornblende (NMNH 111356; Jarosewich, 2002) was analyzed frequently during the session to check for analytical drift and drift correction. Room temperature fluctuations during analyses caused a monotonic decrease in totals during the session, but drift was corrected by using the Arenal hornblende EPMA totals. Table 1 shows the experimental results of Arenal hornblende during the session compared to values reported in the work by Jarosewich *et al.*, (1980); most analyses are close to those reported in the literature for Arenal hornblende, except TiO_2 and Na_2O, which are significantly different than the published values (21% lower and 11% higher, respectively; see section on Mineral Chemistry).

Mineral formula recalculation

EPMA data was culled, and outliers were removed by checking for low totals and anomalously high or low measurements of each oxide in respect to the mineral analyzed. Selected EPMA data of all silicate phases were recalculated using internal spreadsheets used at

Louisiana State University with the most up-to-date mineral configurations. Stoichiometric mineral formula recalculations were additionally recalculated and plotted using the program MinPlot (Walters, 2022) for olivine, plagioclase, garnet, amphibole and pyroxene. Oxide mineral EPMA data was recalculated using the End Members Generator software (Ferracutti *et al.*, 2015). Amphiboles present in these samples prove the most challenging to classify, particularly because OH and trivalent Fe cannot be directly measured with EPMA. The most recent IMA nomenclature (Hawthorne *et al.*, 2012) was used for classification through the MinPlot software. Composition was based on >23 O atoms per formula unit (APFU), and the OH = 2 – 2Ti correction was not implemented, as it produced results that could not be plotted on the Hawthorne *et al.* (2012) plot for calcic amphiboles. To compare with previous literature, the classification of Leake *et al.* (1997) was also implemented.

In-situ LA-ICP-MS

Single minerals in thin section from Saliceto samples AM-IVZ-VM-007, AM-IVZ-VM-006, AM-IVZ-VM-009, and AM-IVZ-VM-017, which are pyroxenite, two olivine gabbros, and gabbro-norite, respectively, were analyzed in-situ with laser ablation inductively coupled plasma mass spectrometry (LA-ICP-MS) at the Department of Earth Sciences at ETH Zurich (Switzerland). A Thermo Element XR Sector-field ICP-MS with the attached 193 nm Resonetics Resolution 155 laser ablation system was used. A spot size of 43 µm was used for all minerals excluding apatite, Fe-Ti oxides, and Al spinel, which were analyzed with a 29 µm spot size. A 5 Hz repetition rate and 3.5 J/cm^2 laser energy density was used. The internal standard used for each mineral was mean Si for silicate minerals, Ca for apatite, and Mg for oxides from EPMA data acquired at Louisiana State University. External standards accompanying the sample analyses included NIST SRM610 (Jochum *et al.*, 2011), BCR-2G (Gao *et al.*, 2002), and GSD-

1G (Guillong *et al.*, 2005). Procedures followed the methods of Woodhead *et al.* (2007), and data was processed using Iolite software (Paton *et al.*, 2011).

Bulk rock analysis

Rock preparation for bulk rock analysis

Bulk rock analyses were conducted at both the University of Lausanne and ETH Zurich (Switzerland). At the Institute of Earth Sciences (ISTE) facilities of the University of Lausanne, 28 samples were analyzed for bulk rock compositions, of which 27 were from the 2017 field mission and one Saliceto pyroxenite (sample AM-IVZ-VM008) from Saliceto. The samples from the 2017 field mission were selected based on their location; all weathered samples were excluded from the set of analyses. Each sample was individually crushed with a hydraulic press to <4 mm. Samples were then transferred to a 110 mL agate mill and milled for 120 seconds. Both hydraulic press and agate mill were cleaned thoroughly with isopropyl alcohol between each cycle of rock crushing and pulverization.

Similarly, three samples of garnet olivine gabbro from Saliceto (AM_VM22_14d, AM_VM22_6fl, AM_VM22_6fd) and a gabbroic sample from Ferrara (AM_VM22_3b) were prepared for bulk rock analysis at the Department of Earth Sciences at ETH Zurich. These samples were crushed with a hydraulic press and milled with a 110 mL agate mill. The agate mill was cleaned with alcohol and pure quartz sand between each cycle of sample crushing and pulverization.

Loss on ignition (LOI) was performed on bulk rock powders. Samples were placed in ceramic crucibles and heated to 1050 °C for two hours at both the University of Lausanne and ETH Zurich facilities. LOI was calculated by measuring the mass of the bulk rock powders before heating and after cooling.

At the University of Lausanne facilities, dried and cooled bulk rock powders were manually ground with mortar and pestle for three minutes. A mass of 6.0000 +/- 0.0002 g of sample was thoroughly mixed with 1.2000 +/- 0.0002 g of lithium tetraborate ($Li_2B_4O_7$). Mixtures were placed in platinum crucibles then melted at 1200 °C to form fused glass disks using a Claisse fluxer. A 1:5 ratio of bulk rock powder to $Li_2B_4O_7$ mixture was used at ETH Zurich facilities and heated to 1080 °C in a Claisse M4® fluxer until fully melted. A releasing agent was used to mitigate the surface tension concavity of the fused glass disk during cooling at ETH Zurich.

Bulk rock XRF

For bulk rock major element analysis, X-ray fluorescence spectrometry (XRF) was performed on fused glass disks using a wavelength dispersive X-ray fluorescence spectrometer PANalytical AxiosmAX equipped with a 4.0 KW Rh X-ray tube housed at the ISTE of the University of Lausanne (Switzerland). At facilities of the Institute of Geochemistry and Petrology of the ETH Zurich, the three Saliceto garnet olivine gabbros and the single Ferrera gabbro (sample AM-IVZ-3b) fused glass disks were analyzed via XRF using a PANalytical AXIOS wavelength-dispersive X-ray fluorescence spectrometer.

Bulk Rock LA-ICP-MS

To quantify trace elements in bulk rock samples, a RESOlution 193 nm excimer laser ablation system coupled to a sector-field Thermo Fisher Scientific Element XR mass spectrometer was used at the ISTE of the University of Lausanne (Switzerland). Bulk rock fused glass disks previously analyzed with XRF were broken, mounted in epoxy and polished. CaO data from XRF was used as the internal standard, and glass standards SRM610, SRM612 (Jochum *et al.*, 2011) and BCR-2G (Gao *et al.*, 2002) were used as external standards. All ICP-

MS signals were checked for quality as well as surface Pb peaks which could indicate contamination. LA-ICP-MS data are reported in Table 2.

Bulk rock trace elements were analyzed similarly at ETH Zurich. After XRF analysis, fused glass disks were broken and mounted to a holder. An ASI RESOlution S-155 excimer laser ablation system coupled to a Thermo Element XR sector-field ICP-MS was used. A spot size of 40 μm, an acceleration voltage of 24 kV, and a repetition rate of 10 Hz was used for external standard NIST610. A spot size of 115 μm and an acceleration voltage of 26 kV was implemented. XRF-derived Ca was used as the internal standard, and BCR-2G (Gao *et al.*, 2002) was used as an external standard. Procedures followed the methods of Woodhead *et al.* (2007), and data was processed using Iolite software (Paton *et al.*, 2011).

Major element bulk rock analysis of olivine gabbro sample AM-IVZ-VM009 was performed at the Peter Hooper Geoanalytical Laboratory of the Washington State University using a ThermoARL Advant XP+ XRF spectrometer. Bulk rock trace elements were subsequently analyzed with an Agilent 7700 ICP-MS. Relevant sample preparation, analytical protocol, and statistical details are provided online at https://environment.wsu.edu/facilities/geoanalytical-lab/technical-notes/.

Data display and reduction with ArcGIS Pro

For in-situ EPMA and LA-ICP-MS data processing and visualization, a previously-unpublished approach was used. This method utilized ESRI software ArcGIS Pro. Each *in-situ* analytical session data was entered into ArcGIS Pro software separately, as were the relevant full thin section scans. For EPMA data gathered at ETH Zurich, a few BSE images with known stage X and Y coordinates were matched to the thin section scans, which were then used to "georeference" the thin section scans. Increments of the electron microprobe stage are in mm,

which was scaled to m (a $x10^3$ linear transformation) and projected as metric UTM coordinates. The ArcGIS Pro map was projected with a Mercator projection to minimize the effects of distortion, and distortion was minimized as scaled coordinates of the stage were near to the "equator". EPMA data points, containing elemental weight percentage (wt.%), were projected onto the georeferenced thin section scans using each point's stage coordinates. Lastly, BSE and element maps were added and georeferenced using the thin section scan base map. Fig. 9 shows the utility of this method for understanding the spatial component of mineral chemistry and the ease of connecting different data types.

Literature data

For bulk igneous rock statistics and principal component analysis of the bulk rock chemistry of the Mafic Complex, bulk rock major and trace element data was gleaned from 16 different publications. The area of study was limited to the Mafic Complex and roof rocks contained within the map of Quick *et al.* (2003); therefore, Mafic Complex rock analyses from Val Strona d'Omegna were not considered in the data compilation in this study. Work by multiple authors has shown that the Mafic Complex near the Finero Peridotite is temporally and chemically distinct from the massive intrusion of the Mafic Complex in the southern IVZ (e.g., Lu *et al.*, 1997; Zanetti *et al.*, 2013). Thus, also this data was not considered in this study.

In total, 559 bulk rock analyses containing, at a minimum, major oxide data were gathered from the following publications: Capedri (1971); Rivalenti *et al.* (1975); Pin and Sills (1986); Voshage *et al,* (1987; 1988; 1990); Burke and Fountain (1990); Mazzucchelli *et al.* (1992a); Bigi *et al.* (1993); Sinigoi *et al.* (1994, 1994, 1996, 2011, 2016); Antonicelli *et al.* (2020); Tribuzio *et al.* (2023). The 33 new bulk rock data presented in this thesis were included in all statistical analyses.

The locations of samples are shown on the map in Figure 10. Approximate stratigraphy and the nomenclature used for the northern Mafic Complex (Val Sesia and Val Mastallone transects) is shown in Figure 11. In Figure 11, boundaries are approximate as not all boundaries between lithological units perfectly parallel the Insubric Line, and there are discrepancies between maps of different authors. Lower Layered Group is from Rivalenti *et al.* (1975) and was divided into the Basal Zone and Intermediate Zone by Rivalenti *et al.* (1984). The Upper Layered Group of Rivalenti *et al.* (1975) was renamed the Upper Zone by Rivalenti *et al.* (1984) and its location in the Val Mastallone transect was provided by Sills (1984) and Pin and Sills (1986). The boundary between the Lower Layered Group and Upper Layered Group is defined differently from one publication to the next, and the location of paragneiss septa in Val Sesia that divides the units varies on different maps. On these different maps, the boundaries vary in location in the Val Mastallone transect, and often these boundaries are not parallel to the Insubric Line. The Lower Layered Group labeled in the Val Mastallone transect is based on the location of the Paragneiss-bearing Belt – Upper Mafic Complex boundary located in the map of Sinigoi *et al.* (2016), and this is supported by the immediate decrease in paragneiss septa at this location moving upward in the section (increased Insubric Line distance) as mapped by Quick *et al.* (2003). The boundary of the Upper Zone – Main Gabbro is as provided by the map of Pin and Sills (1986).

Some issues faced during the creation of this composite dataset were in the methods used for analyses (for example, wet chemical analyses for FeO and Fe_2O_3 versus XRF for total Fe_2O_3), clerical errors (found when computing sums of major oxides versus the sums reported in the published data tables). Additionally, the trace element data of gabbroic rocks provided by Pin and Sills (1984) show unusually jagged trends in the REE normalized to primitive mantle,

contrasting all other trends in the literature; therefore, trace element data was removed but the major element data retained. Lastly, some bulk rock analyses fail to report sample locations or only provide approximate locations. Capedri (1971) provides 39 bulk rock analyses from gabbroic to dioritic rocks in Val Mastallone; the provided map showed sample locations for some samples, but the remainder of samples were approximately located using the provided placenames and elevations. Rivalenti *et al.* (1975) provide the analyses of 113 samples: 26 from ultramafic rocks of the Balmuccia Peridotite Massif, 39 from the "Lower Layered Group," 20 from the "Upper Layered Group," 9 from the "Main Gabbro" for a total of 68 rocks from the Mafic Complex. These include a limited number of paragneiss samples for which no location data was provided nor indicated. Analyses of Balmuccia peridotite were excluded. Pin and Sills (1986) provide a dataset of approximately 40 samples, some including trace element and whole-rock isotopic data. Burke and Fountain (1990) provide major element data for 6 rocks from the Mafic Complex. Voshage *et al.* (1990) present many bulk rock isotopic analyses yet only a few contain major element analyses for gabbroic rocks Sinigoi *et al.* (1991) present 15 analyses, which include a limited list of trace element and isotopic (Sr, O) data for gabbroic rocks to charnockites. Mazzucchelli *et al.* (1992b) provide major element, REE, and some trace element data for gabbroic rocks from the Upper Zone; no sample locations are specified, but some locations have been provided by the author (Mazzucchelli, personal communication). Bigi *et al.* (1993) provide bulk rock analyses, with major elements and Ba for 10 rocks from the Mafic Complex; sample locations are provided with a map. Sinigoi *et al.* (1994) show 22 bulk rock analyses of rocks from the Mafic Complex in Val Sesia; analyses include major and comprehensive trace element data and some isotopic (Sr, O) data, but no sample locations are given; however, maps provided by Sinigoi *et al.* (2011) show sample locations of some samples.

Sinigoi *et al.* (1996) showcase bulk rock data from a sampling traverse in Val Mala, which is south of Val Sesia yet north of Val Sessera (Fig. 10). Sample locations were approximated using the map which provided the linear sampling traverse, and the stratigraphy, in meters. The stratigraphy along the traverse was pinned by the coordinates of sample MAL15 as provided by Sinigoi *et al.* (2011). Sinigoi *et al.* (2011) provide a large (>200) dataset with major and some trace element data for a wide range of rocks including amphibole gabbros, norites, quartz-norites, charnockites, and granitic rocks from mostly the Val Sessera transect (Fig. 10). Approximate coordinates for samples and sample location maps are provided in the online supplements of their work, however the coordinates contained errors in excess of 200 m for some samples, which were then corrected to match the sample map, where both were provided. Sinigoi *et al.* (2016) presents more (> 150) bulk rock analyses in their online supplements, some containing trace and isotopic data for gabbroic samples in the Upper Zone and Main gabbro, as well as leucosomes and paragneiss from the roof, some of which was republished from earlier works. Many analytical data of the same rock samples come from previous publications of the same authors. Sample maps provided by Sinigoi *et al.* (2011) were used to correct some sample locations. Short to long (>400 m) sample traverses provided in the online supplement maps of Sinigoi *et al.* (2011) gave no specific sample locations along the traverse. For one such traverse in Val Sessera, containing >120 samples, locations of samples were approximated by using the reported stratigraphy of each sample. For another sample traverse in Val Sesia, no stratigraphy was reported, so samples were spaced evenly along the traverse line, using sample numbers adjacent and internal sample numbers to determine the order. Although this method relied heavily on assumption, the scales of these traverses are inconsequential at the scales used in analysis (8000 m).

Sinigoi *et al.* (1996) provide the most recent nomenclature of the zonation seen in the Mafic Complex. Samples plotted on the map were each assigned their respective zone based on the map of Sinigoi *et al.* (1996), with the exception that the lithological unit "Diorite" and the map of Quick *et al.* (2003) was used to distinguish these samples from the remainder of the Mafic Complex. For samples with no location data, particularly those of Mazzucchelli *et al.* (1992b) and Voshage *et al.* (1990), their general location was plotted at the center of each sample's ascribed zone (i.e., "Main Gabbro," "Upper Zone").

Determining the lithology of samples reported in the literature proved challenging, as the various authors used different nomenclature for rock types. Attempts were made to determine lithologies if modal abundances of minerals were reported. Groupings used in data analysis were the following: peridotites, pyroxenites, amphibole gabbros (including amphibole norites, amphibole gabbro-norites, and amphibole gabbros *sensu stricto*), gabbros (including norites, gabbro-norites, and gabbros), garnet-bearing gabbros (where reported), olivine-bearing gabbros (where reported), quartz-bearing norites from Sinigoi *et al.* (2011), charnockites, mafic enclaves in diorite (from this study and Sinigoi *et al.*, 2016), leucosomes from the roof of the Mafic Complex in Val Sesia, and Paragneiss from paragneiss septa and the roof of the Mafic Complex. Bulk rock data from the literature was then processed by normalizing oxides to 100 wt.% on an anhydrous basis.

Principal Component Analysis

Principal component analysis (PCA) was performed in three different ways: on ten major and minor oxides (SiO_2, TiO_2, Al_2O_3, FeO, MnO, MgO, CaO, Na_2O, K_2O, and P_2O_5), on 10 selected trace elements (Ni, Nb, Rb, Sr, Zr, Ba, La, Ce, Nd, and Y), and on both these oxides and trace element sets (20 variables). Lastly, PCA was performed on the complete set of trace

elements as above (n=20) for samples containing less than 55 wt.% SiO_2, which encapsulates the ultramafic to dioritic rocks of the Mafic Complex, in order to understand the processes of differentiation and growth of gabbroic rocks, while excluding the extreme products of differentiation and anatexis (i.e., granitoid leucosomes and charnockites). The selection of trace elements was based on usefulness in understanding the evolution of the Mafic Complex and also to maximize the number of samples that could be used. The PCA of these three groups were then also performed on the Mafic Complex as a whole, on the northern Mafic Complex samples in proximity to Val Sesia and Val Mastallone, and lastly on the samples in proximity to Val Sessera but excluding samples from Val Mala in the southern Mafic Complex. These steps resulted in performing PCA ten times. Running PCA on the northern and southern portions of the Mafic Complex separately was to assess whether the same processes of magmatic differentiation were occurring in both regions and to what degree, as the southern domain is dominated by the Lower Mafic Complex and Paragneiss Bearing Belt, whereas the northern domain is dominated by the Upper Mafic Complex (Sinigoi *et al.*, 1996). This geological division also allows plotting of principal components as a function of distance to the Insubric Line, and hence an approximation of the large-scale stratigraphy. Although distance to the Insubric Line approximates the true thickness in the northern Mafic Complex, the Insubric Line does not parallel the gross structure of the Mafic Complex in Val Sessera (see map in Snoke *et al.*, 1999).

To correct for skewness, all concentration data (reported in wt.% and ppm) were $\log_{10}$ transformed. One (1) was added to every value prior to log transformation to eliminate infinite values. PCA was then performed with a correlation matrix using R statistical software (R Core Team, 2022). Because one goal of PCA is to reduce the dimensionality of the data, principal components that fell above the average explained total variance as plotted on a scree plot were

selected. However, some principal components (PCs) which fell below the average if each principal component explained an equal amount of variance were retained for analysis.

As ultramafic lithologies are part of the Mafic Complex intrusion (e.g., Rivalenti *et al.*, 2017; Tribuzio *et al.*, 2023) and represent the cumulus components and end members of magmatic differentiation, they were included in principal component analysis of major elements. However, for PCA that included trace elements, the analyses of peridotite from Roca d'Argimonia (Tribuzio *et al.*, 2023) appeared to dominate the principal components, as they are highly enriched in compatible elements and depleted in incompatible elements. Of the trace element subset used in PCA, no pyroxenite or peridotite sample from Val Sesia and Val Mastallone contained all trace elements used for PCA, with the exception of the pyroxenite from Saliceto (AM-IVZ-VM008).

CHAPTER 4

RESULTS

Field observations and hand samples

The mafic suite of rocks at Saliceto in Val Mastallone is exposed along the roadcut across the Mastallone River from the village of Saliceto and ~6 m below the road level along the river (Fig. 8b). Rock outcrops exposed along the roadcut and along the ravine Rio della Scaravina tend to be masked by the local vegetation (plants, moss, lichen) and the metallic mesh nets used to contain rock falls along the Strada Provinciale 9. Along the roadcut, the outcrop is generally obscured by fractures and weathered surfaces, which result in poorly defined locations of contacts between lithologies (e.g., Fig. 8a). The outcrops exposed along the river are better exposed and some of the lithological contacts are better resolved.

Magmatic structures, contacts, and brittle features

The rocks are in places fractured. The Alpine fault mapped by Quick *et al.* (2003) dissecting the bend of the Mastallone River at Saliceto is recognizable in Rio della Scaravina, in the southwestern section of the field area. Here, garnet-rich olivine gabbros have a brittle contact with leuco-gabbros with fault gouge and a fracture zone (Fig. 12a). This fault is not found along the road outcrop nor along the river exposure where the sequence of lithologies appears to be continuous with no evident tectonic displacement. Fractures do not show notable displacement at lithological contacts along the river outcrop (Fig. 12b).

Structural features observed in Saliceto at outcrop scale are dominantly mineralogical banding and curved lithological contacts. Continuous to discontinuous banding is found

throughout the suite of rocks at Saliceto and is identified by plagioclase-dominant bands (leuco-gabbros) in contact with bands containing relatively increased modal abundances of mafic minerals (mela-gabbros) to ultramafic lithologies. Where exposed, bands vary from sub-centimeter scale to meters (Fig. 13a) in thickness. These bands strike between 10° and 20° and dip subvertically to 80° W.

In places, lithological boundaries are not only defined by changes in modal mineralogy, but also by sharp contacts that are either smooth, curvilinear boundaries between lithologies or brittle, faulted contacts. In particular, on the river exposure, a body of garnet amphibole mela-gabbro (same as sample AM-IVZ-VM011) is in contact with a garnet amphibole leuco-gabbro with a well-defined contact that appears to be sharp and displays local wisps of interacting mela-gabbro and leuco-gabbro (Fig. 13b). The same contact also contains brittle features that are distinguishable from the smooth curvilinear boundaries (Fig. 12b).

Sharp to gradual changes in modal mineralogy are also found in the ultramafic pyroxenite (sample AM-IVZ-VM008), where anorthositic veins crosscut the orthopyroxene- and amphibole-dominant rock. Bands of large (>1 cm) poikilitic amphiboles are found cross-cutting or roughly parallel to mineralogical banding in all lithologies.

The road outcrop in Saliceto transects the banding obliquely, with the northern end of the outcrop representing stratigraphically up and the southern end exposing the lowest stratigraphic section of the Saliceto suite. Lithologies could not be traced down to the river level but, at higher elevations, lithologies could be traced to Rio della Scaravina in the southern portion of the studied section. Therefore, the road outcrop is used as the basis of the overall igneous stratigraphy, given the limits of traceability to the river outcrops and to the Rio della Scaravina gully outcrops.

Samples

In the south-most portion of the road outcrop, north of the Rio della Scaravina culvert, garnet-free, amphibole to amphibole-free gabbro-norites are found. The fault plane found in Rio della Scaravina is defined higher up in the gully, but it is not clearly exposed at road level. The fault does not appear to break the continuity of the stratigraphic section presented in this study.

Northward along the road outcrop, and stratigraphically above leucocratic olivine-free gabbros, olivine and garnet-bearing rocks are encountered (sample AM-IVZ-VM010, Fig. 14a-c). Of note, sample AM-IVZ-VM010 has a high color index (> 90 modal % mafic minerals) and contains a large, poikilitic amphibole crystal measuring 5.4 cm in its longest dimension (Fig. 14b) as well as platy biotite (Fig. 14c), garnet, and olivine. The contact with garnet- and olivine-free rocks to the south of this sample location is not well defined and may be gradational.

Stratigraphically above and northward, rocks are banded and vary between leucocratic gabbros with large proportion of plagioclase and melanocratic gabbros with garnet and amphibole as the dominant mafic. Samples AM-IVZ-VM009 (Fig. 14d-e) and AM-VM22-6 (sub-samples a through f; Fig. 14f-h) were sampled within half a meter of each other perpendicular to banding. Samples AM-IVZ-VM007 (Fig. 15a-b), AM-IVZ-VM008 (Fig. 15d-f) and AM-IVZ-VM006 (Fig. 15c) are stratigraphically above by about three meters and range and appear melanocratic with garnet and amphibole as dominant phases (AM-IVZ-VM006 – VM007) to ultramafic (AM-IVZ-VM008). This ultramafic rock is pyroxenitic and is the most distinctive and unique lithology in the study area due to its high color index (>90) and lack of garnet. Greenish olivine is present in this lithology but not recognizable without the use of a hand lens. The contact of the pyroxenite and the plagioclase-rich olivine gabbro remains undefined due to overgrowths of plants and weathering (e.g., Fig. 8a).

For ~70 m northward along the road exposure, rocks are banded with essential components of plagioclase, orthopyroxene, clinopyroxene and varying percentages of amphibole and garnet but devoid of olivine. Sample AM-IVZ-VM005 is ~20 m from north of the olivine-bearing rocks, separated by a small gully, and contains mesocratic garnet-free amphibole gabbro-norite outcrops (Fig. 16a – b). Northward by ~5 m a garnet amphibole norite (sample AM-IVZ-VM004) outcrops (Fig. 16c – d), and about 4 m northward, an amphibole gabbro with bands of large, elongated (>1.5 cm in longest dimension) poikilitic amphiboles is exposed (sample AM-IVZ-VM003, Fig. 16e – f). Again, northward by ~5 m, a garnet gabbro-norite outcrops (sample AM-IVZ-VM002, Fig. 16g). North of sample AM-IVZ-VM002, rocks are banded and contain varying amounts of amphibole and garnet. Lastly, at the northern end of the outcrop and the northernmost end of the studied section, garnet-free and amphibole-free gabbro-norite (sample AM-IVZ-VM001, Fig. 16h) outcrops.

Along the river, samples were collected from rock exposures where a narrow (< 0.5 m) band of melanocratic, garnet-rich gabbro is in contact with garnet amphibole gabbro-norites stratigraphically below and gabbro-norites and norites ± garnet ± amphibole stratigraphically above (Fig. 17a). The contact of these lithologies is curvilinear and is roughly parallel to banding (Fig. 13b). Sample AM-IVZ-VM014 is a mesocratic garnet amphibole gabbro and is found stratigraphically below the dark, garnetiferous band. Sample AM-IVZ-VM012 captures the contact between the mesocratic garnet amphibole gabbro and the melanocratic garnetiferous rock (Fig. 17c). Sample AM-IVZ-VM011 is a holomelanocratic garnet amphibole gabbro with 10 – 15 vol.% plagioclase (Fig. 17d). Amphibole gabbro-norites are found stratigraphically above the garnetiferous body (Fig. 17e-g).

Southward of the previous sampling location by ~5 m along the river, banded yet relatively homogeneous gabbro-norite outcrops are identified. Banding is noticeable in hand sample, and these gabbro-norites display up to 1 cm thick bands of coarse-grained amphiboles (sample AM-IVZ-VM017, Fig. 18a – b). About 20 m southward and stratigraphically at the base of the studied section, gabbro-norite with strongly-banded appearance outcrops (sample AM-VM22-9a, Fig. 18c). These lithologies display thick (>10 cm) bands, or as narrow (<1 cm) bands that vary both compositionally (relative increase or decrease in pyroxene modal abundance) and in grain size (coarse-grained to medium-grained).

In Rio della Scaravina gully, adjacent to the fault zone mapped by Quick *et al.* (2003), olivine-bearing lithologies are exposed. These rocks are approximately on-strike with the olivine gabbros at the road level. Sample AM-VM22-13 contains pseudotachylite in a fracture, and garnet corona abundance varies within hand sample. Sample AM-VM22-13 appears to be a garnet-free pyroxenite, much like the pyroxenite sample (AM-IVZ-VM008, Fig. 15d – f) but this could not be confirmed as no thin section was created. Garnet amphibole olivine gabbro is dominant in this exposure (Fig. 18e, f), and the contact of mesocratic and melanocratic portions of sample AM-VM22-14 (Fig. 18g) appear to only vary in plagioclase modal abundance.

Rock types and petrographic characteristics

Based on optical observations of the rock thin sections, all samples of Saliceto mafic rocks show varying degrees of mineralogy and textural complexity. Ubiquitous minerals found throughout all the studied rocks are plagioclase and orthopyroxene. Variable modal proportions of amphibole, garnet, olivine, apatite, oxides and sulfides are relevant to discriminate the different lithologies in the suites of rocks in Saliceto. Here, I present a summary of the main mineralogical and textural features based on the characterization of 57 rock thin sections.

All samples show signs, in varying degrees, of secondary alteration and weathering, such as epidotization, chloritization, hematization and surface weathering. In places, these alterations are so widespread that they partially obscure the primary textures. However, in most of the collected rocks, original textures are well preserved and single minerals are identifiable. Brittle microfractures are pervasive in all samples, but none show severe displacement or deformation at mineral scale. Many grains in all lithologies show evidence of annealed microfractures, and deformation twins in plagioclase are common. Epidotization of plagioclase is concentrated in the more-anorthitic cores of plagioclase. In this study, primary magmatic and high-grade metamorphic features are described without focusing on the low-grade features such as chlorite or alteration of olivine.

Rocks in the Saliceto mafic/ultramafic suite are subdivided into two groups: gabbroic rocks and ultramafic rocks. Anorthite content of plagioclase cores in the mafic rocks is mostly $>An_{50}$, and therefore the rock is considered gabbroic. Therefore, the olivine-orthopyroxene-clinopyroxene and pyroxene-plagioclase-hornblende ternaries are utilized for classifying all the Saliceto mafic rocks (Le Maître *et al.*, 2002). Consistently with approaches applied in previous studies on rocks from the Ivrea-Verbano Zone (e.g., Quick *et al.*, 2003), *amphibole* replaces *hornblende* for rock names. The prefix *meta*-, denoting the metamorphic history of these rocks, is excluded for the following rock nomenclature (Rivalenti *et al.*, 1975).

Table 2 contains the mineral name abbreviations used in this work, and Table 3 reports mineral modes of selected samples from point counting using the combination of optical microscope, point-counting stage, and JMicro-Vision software on full thin section scans. Figure 19a shows point counting results on the pyroxene – plagioclase – olivine ternary diagrams and with calculated CIPW norms from bulk rock data (see section: CIPW Norms), and Figure 19b

presents the point count data normalized to the pyroxene – plagioclase – amphibole ternary diagram for selected olivine-bearing thin sections and samples, as well as the pyroxenite sample (sample AM-IVZ-VM008, thin section B3).

Based on mineral modal proportions, the mafic suite of rocks at Saliceto is subdivided in three lithologies: 1) gabbro-norite, which contains essential components of plagioclase and orthopyroxene with varying clinopyroxene, amphibole, and garnet; 2) olivine-bearing gabbro, which contains essential components of plagioclase and olivine, with varying abundances of garnet, amphibole, pyroxene and accessory minerals; and 3) plagioclase-bearing amphibole pyroxenite, which contains the essential component of orthopyroxene with varying amphibole, clinopyroxene, plagioclase, olivine, and accessories. In this work, garnet amphibole olivine-bearing gabbro is called *olivine gabbro* for simplicity. These three groups share many characteristics, but their differences are important to testing the initial hypothesis regarding the emplacement of the original magmas forming these rocks by cooling in the Sesia Magmatic System.

Gabbro-norite

Gabbro-norite is the dominant rock type in the Saliceto mafic suite. There is a relative variability in modal abundance of orthopyroxene to clinopyroxene across this mafic suite. Where clinopyroxene is <5 vol.% normalized with orthopyroxene and plagioclase, the rock is a norite, whereas, in the opposite scenario with clinopyroxene is more abundant than orthopyroxene and plagioclase, the rock is a gabbro (*sensu stricto).* At Saliceto, orthopyroxene is greater than clinopyroxene in modal abundance with limited exceptions. Amphibole and garnet in these olivine-free gabbro-norites both vary from 0 to ~30 vol.%. Minor constituents of gabbro-norites

are apatite, Fe-Ti oxides, spinel, and sulfides. Gabbro-norites are distinguished from the olivine-gabbros by their lack of olivine.

Garnet-free gabbro-norite is found in the southernmost part of the outcrop, which corresponds to the lowest stratigraphic level in the studied section, as inferred from structural relationships documented by Quick *et al.* (2003). Sample AM-VM22-9a is a gabbro-norite and contains accessory oxide minerals and amphibole (Fig. 20). This sample also shows banding defined by mineralogy and grain size noted previously (Fig. 18c). Gabbro-norite is also found in the most northern sampling location and thus the uppermost portion in the studied magmatic stratigraphic sequence (sample AM-IVZ-VM001, Fig. 21). This sample is garnet-free and amphibole-free and contains accessory biotite. Sample AM-IVZ-VM017 is a garnet-free gabbro-norite and contains bands of poikilitic amphiboles (Fig. 18a – b). In thin section A17 of this sample, pyroxenes form sub-continuous bands. Also in this thin section, pyroxene c-axes are parallel to the banding; clinopyroxene increases and oxide minerals decrease in modal abundance closer to the band of amphiboles. Generally, garnet-free gabbro-norites have the basic assemblage of rounded, subhedral orthopyroxene, accompanied by plagioclase and variable amounts of rounded subhedral to coronitic clinopyroxene.

The amphibole norite/gabbro-norites (Fig. 23a) and garnet amphibole gabbros/gabbro-norites (Fig. 23b) appear similar to gabbro-norites from both microstructural and mineralogical standpoint. However, both rocks contain varying modal proportions of garnet coronas (0 – 30 vol.%) and subhedral to corona-type amphibole (< ~30 vol.%). Garnet coronas are rarely to never found in rocks with less than ~5 vol.% amphibole. Garnet amphibole norite containing <10 vol.% plagioclase could be considered an ultramafic rock, but it is included with the gabbro-norite grouping as the primary igneous mineralogy matches that of the norites, yet it also

contains complex symplectites of pyroxene with vermicular magnetite intergrowths, and no chemical data of this rock was gathered that could be used to show it is significantly chemically different from the gabbros and gabbro-norites (Fig. 24).

Figure 25 shows the general petrographic characteristics of gabbro-norite. Orthopyroxene is subhedral and rounded and is, in places, mantled by clinopyroxene. Orthopyroxene generally shows distinctive greenish to pinkish pleochroism in plane-polarized light and parallel to inclined extinction in cross-polarized light. Clinopyroxene is strongly exsolved and may also be found as subhedral grains >1 mm. Plagioclase sometimes contains Al-spinel exsolutions and shows recrystallization. Some samples contain both apatite and Fe-Ti oxides, but some gabbro-norites do not, and this change may be observed in a single thin section (e.g., Fig. 22a).

Olivine gabbro

Garnet amphibole olivine gabbros are distinguished from gabbro-norites by containing olivine (Fig. 26). However, olivine-bearing rocks share most of the characteristics of the garnet amphibole gabbro-norites but are devoid of symplectites. Olivine gabbros contain between 12 and 70 vol.% plagioclase, 8 – 33 vol.% garnet, 3 – 15 vol.% pyroxene (Cpx + Opx), 3 – 19 vol.% olivine, and 9 – 16 vol.% amphibole (Table 2). Opaque minerals in olivine gabbros (~3 – 9 vol.%) are primarily ilmenite with subordinate magnetite, Al spinel, and sulfide minerals (pyrrhotite, pentlandite, chalcopyrite). Apatite ranges from ~1 to 4 vol.%, but apatite was likely undercounted in some thin sections due to the difficulty of distinguishing plagioclase and apatite in full thin section scans when point counted using JMicrovision software. Olivine is skeletal and mantled by multiple corona types (Fig. 27), but in some samples with lower olivine abundance, olivine and plagioclase appear in textural equilibrium and coronas are discontinuous. Of the ~14

olivine gabbro thin sections in this study, only one contains a symplectite composed of vermicular Al spinel in clinopyroxene.

Pyroxenite

Pyroxenites share many characteristics with gabbro-norites and olivine gabbros but is devoid of garnet. Pyroxenites are primarily composed of orthopyroxene and subordinate amphibole and olivine, and with <10 vol.% plagioclase. The single pyroxenite thin section (B3, Fig. 28) is representative of a plagioclase-bearing amphibole-orthopyroxenite portion of sample AM-IVZ-VM008, but other thin sections have higher modal spinel, olivine, and Fe-Ti oxides (e.g., Fig. 27). Anorthositic veins seen in hand sample (Fig. 15f) have sharply-defined yet irregular contacts with the pyroxenitic portions, and these veins contain >99 vol.% plagioclase with trace Al-spinel as exsolutions in plagioclase grain cores and at plagioclase grain boundaries (Fig. 29).

Bulk rock analyses of AM-IVZ-VM008 pyroxenite, analyzed with least squares regression spreadsheet of Li *et al.* (2020) using bulk rock and mineral EPMA data inputs, shows that the bulk rock of the "pyroxenite" is modally orthopyroxene dominant (29 vol.%) with olivine (16 vol.%), clinopyroxene (15 vol.%), amphibole (15 vol.%), spinel (10 vol.%), plagioclase (9 vol.%), and ilmenite (5 vol.%). This rock can be classified as a plagioclase-bearing olivine amphibole spinel pyroxenite (Le Maitre *et al.*, 2002). In this study, this rock will be simply called a pyroxenite. In the orthopyroxene-rich domain, orthopyroxene grains are large (up to 2 cm, e.g., Fig. 28), but other domains show a finer grain (<1 mm) texture as a polygonal mosaic of amphibole and orthopyroxene +/- oxides +/- olivine (Fig. 29).

Mineral petrographic and microstructural characteristics

Pyroxenes

Orthopyroxene is distinguished by its pinkish to greenish pleochroism and biaxial negative optical sign. Orthopyroxene is strongly pleochroic with some grains showing strong green to pink pleochroism in all samples. Orthopyroxene is sometimes mantled by clinopyroxene in a corona-like texture, but clinopyroxene also forms as >1 mm subhedral grains and are strongly exsolved, including corona-like clinopyroxene (Fig. 25). Pyroxenes are elongated parallel to the banding in gabbro-norites. Rare orthopyroxene in olivine gabbro appears primarily as a corona between olivine and other minerals. Orthopyroxene is also accompanied by symplectites with Al spinel in pyroxenite and with magnetite in garnetiferous melanocratic norite (Fig. 24).

Orthopyroxene is the primary constituent in pyroxenites and is found as large (>0.8 cm) grains. These grains sometimes show plastic deformation in the form of curving exsolution planes. Orthopyroxene in both gabbro-norite and pyroxenite contains remarkable clusters of ilmenite or rutile exsolutions, and some of these exsolutions reach 1 mm in length (Fig. 28).

Plagioclase

Plagioclase is modally dominant (> 50-60 vol.%) in gabbro-norite and olivine gabbro, but <10 vol.% in pyroxenite. Plagioclase is recrystallized, showing 120° grain boundaries in some places but curved and irregular in others, and plagioclase grain size is often >2 mm. Additionally, plagioclase shows zonation by different extinction angles between the core and rims of grains. Particularly, in olivine gabbro and pyroxenite, plagioclase contains exsolutions of Al-spinel mainly within the cores of plagioclase grains. Al-spinel exsolutions in plagioclase sometimes contain small (<5 μm) magnetite exsolutions near their tips. Plagioclase grain cores

containing Al spinel exsolutions generally have an extinction angle that is different from the surrounding exsolution-free plagioclase yet the same as the rim. As shown in Fig. 30, there appears to be both a shape-preferred orientation as well as a crystallographic preferred orientation exhibited by plagioclase in olivine gabbro. Crystallographic preferred orientation is identified through plagioclase Albite Law twins identified in cross polarized light (Fig. 30), which form on the (010) plane of plagioclase (e.g., Vance, 1961). Plagioclase grains with twinning at high angles to the overall foliation appear to be subgrains and are shorter in the [100] or [001] direction.

Apatite, oxide minerals, and sulfide minerals

Apatite and Fe-Ti oxides are almost exclusively co-present in gabbro-norite and in olivine gabbro, but this association does not hold in the pyroxenite, which has modally abundant ilmenite but trace apatite. Apatite is subhedral and found as inclusions within other minerals such as orthopyroxene (Fig. 25a), amphibole, and rarely olivine but is often found proximal to or intergrown with ilmenite (Fig. 25a). In sample AM-IVZ-VM008 pyroxenite, two small (<10 μm), euhedral apatite grains are found fully enclosed within a rounded 250 μm grain (Fig. 31). In fact, euhedral to subhedral apatite inclusions within ilmenite are found in most TiO_2-rich rocks of the Mafic Complex presented in this work. In some instances, the c axis of euhedral apatite grains is discordant to the magnetite exsolution planes present in some ilmenite grains. Apatite rarely exceeds 0.5 mm, but a single grain >2 mm is found in the garnetiferous melagabbro in the river outcrop (sample AM-IVZ-VM011). Apatite may also be found within plagioclase-dominant areas (Fig. 25b).

Oxide minerals form complex intergrowths in gabbro-norites and pyroxenites, but ilmenite and magnetite can be found without exsolutions of either, even within the same thin

section. Complex oxy-exsolution microstructures are common and consist of magnetite with little exsolutions of other phases and ilmenite with exsolutions of Al-spinel (hercynite – spinel solid solution), and rarely, corundum (Fig. 32). Granular ilmenite may contain exsolutions of magnetite and vice versa. Also, spinel is commonly found as irregular to blebby grains, often fine exsolutions of magnetite.

Pyrrhotite with inclusions or exsolutions of pentlandite and chalcopyrite are sometimes associated with oxides. Although uncommon, oval-shaped sulfide inclusions are found enclosed within olivine and orthopyroxene. Pyrrhotite is secondarily altered to pyrite and hematite or to an unknown, potentially hydrous, sulfur-bearing mineral.

Amphibole

Amphibole is found in minor amounts in gabbro-norites but also as a major constituent in amphibole gabbro-norites (± garnet), olivine gabbro, and especially in pyroxenite. Amphibole is strongly pleochroic, varying from light to dark brown. Amphibole portrays two different textural arrangements: first, as anhedral corona-like grains that mantle pyroxenes, and secondly, as equant, oikocrystic subhedral to euhedral grains that are commonly >0.5 cm. These two types are rather compositional endmembers, because there is considerable chemical overlap between them. Large amphibole oikocrysts in gabbro-norite sample AM-IVZ-VM017 (Fig. 22) contain a variety of chadacrysts, including pyroxene, euhedral amphibole grains, oxides (which display oxy-exsolution microstructures), apatite, and sulfides (Fig. 33). These amphiboles have exsolutions of clinopyroxene.

Peritectic orthopyroxene and magnetite

In pyroxenite, small, rounded to skeletal olivine grains are often found within large orthopyroxene oikocrysts. In places, olivine is surrounded by oxides and orthopyroxene (Fig.

34). Oxysymplectites, composed of ilmenite or magnetite in orthopyroxene, are rare. Aluminum spinel is found as large (up to 1 mm) subhedral grains often associated with magnetite and ilmenite.

Symplectites

Al-spinel symplectites appear as vermicular Al-spinel grains enclosed in both orthopyroxene and clinopyroxene, but more dominantly in the latter, and this symplectite type is found in the pyroxenite (AM-IVZ-VM008, Fig. 35). Rarely, magnetite and orthopyroxene symplectites are found at olivine and orthopyroxene ± amphibole contacts. The garnetiferous mela-gabbro in the river outcrop (AM-IVZ-VM011) contains symplectites composed of vermicular magnetite and rarely ilmenite enclosed in orthopyroxene grains. Spinel-pyroxene symplectites are found between orthopyroxene and plagioclase primarily, and where the adjacent plagioclase contains Al spinel exsolutions, some of these exsolutions cross the symplectite – plagioclase grain boundary and the alignment of vermicular spinel inside the symplectites is at a different orientation compared to the Al spinel exsolutions (Fig. 36).

Garnet coronas

Garnet is found in both gabbro-norite and in olivine gabbro. It is the only mineral that is fully coronitic in nature found in the rocks from Saliceto considered in this study, and no porphyroblastic garnets were found in proximity to Saliceto. Garnet forms coronas between plagioclase and the following minerals: olivine, orthopyroxene, clinopyroxene, amphibole, and oxide minerals (Fig. 27 and 37). All olivine gabbro rocks contain garnet coronas with some exceptional garnet- and corona-free olivine-plagioclase boundaries; garnet coronas are most extensive in the melanocratic bands of olivine gabbro, but in plagioclase dominant bands, olivine is often found in equilibrium with plagioclase. In the garnetiferous melagabbro at river level

(sample AM-IVZ-VM011, Fig. 24), garnet is found between all mafic minerals and plagioclase and forms continuous coronas. In garnet-bearing gabbro-norites and olivine gabbros, garnet appears to be the last corona to develop (Fig. 28). Aluminum spinel exsolutions generally found in the center of plagioclase grains sometimes abut garnet coronas around plagioclase, but the Al spinel exsolutions do not continue into the garnet coronas. In one instance where exsolutions abut a garnet corona, sub-micron thick, oriented inclusions of an unknown mineral are found within the corona.

Mineral chemistry

Olivine

Olivine is present in both the olivine gabbro and orthopyroxenite, and selected olivine EPMA analyses and their recalculated formulas are presented in Table 4. Olivine gabbro samples AM-IVZ-VM009 and AM-VM22-6c both have mean forsteritic content (Fo) of 57 mol.%. Orthopyroxenite sample AM-IVZ-VM008 has a mean Fo of 63 mol.% (Fig. 38). Nickel oxide concentration is < 0.03 wt.% for all olivine grains here analyzed. Rare Earth elements in olivine are low and close to the limit of detection for *in-situ* LA-ICP-MS analysis, but average Co is ~155 ppm in olivine gabbro and ~150 ppm in pyroxenite (Table 13).

Orthopyroxene

Major element data of orthopyroxene from all rocks analyzed with WDS EPMA shows that orthopyroxene is enstatite in composition (Fig. 39) and elemental data is presented in Table 5. Notably, the enstatite from both the orthopyroxenite and olivine gabbro have the same composition in terms of major elements, yet both are closer to the enstatite endmember (~56 mol.% En) than the gabbronorite (~49 mol.% En) (Fig. 39). Orthopyroxene contains between 3

and 4 wt.% Al_2O_3, and orthopyroxene from olivine gabbro contains between 2.5 and 3 wt.% Al_2O_3 (Fig. 40). The majority of the analyzed orthopyroxenes contain less than 0.15 wt.% TiO_2.

Trace element data is presented in Table 13. Normalized to primitive mantle (Hofmann, 1988) orthopyroxene shows high variability in enrichment for Ba, K, Th, U, and Nb between and within samples (Fig. 41a). Gabbronorite shows variability in Ba for some spot analyses, but, for the other lithologies, Ba concentration is below the limit of detection. All samples show a negative Y anomaly and a strongly negative Sr anomaly. Orthopyroxene in the gabbro-norite and orthopyroxenite show depletion in LREE with increasing enrichment to HREE (Fig. 41a). Most samples show a positive Eu anomaly (Eu/Eu* is equal to chondrite-normalized Eu divided by the geometric mean of chondrite-normalized Sm and Gd); orthopyroxene from pyroxenite has an average Eu/Eu* of 4.2 while gabbronorite has an Eu/Eu* of 1.7. Orthopyroxene from the gabbronorite (AM-IVZ-VM017) is more enriched in MREE to HREE than orthopyroxene from the orthopyroxenite and the olivine gabbro by approximately one order of magnitude (Fig. 41a). The orthopyroxene in the olivine gabbro (AM-IVZ-VM009) does not show the same enrichment in both MREE to HREE; this rock is more enriched in MREE and more depleted in HREE compared to orthopyroxene in pyroxenite (AM-IVZ-VM008, Fig. 41a). Overall, trace element concentrations from the different lithologies overlap in LREE, but the gabbronorite is more enriched in Nd to Lu (Fig. 41a).

Clinopyroxene

Clinopyroxene EPMA elemental data and recalculated formulas are presented in Table 6 and clinopyroxene trace elements are presented in Table 13. Normalized to pyroxene ternary components, clinopyroxene from all samples is mostly diopside (Fig. 39). Clinopyroxene chadacrysts and cumulus clinopyroxene from the gabbro-norite have almost indistinguishable

compositions. Clinopyroxenes from all samples show a range of Ca-tschermak substitution from about 5 to 12 mol.% (Table 6). Coronitic clinopyroxene mantling olivine in olivine gabbro and clinopyroxene from gabbro-norite show decreasing Al_2O_3 with increasing Mg# (Fig. 40c). All clinopyroxene show a positive correlation between Al_2O_3 and TiO_2 (Fig. 40d).

Normalized to primitive mantle (Hofmann, 1988) clinopyroxene is enriched in Zr (Fig. 41b). REE in clinopyroxene show a positive Eu anomaly for all lithologies (Fig. 41b). An increasing enrichment trend from La to Nd (LREE) is observed for both the olivine gabbro (AM-IVZ-VM009) and the gabbro-norite (AM-IVZ-VM017) with similar mean concentrations of La to Eu (Fig. 41b). Clinopyroxene in pyroxenite (AM-IVZ-VM008) has significantly lower REE than olivine gabbro and gabbro-norite and shows a decreasing enrichment trend for the LREE (Fig. 41b). Clinopyroxene in the orthopyroxenite shows a slightly decreasing HREE trend and is significantly depleted compared to the clinopyroxene in the gabbronorite (Fig. 41b). Clinopyroxene in the olivine gabbro shows a strong decreasing trend from Eu to Lu, and clinopyroxene/chondrite is <1 from Tm to Lu (Fig. 41b).

Plagioclase

Geochemical results show that plagioclase minerals found in the rocks from this study mainly consist of labradorite and andesine (Fig. 42). Selected EPMA data is presented in Table 7. Plagioclase in orthopyroxenite sample (AM-IVX-VM008) has a mean anorthite content (An) of ~53 mol.% and ranges from An_{49} to An_{67} (Table 7). There were two EPMA data outliers that had An of 13.4 and 18.4 mol.%, but these analyses were from grains that had An representative of the rest of the plagioclase (Fig. 42). Plagioclase is characterized by normal zonation, showing more anorthitic cores and more albitic rims, but An decreases near patches of Al spinel exsolutions, which are found at the center of plagioclase grains (e.g., Fig. 36). Plagioclase in

olivine gabbro samples (AM-IVZ-VM009 and AM-VM22-6c) have mean An_{48} to An_{53}, respectively. Plagioclase in sample AM-IVZ-VM009 ranges from An_{39} to An_{63}. In sample AM-VM22-6c, plagioclase ranges from An_{36} to An_{64}. Gabbronorite (sample AM-IVZ-VM017) contains two populations of plagioclase based on petrographic observation: one population is part of the cumulate texture, and the other population of plagioclase is represented by the chadacrysts located inside the large amphibole oikocrysts (Fig. 22). Large plagioclase grains in the gabbronorite have a mean value of An_{57}, whereas the chadacrysts in amphibole oikocrysts have a mean of An_{45}. Cumulate plagioclase ranges from An_{54} to An_{59}, whereas the plagioclase chadacrysts range from $An_{1.5}$ to An_{56}. The three albitic chadacryst analyses are from grains that are found together with labradoritic grains.

Plagioclase from olivine gabbro and gabbro-norite contain Eu anomalies of 36 and 38, and pyroxenite plagioclase has an Eu anomaly of 90. A decreasing trend from La to Sm (LREE) in plagioclase is observed for all lithologies, and plagioclase in pyroxenite is less enriched than plagioclase in gabbro-norite and olivine gabbro. All samples show depletion in HREE (Dy to Lu). Normalized to primitive mantle (Hofmann, 1988), plagioclase from all samples show strong positive anomalies of Eu, Ba, and Sr (Fig. 43a). A line of spot analyses transecting 2.5 mm of the plagioclase vein in the pyroxenite (thin section B5, Fig. 29) does not reveal any significant trends in trace elements between the center and edge of the anorthositic vein.

Amphibole

Amphibole EPMA data (Table 8) show a wide compositional range for all rock samples based on the OH content set as OH=2-2Ti. The classified amphiboles are the following: magnesio-ferri-hornblende, Ti-rich magnesio-hastingsite, magnesio-hastingsite, ferri-kaersutite, kaersutite, Ti-rich sadanagaite, Ti-rich ferri-sadanagaite, and Ti-rich pargasite. Using the OH=2-

2Ti parameter, most analyses do not plot within the limits of the ^{A}(Na + K + 2Ca) APFU vs. ^{C}(Al + Fe^{3+} + 2Ti) APFU field, and in the X_{Mg} vs. Si APFU chart, all recalculated formulas fall within the Tschermakite field. Additionally, calculated Fe^{3+}/Fe_{total} ranges from about 0.2 to 0.4. Amphibole names assigned using this spreadsheet seem to vary based on EPMA facility; most hastingsite analyses were from Louisiana State University, where Cl and F were measured, whereas these elements were not analyzed at ETH Zurich facilities. With OH not set as OH=2-2Ti, results are more uniform, and resulting amphiboles are the following: Ti-rich pargasite, Ti-rich sadanagaite, magnesio-ferri-hornblende, rootname4, ferri-rootname4 using the nomenclature of Hawthorne *et al.* (2012). Locock (2014) explains that "rootname4" amphiboles are amphiboles that have not been structurally refined yet. Plotted using the software of Walters (2022), analyses of all amphiboles show that samples are both pargasite and sadanagaite, with high variability within samples and within individual grains (Fig. 44a). However, calculated $Fe^{3+}/Fe_{total} = 0$ for most samples, with outliers exceeding 0.8. Using these same parameters, the W site is assumed to be filled with OH rather than O component. Amphibole formulas recalculated using the approach of Leake *et al.* (1997) show that most amphiboles are pargasite (Fig. 44b) but some analyses of each rock type are kaersutite. Despite variance of Na_2O and K_2O values between Louisiana State University and ETH Zurich facilities, amphibole from pyroxenite appears to be relatively enriched in Na_2O and depleted in K_2O relative to amphibole from both gabbro-norite and olivine gabbro. Transects across two large amphibole oikocrysts in gabbronorite (Fig. 22) reveal increasing K_2O and decreasing Na_2O towards the amphibole rims, where the amphibole is in contact with plagioclase (Fig. 45).

Amphibole trace element data (Table 13) show a slight increase in LREE with increasing atomic number, a positive Eu anomaly, and a monotonic decrease towards HREE when

normalized primitive mantle (Figure 43b). Amphibole from pyroxenite has an average Eu/Eu* of 6.5, whereas gabbronorite amphibole average is 1.6. Amphibole gabbronorite (AM-IVZ-VM017) has significantly higher concentrations of REE than pyroxenite (AM-IVZ-VM008) but pyroxenite average is more enriched in Sr (Fig. 43b). Amphibole trace elements in olivine gabbro were not analyzed.

Garnet

Garnet EPMA data and recalculated formulas on a 12 O atom per formula unit (APFU) basis are presented in Table 9. Garnet coronas, found in olivine gabbro samples AM-VM22-6c and AM-IVZ-VM009 have very limited compositional range (Fig. 46). Almandine mean is 50 and 49 mol.% for samples AM-VM22-6c and AM-IVZ-VM009, respectively. Pyrope content is ~30 mol.% for both samples. Grossular content is ~17 mol.% for both samples, and grossular content increases slightly from amphibole towards contact of garnet corona with plagioclase, from 17 to 19 mol.% (Table 9).

Garnet trace element data is presented in Table 13. Garnet normalized to chondrite (Fig. 47a) shows depletion of LREE with a strongly increasing trend from La to Eu, enrichment of HREE with slight decrease in REE from Eu to Lu, which is steeper for some samples. Normalized to primitive mantle trace elements (Hofmann, 1988) in garnet show depletion in Rb, Ba, Th, U and Nb, and a strong negative Sr anomaly (Fig. 47a). The strong enrichment in garnet MREE – HREE appears antithetical to the MREE – HREE depletion seen in other silicate minerals in olivine gabbro.

Apatite

Representative apatite elemental abundances and recalculated stoichiometric formulas derived from EPMA, as well as trace element data are presented in Table 10 and 13,

respectively. Fluorine and chlorine were not included during EPMA analyses at ETH Zurich, so were therefore excluded from recalculated formulas but were used to check consistency of P_2O_5 and CaO in the apatite composition between samples for internal standards of in-situ LA-ICP-MS. Apatite grains investigated in this study are dominantly apatite-(CaF) with minor apatite-(CaOH) and apatite-(CaCl) components according to the recent classification scheme of Pasero *et al.* (2010) and using the spreadsheet of Ketcham (2015).

Apatite REE normalized to primitive mantle concentrations (Fig. 47b) show enrichment in LREE and decrease toward HREE for all analyzed apatite grains. Olivine gabbro (AM-IVZ-VM009) is more enriched than the gabbro-norite (AM-IVZ-VM017) in terms of LREE, but is more depleted in HREE. Apatite appears to be highly enriched in trace elements with respect to primitive mantle (Hofmann, 1988), with the exception of a few elements that were near or below the LA-ICP-MS limit of detection (Rb, Ba, K) or were significantly depleted such as Nb (Fig. 47b). The single olivine gabbro apatite analysis that shows a trend more similar to the gabbro-norite apatite analyses (point A9-AP7-1) is from an apatite grain that is surrounded by plagioclase and intergrown with spinel, as observed in thin section (Fig. 37). All other apatite minerals in the olivine gabbro are grains in contact or in proximity of garnet (Fig. 37). Apatite grains analyzed in the gabbro-norite sample are found within the poikilitic amphibole vein and are in contact with plagioclase and/or pargasite.

Oxide minerals

Oxide mineral major element data is presented in Table 11. Using the End Member Generator program of Ferracutti *et al.* (2015), spinel mineral formulas were recalculated between many end members. Fig. 48 shows the distributions of the spinel minerals analyzed between endmembers between the Al spinel subgroup: spinel (*sensu stricto*) and hercynite, and the Fe +

Ti spinel subgroups: magnesioferrite + quandilite and magnetite + ülvospinel (Biagioni and Pasero, 2014). In one location in olivine gabbro (thin section A9, sample AM-IVZ-VM009), oxyexsolution appears incomplete, as complex oxide grains containing ilmenite and Al spinel also contain a portion that has intermediate TiO_2 and Al_2O_3 and Mg# (36 and 21 wt.%, and 22 wt.%, respectively) between the average Al spinel and ilmenite. *In-situ* LA-ICP-MS for oxide grains, even using a 29 μm laser spot size, resulted in contaminated and uneven signals, partly owing to the small size of oxide grains and partly due to inclusions and exsolutions found in these grains. Therefore, trace elements of oxides are not presented here. However, preliminary data shows depletion in most trace elements, with the exception of Nb and Zr, which show 10 – 90 and 2 – 10 primitive mantle normalized values, respectively.

Sulfides

EPMA data of pyrrhotite, chalcopyrite and pentlandite and their recalculated formulas based on 8S per formula unit is presented in Table 12. Secondary pyrite was not analyzed because it appeared heterogeneous and altered. Pyrrhotite is prevalent with up to 6 wt.% Ni. Chalcopyrite contains ~34 wt.% Cu. The single pentlandite grain analyzed is found as an inclusion at the perimeter of a 40 μm rounded pyrrhotite inclusion inside an olivine grain. It contains 2.4 Co APFU on an 8 S basis.

Mass-balanced reactions

Garnet coronas in the olivine gabbros and garnet-bearing gabbro-norites (e.g., Fig. 28a, 37) are found between olivine and plagioclase. Using major oxides recalculated to molar percent data of olivine, plagioclase, and garnet from olivine gabbro (sample AM-VM22-6c, thin section 6c), the mass balance of this reaction is calculated using the least-squares spreadsheet of Li *et al.* (2020) using molar proportions of oxides and normalized to 100%. The resulting reaction is best

described then as the following: 0.35Ol + 0.78Pl = 1Grt. The square sum estimate of errors is 184 when the following oxides were used: SiO_2, TiO_2, Al_2O_3, FeO, MnO, MgO, CaO, Na_2O, K_2O. High residuals of FeO and MgO (+10.5 and -6.5, respectively) show are seen in the molar Mg#; olivine has an Mg# of ~58 whereas garnet is ~30.

Thermobarometry

Various types of geothermometers and geobarometers were applied to all relevant phases (pyroxenes, garnet, plagioclase, amphibole, Fe-Ti oxides), but all were out of equilibrium, including within single grains and mineral pairs. For example, many barometers and thermometers were applied to clinopyroxene – orthopyroxene pairs utilizing Fe – Mg exchange for all samples (e.g., Brey and Kohler, 1990), but all were shown to be out of equilibrium. Variation of Fe/Mg within single grains is common but often irregular.

Bulk rock

Bulk rock major elements

New bulk rock data from the Mafic Complex (n=33) generated in this study are divided between the Lower Mafic Complex, Paragneiss-Bearing Belt, Upper Mafic Complex, "Diorites," and samples from Saliceto, of which the latter samples are part of the Upper Mafic Complex. All bulk rock data of the listed magmatic units are presented in Tables 14 – 18, respectively. Division of samples into Lower Mafic Complex (LMC), Paragneiss-bearing Belt (PBB) and Upper Mafic Complex (UMC) is designated by the Sinigoi *et al.* (1996) map and "Diorite" by the location of diorites in the Quick *et al.* (2003) map. Silica ranges from 36 to 55 wt.% of all samples, and samples from all Mafic Complex zones approximately have the same range (Table 14 – 18). Bulk rock SiO_2 ranges between 36 and 48 wt.% in the new bulk rock data.

Al_2O_3 ranges from 11 to 26 wt.% for all Mafic Complex samples and shows an increasing trend with increasing SiO_2 from 36 to ~50 wt.%, with higher SiO_2 concentrations resulting uncorrelated with Al_2O_3 (Fig. 49). When plotted with literature data (Fig. 50 and 51), the positive correlation continues for some samples, with a maximum Al_2O_3 of <30 in anorthosites. For SiO_2 >50 wt.%, Al_2O_3 decreases with increasing SiO_2 content.

MgO in new analyses ranges from 2 to 16 wt.% and shows a negative relationship with SiO_2 (Fig. 49). Samples show the same trend, but the pyroxenite (sample AM-IVZ-VM008) does not fit this trend. Sample MC_19_02_Tba is a mafic enclave in the "diorites" and has the highest MgO concentration, similar to that of the orthopyroxenite from Saliceto. Including literature data (Fig. 50 and 51), peridotites and pyroxenites from the PBB and LMC have markedly high MgO in contrast to the gabbros of the Mafic Complex.

Total FeO in new bulk rock analyses ranges from 5 to 25 wt.% with FeO showing a negative relationship with SiO_2 (Fig. 49). The samples from this study conform to this trend and vary between 11 and 25 wt.% total FeO. This trend is in line with literature data (Fig. 50 and 51). Notably, paragneiss septa samples are enriched in FeO for a given SiO_2.

CaO ranges from 6 to 14 wt.% and, for most data generated through the analyses of new samples in this study, shows a negative relationship with SiO_2, with the Saliceto samples and two other rocks as outliers (Fig. 49). For <50 wt.% SiO_2, the Lower Mafic Complex samples show higher CaO concentrations than rocks from the other gabbroic units of the Mafic Complex (Fig. 49 and 50). The rocks from Saliceto, except pyroxenite, show an increasing trend of CaO with respect to SiO_2 (Fig. 49).

Bulk rock Na_2O ranges from 0.5 to 5.3 wt.%. Na_2O shows a positive relationship with SiO_2 (Fig. 49). Saliceto samples range from 0.6 to 4.0 wt.% Na_2O, and Na_2O in these samples

shows a roughly linear, positive relationship with SiO_2. For SiO_2 less than 50 wt.%, Saliceto samples are more enriched in Na_2O than most other samples from the Mafic Complex (Fig. 50 and 51).

K_2O in all Mafic Complex samples analyzed ranges from 0.02 to 4.8 wt.%, and mean K_2O is 0.5 wt.% (Table 17). Rocks from the "Diorite" zone show highly elevated K_2O content in contrast to rocks of the other zones, with the exception of the mafic enclave in the diorite (sample MC_19_02_Tba). When plotted with literature data (Fig. 50 and 51), leucosomes, paragneiss, and some quartz-norites show elevated K_2O but at higher SiO_2 (>60 wt.%).

TiO_2 ranges from 0.3 to 5.7 wt.% in all samples analyzed, and the samples from Saliceto range from 1.3 to 5.7 wt.% TiO_2. P_2O_5 ranges from 0.01 to 1.6 wt.% within the spectrum of rocks from the Mafic Complex here analyzed, and Saliceto samples range from 0.04 to 1.6 wt.% P_2O_5 (Tables 14 – 18). The relationship between P_2O_5 and TiO_2 is strong and positive for the olivine gabbros from Saliceto, excluding the pyroxenite (AM-IVZ-VM008), which has 3.4 wt.% TiO_2 and 0.04 wt.% P_2O_5 (Fig. 53b). TiO_2 in bulk rock data appears to create an upper limit of P_2O_5.

MnO is minor in all samples and ranges from 0.05 to 0.4 wt.%. Plotted against SiO_2, MnO shows a decrease with increasing SiO_2 (Fig. 50 and 51). All samples from Saliceto contain < 0.01 wt.% Cr_2O_3. Including all rock types of the Mafic Complex from the literature, Mg# (molar Mg/[Mg + Fe]) shows a decrease with increasing SiO_2, with peridotites and pyroxenites containing the highest Mg# (~90; Tribuzio *et al.*, 2023) (Fig. 50 and 51). Some of the scatter at higher SiO_2 may be due to low absolute Fe and Mg contents.

Figure 52 shows oxides plotted against molar Mg# for selected magmatic rocks from the Mafic Complex. Notably, Na_2O and TiO_2 show a gradual increase with decreasing Mg#, but

P_2O_5 increases dramatically at around at Mg# less than 65 and lower. Figure 53a is an AFM diagram showing that the magmatic rocks of the Mafic Complex showing varying degrees of calc-alkaline to tholeiitic characteristics.

Figure 54 shows the major element concentrations of all rocks from the northern Mafic Complex (Val Sesia and Val Mastallone, Fig. 11) as a function of distance to the Insubric Line. Therefore, the plots may be viewed as cross section, facing north, with the deepest portions of the section to the left (west). The analyses presented are from a complete dataset of literature and new data. Paragneiss and charnockites analyses presumed to be from the northern Mafic Complex (Rivalenti *et al.*, 1975) are included to the left for reference although the distance from the Insubric Line is not known for this suite of rocks. Across the crustal section, high SiO_2 is dominated by paragneiss, charnockites, and leucosomes, and anorthosites typically contain higher SiO_2 than the gabbroic rocks at the same Insubric Line distance.

Again, anorthosites typically contain the highest Al_2O_3 and Na_2O contents, and pyroxenites and peridotites generally the lowest. K_2O rises dramatically starting around 6000 m and upwards in diorites *sensu stricto*, up to >6 wt.%. At 2000 +/- 200 m and at 4000 +/- 200 m, rocks are enriched in P_2O_5 and TiO_2, and this corresponds to the rocks of the Upper Zone and the Main Gabbro, respectively (Fig. 11). Olivine gabbros have some of the highest MnO values in the section. Some of the other rocks marked as "gabbros" that have high MnO could also be olivine-bearing, but reports of sample modal mineralogy are lacking in some of the literature (e.g., Sinigoi *et al.*, 2011; 2016).

Bulk rock trace elements

New bulk rock trace element analyses of magmatic rocks from the Mafic Complex are presented in Tables 14 to 18. Normalized to primitive mantle values of Hofmann (1988), most

samples show positive Ba, Eu, and Sr anomalies and show a negative Th anomaly (Fig. 55 – 59). Besides these anomalies, most samples show enrichment in the light rare earth elements (LREE) and steady depletion towards the heavy rare earth elements (HREE).

Samples from the Lower Mafic Complex have a trend comparable to other Mafic Complex units when normalized to primitive mantle (Fig. 55). They show a strongly negative U anomaly, except for sample MC_26_03_TBb, which has a strong positive U and Zr anomalies. With the exception of the positive Eu anomaly in sample MC_26_03_TBb, Lower Mafic Complex rocks have no Eu anomaly and are relatively depleted in La in contrast to the average of the other Mafic Complex units. Lower Mafic Complex samples have a strong positive Sr anomaly. Sample MC_26_03_TBb has a stronger positive Sr anomaly and a very strong Zr anomaly in contrast to the other rocks of the Lower Mafic Complex. Sample MC_26_03_TBb also has the highest La of any rock analyzed in this study and shows an increase in HREE from Dy to Lu.

Paragneiss-bearing belt samples have greater variance in trace elements than other units, but largely they have a similar depletion from LREE to HREE (Fig. 56). Overall, the rocks of the paragneiss-bearing belt show positive Ba and Sr anomalies and negative Th and U anomalies. Sample MC_04, located proximal to a paragneiss septum and containing ~60 vol.% porphyroblastic garnet, shows the greatest differences in contrast to this rock suite. Sample MC_04 does not show a positive Ba anomaly and shows a depletion in LREE with a monotonic enrichment of MREE and high HREE in contrast to all other Mafic Complex samples. The remainder of the paragneiss-bearing belt samples have a similar range of HREE compared to the mafic rocks of the Mafic Complex.

Upper Mafic Complex trace elemental data (n=14) show positive to strongly positive Ba, Sr, and Eu anomalies, weakly to strongly negative Th, U, and Nb anomalies (Fig. 57). One sample (MC_13) has anomalously high Zr (3255 μg/g), reflecting the presence of zircon, which appears modally abundant in thin section.

"Diorite" zone samples roughly follow the same pattern normalized to primitive mantle (Fig. 58), except for the analysis of a mafic enclave (sample MC_19_02_Tba). These samples show very strong positive Ba anomalies and positive Eu and Sr anomalies. The mafic enclave analysis (sample MC_19_02_Tba) shows the most unique pattern in this new dataset, as it is depleted in most compatible elements, a steady increase from LREE to HREE (much like sample MC_04, the garnet-dominant gabbro) and a negative Sr anomaly. This sample contains high modal orthopyroxene.

Saliceto samples normalized to primitive mantle show a pattern very similar to that of other Upper Mafic Complex samples but dip slightly more steeply in the HREE (Fig. 59). All Saliceto samples show positive Ba, Eu, and Sr anomalies. Notably, pyroxenite from Saliceto (AM-IVZ-VM008) is considerably more depleted in REE than all other Mafic Complex samples analyzed. The samples from Saliceto are ordered by decreasing REE abundances as follows: AM-VM22-14D > MC_12_02_Tae ≈ AM-VM22-6fD > AM-IVZ-VM009 > AM-VM22-6fL >> AM-IVZ-VM008. Total REE is positively correlated with P_2O_5, TiO_2, and FeO.

Trace elements (Fig. 60) and REE (Fig. 61) plotted as a function of distance to the Insubric Line for the northern Mafic Complex show enrichment in Cr in the Paragneiss-bearing Belt (LLG of Rivalenti *et al.,* 1975) of up to ~5000 ppm and a progressive decrease from the base of the Upper Mafic Complex to the diorites. Some noteworthy trends are observed in the Paragneiss-bearing Belt which corresponds to the Lower Layered Group (<1800 m from the

Insubric Line); these trends include the scatter of some elements (Ni, Sr), high Cr and Ni, depletion in Ba and LREE, and enrichment in HREE. The Upper Zone (around 2000 m stratigraphy) shows considerable scatter in most elements but showing higher Ba (with Saliceto samples having lower Ba), enrichment in LREE and scatter in HREE. Transition to the Main Gabbro at around 2500 m is transitional for most elements and a monotonic decrease is seen in Ba most notably, as well as LREE. Some element trends from the Upper Zone upward through the lower Main Gabbro show a U shape (decrease then increase) up to around 4000 m from the Insubric Line. These elements include Zr, Ba, and Rb. Rb shows a steady increase with increasing stratigraphic height (as measured by distance to the Insubric Line) from the base of the Main Gabbro to the 4000 m mark, a fairly abrupt decrease at the ~4000 m mark, then monotonic rise into the diorites. Diorites are enriched in Rb, Ba, and LREE.

CIPW norms

Normative mineralogy using the CIPW norm calculated with major oxides and Cr, Ni, Sr and Ba using the spreadsheet of Hollocher (2022) is shown in Table 19. Since normative mineralogy is calculated on an anhydrous basis, hydrous minerals such as amphibole and biotite are excluded. Additionally, a few minerals present in these samples are not included, such as spinel, baddeleyite, apatite and sulfide minerals, which are all relatively volumetrically insignificant in the modal mineralogy of each studied rock as compared to the silicate phases. Garnet, while modally abundant in some samples does not appear to influence the bulk composition and therefore its exclusion from norm calculation is not influential on the normative mineralogy.

Results of normative mineralogy calculations show a range of olivine modal percentage ranging from 7 to 38 vol.%. Plagioclase ranges from 35 (AM-VM22-14D) to 80 vol.% (AM-

VM22-6fL), and calculated An ranges from 65 to 80 mol.%. Calculated orthoclase modal percentage ranges from 1.1 – 2.4 vol.%. Modal percentage ranges of ilmenite and magnetite are 1.5 – 7.7 vol.% and 0.6 – 3.2 vol.%, respectively. Hypersthene ranges from 0 to 20 vol.%, whereas diopside ranges from 0 to 2.2 vol.%. Plotted on the gabbroic ternary (Fig. 19a), normative mineralogy indicates that these olivine gabbros range from leuco-troctolites to olivine gabbro-norites.

Principal Component Analysis: Major elements

PCA of major elements of all lithologies from the Mafic Complex yields four principal components that cumulatively explain 88% of the variance in the dataset (n=559). PC1, PC2, PC3, and PC4 explain 45.4, 26.1, 11.2, and 6.1%, respectively (Fig. 62a). Loadings of each trace element are presented in Table 20; important loadings are those that have greater magnitude than a single variable's worth. SiO_2, K_2O, and Na_2O have strong positive loadings on PC1, and MgO, FeO, and MnO have strong negative loadings on PC1. Al_2O_3, TiO_2, CaO, P_2O_5, and Na_2O have strong positive loadings on PC2, and no oxides have strong negative loadings on PC2. PC3 has strong positive loadings of P_2O_5 and K_2O and strong negative loadings of CaO and Al_2O_3. P_2O_5 has a strong positive loading on PC4 and MnO and K_2O have strong negative loadings on PC4.

PCA of major elements: PC1 and PC2

On the distance bi-plot of PC2 vs PC1 (Fig. 63), ultramafic lithologies plot strongly negative on PC1 and strongly negative on PC2; peridotites plot more strongly negative than the pyroxenites, and particularly, ultramafic rocks from the Paragneiss-Bearing Belt in Val Sesia plot more negatively on PC1 than ultramafic rocks from the Lower Mafic Complex in Val Sesia. Olivine gabbros and garnet gabbros dominate the highest PC2 values. The Saliceto olivine gabbros are strongly correlated with PC1, with the most melanocratic olivine gabbro (AM-

VM22-14D) plotting farthest negative, and increasingly leucocratic and positive on PC1 to sample AM-VM22-6fL. Saliceto olivine gabbros show little variance with PC2, but sample IV37 of Capedri (1971) has a lower PC2 score, similar to that of the gabbro and norite from Saliceto. Saliceto pyroxenite (sample AM-IVZ-VM008) has the most negative PC2 score. Amphibole gabbros and gabbroic rocks do not show any clear correlation with either PC1 or PC2, except gabbroic rocks with relatively higher values on PC1 vary less on PC2; this trend continues further positive into quartz norites. Charnockites are strongly correlated with PC1, and this trend continues positively on PC1 and negatively on PC2 to leucosomes. Diorites largely overlap gabbros. Anorthosites overlap with quartz norites on PC2 yet have higher PC2 values. Paragneiss shows a strong correlation with PC1, overlapping most lithologies, and less variation on PC2; paragneiss scores are more negative on PC2 and fall between the majority of gabbros and leucosomes.

Magnesium number (Mg#) generally decreases with increasing samples scores on PC1 and PC2 (Fig. 64). However, samples with high PC2 scores and low PC1 scores have low Mg#. Therefore, excluding SiO_2-rich samples (PC1 scores >0), the decrease in Mg# is most notable with increasing PC2 scores. Also, there appears to be a positive correlation between PC1 and $^{87}Sr/^{86}Sr$ (Fig. 65a) and $\delta^{18}O$ (Fig. 65b). There does not appear to be a relationship between PC2 and $^{87}Sr/^{86}Sr$ (Fig. 65c).

Major element PC1 plotted against the stratigraphy for the northern Mafic Complex is shown in Figure 66; in the northern Mafic Complex, a slight increase in PC1 scores is noted with increasing height in the section for gabbroic to dioritic rocks. When PC2 of PCA performed on northern Mafic Complex samples is plotted as function of distance to the Insubric Line (Fig. 66), the highest PC2 scores are found at around the 2000 and 4000 meter marks, which are

approximately the Upper Zone and in the Main Gabbro, respectively (Rivalenti *et al.*, 1984). As Figure 54 shows, TiO_2 and P_2O_5 are both elevated at these stratigraphic levels.

PCA of major elements: PC3 and PC4

The PC4 vs PC3 distance biplot is shown in Figure 67. All zones and all lithologies appear to overlap to some extent on both PC3 and PC4. Anorthosites have the most negative PC3 scores. Samples from the Upper Mafic Complex have the highest PC4 scores. Olivine gabbros from Saliceto are correlated to PC3 but show less variance on PC4; the pyroxenite from Saliceto has lower PC4 score than the olivine gabbro. Garnet-bearing gabbros largely overlap some ultramafic lithologies; this may be explained by the garnet-bearing gabbros from the UMC/ Upper Zone enriched in P_2O_5 and by the ultramafic rocks having less CaO than most other rocks, while containing very little P_2O_5. Gabbroic rocks and amphibole gabbros dominate the negative PC3 space, whereas diorites and paragneiss dominate the negative PC4 space.

PC3, showing strong positive loadings of P_2O_5 and K_2O and negative loadings of CaO and Al_2O_3 (Table 20), has high positive scores for ultramafic lithologies (reflecting low CaO and Al_2O_3) and Upper Zone gabbros. A striking divergence occurs again around the 4000 m mark (Fig. 66), where gabbroic rocks and olivine-bearing gabbros have high PC3 scores, whereas the other gabbroic rocks of the Main Gabbro have negative scores. At farther distances from the Insubric Line, PC3 scores become more positive with increasing Insubric Line distance. High PC4 scores are dominated by Upper Zone gabbroic rocks and anorthosites.

PCA of trace elements

PCA performed on trace elements yields PC1, PC2, PC3, and PC4 that explain 47.4, 16.2, 11.6, and 7.23%, respectively, of the total variance in the explored dataset (n=361); cumulatively, these principal components cover 82.5% of the total variance (Fig. 62d). This

statistical analysis helps observe the potential trace element geochemistry variation from one valley to another across the magmatic domain of the exposed lower crust of the Ivrea-Verbano Zone. Regarding the PCA of trace elements from Val Sesia and Val Mastallone, it is observed from PC1 to PC4 that each PC explains 46.1, 15.8, 11.2, and 8.4%, respectively, of the total variance (Fig. 62e). Together, PC1 through PC4 explain 81.4% of the total variance in trace elements. Regarding the PCA of trace elements from Val Sessera, PC1 through PC4 each explain 49.7, 20.8, 12.4, and 5.1%, respectively, of variance in the selected trace elements in Val Sessera bulk rock analyses (Fig. 62f). Cumulatively, the first four principal components explain 87.9% of the variance. For all PCAs performed on trace elements, PCA mostly has positive loadings for incompatible elements, while Ni has a negative loading. However, for principal components 2 through 4, differences are seen between all three PCAs. PC2 for PCA performed on trace elements for the northern Mafic Complex has strong, positive loadings of Sr and Ba and negative loadings of Y, PCA of trace elements from the southern Mafic Complex shows strong positive loadings of Sr, Ni, Y and Nd and negative loadings of Ba and Rb. PC3 for the entire Mafic Complex, including the individual PCAs of northern and southern MC, highlight the opposing behavior of Sr (strong negative loadings) and Rb (strong positive loadings).

PCA of major and trace elements

Results of PCA on 361 samples with the combined datasets of major and selected trace elements (20 variables) yield four PCs that cumulatively explain 76.1% of the total variance in the dataset. PC1 through PC4 explain 37.6, 25.1, 9.8, and 5.7%, respectively, of the total variance of the dataset (Fig. 62). Loadings of principal components are shown in Table 22. SiO_2, Na_2O, K_2O, Ba, La, and Ce, and FeO, MgO, CaO, and Ni have positive and negative loadings, respectively, on PC1. TiO_2, FeO, MnO, P_2O_5, and most incompatible trace elements have strong

positive loadings on PC2. PC1 and PC2 loadings from PCA performed on the northern and southern Mafic Complex separately are very similar to that of the PCA performed on all samples. Al_2O_3, Na_2O, and Sr have strong positive loadings on PC3, whereas MnO, Rb, Ni and Y have strong negative loadings on PC3. Lastly Y has a strong positive loading while K_2O, P_2O_5, Sr, Ba, and Rb have strong negative loadings on PC4.

In the distance biplots of PC2 vs PC1 (Fig. 69), Upper Mafic Complex and LMC samples are largely discriminated by that amphibole gabbros from the Lower Mafic Complex have lower PC1 scores than gabbroic samples from the Upper Mafic Complex. Like with the major element PCA, quartz-bearing norites, paragneiss, and granitoids/charnockites have the highest PC1 scores, as expected by their high SiO_2 and K_2O contents. PC4 vs PC3 distance biplot (Fig. 70) reveals the distinctions between Lower Mafic Complex gabbros and Upper Mafic Complex gabbros; Lower Mafic Complex samples have positive PC4 scores, but Upper Mafic Complex and "Diorite" samples have negative PC4 scores. Additionally, diorites have more negative PC3 scores than Upper Mafic Complex gabbros. Paragneiss-bearing Belt samples mostly overlap that of the Lower Mafic Complex but also to a limited extent, Upper Mafic Complex samples.

Scores of samples plotted as a function of distance to the Insubric Line yield notable patterns (Fig. 71). PC1 scores are generally <0 from the Insubric Line to about 5000 m (excluding charnockites, which have high PC1 scores) then increase upwards into the diorites. PC2 scores show are low in the Lower Layered group (<1500 m), very high but variable in the Upper Zone (1500 – 2500 m), then show a monotonic increase from 3000 to ~4000 m. Upwards of 4000 m, scores abruptly drop then increase into the diorites.

CHAPTER 5

IN-SITU DIFFERENTIATION IN THE UPPER ZONE OF THE MAFIC COMPLEX

The mafic to ultramafic suite investigated at Saliceto represents a collection of rocks that highlights *in-situ* magmatic differentiation within the Upper Zone of the Upper Mafic Complex (Fig. 11). The Upper Zone was first studied by Capedri (1971) studying the mafic rocks in Val Mastallone and by Mazzucchelli (1983) and Mazzucchelli *et al.* (1992a; 1992b) analyzing a similar suite of rocks in Val Sesia. From a petrographic standpoint, the olivine gabbros here studied are very closely related to the mineralogy and texture of olivine gabbros reported in Capedri (1968, 1971). Specifically, the olivine gabbro sample IV38 from Capedri (1971) shows similar modal proportions of amphibole, apatite, and oxides identified in sample AM-VM22-14A1 (Fig. 26b). The two sets of rocks differ by the modal proportion of olivine, plagioclase and garnet between each other, but they share an almost identical texture made of skeletal olivine and subhedral plagioclase with pyroxene, garnet, and amphibole coronas (compare Fig. 1 from Capedri, 1968, and Fig. 5 from Capedri, 1971, with Fig. 37b). The proportions of amphibole, apatite, and oxides are key to identify the signs of potential melt extraction in the suite of rocks at Saliceto.

The identification of the field relations is challenged by limited exposure (Fig. 8) and, in places, by Alpine-age faulting (Fig. 12). However, the rocks identified in the field appear to constitute a comprehensive block that did not suffer significant tectonic displacement (Quick *et al.*, 2003), in line with the overall preserved integrity of the continental crustal section in the Ivrea-Verbano Zone. Here, I present a cohesive geochemical dataset suggestive of *in-situ*

magmatic differentiation leading to differentiated units of cumulate and evolved members. There is no evidence that the geochemically distinctive rocks are separate intrusive bodies predating or postdating the gabbroic units of the Mafic Complex, and therefore the parental magmas of these rocks were likely intruded between 286 and 282 Ma using the most recent geochronological constraints (Karakas *et al.*, 2019).

The three distinctive yet general lithologies identified in this study through petrographic and geochemical analysis at mineral to bulk rock scale are pyroxenite, olivine gabbro, and gabbro-norite, including garnetiferous and amphibole-rich members. Supra- and subsolidus mineral reactions (e.g., the reaction of olivine and melt creating orthopyroxene and magnetite) challenge attempts at using standard rock classification schemes which rely on modal abundance; however, these three lithologies are unique microstructurally and geochemically. At the outcrop scale in Saliceto, pyroxenite is a cumulate plagioclase-bearing ultramafic body surrounded by olivine gabbro and cumulate gabbro-norite, which are potentially differentiated units derived from an evolved melt, or each crystallized from initially distinct crystal-poor magmas and were later affected by pervasive reactive melt flow. Here, evidence for both processes is assessed along with other processes that tend to obscure evidence of melt flow during magma differentiation of the Upper Zone in the Mafic Complex.

Evidence of advanced subsolidus re-equilibration

Largely, trace element patterns of minerals show advanced re-equilibration, which complicates the use of major and trace elements in minerals to estimate the super-solidus chemistry of the coexisting melt and the melt's evolution. This is exemplified particularly by the depletion in HREE in all minerals analyzed in olivine gabbro and the enrichment of HREE in garnet (Fig. 41, 43, 47). Yet mineral re-equilibration does not appear to affect the bulk rock

composition in terms of REE (Fig. 59). Additionally, the extent of re-equilibration appears to be localized; this is shown by the variance in trace elements of each phase analyzed and shown by the single analysis of an apatite grain appearing to be fully enclosed in plagioclase (Fig. 37 and 47) that does not show the extreme HREE depletion shown by apatite in proximity to garnet. Depletion of HREE in other minerals from garnet growth has been previously studied in the Mafic Complex gabbros (Bea *et al.*, 1997; Bea and Montero, 1999). As noted by Mazzucchelli *et al.*, (1992b), any calculation of trace element composition of the melt from which minerals in these rocks crystallized through solid-melt partitioning modeling would be futile. Likewise, important trace element records of reactive melt flow, which can be demonstrated with mineral chemical zoning (e.g., Sanfilippo *et al.,* 2020), appear to be erased by this re-equilibration. However, trace element patterns that are consistent in minerals and bulk rock of each sample can still be used to reinforce the idea of the overall genetic trends of the suite.

Rock fabric and microtextures produced by supra- and subsolidus processes

All rocks at Saliceto show the effects of recrystallization, but some primary textures are preserved. Features that suggest recrystallization are most clearly seen by the formation of smooth grain boundaries and ~120° grain junctions between plagioclase grains. Additionally, concentrations of Al spinel exsolutions found generally within the cores of plagioclase grains often do not parallel the observed recrystallized plagioclase-plagioclase boundaries, and sometimes these concentrations of Al spinel exsolutions reach plagioclase-plagioclase grain boundaries. Also, recrystallization of plagioclase appears to have taken place before growth of garnet coronas; garnet formation consumes plagioclase across its grain boundary junctions. Additionally, garnet coronas are chemically zoned with higher grossular content (relatively enriched in CaO) and lower HREE where the coronas are in contact with plagioclase versus

where the coronas are in contact with olivine or pyroxene. Aluminum spinel + pyroxene symplectites appear to have grown after the exsolution of spinel (Fig. 36).

These observations also point to exsolution of spinel prior to dynamic recrystallization. Wass (1973) found similar spinel exsolutions in plagioclase in basaltic rocks from Australia. Capedri (1971), too, noted spinel exsolutions in plagioclase in the Mafic Complex, yet suggested that formation of these exsolutions would require ion diffusion (Fe and Mg) from outside the grain. More recently, Mollo *et al.* (2011) showed that increase in temperature favors increasing Fe and Mg partitioning into plagioclase using experimental crystallization of plagioclase from basaltic melt at 500 MPa. Therefore, the growth of spinel exsolutions in plagioclase may result from cooling effects prior to dynamic recrystallization. The extinction halos around these spinel exsolutions in plagioclase, due to a local decrease in An content and increase in Ab content as seen in EPMA data, can be explained by the well-known coupled substitution reaction of Al + Ca and Na + Si (Blundy and Holland, 1990). Indeed, incompatibility of Fe and Mg, driven by decreasing temperature, locally removes Al from plagioclase to grow Al-spinel grains with consequent increase of the Ab content of the halo around the single spinel inclusion. Development of these spinel exsolutions may have been accompanied by growth of clinopyroxene coronas, in which clinopyroxene could have taken in Na and Ca yet very little Al during growth. The strong Eu anomalies in clinopyroxene may point to clinopyroxene as a reaction product of plagioclase + orthopyroxene or olivine.

Yet despite these clear evidences of subsolidus recrystallization (from garnet coronas to equilibrium textures in plagioclase), magmatic textures are preserved in the rocks at Saliceto. Evidence of primary magmatic foliation include a preferred orientation of grains defining a foliation and magmatic mesoscopic layering defined by leucocratic (plagioclase-rich) to

mesocratic to melanocratic bands (rich in olivine, pyroxene, amphibole, oxide, and/or garnet) (Fig. 13 and 14). Discrimination between mineral lineation and foliation is limited in this study, because thin sections prepared were cut normal to the layering but without record of orientation. However, foliation is readily recognizable in thin section (Fig. 30). While the shape-preferred orientation seen in plagioclase can be explained by recrystallization (Holness *et al.*, 2017), concentrations of earlier-forming Al spinel exsolutions approximately show elongation parallel to the overall fabric and generally do not occur in lobes of recrystallization-driven, precipitated plagioclase. Following this line of thinking and based on the work of Holness *et al.* (2017) on the rock fabrics of the Skaergaard pluton, it may be proposed that the foliation is primary, caused by grain settling and, potentially, magmatic deformation linked to magma emplacement. Ensuing subsolidus deformation, creating a metamorphic overprint, parallels the original magmatic foliation and the large scale, subvertical orientation of the entire suite. This interpretation is comparable with the map of Quick *et al.* (2003), which shows the strike and dip of foliation, not magmatic layering, in the Saliceto vicinity.

Of particular interest, the coarse-grain to fine grain banding seen in gabbro-norite sample AM-VM22-9 (Fig. 13, 18, and 20), which also shows shape-preferred orientation defining a foliation parallel to banding, could result from grain size-based sorting at the base of a crystal-poor magma; although indistinct, the coarse-grained, leucocratic band in thin section appears to grade, albeit rather steeply, into the finer-grained, mesocratic band stratigraphically above (Fig. 20). Stratigraphically below is thick (>30 cm) fine-grained gabbro-norite and above is thick-banded leucocratic gabbro-norite, and together with the fine-scale alternations may exclude a subsolidus process in their formation. While magmatic deformation may drive this size-based sorting, the miniscule grains size of the fine-grained band (< 0.5 mm) complicates the picture.

Can the minerals present in the fine-grained band be considered adcumulates in contrast to the hypothesis that the other lithologies in at Saliceto show adcumulus features and mineral-melt reactions (e.g., coronitic clinopyroxene, poikilitic orthopyroxene and amphibole) suggestive of reactive melt flow? This sample is from the base of the studied stratigraphic section; the fine-grained nature of the bands may therefore indicate that melt percolation through a porous cumulus pile was not as pervasive in this stratigraphic level of the Mafic Complex. Banding observed at the sub-centimeter to meter scale is likely to be a primary magmatic structure, but subsolidus processes may result in similar banding (e.g., compositional banding in gneiss).

Common magmatic parent of Saliceto rocks

The interpretation that the olivine gabbro suite of rocks exposed at Saliceto showcases in-situ magmatic differentiation is based on bulk rock and mineral chemistry from this study. Experimental work (Villiger *et al.*, 2007; Nandedkar *et al.*, 2014) has shown that equilibrium or fractional crystallization within a closed system likely would not produce the association of the olivine- and plagioclase-bearing pyroxenite and the troctolitic olivine gabbro found at Saliceto, and this is particularly supported by differing Mg# of these rocks, the Fo content of olivine in both lithotypes, and the different trace element signatures. Yet, common features such as the overall shape of bulk rock trace element profiles (Fig. 59), including the strongly positive Eu and Sr anomalies and enrichment in LREE, point to similar parent liquid, at least at the scale of the Upper Zone (Mazzucchelli *et al.*, 1992a).

Saliceto pyroxenite: evidence of reactive melt flow

The pyroxenite body identified within the suite of rocks at Saliceto (Fig. 15) represents the most efficiently separated member of the series that was subjected to reactive melt flow. The pyroxenite framework of coarse-grained orthopyroxenes along with embayed olivine and oxides

(Al-spinel, ilmenite, and magnetite) compose an adcumulus texture, which is characterized by reactions between the mafic minerals and melt (Fig. 34). In some places, reaction between olivine and oxide minerals and melt appears to have consumed all the olivine, generating pegmatoidal orthopyroxene (Fig. 28) that is crosscut by bands of plagioclase (Fig. 15, 29). Lastly, percolation of a hydrous melt along grain boundaries partially dissolved mafic minerals and plagioclase before crystallizing amphibole (Fig. 35).

The oikocrystic texture and size of individual amphibole grains suggest reactive melt flow (Fig. 28 and 35a). Amphibole in pyroxenite is depleted to the same degree as the other minerals are in REE and generation of amphibole as a product of H_2O + plagioclase + orthopyroxene is largely mass balanced. This may suggest a purely hydrous reaction, but since all minerals are re-equilibrated and partition coefficients are largely similar between amphibole and plagioclase as in gabbro-norite, determining the precise process behind the formation of amphibole is challenging.

Basic phase relationships, microstructures, and trace element signatures in the pyroxenite can be explained by the following series of events. Cumulus olivine, spinel, and Fe-Ti oxide fractionally crystallized and settled, creating a porous framework at the base of a melt-rich magma reservoir. Interstitial liquid reacted with the olivine, and through the peritectic reaction, corroded the olivine and crystallized poikilitic orthopyroxene followed by interstitial plagioclase. Deformation of the crystallizing mush after the cessation of orthopyroxene crystallization caused dilatant fractures, which were filled by the interstitial liquid, which then crystallized plagioclase. Evolved melts were efficiently removed, leaving a geochemical signature in the bulk rock showing strong depletion in trace elements.

Although apatite is scarce in this rock (0.04 wt.% P_2O_5), microscopic (<10 μm) euhedral apatite inclusions are found fully contained within ilmenite grains (Fig. 31) and this association is found in many of the TiO_2-rich rocks from the entire Mafic Complex presented in this study. Coupled with the depletion of REE in the bulk rock, the pyroxenite may thus represent early accumulation in the Saliceto sequence of rocks which crystallized almost completely before the formation of the surrounding gabbro-norites and olivine gabbro.

In all samples, labradorite to andesine plagioclase is characterized by large Eu positive anomaly (Eu/Eu* = 52 to 100, Fig. 43a; where Eu/Eu* = $Eu_N/(Gd_N*Sm_N)$^0.5, where N indicates primitive mantle normalization; after McLennan, 1989) indicating that this phase is cumulate and may derive from a residual melt within the pyroxenitic cumulate body (Fig. 42 and 43). However, Mazzucchelli *et al.* (1992) noted strongly positive Eu anomalies in minerals of other rocks of the Upper Zone and determined through replenishment, tapping, and fractional crystallization modeling that this Eu anomaly cannot be explained by plagioclase accumulation alone and that the parental melt must have already contained an Eu anomaly, possibly from contaminating anatectic melts. Indeed, pyroxenes, plagioclase, and amphibole from all analyzed lithologies contain Eu anomalies, and this in turn is reflected in each rock bulk Eu anomaly (Table 18). Saliceto bulk rock Eu anomalies range from 1.63 to 3.95, and these anomalies positively correlate with increasing modal abundance of plagioclase with the exception of pyroxenite, which has an intermediate Eu anomaly and <10 vol.% modal plagioclase.

Evidence of in-situ differentiation

Plagioclase (Fig. 42) is the common denominator that showcases the potential extraction of a compositionally evolving melt. Indeed, plagioclase tends to remain constant (labradorite to andesine) throughout the different lithologies (from An67 in pyroxenite to An64 in olivine

gabbro and An59 in gabbro-norite; Fig. 42). However, the trace element record in plagioclase displays an increase of LREE, Ba, Rb, and K from pyroxenite to olivine gabbro and gabbro-norite (Fig. 43). Throughout this mafic rock suite, plagioclase appears to be zoned with evolved rims compared to the core (An54 vs. An59; Fig. 42) possibly related to cooling effects under suprasolidus conditions, particularly during the growth of Ca- and Al-rich garnet. Plagioclase modal proportions increases from pyroxenite (< 10%) to olivine gabbro (12 to 70%) and gabbro-norite (40 to 60%) (Table 3).

The determination of modal proportion of minerals in the studied rocks is hindered by the complex banding identified at thin section to outcrop scale (Figs. 18, 21). Magmatic banding also well correlates with the processes of in-situ differentiation of mafic rocks as previously identified in well-studied geological locations exposing layered intrusions such as Bushveld and Skaergaard (Cawthorn, 2015). In the case of the rocks from Saliceto, the *in-situ* differentiation is manifested through plagioclase, orthopyroxene, and olivine bands (Figs. 15g). Bulk rock composition of centimeter-scale banding in olivine gabbro shows significant differences in major and trace elements. Specifically, mesocratic bands in olivine gabbro are enriched in TiO_2, P_2O_5, MgO, FeO and REE relative to adjacent leucocratic bands, and this indicates the transition from concurrent crystallization of apatite, ilmenite and olivine to bands containing dominantly plagioclase (Fig. 15g, Table 3). Indeed, the positive correlations between bulk rock P_2O_5, TiO_2, and FeO (Fig. 53b) seem to indicate that the co-crystallization of ferromagnesian silicates, ilmenite, and apatite occurs across the entire exposure of olivine gabbro and pyroxenite.

Overall, the incipient metamorphic features formed at sub-solidus conditions do not modify the original bulk rock composition of the studied rocks. Additionally, fluid-mobile elements such as the LILE are not differentially depleted within samples nor within grains, and

LILE conform to trends of the Upper Mafic Complex (Fig. 59), contrary to early authors suggesting pervasive metasomatism (e.g., Capedri, 1971). Even in samples from the Mafic Complex that showed pervasive alteration of the primary plagioclase and pyroxene, no depletion in fluid-mobile elements such as Rb is noted (sample AM-VM22-3b from the Upper Mafic Complex, Table 18).

Further evidence of percolation of melts from cumulus bodies to evolved, extracted magmas is related to the poikilitic to coronitic amphibole throughout the different rocks. The presence of amphibole, whose modal abundance tends to vary throughout the mafic rock suite (from <1 to 20%; Table 3), testifies to the percolation of a tardive hydrous melt along the grain boundaries of plagioclase, orthopyroxene, and olivine (Figs. 22, 27b, 28). Amphibole is compositionally identical in both poikilitic to coronitic textures in each studied rock in terms of major elements, but, similarly to plagioclase, the trace element record tends to change along with the alkalis (K and Na) concentration. Specifically, amphibole gets enriched in K and REE and depletes in Na from pyroxenite to gabbro-norite and olivine gabbro (Tables 8 and 13). This observation leads to the interpretation that the original melt got enriched in incompatible elements (K and REE) and got depleted in Na with crystallization of the plagioclase rims (An58) and chadacrysts (An53 to An1.5) within amphibole in the gabbro-norite. Amphibole is one of the ultimate primary minerals precipitating from the residual melt as testified by the crystallization sequence inferred from all lithologies. We expect that the residual melt evolves through peritectic relationships involving both the well-known olivine + liquid = orthopyroxene reaction as well as pyroxene +liquid = amphibole as reported in previous experimental studies (Ulmer *et al.*, 2018, and references therein). Difficulties arise, however, when mineral trace element chemistry is used to assess the trace element enrichment of the late-stage melt that formed the

amphibole due to the prolonged cooling history of the Mafic Complex, which allowed for subsolidus re-equilibration (Mazzucchelli *et al.*, 1992b).

However, while most rocks of the Saliceto mafic suite contain amphibole, some gabbro-norite samples (e.g., AM-VM22-9, Fig. 21) contain only trace amphibole and display an anhydrous mineral assemblage. Assuming that the percolating melt was water-saturated across the whole domain of the Upper Mafic Complex, this suggests that the tardive, hydrous melts that formed amphibole elsewhere were not pervasive in every location.

Variations in oxidation state during cooling history at Saliceto

Oxygen fugacity (fO_2) during crystallization and subsequent cooling appears to be variable within the rocks of Saliceto. The presence of magnetite early on in the crystallization sequence of the gabbro-norite indicates that conditions were fairly oxidizing during early crystallization. Olivine surrounded by magnetite and orthopyroxene (e.g., Fig. 34 can be modelled by the reaction: olivine + O_2 = orthopyroxene and magnetite) potentially indicate that fO_2 increased after the crystallization of cumulus olivine in the pyroxenite. There is evidence of complex oxy-exsolution in both gabbro-norite and pyroxenite oxide grains composed of magnetite with ilmenite exsolutions, where the ilmenite may contain Al spinel and even corundum exsolutions. However, incomplete oxy-exsolution does not seem to have progressed to completion in some oxide grains, leading to intermediate compositions that fall between the Al spinel, ilmenite, and magnetite end members (Fig. 48). Oxy-exsolution in these grains have complex internal structures (Fig. 32), but these structures are contained within the subhedral proto-spinel grain, showing that this increase in oxygen fugacity may have occurred under subsolidus conditions, yet that the oxidation was incomplete or not pervasive, even on a mm scale.

Interestingly, the garnetiferous mela-norite (sample AM-IVZ-VM11, Figs. 17d, 24) may be a relict olivine-bearing gabbro. In this rock, orthopyroxene is full of vermicular intergrowths of magnetite. Oxidation of olivine can explain this relationship. This garnetiferous mela-norite is on strike with the olivine gabbro found at road level; if this garnetiferous norite with magnetite exsolutions is part of the olivine gabbro suite, this may indicate heterogeneities of oxidation within this suite, potentially during the percolation of late-stage melts within the suite, yet before the formation of amphibole.

CHAPTER 6

MAGMA EMPLACEMENT AND DIFFERENTIATION IN THE MAFIC COMPLEX

Here I show how bulk rock geochemistry can be insightful into magma differentiation and crustal assimilation processes that operated during the emplacement and buildup of the Mafic Complex.

Major element bulk rock signatures

As is shown in major element plotted versus silica enrichment (Fig. 50 and 51) and magnesium number (Fig. 52), major elements in rocks of the Mafic Complex show trends that are the product of magmatic evolution, namely the liquid line of decent showing a decrease in Mg# and increase in SiO_2 during progressive evolution. Principal component analysis attempts to encapsulate the correlations observed in simple binary plots (Figures 50 and 51) into a smaller number of components that explain the greatest variance, which may then be ascribed to specific processes controlling this variance. However, as pointed out by Ueki and Iworami (2017), caution must be exercised when assigning specific processes to principal components, as geochemical data in nature does not always follow a Gaussian distribution, and the bulk rock data used in this study is no exception (e.g., P_2O_5 in this dataset does not approximate a normal distribution after $\log_{10}$ transformation).

PC1 of major element PCA, which accounts for 45.4 % of the variance in the dataset, shows that this greatest variance can be explained by both fractional crystallization as well as crustal assimilation. Fractional crystallization is highlighted by the strong, negative loadings on PC1 of FeO and MgO, and to some extent, the positive loadings of SiO_2, K_2O, and Na_2O (Table

20; Fig. 63). The ultramafic rocks of the Mafic Complex are associated to the negative loadings with the lowest PC1 scores, which have been identified as cumulate rocks by a number of authors (e.g., Rivalenti *et al.*, 1981; Tribuzio *et al.*, 2023) where mafic minerals (olivine, pyroxene) crystallized and were subsequently separated from their parent melt. In a broad sense, removal of FeO and MgO through the production of these ultramafic cumulates would increase the concentrations of elements that are incompatible or relatively less compatible in these rocks. The positive loadings of Na_2O, K_2O and SiO_2 on PC1 can thus be explained by this opposing behavior caused by crystallization of ferromagnesian silicates and thus magmatic differentiation. This idea is further supported by the general decrease in Mg# from negative to positive PC1 space, excluding samples with high PC2 scores (Fig. 64). Additionally, olivine gabbros from Saliceto (Fig. 63a) vary greatly along PC1, further supporting the importance of fractional crystallization and accumulation on PC1. Conversely, assimilation into the basaltic of melts derived from anatexis of the country rock metapelites has been demonstrated through a variety of methods including bulk rock isotopes, mixing models, and Hf in zircon (Voshage *et al.*, 1990; Mazzucchelli *et al.*, 1992a; Sinigoi *et al.*, 2011, 2016; Storck *et al.*, 2021). When $^{87}Sr/^{86}Sr$ is plotted versus PC1 (Fig. 65a), there is a positive correlation between PC1 and $^{87}Sr/^{86}Sr$, at least for the samples in the dataset that include Sr isotopic ratios. Increasing radiogenic Sr isotopic ratios has been linked to increasing assimilation of a crustal component (e.g., Sinigoi *et al.*, 1996). And similarly, $\delta^{18}O$ plotted against PC1 shows a roughly positive correlation (Fig. 65b), further showing the signature of the contaminant as expressed in high-SiO_2 rocks. Charnockites and leucosomes may represent frozen anatectic melts (Sinigoi *et al.*, 1991; 1994), and accordingly, these lithologies have the highest PC1 scores. Depleted paragneiss septa, on the other hand, have varying PC1 scores that are mostly >1, yet some paragneiss septa samples are

not distinguishable from gabbroic rocks on both PC1 and PC2, potentially indicating that these restitic metapelites may have achieved thermodynamic equilibrium with the intruding mafic magmas to some degree in terms of major elements. Thus, the greatest variance in the major element bulk composition of the Mafic Complex is due to the combined effects of both fractional crystallization and crustal contamination processes.

When samples scores are plotted using the stratigraphic units of Sinigoi *et al.* (1996), samples from the Upper Mafic Complex have some of the highest PC2 scores. Additionally, disregarding the high-SiO_2 samples (those with high PC1 scores), Mg# decreases with increasing PC2 scores (Fig. 64). As bulk rock major element chemistry is largely dictated by mineral abundances and solid solution in minerals (e.g., forsterite content in olivine), these strong positive loadings may indicate the presence of cumulus Fe-Ti oxides and apatite, as well as plagioclase (anorthosites have lower PC2 scores likely because they do not contain much apatite nor Fe-Ti oxides) and a general iron enrichment trend.

Fe-Ti oxides and apatite accumulations have been well-documented in the Upper Zone, of which the Saliceto outcrops are part (Rivalenti *et al.*, 1981, 1984; Mazzucchelli, 1983), but no literature has pointed out the enrichment of apatite and Fe-Ti oxides that is found at 4000 m from the Insubric Line, in both Val Sesia and Val Mastallone, despite that the analyses that point to this enrichment come from numerous publications. Additionally, some olivine-bearing gabbros with lower bulk rock Mg# compared to the Main Gabbro (<45) (sample MC_13, this study) are found close to this stratigraphic level (Fig. 54).

The trend of decreasing Mg# with increasing PC2 scores indicates iron enrichment with negligible SiO_2 change, which is consistent with a tholeiitic trend of differentiation (Irvine and Baragar, 1971). However, Na_2O also has a strong positive loading on PC2, showing the

simultaneous increase in alkalis. Although assimilation may, to some degree, be a control on PC2, both cumulus ultramafic rocks as well as charnockites and granitoids have more negative PC2 scores (Fig. 64b). Even more, when $^{87}Sr/^{86}Sr$ is plotted versus PC2 (Fig. 65c), there does not appear to be a relationship between PC2 and crustal contamination. Therefore, increasing PC2 scores may represent differentiation on a tholeiitic trend, and potentially the coeval crystallization of apatite and Fe-Ti oxides. Over the past few decades, researchers have attempted to decipher the differentiation trend of the Mafic Complex as a whole or individual units, with most concluding that the overarching trend is calc-alkaline, while acknowledging iron enrichment does occur (Rivalenti *et al.*, 1975; Pin and Sills, 1986). For example, the Mg# of the Main Gabbro varies but does not show a strong pattern of Mg# with increasing stratigraphic level (Fig. 53), indicating that iron enrichment is not pervasive. Within the suite of olivine gabbros at Saliceto, Mg# decreases only with limited extent, from 48 to 45 (excluding sample IV38 of Capedri [1971], which does not have a known stratigraphic position in the Saliceto outcrop), with increasing modal plagioclase and SiO_2 and decreasing olivine, P_2O_5, and TiO_2 (Table 3, 18). Thus, PC2 may represent the shift from calc-alkaline to tholeiitic differentiation, showing a gradational change within all units and within most lithologies. The AFM diagram shows some calc-alkaline trends (Fig. 53a) for gabbroic rocks, but at the same time, there does appear to be notable iron enrichment, with the exception of the high Mg# ultramafic cumulates found within the Lower Mafic Complex and Paragneiss-bearing belt. Additionally, tholeiitic versus calc-alkaline differentiation occurs at different levels and does not appear to occur at discrete intervals.

Enrichment of Fe, Ti, and P in cumulates is associated with tholeiitic differentiation (Namur *et al.*, 2012). The Sept Iles layered intrusion in Canada shows features similar to that of

the Ti- and P-rich gabbros of the Upper Mafic Complex. The work by Namur *et al.* (2012) demonstrated that the formation of two thick Fe – Ti – P gabbro layers from this intrusion was the result of liquid immiscibility for one of these layers and simple fractional crystallization for the other. Although Sept Iles Fe – Ti – P gabbros contain extremely high Fe-Ti oxides and apatite (>70 wt.% and >25 wt.%, respectively), striking similarities of trends observed in the Upper Mafic Complex emerge. One aspect that directly relates to rocks of the Mafic Complex is the evolutionary trend noted in the Sept Iles intrusion is fractional crystallization evolutionary trends of Megacyclic Unit I with increasing stratigraphic height leading to the onset of Fe – Ti – P gabbros (see Figure 1 in Namur *et al.*, 2012). Similarly, taking the Mafic Complex as a whole, onset of cumulus apatite crystallization as indicated by bulk rock P_2O_5 exceeding 0.2 wt.%, increases dramatically with bulk rock Mg# <60 (Fig. 52). Silicate liquid immiscibility is unlikely to have occurred in the Mafic Complex. The observed enrichment of P_2O_5 may indicate the crystallization of evolved, trapped melt, consistent with the proposal that the rocks at Saliceto formed through *in-situ* differentiation. In the northern Mafic Complex transect (Fig. 54), P_2O_5 and TiO_2 are incredibly enriched at the 2000 and 4000 m distance from the Insubric Line, and to less of an extent, in the diorites (>6000 m), showing that this trend of differentiation is potentially repeated at stratigraphic levels higher up in the Mafic Complex.

PCA of major elements: PC3 and PC4

PC3 of major elements PCA has strong, positive loadings of P_2O_5 and K_2O, while the loadings of CaO and Al_2O_3 have negative loadings (Table 20). Phosphorous pentoxide has a strong positive loading on PC4, and K_2O and MnO have negative loadings. In the distance biplot of PC4 vs PC3, the effect of the positively skewed distribution of P_2O_5, which is not corrected by the $\log_{10} + 1$ transformation (see Methods) becomes apparent for both PC3 and PC4 (Fig. 67).

Additionally, ultramafic samples almost devoid of P_2O_5 have higher PC3 scores, owing to their lack of CaO and Al_2O_3. Besides the ultramafic rocks that lack the phases dictated by the strong loadings, PC3 may show the opposing behavior of apatite and ilmenite accumulation versus plagioclase accumulation as observed in PC2 with the olivine gabbros at Saliceto (Fig. 67). The olivine gabbro with highest modal abundance of olivine, ilmenite, and apatite (AM-VM22-14D) has the highest PC3 score, whereas the leucocratic olivine gabbro (AM-VM22-6fL) is plagioclase-rich and has the lowest PC3 score, yet not as low as the anorthosites (Fig. 67). In the traverse across the crustal section in the northern Mafic Complex, indicated as Insubric Line distance (Fig. 66), olivine gabbros from Saliceto and gabbros from the Upper Zone have varying high and low PC3 scores, potentially indicating magmatic differentiation generating both apatite-rich (up to 5 vol.%) rocks and anorthosite layers. Gabbros at the 4000 m level in the Main Gabbro show a marked positive loading in PC3 scores while gabbros both stratigraphically above and below generally show negative loading in PC3 scores. This latter observation could be an artifact of lower rock sampling density in the Main Gabbro domain, or alternatively, that apatite enrichment could be occurring within a thicker (~400 m) band as compared to the Upper Zone, where almost full ranges of PC3 values occur at the centimeter scale as demonstrated by the detailed study at Saliceto. Diorites show progressive increase in PC3 with increasing Insubric Line distance; this could reflect an increase in the modal K-feldspar/plagioclase with simultaneous increase in apatite. Both these elements are enriched in the diorite body. Lastly, PC4, which explains about 5% of the total variance in the dataset, shows the opposing behavior of P_2O_5 versus K_2O and MnO. The gabbros of the Upper Mafic Complex show the highest PC4 values, and diorites and some paragneiss show the lowest PC4 scores. This could be explained

by the high modal abundance of K-bearing minerals in the diorites yet not in the remainder of the Upper Mafic Complex, even with similar P_2O_5 enrichment.

Bulk rock trace elements

The trace element record in the rocks of the Mafic Complex show noteworthy trends. Lower Mafic Complex amphibole gabbros (Fig. 55) show little to no Eu anomaly and general depletion of LREE. Sinigoi *et al.* (2011) showed that Lower Mafic Complex trace element trends are comparable to a primitive dyke from Balmuccia Peridotite Massif (sample TS4; Voshage *et al.*, 1988) and interpreted that these amphibole gabbros formed from a MORB-like melt and were contaminated by anatectic melts derived from paragneiss that had already been depleted of Ba and K_2O and enriched in Sr. New data from this study appears to support this interpretation. The LREE-enriched samples from the Lower Mafic Complex, in accordance with this hypothesis, may therefore be ascribed to a higher amount of contamination, particularly to the Zr enriched sample MC_26_03, which contains 757 ppm Zr and abundant zircon, compared to ~20 ppm in the remainder of the samples. Almost all the Upper Mafic Complex samples show a pronounced Eu anomaly, as well as Ba anomalies, and some authors have demonstrated that these anomalies reflect crustal contamination (Mazzucchelli *et al.*, 1992a; Sinigoi *et al.*, 1994).

Likewise, Saliceto samples show the same trace element anomalies. Notably, pyroxenite, although strongly depleted relative to all other analyses presented in this sample, shows a slight increase in HREE (Fig. 59) which can be ascribed to the high modal abundance of orthopyroxene. Also, bulk LREE of Saliceto samples shows varying steepness in LREE, with the most melanocratic olivine gabbro (AM-VM22-14D) to the pyroxenite showing increasing steepness, and the La_N/Nd_N negatively correlates with P_2O_5. Total REE abundance also positively correlates with P_2O_5 for Saliceto samples, but this correlation does not hold for the

entire dataset. From a classical magmatic differentiation standpoint where incompatible trace elements are increasingly enriched in the residual melt during crystallization (Winter, 2014), this could indicate that the melanocratic olivine gabbro is the most evolved member of the olivine gabbro series. However, the decreasing bulk rock Mg# from the melanocratic olivine gabbro (47.6) to the leucocratic olivine gabbro (45.3) and the incredible decrease in modal abundance of mafic minerals suggests the opposite: the pyroxenite represents the least evolved member, and the leucocratic olivine gabbro the most evolved.

Importantly, the lateral continuity of zones between the Val Sesia and Val Mastallone transect (Fig. 11) is strongly supported by trace element profiles along the transect, and the Insubric Line serves as a good stratigraphic benchmark at the 8 km scale of the Mafic Complex. At distances closer to the Insubric Line, the lateral continuity of the base of the Upper Zone shows discrepancies between the Sesia and Mastallone (Fig. 11), because the upper Zone appears thicker, as deduced by the trajectories of foliation and banding mapped by Snoke *et al.* (1999). South of the Val Sesia, trajectories curve southward and eastward (based on the maps of Snoke *et al.*, 1999, and Quick *et al.*, 2003), thereby the Insubric Line serves as an appropriate stratigraphic benchmark for the northern Mafic Complex. The strongly compatible elements Cr and Ni are enriched in both ultramafic and gabbroic rocks at the base of the section in the Paragneiss-bearing Belt or the Lower Layered Group and decreasing upwards into the Upper Zone, consistent with the findings of Rivalenti *et al.* (1981).

PCA of trace elements

PCA of trace elements (Ni, Sr, Rb, Ba, Zr, Nb, La, Ce, Nd, Y) performed on all samples of the Mafic Complex potentially shows the effects of magmatic differentiation and contamination. PC1 is dominated by strong, positive loadings of incompatible elements (LREE,

Nb, Zr) and a weak negative loading of Ni (Table 21). Samples from the Diorites, the roof, and the Paragneiss-bearing Belt have the highest scores, and lithologies with the highest PC1 scores tend to be paragneiss, quartz-bearing norites, diorites, and some gabbros (Fig. 69). LREE enrichment in paragneiss and the resulting enrichment in LREE of the most "contaminated" rocks, particularly within some rocks of the Paragneiss-bearing Belt and the Diorites, has been noted by many previous authors (e.g., Sinigoi *et al.*, 2016). Therefore, element compatibility appears to be a factor governing PC1, yet this process of enrichment in incompatible elements can be produced by both magmatic differentiation and assimilation processes. As discussed above, the most melanocratic, apatite-rich olivine gabbro from Saliceto is the most enriched in LREE compared to other rocks analyzed from Saliceto, whereas the pyroxenite is the most depleted in LREE and has the lowest PC1 score, and the leucocratic olivine gabbro from Saliceto (AM-VM226fL) has the second lowest score of Saliceto samples.

PC2 has strong positive loadings of Y and Ni, and negative loadings of Rb and Ba. Accordingly, diorites have the some of the lowest scores (Fig. 69), as would be predicted by their high Rb and Ba contents, along with charnockites and granitic leucosomes (Fig. 60). Strikingly, PC2 separates the rocks of the Lower Mafic Complex (higher scores) from those of the Upper Mafic Complex (lower scores), showing that the Lower Mafic Complex samples are more enriched in Ni, and to a lesser extent, Sr and Y. The separation of the Lower and Upper Mafic Complex on PC2 supports the hypothesis that the Lower Mafic Complex formed from distinctly different magmas partially caused by different contaminants (Sinigoi *et al.*, 2016). Conversely, the enrichment of rocks from Saliceto and the Upper Zone in incompatible elements may therefore represent evolved melts produced by fractional crystallization of the Lower Layered Group, an idea that goes back to some of the earliest investigators of the Mafic Complex (e.g.,

Rivalenti *et al.*, 1975) and in contrast to the more recent literature that supports crustal contamination that produced these enrichments.

Major and trace elements in concert

PCA of major and trace elements, all samples

Together, major and trace elements display the strongest evidence of magmatic differentiation in the Mafic Complex. Since major elements have similar loadings on PC1 and PC2 in major + trace element PCA as when PCA is performed on major elements only, trace element loadings may then be used to check the conclusions drawn from major element PCA. Of note, the strong, negative loading and Ni, a highly compatible element, and the strong, positive loadings of highly incompatible elements (Rb, Ba, Ce, and La) support the idea that magmatic differentiation may be a component driving the variation explained by PC1. But like with PCA of major and PCA of trace elements, leucosomes, paragneiss and charnockites have high PC1 scores (Fig. 69), showing that these same elements could be the signature of the crustal contaminant, and this is consistent with the literature (e.g., Sinigoi *et al.*, 2011; 2016).

PC2 furthers the idea of magmatic differentiation as a controlling factor on the variance in bulk rock chemistry of the Mafic Complex. Like with PCA of major elements, the iron enrichment trend towards higher PC2 scores suggests tholeiitic differentiation trend. The strong, positive loadings of LREE, Nb, Y, and Zr are contrasted to the negative sample scores of leucosomes and charnockites (Fig. 69), showing that contamination is likely not the source of the variation explained by PC2. Also, lower silica igneous rocks of all rock types and from each zone of the Mafic Complex show great variance on PC2, including the rocks from Saliceto. This may be then explained by varying abundances of trace elements within rocks that is linked to in-situ differentiation. Iron enrichment is also exhibited with increasing PC2 score, suggesting these

processes are not competing processes and actually may be inherently linked for the Mafic Complex.

PC3 of major and trace elements PCA shows strong, positive loadings of Sr, Al_2O_3, and Na_2O, and strong negative loadings of Y, MnO, and Rb (Table 22). Since Sr is highly compatible in plagioclase, this may indicate accumulation of plagioclase, specifically albitic plagioclase towards positive PC3. Conversely Rb is also compatible in plagioclase yet more compatible in K-feldspar. Scores of all zones are spread across the range of PC3, with the exception of the Diorites, which tend to have more negative scores than the those of the Upper Mafic Complex (Figure 70). For Saliceto samples, PC3 and modal plagioclase appear to be strongly correlated. As seen with PC2 of trace element PCA, PC4 discriminates strongly between Lower Mafic Complex samples (positive values) and Upper Mafic Complex (negative scores), and again, Y has a strong, positive loading whereas Ba, Rb, K_2O have the strongest negative loadings on PC4. The rocks of the Paragneiss-bearing Belt overlap both groups; Paragneiss-bearing Belt samples have PC4 scores that range from strongly negative to strongly positive. Although preliminary, it may be suggested that this change from the base of the Mafic Complex to the top may indicate a genetic relationship between successive units as shown by PC4.

PCA of major and trace for the northern Mafic Complex

Largely, principal components generated from PCA of major and trace elements for the northern Mafic Complex show the same sequence of element loadings (Table 22). When scores of each sample are plotted against stratigraphy (Fig. 71), trends emerge that explain the compositional heterogeneities of the northern Mafic Complex. High scores of PC1 are dominated by leucosomes, charnockite and paragneiss, while two of the most primitive rocks in the sequence of samples used, the pyroxenite from Saliceto (sample AM-IVZ-VM008) and a noritic

enclave from the Diorites (sample MC_19) have the lowest scores. Therefore, once again, the greatest variation of the dataset is due to combined processes of assimilation and magmatic differentiation.

The variance explained by PC2, as postulated above, could be the result of magmatic differentiation along the tholeiitic trend. Notably, as seen along the stratigraphy, a trend emerges from the Upper Zone (~2000 m) to the roof at the diorites (Fig. 71). Along this profile upwards, scores decline from 2000 to 3000 m distance to the Insubric Line, then rise dramatically from 3000 m to 4000 m, culminating with the zircon-rich, apatite-rich sample MC_13. Overall, this trend of PC2 scores, forming a U shape, is similar to those seen in individual elemental profiles (e.g., La, P_2O_5, Zr; Fig. 60 and 61), yet seemingly more distinct than individual element profiles. Upwards of 4000 m, scores drop dramatically and increase monotonically through the transition with Diorites. The lower trend observed can potentially be explained by a thick magma chamber in which differentiation occurred upwards, or by a thick mush with evolving melts migrating upwards. The variable trend within the Main Gabbro body probably is not explained by differing contamination, as Voshage *et al.* (1990) demonstrated the Main Gabbro is mostly isotopically homogeneous. Since Mg# does not show such a clearly defined trend for this interval, the classical trend of fractional crystallization and physical separation of crystal and melt may not apply here, but widespread yet stratigraphically-controlled and potentially temporally-controlled processes such as reactive melt flow may allow for these trends observed.

The petrographic analysis of the rocks at Saliceto further corroborates the idea of magmatic differentiation occurring in the Upper Zone and Main Gabbro. Sample MC_13, an apatite-rich olivine-gabbro containing garnet coronas, is found around 4000 m stratigraphy. This

sample contains >3500 ppm Zr and abundant zircon. Zircon is found in proximity to apatite, and euhedral zircon grains are fully enclosed within ilmenite grains.

PC3 with strong, negative loadings of Sr, Al_2O_3, Na_2O, and Ba may be explained by feldspar accumulation; this is supported by the strong, positive relationship between modal plagioclase in rocks from Saliceto and PC3. The noritic mafic enclave MC_19 in the Diorites has an anomalously high PC3 score, which is also seen in this sample's uniquely strong, negative Sr anomaly. Overall, no trends are readily observable in terms of stratigraphy (Fig. 71) with PC3 variance, except that Lower Layered Group samples within the Paragneiss-bearing Belt have higher scores, attributed to higher HREE and Y.

Lastly, PC4, dominated by strong positive loadings of incompatible elements (Rb, Zr, K_2O, Ba) may indicate the overall evolution of the northern Mafic Complex. This is evidenced by the monotonic yet incredibly variable increase in sample scores from the base of the Mafic Complex to near the roof at 6000 – 7000 m Insubric Line distance (Fig. 71). A major control of PC4 could be the introduction of biotite on the liquidus, which has a high partition coefficient for K_2O, Rb, and Ba (Bigi *et al.*, 1993); this is partly demonstrated by the higher PC4 scores of diorites. While the melt that formed the diorites could be the extreme end product of reactive melt flow in a small magma chamber at the roof of the complex (Solano *et al.*, 2014), the overall trend of PC4 with increasing stratigraphic height could duly indicate a genetic fingerprint that showcases the cohesive evolution of the Upper Mafic Complex upwards.

CHAPTER 7

CONCLUSIONS

From a transcrustal perspective, the features observed from micrometer scale to kilometer scale are important to understand how the intrusion of basaltic melts into the lower crust may give rise to upward migrating melts that form intrusions in the upper crust, even to erupting at the surface. Clearly, the complex mineralogy and bulk rock geochemistry of the Mafic Complex hampers a straightforward conclusion concerning the development of melts that may escape the lower crust. But through these careful observations, it is possible to reconcile this connection.

Study of a suite of mafic rocks from the Upper Zone of the Mafic Complex (Ivrea-Verbano Zone, Alps, Italy) yields a number of conclusions regarding the emplacement, cooling dynamics, reactive melt flow, and heterogeneities on a meter to centimeter scale:

1. The body of pyroxenite within the Saliceto suite likely formed from the accumulation of olivine, spinel, and Fe-Ti oxides. Liquid percolating through this body reacted with the olivine through a peritectic reaction, causing the crystallization of large, poikilitic orthopyroxene grains accompanied by and followed by the crystallization of plagioclase. Depletion in bulk rock REE and low P_2O_5 indicates that the coexisting melt that formed this rock had not evolved significantly, or alternatively, that the depleted character of melt – rock reaction products (orthopyroxene, amphibole) formed in a closed system. Furthermore, cumulus Fe-Ti oxides in this rock point indicate that this rock formed from oxidizing melt. Later, percolating fluids or H_2O rich-melt along grain boundaries reacted with plagioclase, pyroxene, olivine, and oxides and crystallized coronitic to poikilitic amphibole. Symplectites of Al-spinel and

pyroxene formed at the expense of plagioclase, and to a lesser extent, pyroxenes and oxides. The development of symplectites versus garnet seems to be a compositional control.

2. The olivine gabbro crystallized initially as a banded troctolite, with *in-situ* differentiaion forming centimeter-scale bands of olivine, Fe-Ti oxides, spinel, and apatite alternating with a crystallizing plagioclase. Later, percolation of melts through these cumulates formed coronas of orthopyroxene, followed by clinopyroxene. Amphibole then crystallized due to percolation of a hydrous melt or fluid. Lastly, garnet rims between plagioclase and olivine, pyroxenes, amphibole, and Fe-Ti oxides formed, potentially from a protracted cooling history.
3. The three major lithologies formed from the same melt, as indicated by their common trace element signatures. Pyroxenite represents the earliest-formed rock of the suite as indicated by its depletion in incompatible elements and adcumulus structure and mineralogy. Olivine gabbro may have been the product of this differentiation, followed by the common gabbro-norite. Mechanisms that may explain the sharp changes from one lithology to the next remain unclear.

The statistical analysis compilation of bulk rock geochemical data of the entire Mafic Complex of the Ivrea-Verbano Zone yields conclusions that point to magmatic differentiation at varying scales:

a. The greatest source of variation in terms major elements across the entire Mafic Complex is due to the combined processes of magmatic differentiation as well as crustal contamination.
b. As a whole, the Mafic Complex likely differentiated along a tholeiitic trend as evidenced by iron enrichment associated with enrichment in P_2O_5 and TiO_2. Evolution along this trend was accompanied by enrichment in incompatible elements.

c. As revealed by trace elements, the Lower Mafic Complex and the Upper Mafic Complex are distinguishable, and this may have been the product of a different source of contamination.
d. Discrete, large scale (>1000 m thick) trends in the Upper Zone to the diorites, in terms of both major and trace elements, point to magmatic differentiation causing a specific package in the Main Gabbro to differentiate upwards, culminating in the crystallization of apatite and even zircon. These large-scale trends are similar to those noted in large layered igneous intrusions such as Bushveld and Skaergaard. This may contrast the predictions of models that assume that the Mafic Complex formed from intrusions of magma at a fixed depth in the Mafic Complex sequence and the work of previous researchers who demonstrated the homogeneity of the Main Gabbro.

Work in the future could include isotopic analyses of bulk rock and individual minerals of Saliceto samples. Bulk rock isotopes (e.g., Sr, Nd) could help determine the degree of crustal contamination of Saliceto rocks, and if the crustal fingerprint (high Sr_i) varies between lithologies and within lithologies. Isotopic tracers may also help constrain reactions within lithologies, for example, the enigmatic origins of amphibole found throughout the Mafic Complex. Future work should also include accessing the rock data repositories at the University of Trieste (Italy) for including additional bulk rock analyses and rock sampling location data along with microstructural and petrological observations of samples that have not been published. This “hidden” rock dataset from unpublished Master-level thesis research directed by Emeritus Prof. Sinigoi (University of Trieste) may fill potential gaps that still exist in the petrological and geochemical characterization of the continental crustal section of the Ivrea-Verbano Zone. In particular, this rock dataset may fill the sampling gaps in the lithological groups of the Mafic Complex along the Val Mastallone, Val Mala, and Val Sessera transects.

REFERENCES

Annen, C. (2011). Implications of incremental emplacement of magma bodies for magma differentiation, thermal aureole dimensions and plutonism–volcanism relationships. *Tectonophysics* **500**, 3–10.

Annen, C., Blundy, J. D. & Sparks, R. S. J. (2006). The Genesis of Intermediate and Silicic Magmas in Deep Crustal Hot Zones. *Journal of Petrology* **47**, 505–539.

Antonicelli, M., Tribuzio, R., Liu, T. & Wu, F.-Y. (2020). Contaminating melt flow in magmatic peridotites from the lower continental crust (Rocca d'Argimonia sequence, Ivrea–Verbano Zone). *European Journal of Mineralogy*. Copernicus GmbH **32**, 587–612.

Bachmann, O. & Bergantz, G. (2008). The Magma Reservoirs That Feed Supereruptions. *Elements* **4**, 17–21.

Bachmann, O. & Bergantz, G. W. (2004). On the Origin of Crystal-poor Rhyolites: Extracted from Batholithic Crystal Mushes. *Journal of Petrology* **45**, 1565–1582.

Barboza, S. A. & Bergantz, G. W. (2000). Metamorphism and Anatexis in the Mafic Complex Contact Aureole, Ivrea Zone, Northern Italy. *Journal of Petrology* **41**, 1307–1327.

Barboza, S. A., Bergantz, G. W. & Brown, M. (1999). Regional granulite facies metamorphism in the Ivrea zone: Is the Mafic Complex the smoking gun or a red herring? *Geology* **27**, 447.

Bea, F. & Montero, P. (1999). Behavior of accessory phases and redistribution of Zr, REE, Y, Th, and U during metamorphism and partial melting of metapelites in the lower crust: an example from the Kinzigite Formation of Ivrea-Verbano, NW Italy. *Geochimica et Cosmochimica Acta* **63**, 1133–1153.

Bea, F., Montero, P., Garuti, G. & Zacharini, F. (1997). Pressure-Dependence of Rare Earth Element Distribution in Amphibolite- and Granulite- Grade Garnets. A LA-ICP-MS Study. *Geostandards Newsletter* **21**, 253–270.

Berckhemer, H. (1969). Direct evidence for the composition of the lower crust and the moho. *Tectonophysics* **8**, 97–105.

Berno, D., Tribuzio, R., Zanetti, A. & Hémond, C. (2020). Evolution of mantle melts intruding the lowermost continental crust: constraints from the Monte Capio–Alpe Cevia mafic–ultramafic sequences (Ivrea–Verbano Zone, northern Italy). *Contributions to Mineralogy and Petrology* **175**, 2.

Bertolani, M. (1968). Fenomeni di transformazione granulitica nella formazione basica Ivrea-Verbano (Alpi Occidentali Italiane). *Schweizerische Mineralogische und Petrographische Mitteilungen* **48**, 21–30.

Biagioni, C. & Pasero, M. (2014). The systematics of the spinel-type minerals: An overview. *American Mineralogist*. De Gruyter **99**, 1254–1264.

Bigi, S., Brigatti, M. F., Mazzuchelli, M. & Rivalenti, G. (1993). Crystal chemical variations in Ba-rich biotites from gabbroic rocks of lower crust (Ivrea Zone, NW Italy). *Contributions to Mineralogy and Petrology* **113**, 87–99.

Blundy, J. D. & Holland, T. J. B. (1990). Calcic amphibole equilibria and a new amphibole-plagioclase geothermometer. *Contributions to Mineralogy and Petrology* **104**, 208–224.

Boriani, A., Burlini, L. & Sacchi, R. (1990). The Cossato-Mergozzo-Brissago Line and the Pogallo Line (Southern Alps, Northern Italy) and their relationships with the late-Hercynian magmatic and metamorphic events. *Tectonophysics* **182**, 91–102.

Brack, P. & Ulmer, P. (2010). A crustal-scale magmatic system from the Earth's mantle to the Permian surface − Field trip to the area of lower Valsesia and Val d'Ossola (Massiccio dei Laghi, Southern Alps, Northern Italy). 19.

Brey, G. P. & Köhler, T. (1990). Geothermobarometry in Four-phase Lherzolites II. New Thermobarometers, and Practical Assessment of Existing Thermobarometers. *Journal of Petrology* **31**, 1353–1378.

Burke, M. M. & Fountain, D. M. (1990). Seismic properties of rocks from an exposure of extended continental crust—new laboratory measurements from the Ivrea Zone. *Tectonophysics* **182**, 119–146.

Capedri, S. (1968). Sulle rocce basiche della formazione Ivrea-Verbano: 1. Considerazioni petrografiche e petrogenetiche sulla Bassa Val Mastalone. **48**, 103–112.

Capedri, S. (1971). Sulle rocce della formazione basica Ivrea-Verbano: 2. Petrografia delle granuliti e rocce derivate affiorante nella Val Mastallone (Vercelli) e loro evoluzione petrogenetica. *Mem. Soc. Geol. Ital.* **10**, 227–312.

Caricchi, L., Annen, C., Blundy, J., Simpson, G. & Pinel, V. (2014). Frequency and magnitude of volcanic eruptions controlled by magma injection and buoyancy. *Nature Geoscience*. Nature Publishing Group **7**, 126–130.

Cashman, K. V. & Giordano, G. (2014). Calderas and magma reservoirs. *Journal of Volcanology and Geothermal Research* **288**, 28–45.

Cawthorn, R. G. (2015). The Bushveld Complex, South Africa. In: Charlier, B., Namur, O., Latypov, R. & Tegner, C. (eds) *Layered Intrusions*. Dordrecht: Springer Netherlands, 517–587.

Decarlis, A., Zanetti, A., Ogunyele, A. C., Ceriani, A. & Tribuzio, R. (2023). The Ivrea-Verbano tectonic evolution: The role of the crust-mantle interactions in rifting localization. *Earth-Science Reviews* **238**, 104318.

Demarchi, G., Quick, J. E., Sinigoi, S. & Mayer, A. (1998). Pressure Gradient and Original Orientation of A Lower-Crustal Intrusion in the Ivrea-Verbano Zone, Northern Italy. *The Journal of Geology* **106**, 609–622.

Ferracutti, G. R., Gargiulo, M. F., Ganuza, M. L., Bjerg, E. A. & Castro, S. M. (2015). Determination of the spinel group end-members based on electron microprobe analyses. *Mineralogy and Petrology* **109**, 153–160.

Fountain, D. M. & Salisbury, M. H. (1981). Exposed cross-sections through the continental crust: implications for crustal structure, petrology, and evolution. *Earth and Planetary Science Letters* **56**, 263–277.

Gonzalez, C. M., Fiorentini, M. L., Gorczyk, W. & Dering, G. (2020). Numerical modeling of post-collisional carbonated alkaline magmatism: Variscan style Orogeny (the Ivrea Zone as natural laboratory). *Solid Earth Sciences* **5**, 131–152.

Handy, M. R., Franz, L., Heller, F., Janott, B. & Zurbriggen, R. (1999). Multistage accretion and exhumation of the continental crust (Ivrea crustal section, Italy and Switzerland). *Tectonics* **18**, 1154–1177.

Handy, M. R. & Zingg, A. (1991). The tectonic and rheological evolution of an attenuated cross section of the continental crust: Ivrea crustal section, southern Alps, northwestern Italy and southern Switzerland. *GSA Bulletin* **103**, 236–253.

Henk, A., Franz, L., Teufel, S. & Oncken, O. (1997). Magmatic Underplating, Extension, and Crustal Reequilibration: Insights From A Cross-Section Through the Ivrea Zone and Strona-Ceneri Zone, Northern Italy. *The Journal of Geology* **105**, 367–378.

Hofmann, A. W. (1988). Chemical differentiation of the Earth: the relationship between mantle, continental crust, and oceanic crust. *Earth and Planetary Science Letters* **90**, 297–314.

Hollocher, K. (2022). NORM4 Excel spreadsheet programs to calculate petrologic norms from whole-rock chemical analyses. Zenodo.

Holness, M. B., Vukmanovic, Z. & Mariani, E. (2017). Assessing the Role of Compaction in the Formation of Adcumulates: a Microstructural Perspective. *Journal of Petrology* **58**, 643–673.

Holwell, D. A., Fiorentini, M. L., Knott, T. R., McDonald, I., Blanks, D. E., Campbell McCuaig, T. & Gorczyk, W. (2022). Mobilisation of deep crustal sulfide melts as a first order control on upper lithospheric metallogeny. *Nature Communications* **13**, 573.

Huismans, R. S. & Beaumont, C. (2008). Complex rifted continental margins explained by dynamical models of depth-dependent lithospheric extension. *Geology* **36**, 163–166.

Huismans, R. S. & Beaumont, C. (2014). Rifted continental margins: The case for depth-dependent extension. *Earth and Planetary Science Letters* **407**, 148–162.

Irvine, T. N. & Baragar, W. R. A. (1971). A Guide to the Chemical Classification of the Common Volcanic Rocks. *Canadian Journal of Earth Sciences*. NRC Research Press **8**, 523–548.

Jackson, M. D., Blundy, J. & Sparks, R. S. J. (2018). Chemical differentiation, cold storage and remobilization of magma in the Earth's crust. *Nature*. Nature Publishing Group **564**, 405–409.

Jarosewich, E., Nelen, J. a. & Norberg, J. A. (1980). Reference Samples for Electron Microprobe Analysis*. *Geostandards Newsletter* **4**, 43–47.

Karakas, O., Wotzlaw, J.-F., Guillong, M., Ulmer, P., Brack, P., Economos, R., Bergantz, G. W., Sinigoi, S. & Bachmann, O. (2019). The pace of crustal-scale magma accretion and differentiation beneath silicic caldera volcanoes. *Geology* **47**, 719–723.

Ketcham, R. A. (2015). Technical Note: Calculation of stoichiometry from EMP data for apatite and other phases with mixing on monovalent anion sites. *American Mineralogist*. De Gruyter **100**, 1620–1623.

Klötzli, U. S., Sinigoi, S., Quick, J. E., Demarchi, G., Tassinari, C. C. G., Sato, K. & Günes, Z. (2014). Duration of igneous activity in the Sesia Magmatic System and implications for high-temperature metamorphism in the Ivrea–Verbano deep crust. *Lithos* **206–207**, 19–33.

Kusznir, N. J. & Karner, G. D. (2007). Continental lithospheric thinning and breakup in response to upwelling divergent mantle flow: application to the Woodlark, Newfoundland and Iberia margins. *Geological Society, London, Special Publications*. The Geological Society of London **282**, 389–419.

Le Maitre, R. W., Streckeisen, A., Zanettin, B., Le Bas, M. J., Bonin, B. & Bateman, P. (eds) (2002). *Igneous Rocks: A Classification and Glossary of Terms*. Cambridge: Cambridge University Press.

Leake, B. *et al.* (1997). Nomenclature of amphiboles; Report of the Subcommittee on Amphiboles of the International Mineralogical Association, Commission on New Minerals and Mineral Names. *American Mineralogist* **82**, 1019–1037.

Li, X., Zhang, C., Almeev, R. R. & Holtz, F. (2020). GeoBalance: An Excel VBA program for mass balance calculation in geosciences. *Geochemistry* **80**, 125629.

Locock, A. J. (2014). An Excel spreadsheet to classify chemical analyses of amphiboles following the IMA 2012 recommendations. *Computers & Geosciences* **62**, 1–11.

Mazzucchelli, M. (1983). The upper zone of the Ivrea·Verbano layered complex (ltalian Western Alps). *Neues Jahrbuch für Mineralogie - Abhandlungen* **146**, 101–116.

Mazzucchelli, M., Rivalenti, G., Vannucci, R., Bottazzi, P., Ottolini, L., Hofmann, A. W. & Parenti, M. (1992a). Primary positive Eu anomaly in clinopyroxenes of low-crust gabbroic rocks. *Geochimica et Cosmochimica Acta* **56**, 2363–2370.

Mazzucchelli, M., Rivalenti, G., Vannucci, R., Bottazzi, P., Ottolini, L., Hofmann, A. W., Sinigol, S. & Demarchin, G. (1992b). Trace element distribution between clinopyroxene and garnet in gabbroic rocks of the deep crust: An ion microprobe study. *Geochimica et Cosmochimica Acta* **56**, 2371–2385.

McDonough, W. F. & Sun, S. -s. (1995). The composition of the Earth. *Chemical Geology* **120**, 223–253.

Mollo, S., Putirka, K., Iezzi, G., Del Gaudio, P. & Scarlato, P. (2011). Plagioclase–melt (dis)equilibrium due to cooling dynamics: Implications for thermometry, barometry and hygrometry. *Lithos* **125**, 221–235.

Namur, O., Charlier, B. & Holness, M. B. (2012). Dual origin of Fe–Ti–P gabbros by immiscibility and fractional crystallization of evolved tholeiitic basalts in the Sept Iles layered intrusion. *Lithos* **154**, 100–114.

Nandedkar, R. H., Ulmer, P. & Müntener, O. (2014). Fractional crystallization of primitive, hydrous arc magmas: an experimental study at 0.7 GPa. *Contributions to Mineralogy and Petrology* **167**, 1015.

Pasero, M., Kampf, A. R., Ferraris, C., Pekov, I. V., Rakovan, J. & White, T. J. (2010). Nomenclature of the apatite supergroup minerals. *European Journal of Mineralogy* **22**, 163–179.

Percival, J. A., Stern, R. A. & Skulski, T. (2001). Crustal growth through successive arc magmatism: reconnaissance U–Pb SHRIMP data from the northeastern Superior Province, Canada. *Precambrian Research* **109**, 203–238.

Peressini, G., Quick, J. E., Sinigoi, S., Hofmann, A. W. & Fanning, M. (2007). Duration of a Large Mafic Intrusion and Heat Transfer in the Lower Crust: a SHRIMP U-Pb Zircon Study in the Ivrea-Verbano Zone (Western Alps, Italy). *Journal of Petrology* **48**, 1185–1218.

Petri, B., Duretz, T., Mohn, G., Schmalholz, S. M., Karner, G. D. & Müntener, O. (2019). Thinning mechanisms of heterogeneous continental lithosphere. *Earth and Planetary Science Letters* **512**, 147–162.

Petri, B., Mohn, G., Štípská, P., Schulmann, K. & Manatschal, G. (2016). The Sondalo gabbro contact aureole (Campo unit, Eastern Alps): implications for mid-crustal mafic magma emplacement. *Contributions to Mineralogy and Petrology* **171**, 52.

Pin, C. & Sills, J. D. (1986). Petrogenesis of layered gabbros and ultramafic rocks from Val Sesia, the Ivrea Zone, NW Italy: trace element and isotope geochemistry. *Geological Society, London, Special Publications* **24**, 231–249.

Pistone, M., Müntener, O., Ziberna, L., Hetényi, G., & Zanetti, A. (2017). Report on the ICDP Workshop DIVE (Drilling the Ivrea-Verbano zonE). *Scientific Drilling* **23**, 47–56.

Pistone, M., Ziberna, L., Hetényi, G., Scarponi, M., Zanetti, A. & Müntener, O. (2020). Joint Geophysical-Petrological Modeling on the Ivrea Geophysical Body Beneath Valsesia, Italy: Constraints on the Continental Lower Crust. *Geochemistry, Geophysics, Geosystems* **21**, e2020GC009397.

Quick, J. E., Sinigoi, S. & Mayer, A. (1994). Emplacement dynamics of a large mafic intrusion in the lower crust, Ivrea-Verbano Zone, northern Italy. *Journal of Geophysical Research: Solid Earth* **99**, 21559–21573.

Quick, J. E., Sinigoi, S. & Mayer, A. (1995). Emplacement of mantle peridotite in the lower continental crust, Ivrea-Verbano zone, northwest Italy. *Geology* **23**, 739.

Quick, J. E., Sinigoi, S., Negrini, L., Demarchi, G. & Mayer, A. (1992). Synmagmatic deformation in the underplated igneous complex of the Ivrea-Verbano zone. *Geology* **20**, 613.

Quick, J. E., Sinigoi, S., Peressini, G., Demarchi, G., Wooden, J. L. & Sbisà, A. (2009). Magmatic plumbing of a large Permian caldera exposed to a depth of 25 km. *Geology* **37**, 603–606.

Quick, J. E., Sinigoi, S., Snoke, A. W., Kalakay, T. J., Mayer, A. & Peressini, G. (2003). *Geologic map of the southern Ivrea-Verbano zone, northwestern Italy*. USGS Numbered Series. .

Redler, C., Johnson, T. E., White, R. W. & Kunz, B. E. (2012). Phase equilibrium constraints on a deep crustal metamorphic field gradient: metapelitic rocks from the Ivrea Zone (NW Italy). *Journal of Metamorphic Geology* **30**, 235–254.

Rivalenti, G., Garuti, G. & Rossi, A. (1975). The origin of the Ivrea-Verbano Basic Formation (Western Italian Alps) - Whole rock geochemistry. *Boll. Soc. Geol. Ital.*

Rivalenti, G., Garuti, G., Rossi, A., Siena, F. & Sinigoi, S. (1981a). Existence of Different Peridotite Types and of a Layered Igneous Complex in the Ivrea Zone of the Western Alps. *Journal of Petrology* **22**, 127–153.

Rivalenti, G., Garuti, G., Rossi, A., Slena, F. & Sinigoi, S. (1981b). Chromian spinel in the Ivrea-Verbano layered igneous complex, western Alps, Italy. *TMPM Tschermaks Mineralogische und Petrographische Mitteilungen* **29**, 33–53.

Rivalenti, G., Rossi, A., Siena, F. & Sinigoi, S. (1984). The layered series of the Ivrea-Verbano igneous complex, we tern Alps, Italy. *TMPM Tschermaks Mineralogische und Petrographische Mitteilungen* **33**, 77–99.

Royden, L. & Keen, C. E. (1980). Rifting process and thermal evolution of the continental margin of Eastern Canada determined from subsidence curves. *Earth and Planetary Science Letters* **51**, 343–361.

Rudnick, R. L. & Presper, T. (1990). Geochemistry of Intermediate/- to High-Pressure Granulites. In: Vielzeuf, D. & Vidal, Ph. (eds) *Granulites and Crustal Evolution*. Dordrecht: Springer Netherlands, 523–550.

Sanfilippo, A., MacLeod, C. J., Tribuzio, R., Lissenberg, C. J. & Zanetti, A. (2020). Early-Stage Melt-Rock Reaction in a Cooling Crystal Mush Beneath a Slow-Spreading Mid-Ocean Ridge (IODP Hole U1473A, Atlantis Bank, Southwest Indian Ridge). *Frontiers in Earth Science* **8**.

Schmid, R. & Wood, B. J. (1976). Phase relationships in granulitic metapelites from the Ivrea-Verbano zone (Northern Italy). *Contributions to Mineralogy and Petrology* **54**, 255–279.

Schmid, S. M. (1993). Ivrea Zone and Adjacent Southern Alpine Basement. In: von Raumer, J. F. & Neubauer, F. (eds) *Pre-Mesozoic Geology in the Alps*. Berlin, Heidelberg: Springer, 567–583.

Schmid, S. M., Zingg, A. & Handy, M. (1987). The kinematics of movements along the Insubric Line and the emplacement of the Ivrea Zone. *Tectonophysics* **135**, 47–66.

Schnetger, B. (1994). Partial melting during the evolution of the amphibolite- to granulite-facies gneisses of the Ivrea Zone, northern Italy. *Chemical Geology* **113**, 71–101.

Siegesmund, S., Layer, P., Dunkl, I., Vollbrecht, A., Steenken, A., Wemmer, K. & Ahrendt, H. (2008). Exhumation and deformation history of the lower crustal section of the Valstrona di Omegna in the Ivrea Zone, southern Alps. *Geological Society, London, Special Publications*. The Geological Society of London **298**, 45–68.

Sills, J. D. (1984). Granulite facies metamorphism in the Ivrea Zone, NW Italy. *Schweizerische Mineralogische und Petrographische Mitteilungen* **64**, 169--191.

Sinigoi, S., Antonini, P., Demarchi, G., Longinelli, A., Mazzucchelli, M., Negrini, L. & Rivalenti, G. (1991). Intractions of mantle and crustal magmas in the southern part of the Ivrea Zone (Italy). *Contributions to Mineralogy and Petrology* **108**, 385–395.

Sinigoi, S., Quick, J. E., Clemens-Knott, D., Mayer, A., Demarchi, G., Mazzucchelli, M., Negrini, L. & Rivalenti, G. (1994). Chemical evolution of a large mafic intrusion in the lower crust, Ivrea-Verbano Zone, northern Italy. *Journal of Geophysical Research: Solid Earth* **99**, 21575–21590.

Sinigoi, S., Quick, J. E., Demarchi, G. & Klötzli, U. (2011). The role of crustal fertility in the generation of large silicic magmatic systems triggered by intrusion of mantle magma in the deep crust. *Contributions to Mineralogy and Petrology* **162**, 691–707.

Sinigoi, S., Quick, J. E., Demarchi, G. & Klötzli, U. S. (2016). Production of hybrid granitic magma at the advancing front of basaltic underplating: Inferences from the Sesia Magmatic System (south-western Alps, Italy). *Lithos* **252–253**, 109–122.

Sinigoi, S., Quick, J. E., Demarchi, G. & Peressini, G. (2010). The Sesia Magmatic System. *Journal of the Virtual Explorer* **36**.

Sinigoi, S., Quick, J. E., Mayer, A. & Budahn, J. (1996). Influence of stretching and density contrasts on the chemical evolution of continental magmas: an example from the Ivrea-Verbano Zone. *Contributions to Mineralogy and Petrology* **123**, 238–250.

Sinigoi, S., Quick, J. E., Mayer, A. & Demarchi, G. (1995). Density-controlled assimilation of underplated crust, Ivrea-Verbano zone, Italy. *Earth and Planetary Science Letters* **129**, 183–191.

Smye, A. J., Lavier, L. L., Zack, T. & Stockli, D. F. (2019). Episodic heating of continental lower crust during extension: A thermal modeling investigation of the Ivrea-Verbano Zone. *Earth and Planetary Science Letters* **521**, 158–168.

Snoke, A. W., Kalakay, T. J., Quick, J. E. & Sinigoi, S. (1999). Development of a deep-crustal shear zone in response to syntectonic intrusion of mafic magma into the lower crust, Ivrea–Verbano zone, Italy. *Earth and Planetary Science Letters* **166**, 31–45.

Solano, J. M. S., Jackson, M. D., Sparks, R. S. J. & Blundy, J. (2014). Evolution of major and trace element composition during melt migration through crystalline mush: Implications for chemical differentiation in the crust. *American Journal of Science*. American Journal of Science **314**, 895–939.

Sparks, R. S. J., Annen, C., Blundy, J. D., Cashman, K. V., Rust, A. C. & Jackson, M. D. (2019). Formation and dynamics of magma reservoirs. *Philosophical Transactions of the Royal Society A: Mathematical, Physical and Engineering Sciences* **377**, 20180019.

Storck, J.-C., Laurent, O., Karakas, O., Wotzlaw, J.-F., Galli, A., Sinigoi, S., Bachmann, O. & Chelle-Michou, C. (2021). Mantle versus crustal contributions in crustal-scale magmatic systems (Sesia Magmatic System, northern Italy) from coupling Hf isotopes and numerical modelling. *Contributions to Mineralogy and Petrology* **176**, 95.

Tribuzio, R., Renna, M. R., Antonicelli, M., Liu, T., Wu, F.-Y. & Langone, A. (2023). The peridotite-pyroxenite sequence of Rocca d'Argimonia (Ivrea-Verbano Zone, Italy): Evidence for reactive melt flow and slow cooling in the lowermost continental crust. *Chemical Geology* **619**, 121315.

Vance, J. A. (1961). Polysynthetic twinning in plagioclase. *American Mineralogist* **46**, 1097–1119.

Villiger, S. (2005). Evolution of anhydrous mantle-derived tholeiitic liquids by fractional and equilibrium crystallisation at 1.0 and 0.7 GPa: An experimental study. Doctoral Thesis, ETH Zurich.

Villiger, S., Ulmer, P. & Müntener, O. (2007). Equilibrium and Fractional Crystallization Experiments at 0·7 GPa; the Effect of Pressure on Phase Relations and Liquid Compositions of Tholeiitic Magmas. *Journal of Petrology* **48**, 159–184.

Voshage, H., Hofmann, A. W., Mazzucchelli, M., Rivalenti, G., Sinigoi, S., Raczek, I. & Demarchi, G. (1990). Isotopic evidence from the Ivrea Zone for a hybrid lower crust formed by magmatic underplating. *Nature* **347**, 731–736.

Voshage, H., Hunziker, J. C., Hofmann, A. W. & Zingg, A. (1987). A Nd and Sr isotopic study of the Ivrea zone, Southern Alps, N-Italy. *Contributions to Mineralogy and Petrology* **97**, 31–42.

Voshage, H., Sinigoi, S., Mazzucchelli, M., Demarchi, G., Rivalenti, G. & Hofmann, A. W. (1988). Isotopic constraints on the origin of ultramafic and mafic dikes in the Balmuccia peridotite (Ivrea Zone). *Contributions to Mineralogy and Petrology* **100**, 261–267.

Walters, J. B. (2022). MinPlot: A mineral formula recalculation and plotting program for electron probe microanalysis. *Mineralogia* **53**, 51–66.

Wass, S. Y. (1973). Plagioclase-spinel intergrowths in alkali basaltic rocks from the Southern Highlands, N.S.W. *Contributions to Mineralogy and Petrology* **38**, 167–175.

Winter, J. D. (2014). *Principles of igneous and metamorphic petrology*. Harlow: Pearson Education.

Wyatt, D. C., Smye, A. J., Garber, J. M. & Hacker, B. R. (2022). Assembly and Tectonic Evolution of Continental Lower Crust: Monazite Petrochronology of the Ivrea-Verbano Zone (Val Strona di Omegna). *Tectonics* **41**, e2021TC006841.

Zingg, A. (1980). Regional metamorphism in the Ivrea zone (Southern Alps, N-Italy) : field and microscopic investigations. bis 1977 Leemann / ab 1978 Stäubli.

Zingg, A. (1983). The Ivrea and Strona-Ceneri Zones (Southern Alps, Ticino and N-Italy)-A Review. *Schweizerische Mineralogische und Petrographische Mitteilungen* **63**, 361–392.

Zingg, A., Bernoullisrrasse, I. & Instirut, G. (1990). Teotonometamorphic history of the Ivrea Zone and its relationship to the crustal evolution of the Southern Alps. 24.

Table 1: Arenal hornblende (USNM 111356) analyses from ETH Zurich EPMA session compared to published values.

	Experimental average (n=44)	standard deviation	Jarosewich *et al.* (1980)
SiO_2	41.34	0.626	41.46
TiO_2	1.11	0.018	1.41
Al_2O_3	14.26	0.193	15.47
Cr_2O_3	0.01	0.004	
Fe_2O_3			5.60
FeO			6.43
FeO(total)	11.23	0.106	
NiO	0.00	0.012	
MnO	0.16	0.012	0.15
MgO	14.43	0.088	14.24
CaO	11.26	0.070	11.55
Na_2O	2.12	0.027	1.91
K_2O	0.19	0.011	0.21
P_2O_5			<0.01
H_2O			1.21
TOTAL	96.11	0.806	99.64

*FeO was measured as FeO total at ETH Zurich.

Table 2: mineral abbreviations used in this work, adapted from Whitney and Evans (2010).

Symbol	Mineral name
Ab	albite
Alm	almandine
Amp	amphibole (group)
An	anorthite
Ap	apatite (group)
Bdy	baddeleyite
Bt	biotite (group)
Ccp	chalcopyrite
Di	diopside
En	enstatite
Ep	epidote (group)
Fa	fayalite
Fs	ferrosilite
Fo	forsterite
Grt	garnet (group)
Grs	grossular
Hem	hematite
Hc	hercynite
Hbl	hornblende (group)
Ilm	ilmenite
Mag	magnetite
Ol	olivine
Opq	opaque mineral (informal)
Prg	pargasite
Pn	pentlandite
Pl	plagioclase (group)
Py	pyrite
Prp	pyrope
Po	pyrrhotite
Qz	quartz
Spl*	spinel (Al-spinel)
Ts	tschermakite
Usp	ulvöspinel
Wo	wollastonite

*Spl refers to Al-spinel (spinel – hercynite solid solution) in this work after Arguin *et al.* (2018).

Table 3: Modal mineralogy in volume % for selected samples in the Mafic Complex and at Saliceto

Sample	MC09-02 TA	MC10-01 TA	MC07-02 TA	AM-VM22-6c	AM-IVZ-VM008	AM-VM22-6f2(L)	AM-VM22-6f1(D)	AM-VM22-14a1(D)	AM-IVZ-VM017	AM-IVZ-VM006	MC_12_TA	AM-IVZ-VM009
Zone	PBB	UMC	UMC	Saliceto	Saliceto	Saliceto	Saliceto	Saliceto	Saliceto	Saliceto	Saliceto	Saliceto
Thin Section	MC09-02 TA	MC10-01 TA	MC07-02 TA	6c	B3	6f2	6f1	14a1	A17	A6	MC_12_Tae	A9
Pl	53.3	62.8	85.5	48.2	2.96	69.4	57.4	11.6	60	40.5	40.2	44.9
Grt	27.1	11.1		19.5		8.4	18.2	33.4		18.3	32.8	21.4
Opx	1.4	12.6	7.9		69.6	0	0.6	11.6	24.2			
Cpx	15.6	11.5	2.8	3.9	2.4	3	4	3.8	11.3			
Opx + Cpx	17.1	24.1	10.8	3.9	72	3	4.6	15.4	35.6	6.9	5.7	4.4
Ol				6.23	0.2	2.97	3.04	18.7		14.62	6.09	6.85
Amp			2.31	15.6	19.5	12.9	12.2	8.7	0.4	13.7	11.5	15.7
Opaque	2.09	1.56	1.28	3.5	5.33	2.5	3.9	8.61	3.92	4.15	3.04	5.1
Ap	0.48	0.43	0.13	2.92		0.99	0.61	3.52	0.1	1.78	0.65	1.68
Bt								0.12				

Px (Cpx + Opx) is indicated for all samples, but Opx and Cpx were not differentiated in all thin sections. Zones are by Sinigoi *et al.* (1996), and Saliceto samples are in the Upper Mafic Complex. See table 18 for precise sample locations. In sample names, (D) and (L) indicate the approximate dark and light, respectively, bands in the samples and this roughly corresponds to D and L in bulk rock analyses. Where orthopyroxene and clinopyroxene were difficult to distinguish in unpolished thin sections, total pyroxene was point counted. The thin section area point-counted for Saliceto gabbro-norite sample AM-IVZ-VM017 excluded the amphibole-bearing band. Saliceto olivine gabbro sample AM-VM22-14a1(D) point counting was limited to the area most representative for the melanocratic portion of the sample, so only point counting was limited to a 1 X 1 cm area, and a 0.4 X 1 mm grid was used. Mineral abbreviations are Pl, plagioclase; Grt, garnet; Opx, orthopyroxene; Cpx, clinopyroxene; Ol, olivine; Amp, amphibole; Ap, apatite; Bt, biotite after Whitney and Evans (2010) (Table 2).

Table 4: Selected EPMA analyses of olivine and recalculated stoichiometric formulas

Lithology	olivine gabbro		pyroxenite
Sample	AM-IVZ-VM009	AM-VM22-6c	AM-IVZ-VM008
Thin section	A9	6c	B5
Facility	LSU	ETH	LSU
Analysis pt. #	7	504	14
SiO_2	35.7	36.0	36.5
FeO*	36.6	36.1	32.0
MnO	0.24	0.20	0.40
MgO	27.4	27.3	31.1
NiO	0.00	0.00	0.00
CaO	0.01	0.02	0.00
Total	100.0	99.7	100.1
Structural formula based on 4 oxygens			
T (iv) site: Si	1.00	1.01	1.00
Fe^{3+}	0	0	0
Fe^{2+}	0.86	0.84	0.73
Mn^{2+}	0.01	0.00	0.01
Mg	1.14	1.14	1.27
Ni	0	0.0	0
Ca	0.00	0.00	0
A-site total	2.01	1.99	2.01
Olivine components			
Forsterite (mol.%)	57.0	57.3	63.1
Fayalite (mol.%)	42.7	42.5	36.4
Tephroite (mol.%)	0.3	0.2	0.5

* FeO is total FeO.

Table 5: Selected EPMA analysis data of orthopyroxene.

Sample	AM-IVZ-VM009	AM-IVZ-VM008	AM-IVZ-VM008	AM-IVZ-VM008	AM-IVZ-VM017
Analysis point	254	284	631	661	270
Facility	LSU	LSU	ETHZ	ETHZ	ETHZ
Thin Section	A9	B5	A7	A7	A17
Lithology	olivine gabbro	pyroxenite	pyroxenite	pyroxenite	gabbro-norite
Type	Symplectite	Symplectite	Magmatic	Symplectite	Magmatic
SiO_2	52.2	51.3	52.4	51.7	50.6
TiO_2	0.1	0.1	0.1	0.1	0.1
Al_2O_3	2.6	4.1	3.3	4.3	4.0
Cr_2O_3	0.0	0.0	0.0	0.0	0.0
FeO	21.4	19.7	20.3	20.5	23.6
MnO	0.2	0.4	0.4	0.4	0.6
MgO	22.6	23.5	23.0	22.8	19.8
CaO	0.5	0.6	0.5	0.5	0.5
Na_2O		0.0	0.0	0.0	0.0
K_2O		0.0	0.0	0.0	0.0
Cl					
F		0.0			
Total	99.7	99.9	100.0	100.4	99.3
Recalculated formulas on 6 oxygen basis					
Fe^{3+}/(Fetot)	0.01	0.08	0	0.02	0
Mg/(Mg+Fetot)	0.65	0.68	0.67	0.66	0.60
Wo	1.2	1.4	1.1	1.0	1.2
En	64.6	68.7	65.9	65.901067	58.8
Fs	34.3	30.0	33.0	33.1	40.0
Pyroxene components (%)					
Diopside	1.4	1.7	1.4	1.2	1.3
Hedenbergite	0.7	0.7	0.7	0.6	0.8
Enstatite	59.4	58.9	59.5	57.7	51.6
Ferrosilite	31.5	25.7	29.8	29.0	35.1
Mg-tschermak	3.4	4.4	4.7	5.8	5.2
Fe-tschermak	1.8	1.9	2.3	2.9	3.5
Aegerine	0	0.2	0	0.2	0
Mg-Fe^{3+}-tschermak	0.3	3.3	0	0.5	0
Fe-Fe^{3+}-tschermak	0.2	1.4	0	0.2	0
Kanoite	0.6	1.3	1.2	1.3	2.0
MgTi-tschermak	0.4	0.4	0.1	0.4	0.2
FeTi-tschermak	0.2	0.2	0.1	0.2	0.2
Non-quad components	6.8	13.1	8.6	11.5	11.1

Table 6: Selected EPMA analysis data of clinopyroxene.

Sample	AM-IVZ-	AM-IVZ-	AM-VM22-	AM-IVZ-	AM-IVZ-	AM-IVZ-
BSE Pt. ID	299	658	386	261	114	281
Facility	LSU	ETHZ	ETHZ	LSU	ETHZ	ETHZ
Thin section	B5	A7	6c	A9	A17	A17
Lithology	pyroxenite	pyroxenite	olivine gabbro	olivine gabbro	gabbro-norite	gabbro-norite
Type	symplectite	symplectite	corona	corona	chadacryst	magmatic
SiO_2	50.4	50.4	52.7	50.3	50.3	49.6
TiO_2	0.9	0.8	0.5	1.0	0.7	0.7
Al_2O_3	6.6	6.5	4.8	6.7	5.9	6.2
Cr_2O_3	0.1	0.0	0.0	0.0	0.0	0.0
FeO	8.2	7.9	7.4	8.3	9.2	9.4
MnO	0.2	0.2	0.1	0.1	0.3	0.3
MgO	11.7	12.1	12.7	11.7	11.6	11.5
CaO	20.8	21.4	21.2	20.5	21.3	21.3
Na_2O	1.2	1.2	1.4	1.4	0.9	0.9
K_2O		0.0	0.0		0.0	0.0
F	0.1			0.1		
Total	100.1	100.5	100.9	100.0	100.2	100.0
Recalculated formulas based on 6 oxygens PFU						
$Fe^{3+}/(Fe_{tot})$	0.05	0.19	0.01	0.10	0.09	0.17
$Mg/(Mg+Fe_{tot})$	0.72	0.73	0.75	0.71	0.69	0.69
Wo (normalized)	44.5	45.3	45.7	44.4	44.7	44.7
En (normalized)	40.3	42.2	41.0	40.8	39.3	40.1
Fs (normalized)	15.2	12.5	13.3	14.7	16.0	15.2
Pyroxene components (mol.%)						
Diopside	51.7	55.1	58.2	51.4	52.0	51.1
Hedenbergite	19.5	16.3	18.9	18.6	21.2	19.4
Enstatite	6.4	5.7	5.4	6.5	6.2	6.0
Ferrosilite	2.4	1.7	1.8	2.3	2.5	2.3
Ca-tschermak	10.8	12.3	5.7	10.8	10.9	12.3
Jadeite	4.9	1.5	7.9	4.6	1.7	0.0
Aegerine	1.2	4.6	0.2	2.6	2.5	5.1
Johannsenite	0.6	0.6	0.3	0.3	0.9	0.9
Kosmochlor	0.1	0.0	0.1	0.0	0.1	0.1
NaTi-tschermak	2.5	2.3	1.5	2.8	2.1	1.4
CaMgTi-						1.1
CaFeTi-tsermak						0.4
Non-quad	20.1	21.2	15.7	21.2	18.1	21.2

Table 7: Selected EPMA analyses of plagioclase and recalculated stoichiometric formulas

Lithology	Pyroxenite		Olivine gabbro			Gabbro-norite	
Sample	AM-IVZ-VM008	AM-IVZ-VM008	AM-VM22-6c	AM-VM22-6c	AM-IVZ-VM009	AM-IVZ-VM017	AM-IVZ-VM017
Thin Section	B5	A7	6c	6c	A9	A17	A17
Facility	LSU	ETH	ETH	ETH	LSU	ETH	ETH
Type	Cumulate	Cumulate	Cumulate (core)	Cumulate (rim)	Cumulate	Cumulate	Chadacryst
Analysis Number	219	646	429	542	203	249	149
SiO_2	55.27	54.99	54.94	58.77	55.49	54.51	55.22
TiO_2		0.01	0.02	0.01	0.01	0.02	0.01
Al_2O_3	28.16	29.95	28.88	27.26	27.98	29.86	29.52
FeO*	0.12	0.06	0.05	0.20	0.02	0.27	0.25
MgO	N/A	0.01	0.01	0.01	N/A	0.02	0.01
CaO	10.16	10.92	11.08	8.45	9.88	11.60	11.16
SrO	0.20	N/A	N/A	N/A	0.28	N/A	N/A
BaO	<dl	N/A	N/A	N/A	0.06	N/A	N/A
Na_2O	5.64	5.22	5.26	6.67	5.66	4.81	5.14
K_2O	0.11	0.07	0.21	0.39	0.44	0.19	0.18
TOTAL	99.66	101.22	100.48	101.77	99.83	101.30	101.52
Recalculated formulas							
T (iv) site: Si	2.50	2.45	2.47	2.59	2.51	2.43	2.45
Al	1.50	1.57	1.53	1.41	1.49	1.57	1.55
Fe^{3+}	0.00	0.00	0.00	0.00	0.00	0.00	0.00
T site total	4.00	4.02	4.00	4.00	4.00	4.00	4.00
Fe^{3+} (assumed)	0.00	0.00	0.00	0.00	0.00	0.00	0.00
Fe^{2+} (assumed)	0.00	0.00	0.00	0.01	0.00	0.01	0.01
Mn	0.00	0.00	0.00	0.00	0.00	0.00	0.00
Ca	0.49	0.52	0.53	0.40	0.48	0.55	0.53
Ba							
Sr	0.01	0.00	0.00	0.00	0.01	0.00	0.00
Na	0.49	0.45	0.46	0.57	0.50	0.42	0.44
K	0.01	0.00	0.01	0.02	0.03	0.01	0.01
M-site total	1.00	0.97	1.00	0.99	1.01	0.98	0.99
albite (mol.%)	49.81	46.20	45.68	57.52	49.54	42.39	45.00
anorthite (mol.%)	49.58	53.38	53.11	40.28	47.80	56.53	53.98
orthoclase (mol.%)	0.62	0.42	1.21	2.20	2.56	1.08	1.02

*FeO is FeO total.

Table 8: Selected EPMA analyses of amphibole

Lithology	Pyroxenite		Olivine gabbro	Gabbro-norite
Sample	AM_IVZ-VM008		AM-VM22-6c	AM_IVZ-VM017
Thin section	B5	A7	6c	A17
EPMA session point	273	642	498	223
Facility	LSU		ETH	
SiO_2	39.9	40.9	39.8	39.9
TiO_2	4.29	4.33	4.36	4.07
Al_2O_3	15.15	14.11	14.75	14.83
Cr_2O_3	0.02	0.07	0.02	0.05
MnO	0.10	0.12	0.06	0.18
FeO*	12.6	12.1	12.5	13.9
MgO	11.4	10.8	10.3	9.1
CaO	11.1	11.2	11.1	11.2
Na_2O	3.23	2.82	2.74	2.29
K_2O	0.59	0.76	1.33	1.62
F	0.1164			
Cl	0			
Calculated species	Ti-rich ferri-sadanagaite	Ti-rich sadanagaite	Ti-rich sadanagaite	Ti-rich pargasite

*FeO is total FeO. Calculated species is from the spreadsheet of Locock (2014).

Table 9: Select EPMA analyses of garnet from olivine gabbro.

Sample	AM-IVZ-VM009	AM-VM22-6c	AM-VM22-6c
BSE Pt. ID	320	307	311
Facility	LSU	ETH	ETH
Thin Section	A9	6c	6c
Type	Corona	corona, plagioclase side	corona, amphibole side
SiO_2	39.1	38.8	39.2
TiO_2	0.1	0.1	0.1
Al_2O_3	22.0	22.8	22.6
Cr_2O_3	N/A	0.0	0.0
FeOt	23.5	23.2	23.5
MnO	0.5	0.6	0.6
MgO	8.0	8.3	8.3
CaO	6.6	7.0	6.3
Na_2O	N/A	0.0	0.0
K_2O	N/A	0.0	0.0
F	0.0	N/A	N/A
TOTAL	99.8	100.7	100.8
Recalculated formulas			
$Fe^{3+}/(Fe_{tot})$	0.0	0.0	0.0
$Mg/(Mg+Fe_{tot})$	0.4	0.4	0.4
$Mg/(Mg+Fe^{2+})$	0.4	0.4	0.4
Calculated mol.% garnet			
Almandine	50.4	46.7	49.6
Pyrope	30.4	31.2	31.3
Spessartine	1.1	1.3	1.3
Grossular	17.5	18.9	16.8
Remainder	0.6	1.8	0.6

Table 10: Selected EPMA analyses of apatite

Lithology	Olivine gabbro			Gabbro-norite
SAMPLE	AM-IVZ-VM009			AM-IVZ-VM017
TS	A9			A17
Facility	LSU			ETH
SiO_2	0.019	0.032	0.035	0.079
PbO	0.019			
Al_2O_3				
Y_2O_3	0.019	0.037		
FeO*	0.076	0.095	0.116	0.067
MnO			0.024	0.037
MgO	0.050	0.041	0.073	
CaO	53.5	53.8	53.7	55.1
SrO	0.134	0.102	0.094	
Na_2O	0.086	0.071	0.072	
P_2O_5	40.7	40.8	40.4	41.8
Cl	0.133	0.125	0.145	
F	2.919	3.071	3.134	
O = F, Cl	-0.715	-0.746	-0.768	
TOTAL	96.924	97.368	97.009	97.301

Note that P_2O_5 was analyzed with EDS only at ETH Zurich (see Methods). *FeO is total FeO.

Table 11: Selected EPMA analyses of oxide minerals.

Mineral		Ilmenite			Magnetite		Intermed.	Intermed.	Al-spinel			
Lithology	Pyroxenite	Olivine gabbro	Gabbro-norite	Olivine gabbro	Pyroxenite	Gabbro-norite	Olivine gabbro		Pyroxenite		Olivine gabbro	Gabbro-norite
Type	blebby	blebby	Oxide exsolution	blebby	blebby	Oxide exsolution	Oxide exsolution	Oxide exsolution	Exsolution in Pl	Symplectite in Cpx	Exsolution in Pl	Oxide exsolution
Thin section	B5	A9	A17	A9	B5	A17	A9	A9	B5	B5	A9	A17
EPMA point number	124	82	360	75	139	351	91	16	160	59	112	361
SiO_2												0.228
TiO_2	50.5	51.2	49.7	0.22	0.29	0.42	9.71	35.8	0.04	0.02	0.06	0.77
ZnO	0.02	0.07	0.10					2.95	0.17	0.09	0.63	1.78
Al_2O_3	0.02	0.06	1.34	1.01	0.32	0.35	3.23	20.52	60.65	59.78	59.28	61.60
V_2O_3		0.13	0.17	1.56	1.04	1.35	1.53	0.10	0.14			0.09
Cr_2O_3			0.06	0.15	0.26	0.43	0.38	0.17	0.34	0.02	0.02	0.99
Fe_2O_3	5.18	3.92	5.35	66.04	67.04	65.96	45.44	0.00	3.53	3.69	5.40	0.35
FeO*	46.2	45.0	46.1	90.2	91.3	90.6	79.6	34.7	26.4	29.7	28.4	22.0
FeO	41.59	41.50	41.24	30.81	30.93	31.29	38.75	34.65	23.23	26.40	23.54	21.71
NiO									0.01	0.02	0.03	
MnO	1.00	0.29	1.34	0.01	0.05	0.03	0.12	0.27	0.18	0.18	0.09	0.31
MgO	1.13	1.87	0.60	0.18	0.06	0.03	0.85	5.55	11.68	9.58	11.01	12.26
Cl		0.00						0.00				
F	0.10	0.11	0.13	0.05	0.05	0.01	0.07	0.11	0.02	0.01	0.05	0.06
TOTAL	99.52	99.14	100.08	100.03	100.05	99.87	100.08	100.09	100.00	99.80	100.12	100.14
Mg#	4.60	7.42	2.52	1.04	0.34	0.19	3.77	22.20	47.27	39.28	45.46	50.18
Cr#	13.80	0.00	2.84	8.91	35.49	45.24	7.31	0.56	0.38	0.02	0.02	1.07
Fe^{2+}/Fe^{3+}	8.93	11.77	8.56	0.52	0.51	0.53	0.95		7.32	7.94	4.85	69.26
$Fe^{2+}/\sum Fe$	0.90	0.92	0.90	0.34	0.34	0.35	0.49		0.88	0.89	0.83	0.99

FeO* is total FeO, but FeO and Fe_2O_3 were calculated using stoichiometry. Intermediate notes grains with intermediate compositions between Al-spinel, magnetite and ilmenite. Blanks indicate below limit of detection. All analyses presented were performed at LSU.

Table 12: Sulfide mineral EPMA data and recalculated formulas on 8 S PFU basis.

	Pyrrhotite					Chalcopyrite		Pentlandite
Sample	AM-IVZ-VM009				AM-IVZ-VM008	AM-IVZ-VM009		
Lithology	Olivine gabbro	Olivine gabbro	Olivine gabbro	Olivine gabbro	Pyroxenite	Olivine gabbro	Olivine gabbro	Olivine gabbro
Thin section	A9	A9	A9	A9	B5	A9	A9	A9
BSE Pt. ID	184	185	187	188	191	189	190	186
Facility	LSU	LSU	LSU	LSU	LSU	LSU	LSU	LSU
Si wt.%							0.51	0.137
Zn wt.%								
Pb wt.%	0.22	0.20	0.22	0.24	0.21	0.18	0.15	0.18
Al wt.%							0.14	0.04
Fe wt.%	61.6	61.6	61.5	61.4	61.0	30.8	30.6	24.3
Co wt.%	0.07	0.09	0.22	0.21	0.16		0.02	18.49
Ni wt.%	0.29	0.33	0.56	0.51	0.17	0.04	0.05	24.18
Cu wt.%				0.04		33.85	33.59	0.06
Mg wt.%				0.01	0.03	0.02		0.03
Na wt.%								
P wt.%	0.01	0.01	0.04	0.03	0.03		0.03	0.06
S wt.%	37.5	37.5	37.5	37.4	38.2	34.7	34.9	33.3
TOTAL	99.7	99.8	99.9	99.9	99.8	99.5	100.0	100.8
Formula on 8 S basis								
Si							0.13	0.04
Zn								
Pb	0.01	0.01	0.01	0.01	0.01	0.01	0.01	0.01
Al							0.04	0.01
Fe	7.54	7.55	7.54	7.54	7.34	4.08	4.03	3.35
Co	0.01	0.01	0.03	0.02	0.02		0.00	2.42
Ni	0.03	0.04	0.06	0.06	0.02	0.00	0.01	3.17
Cu				0.00		3.94	3.89	0.01
Mg				0.00	0.01	0.00		0.01
Na								
P	0.00	0.00	0.01	0.01	0.01		0.01	0.02
S	8	8	8	8	8	8	8	8

Table 13: Mean *in-situ* LA-ICP-MS analyses for each sample of amphibole, orthopyroxene, clinopyroxene, plagioclase, olivine, amphibole, apatite, and garnet.

Mineral	Amphibole				Orthopyroxene				Clinopyroxene					
Thin section	A17 (n=42)		B5 (n=29)		A17 (n=24)		B5 (n=26)		A17 (n=47)		A9 (n=17)		B5 (n=10)	
	mean	σ	mean	σ	mean	σ	mean	σ	mean	σ	mean	σ	mean	σ
Co (ppm)	42.93	1.30	43.87	1.29	57.09	1.93	56.95	2.89	26.19	1.81	22.82	1.87	26.53	2.66
Ni	22.55	1.24	27.10	0.91	15.41	2.15	17.65	1.24	10.43	2.16	14.06	0.96	11.59	1.53
Zn	98.66	2.53	7.21	0.61	255.24	9.54	20.40	2.86	67.36	5.16	39.58	5.75	10.84	13.07
Rb	7.66	0.96	3.36	0.19	0.19	0.41	0.00	0.00	0.04	0.07	0.00	0.01	0.01	0.01
Sr	229.33	19.69	391.07	57.60	0.57	1.11	0.15	0.10	25.57	16.02	40.91	4.25	79.99	18.92
Y	41.99	2.32	4.75	0.20	2.18	1.08	0.12	0.02	27.86	3.28	2.48	0.72	3.03	0.34
Zr	162.38	8.63	54.29	4.12	8.58	5.27	2.91	0.82	153.02	22.30	104.71	5.48	76.63	3.08
Nb	9.86	0.51	5.40	0.55	0.01	0.02	0.00	0.00	0.06	0.02	0.08	0.01	0.05	0.01
Ba	620.58	43.96	426.89	71.15	1.01	1.80	0.15	0.15	2.78	6.28	0.07	0.05	1.01	1.30
La	14.46	0.71	6.34	0.13	0.09	0.29	0.01	0.01	6.21	0.57	6.03	0.44	3.38	0.18
Ce	50.33	2.32	14.13	1.24	0.37	1.19	0.02	0.01	26.23	3.06	23.68	1.59	7.71	0.54
Pr	8.91	0.39	1.79	0.20	0.07	0.22	0.00	0.00	5.01	0.61	4.48	0.29	1.00	0.08
Nd	49.14	2.17	7.71	0.98	0.44	1.29	0.01	0.01	28.38	3.51	25.68	1.64	4.38	0.37
Sm	11.85	0.64	1.40	0.12	0.14	0.30	0.01	0.00	7.10	0.80	5.51	0.45	0.86	0.09
Eu	6.22	0.26	2.84	0.29	0.09	0.16	0.01	0.00	3.85	0.41	2.85	0.15	1.58	0.12
Gd	11.78	0.71	1.26	0.09	0.20	0.30	0.01	0.01	7.08	0.78	3.50	0.51	0.78	0.10
Tb	1.653	0.106	0.177	0.011	0.039	0.042	0.003	0.001	1.024	0.105	0.293	0.058	0.114	0.020
Dy	9.083	0.542	0.968	0.056	0.315	0.235	0.018	0.005	5.974	0.661	0.986	0.229	0.647	0.080
Ho	1.881	0.108	0.207	0.013	0.091	0.046	0.006	0.002	1.249	0.138	0.118	0.033	0.137	0.019
Er	4.483	0.246	0.534	0.037	0.330	0.108	0.022	0.005	3.192	0.394	0.174	0.050	0.362	0.050
Tm	0.610	0.033	0.080	0.008	0.068	0.017	0.005	0.002	0.459	0.057	0.015	0.004	0.056	0.008
Yb	3.325	0.191	0.512	0.047	0.555	0.094	0.044	0.009	2.654	0.353	0.062	0.021	0.359	0.035
Lu	0.478	0.026	0.083	0.009	0.107	0.015	0.010	0.002	0.394	0.054	0.007	0.002	0.060	0.006
Hf	4.522	0.234	1.389	0.093	0.266	0.120	0.095	0.030	4.016	0.925	2.920	0.227	2.145	0.204
Ta	0.495	0.031	0.317	0.033	0.001	0.001	0.000	0.000	0.018	0.003	0.023	0.004	0.016	0.003
Pb	1.846	0.079	1.583	0.070	0.025	0.069	0.018	0.013	0.203	0.078	0.217	0.014	0.197	0.013
Th	0.169	0.011	0.196	0.011	0.013	0.025	0.005	0.010	0.088	0.032	0.035	0.009	0.109	0.020
U	0.037	0.004	0.055	0.005	0.002	0.003	0.001	0.002	0.021	0.003	0.010	0.002	0.042	0.006
Eu/Eu*	1.60		6.51		1.68		4.21		1.66		1.98		5.88	

Table 13 *cont.*

Mineral	Plagioclase						Olivine					
Thin section	A17 (n=28)		A9 (n=18)		B5 (n=9)		A6 (n=9)		A9 (n=20)		B5 (n=4)	
Group	mean	σ	mean	σ	mean	σ	mean	σ	mean	σ	mean	σ
Co	0.16	0.31	0.03	0.07	0.42	0.67	161.48	1.67	154.55	7.62	147.89	7.53
Ni	0.00	0.00	0.00	0.00	0.26	0.79	52.96	2.07	96.82	6.57	68.36	6.96
Zn	1.87	1.00	0.51	0.40	1.73	4.06	245.35	21.3	199.9	22.3	5.88	0.43
Rb	0.35	0.12	0.15	0.05	0.07	0.06	0.00	0.00	0.01	0.03	0.01	0.01
Sr	833.84	73.95	1288.6	58.78	1249.40	115.5	0.04	0.09	0.07	0.20	0.22	0.24
Y	0.20	0.08	0.03	0.01	0.03	0.01	0.01	0.00	0.01	0.00	0.06	0.04
Zr	0.21	0.49	0.01	0.01	0.00	0.01	0.08	0.02	0.05	0.02	0.18	0.26
Nb	0.03	0.07	0.00	0.00	0.00	0.00	0.00	0.00	0.00	0.00	0.00	0.00
Ba	328.23	50.55	417.6	42.47	237.75	18.70	0.02	0.02	0.09	0.27	0.60	0.84
La	8.17	0.94	10.54	0.60	5.30	0.95	0.01	0.01	0.01	0.01	0.04	0.03
Ce	11.24	1.36	14.65	0.85	4.57	0.76	0.02	0.01	0.02	0.02	0.09	0.07
Pr	0.98	0.12	1.32	0.10	0.29	0.06	0.00	0.00	0.00	0.00	0.01	0.01
Nd	3.04	0.35	4.20	0.38	0.71	0.18	0.01	0.01	0.01	0.01	0.05	0.04
Sm	0.25	0.03	0.28	0.04	0.04	0.01	0.01	0.00	0.01	0.00	0.02	0.01
Eu	2.27	0.42	1.84	0.11	0.81	0.06	0.00	0.00	0.00	0.00	0.03	0.02
Gd	0.13	0.04	0.08	0.03	0.02	0.02	0.01	0.00	0.01	0.00	0.02	0.01
Tb	0.011	0.004	0.003	0.002	0.002	0.001	0.001	0.00	0.001	0.00	0.002	0.00
Dy	0.047	0.023	0.008	0.006	0.006	0.006	0.003	0.002	0.003	0.002	0.017	0.013
Ho	0.008	0.005	0.001	0.001	0.001	0.001	0.001	0.000	0.001	0.001	0.004	0.003
Er	0.013	0.008	0.002	0.003	0.002	0.002	0.002	0.001	0.003	0.002	0.013	0.010
Tm	0.002	0.002	0.001	0.001	0.000	0.001	0.001	0.000	0.001	0.000	0.003	0.002
Yb	0.010	0.011	0.001	0.003	0.001	0.001	0.002	0.001	0.004	0.002	0.014	0.013
Lu	0.001	0.002	0.000	0.000	0.000	0.000	0.000	0.000	0.000	0.000	0.004	0.002
Hf	0.006	0.011	0.001	0.001	0.001	0.002	0.003	0.001	0.002	0.001	0.003	0.002
Ta	0.001	0.002	0.000	0.000	0.000	0.000	0.000	0.000	0.000	0.001	0.000	0.000
Pb	2.891	0.178	3.397	0.201	2.553	0.216	0.007	0.007	0.023	0.056	0.040	0.027
Th	0.001	0.001	0.000	0.000	0.001	0.000	0.001	0.001	0.001	0.001	0.005	0.008
U	0.001	0.001	0.000	0.000	0.000	0.000	0.001	0.001	0.000	0.000	0.005	0.007
Eu/Eu*	38.22		36.46		90.35							

Table 13 *cont.*

Mineral	Garnet				Apatite			
Thin section	A6 (n=5)		A9 (n=33)		A17 (n=14)		A9 (n=7)	
Group	mean	σ	mean	σ	mean	σ	mean	σ
Co	29.16	0.27	28.81	0.78	0.21	0.33	0.25	0.26
Ni	0.00	0.00	0.25	0.70	0.39	1.47	0.00	0.00
Zn	27.79	1.94	20.84	2.67	1.86	2.53	0.60	0.76
Rb	0.01	0.01	0.01	0.01	0.03	0.07	0.00	0.00
Sr	0.09	0.07	0.10	0.17	382.06	27.76	998.87	94.85
Y	33.52	6.96	34.10	11.10	162.79	19.68	44.40	47.32
Zr	47.00	18.10	39.33	10.61	9.47	2.28	9.16	3.01
Nb	0.01	0.00	0.00	0.01	0.01	0.00	0.00	0.00
Ba	0.03	0.03	0.04	0.09	2.66	2.90	3.45	1.16
La	0.05	0.09	0.10	0.25	319.34	33.59	522.55	38.57
Ce	0.20	0.21	0.24	0.34	804.38	80.06	1191.54	67.92
Pr	0.07	0.03	0.08	0.04	103.55	10.93	153.21	9.26
Nd	1.27	0.43	1.35	0.47	472.76	53.69	702.95	44.46
Sm	1.96	0.34	2.01	0.41	73.62	8.80	96.30	11.29
Eu	2.11	0.30	2.08	0.23	27.26	1.92	37.01	2.34
Gd	5.66	0.94	5.58	1.10	60.75	7.47	58.05	16.67
Tb	1.054	0.179	1.056	0.250	6.713	0.844	4.141	2.000
Dy	6.556	1.404	6.553	1.879	32.909	4.072	13.651	10.465
Ho	1.476	0.328	1.467	0.498	6.176	0.778	1.819	1.988
Er	3.441	0.783	3.539	1.323	14.401	1.696	3.000	4.176
Tm	0.448	0.110	0.458	0.185	1.649	0.208	0.236	0.362

Table 13 *cont.*

Yb	2.276	0.550	2.405	1.012	8.575	1.018	0.653	0.821
Lu	0.342	0.095	0.353	0.164	1.213	0.128	0.112	0.199
Hf	0.559	0.202	0.438	0.112	0.012	0.006	0.016	0.007
Ta	0.000	0.000	0.000	0.001	0.000	0.000	0.000	0.001
Pb	0.019	0.010	0.013	0.024	0.783	0.077	1.278	0.098
Th	0.002	0.004	0.005	0.007	13.084	0.885	9.764	1.276
U	0.002	0.003	0.003	0.006	5.548	0.541	3.798	0.435
Eu/Eu*	1.92		1.89		1.24		1.51	

Analyses that were below limit of detection were set to zero for mean and standard deviation calculation. Thin section A17 is sample AM-IVZ-VM017 and is a gabbro-norite. Thin section A9 is sample AM-IVZ-VM009 and is a garnet amphibole olivine gabbro. Thin section A6 is sample AM-IVZ-VM006 and is a garnet amphibole olivine gabbro. Thin section B5 is from sample AM-IVZ-VM008 and is an olivine-bearing pyroxenite. Eu anomaly (Eu*) is calculated as $Eu^* = Eu_{CN}/(Gd_{CN}*Sm_{CN})^{0.5}$, where CN is normalization to chondrite values of (McDonough and Sun, 1995).

Table 14: Bulk rock data of the Lower Mafic Complex

Sample	MC_22_01_TBd	MC_24_02_TBd	MC_25_01_TAd	MC_26_03_TBb	MC_27_02_TAb	MC_33_02_TAa
Facility	UNIL	UNIL	UNIL	UNIL	UNIL	UNIL
Rock Type	Amp-G	Amp-GN	Amp-G	GN	Amp-N	Amp-G
Northing (m)	5060664	5059959	5059427	5059068	5059414	5059945
Easting (m)	429789	430091	430242	430673	431327	432090
SiO_2 (wt.%)	39.78	44.54	39.09	53.45	37.81	46.65
TiO_2	2.41	1.23	2.14	0.89	2.59	0.83
Al_2O_3	20.72	22.23	19.55	22.96	17.97	20.02
Fe_2O_3	13.95	8.54	16.04	6.19	18.01	8.71
MnO	0.14	0.13	0.14	0.14	0.13	0.17
MgO	6.02	7.61	8.28	2.11	8.84	10.42
CaO	13.54	13.69	12.78	8.12	12.66	12.05
Na_2O	2.15	1.93	1.60	5.30	1.55	1.37
K_2O	0.19	0.20	0.22	0.21	0.20	0.10
P_2O_5	0.86	0.04	0.03	0.39	0.01	0.02
Cr_2O_3	0.00	0.02	0.01	0.00	0.01	0.04
NiO	<dl	<dl	<dl	<dl	<dl	0.02
LOI	0.58	0.52	0.65	0.51	0.55	0.41
Total	100.35	100.68	100.50	100.26	100.32	100.81
Sc (µg/g)	44.7	40.7	62.6	8.8	70.5	38.0
V	476.5	245.4	602.4	88.7	789.2	186.9
Co	39.1	35.0	53.7	10.2	64.8	36.5
Ni	24.3	43.0	29.8	14.4	14.9	145.1
Cu	29.5	19.2	64.4	11.5	82.4	25.8
Zn	214	190	184	189	206	170
Rb	0.6	1.3	1.9	0.8	1.1	0.6
Sr	678	668	436	1052	366	590
Y	28.4	20.0	18.7	12.4	18.8	10.7
Zr	25.3	78.3	21.6	757.4	19.8	14.4
Nb	3.8	2.7	1.6	5.3	1.6	1.0
Cs	0.1	0.1	0.1	0.2	0.1	0.0
Ba	48.6	43.0	36.1	167.5	31.8	29.7
La	12.0	5.4	1.8	37.6	1.0	3.1
Ce	36.1	18.0	7.7	65.2	5.8	8.7
Pr	6.0	3.3	1.7	7.2	1.5	1.6
Nd	31.4	17.4	10.9	27.6	10.1	8.6
Sm	7.73	4.55	3.69	4.08	3.62	2.49
Eu	2.15	1.47	1.17	2.49	1.19	0.89
Gd	7.03	4.41	4.08	2.97	4.20	2.48

Tb	0.97	0.63	0.62	0.34	0.63	0.35
Dy	5.50	3.76	3.67	1.87	3.84	2.13
Ho	1.05	0.75	0.74	0.42	0.74	0.41
Er	2.75	2.02	1.94	1.29	1.89	1.07
Tm	0.34	0.27	0.24	0.21	0.25	0.14
Yb	2.07	1.77	1.49	1.62	1.46	0.89
Lu	0.27	0.25	0.20	0.29	0.19	0.12
Hf	1.19	2.44	1.02	14.96	1.00	0.65
Ta	0.13	0.09	0.06	0.23	0.06	0.04
Pb	2.05	3.03	2.46	8.15	3.10	2.44
Th	0.003	0.002	0.008	1.271	0.003	0.002
U	0.005	0.004	0.004	1.035	0.004	0.010

G, gabbro; N, norite; GN, gabbro-norite; Amp, amphibole. SiO_2 through Total are in wt.% as measured by XRF. Fe measured as Fe2O3 total. Trace elements Sc through U are in µg/g as measured by LA-ICP-MS.

Table 15: Bulk rock data of the Paragneiss-Bearing Belt

Sample	MC_04_01_TBh	MC_06_01_TBb	MC_09_02_TAb	MC_01_03_TBf	MC_18_01_TBc	MC_31_01_TAd
Facility	UNIL	UNIL	UNIL	UNIL	UNIL	UNIL
Rock Type	GN	Grt-G	Grt-N	GN	N	Amp-GN
Northing (m)	5082367	5081608	5081218	5074942	5075358	5060969
Easting (m)	435991	436113	435649	435177	435889	433497
SiO_2 (wt.%)	41.02	48.39	45.51	50.16	47.52	53.59
TiO_2	1.87	1.73	1.36	0.28	2.46	1.20
Al_2O_3	22.13	21.77	20.38	17.50	22.71	19.84
Fe_2O_3	19.13	8.99	13.09	8.31	9.76	9.50
MnO	0.36	0.11	0.20	0.14	0.15	0.15
MgO	8.19	4.57	6.69	9.92	3.80	3.20
CaO	6.71	9.64	11.09	11.01	10.53	7.47
Na_2O	0.67	3.33	1.78	1.85	3.24	4.15
K_2O	0.07	0.51	0.17	0.22	0.31	0.67
P_2O_5	0.04	0.19	0.23	0.02	0.15	0.34
Cr_2O_3	0.04	0.01	0.01	0.05	0.00	0.00
NiO	<dl	<dl	<dl	0.01	<dl	<dl
LOI	-0.84	1.38	0.11	1.19	0.08	0.11
Sum	100.24	100.60	100.63	100.65	100.72	100.21
Sc (µg/g)	59.5	19.8	83.3	38.0	22.6	31.0
V	394.6	249.8	449.4	192.2	185.4	167.7
Co	36.3	29.6	38.6	40.9	30.4	20.7
Ni	43.6	18.6	21.1	75.6	24.7	23.5
Cu	19.3	23.1	19.5	10.7	15.4	14.3
Zn	294	236	239	172	229	271
Rb	2.2	6.3	3.2	1.8	2.3	1.3
Sr	354	509	358	351	702	386
Y	90.5	7.1	37.6	11.2	3.6	25.1
Zr	88.4	32.2	47.3	25.6	40.8	264.1
Nb	8.9	5.9	8.9	0.1	5.0	16.9
Cs	0.3	0.2	0.3	0.2	0.1	0.1
Ba	23.8	156.6	65.0	61.9	504.8	500.3
La	5.3	3.8	7.9	3.8	6.2	20.4
Ce	9.5	9.2	22.3	8.6	12.1	43.3
Pr	1.1	1.4	3.8	1.2	1.5	5.6
Nd	5.6	7.0	20.3	5.9	6.7	24.7
Sm	2.59	1.82	6.32	1.59	1.19	5.62
Eu	1.32	1.07	1.79	0.60	2.58	1.95
Gd	7.18	1.69	7.25	1.74	1.00	5.24

Tb	1.73	0.25	1.18	0.29	0.13	0.78
Dy	13.74	1.43	7.25	1.96	0.70	4.77
Ho	3.27	0.27	1.47	0.41	0.14	0.97
Er	9.84	0.72	3.97	1.24	0.35	2.71
Tm	1.45	0.09	0.52	0.18	0.05	0.36
Yb	10.23	0.58	3.34	1.22	0.27	2.46
Lu	1.49	0.08	0.44	0.18	0.05	0.36
Hf	1.92	0.89	1.38	0.81	0.82	6.19
Ta	0.36	0.23	0.35	0.01	0.33	0.50
Pb	4.06	3.39	2.38	1.85	2.61	7.82
Th	0.050	0.013	0.022	0.028	0.107	0.104
U	0.029	0.014	0.020	0.018	0.049	0.353
Eu*						

G, gabbro; N, norite, GN, gabbro-norite; Amp, amphibole; Grt, garnet. Oxides SiO_2 through Total are in wt.% as measured by XRF. Fe measured as Fe_2O_3 total. Trace elements Sc through U are in µg/g as measured by LA-ICP-MS.

Table 16: Bulk rock data of the Upper Mafic Complex

Sample	MC_10_02_TBd	MC_07_01_TBc	MC_13_02_TBa	MC_02_02_TAc	MC_03_02_h	MC_36_02_TBb	MC_35_01_TAb	AM-VM-3b	MC_29_02_TAa
Facility	UNIL	UNIL	UNIL	UNIL	UNIL	UNIL	UNIL	ETH	UNIL
Rock Type	Grt-GN	GN	Grt-OG	GN	G	GN	N	GN	GN
Zone	UMC	UMC	UMC	UMC	UMC	UMC	UMC	UMC	UMC
Northing (m)	5080484	5077502	5077709	5075755	5074429	5061702	5062625	5080003	5060791
Easting (m)	436200	437579	439240	437769	438950	436114	436495	436810	434288
SiO_2	46.00	50.66	42.35	45.27	45.86	48.89	48.69	47.20	49.59
TiO_2	1.88	0.53	2.79	1.79	2.46	1.97	2.24	2.11	1.76
Al_2O_3	20.23	22.81	17.08	18.00	19.75	21.59	21.35	23.47	20.66
Fe_2O_3	13.18	6.22	20.16	13.96	12.02	8.98	9.50	7.46	8.62
FeO	N/A	N/A	N/A	N/A	N/A	N/A	N/A	N/A	N/A
MnO	0.21	0.11	0.41	0.20	0.22	0.14	0.15	0.13	0.13
MgO	5.48	4.92	4.88	8.06	4.77	4.00	3.84	3.44	5.02
CaO	10.82	11.57	7.85	11.61	10.40	10.95	9.87	9.78	11.12
Na_2O	2.12	3.10	2.83	1.55	2.87	3.05	3.31	3.61	3.03
K_2O	0.16	0.37	0.44	0.15	0.38	0.26	0.32	0.33	0.25
P_2O_5	0.34	0.04	1.00	0.02	0.08	0.84	0.77	0.04	0.42
Cr_2O_3	0.01	0.01	0.01	0.02	0.01	0.01	0.00	0.00	0.01
NiO	<dl	<dl	<dl	<dl	<dl	<dl	<dl	0.01	<dl
LOI	-0.16	0.08	-0.98	0.26	1.40	-0.07	0.22	1.92	0.16
Sum	100.44	100.41	99.80	100.88	100.21	100.67	100.26	99.50	100.76
Sc(µg/g)	46.0	24.6	26.7	49.0	48.3	30.2	25.4	18.7	29.3
V	339.4	187.3	176.5	722.9	438.3	283.4	290.2	307.2	331.4
Co	36.7	20.7	25.5	39.0	38.3	23.5	26.4	16.6	26.9
Ni	22.2	22.8	29.9	30.3	20.5	18.7	16.5	9.3	20.2
Cu	21.4	14.7	27.4	28.6	32.2	13.1	10.6	3.8	12.5
Zn	239	223	287	204	258	195	228	38	164
Rb	2.0	2.7	2.3	3.3	2.1	1.8	2.0	1.9	1.2
Sr	325	685	519	474	558	617	751	724	534
Y	31.2	5.0	22.1	6.6	8.8	15.1	12.7	3.7	10.0
Zr	41.5	28.6	3255.4	59.6	261.3	29.2	45.0	39.2	23.4
Nb	10.7	0.5	10.1	0.6	4.3	7.4	6.1	2.0	3.7
Cs	0.2	0.2	0.1	0.3	0.1	0.1	0.0	0.1	0.0
Ba	56.2	418.4	574.7	122.2	365.9	165.3	547.0	870.4	96.6
La	8.4	5.4	23.2	3.3	12.4	11.5	13.1	4.6	8.0
Ce	23.0	10.0	52.1	7.0	23.5	26.9	29.3	8.6	19.2
Pr	3.6	1.2	7.0	1.0	2.8	3.8	4.0	1.1	2.8

Nd	18.8	5.8	33.4	5.0	12.2	18.1	18.8	4.6	13.5
Sm	5.38	1.12	6.12	1.28	2.21	3.96	3.81	0.80	3.27
Eu	1.54	2.36	5.04	1.16	2.01	2.25	3.20	1.90	1.21
Gd	5.53	1.13	5.33	1.36	1.98	3.89	3.39	0.86	2.64
Tb	0.91	0.15	0.65	0.20	0.28	0.52	0.44	0.12	0.36
Dy	5.79	0.95	3.78	1.25	1.63	2.86	2.39	0.72	2.00
Ho	1.18	0.18	0.80	0.26	0.35	0.55	0.47	0.13	0.38
Er	3.32	0.52	2.46	0.75	0.97	1.42	1.19	0.34	0.99
Tm	0.44	0.07	0.37	0.10	0.14	0.18	0.15	0.05	0.13
Yb	2.81	0.45	2.68	0.70	0.95	1.11	0.95	0.37	0.79
Lu	0.40	0.07	0.46	0.11	0.16	0.16	0.14	0.05	0.11
Hf	1.11	0.66	48.81	1.47	4.60	0.69	0.90	0.82	0.69
Ta	0.46	0.03	0.54	0.04	0.23	0.45	0.37	0.14	0.23
Pb	2.15	2.52	4.01	2.03	1.98	2.86	3.01	1.23	3.37
Th	0.006	0.094	1.001	0.064	0.348	0.266	0.307	0.164	0.258
U	0.008	0.033	1.287	0.026	0.178	0.121	0.135	0.048	0.066
Eu*									

G, gabbro; N, norite, GN, gabbro-norite; Grt, garnet. Oxides SiO_2 through Total are in wt.% as measured by XRF. Fe measured as Fe_2O_3 total. Trace elements Sc through U are in µg/g as measured by LA-ICP-MS.

Table 17: Bulk rock data of the "diorites"

Sample	MC_14_01_TBc	MC_15_01_TAd	MC_16_02_TBd	MC_21_01_TBc	MC_19_02_TBa	MC_20_02_TBa
Facility	UNIL	UNIL	UNIL	UNIL	UNIL	UNIL
Rock Type	Di	Di	Di	Di	GN	Di
Northing (m)	5078051	5077506	5077049	5076290	5074417	5074231
Easting (m)	440770	441024	441687	442551	440207	441131
SiO_2	48.02	47.58	54.02	49.01	41.02	45.12
TiO_2	1.01	1.30	1.09	1.29	0.62	1.69
Al_2O_3	25.93	21.34	19.67	23.74	15.80	19.31
Fe_2O_3	4.96	8.86	8.12	6.87	13.24	12.25
MnO	0.08	0.16	0.17	0.09	0.27	0.23
MgO	3.85	6.14	1.88	2.17	16.05	6.64
CaO	11.54	11.43	5.47	9.56	12.29	10.98
Na_2O	2.58	1.89	3.53	3.97	0.51	2.00
K_2O	1.27	1.35	4.68	1.47	0.02	1.13
P_2O_5	0.23	0.05	0.48	0.54	0.01	0.02
Cr_2O_3	0.02	0.01	0.00	0.00	0.01	0.02
NiO	0.01	<dl	<dl	<dl	0.01	<dl
LOI	0.36	0.29	0.10	1.61	1.15	0.89
Sum	99.84	100.41	99.20	100.34	101.01	100.29
Sc (µg/g)	14.9	54.2	22.2	11.0	88.2	70.1
V	116.6	238.3	83.9	183.5	419.0	368.0
Co	19.2	27.2	11.0	15.8	90.8	30.7
Ni	73.7	27.0	22.7	20.2	108.4	34.7
Cu	21.9	18.8	9.5	9.1	82.9	16.0
Zn	448	391	659	296	169	241
Rb	19.5	20.4	33.2	21.0	0.6	11.4
Sr	664	514	476	799	24	410
Y	4.0	7.3	15.0	10.5	35.7	31.6
Zr	45.2	95.8	1461.9	99.5	22.0	161.7

Nb	1.3	1.7	4.9	3.1	0.0	8.3
Cs	0.2	0.2	0.5	0.3	0.3	0.1
Ba	3161.8	2482.8	5148.8	1628.4	8.6	603.4
La	10.5	7.8	27.4	26.7	0.6	19.7
Ce	18.7	14.7	53.9	51.9	2.6	54.4
Pr	2.2	1.9	6.8	6.3	0.6	8.4
Nd	9.0	8.8	29.3	26.5	3.9	40.5
Sm	1.44	1.89	4.88	4.17	1.75	8.81
Eu	2.69	2.49	6.08	4.64	0.66	3.09
Gd	1.15	1.79	3.97	3.36	2.93	7.71
Tb	0.13	0.23	0.49	0.38	0.61	1.07
Dy	0.71	1.40	2.72	2.04	5.01	6.29
Ho	0.14	0.29	0.56	0.39	1.31	1.26
Er	0.39	0.80	1.59	0.98	4.39	3.30
Tm	0.05	0.11	0.23	0.12	0.70	0.44
Yb	0.32	0.76	1.58	0.71	5.12	2.76
Lu	0.05	0.13	0.28	0.11	0.78	0.39
Hf	0.77	1.95	22.39	1.78	0.69	4.06
Ta	0.05	0.06	0.23	0.16	0.01	0.28
Pb	5.48	3.60	8.79	5.84	4.73	8.83
Th	0.149	0.170	1.083	0.846	0.018	0.114
U	0.058	0.064	0.772	0.301	0.005	0.035
Eu/Eu*						

Di, diorite; GN, gabbro-norite. Sample MC_19_02_Tba is a mafic enclave in the diorite. Oxides SiO_2 through Total are in wt.% as measured by XRF. Fe measured as Fe_2O_3 total. Trace elements Sc through U are in µg/g as measured by LA-ICP-MS.

Table 18: Bulk rock data of Saliceto rocks

Sample	AM_IVZ_VM008	AM_IVZ_VM_009	MC_12_02_TAe	AM-VM22-14-D	AM-VM22-6f-D	AM-VM22-6f-L
Facility	UNIL	WSU	UNIL	ETH	ETH	ETH
Rock Type	PX	Grt-OG	Grt-OG	Grt-OG	Grt-OG	Grt-OG
Zone	UMC	UMC	UMC	UMC	UMC	UMC
Northing (m)	5078996	5078988	5079028	5078902	5078994	5078994
Easting (m)	437244	437238	437261	437211	437242	437242
SiO_2 (wt.%)	39.03	44.44	39.81	35.37	39.56	47.30
TiO_2	3.36	2.16	3.67	5.57	3.54	1.28
Al_2O_3	12.84	22.37	16.82	10.41	16.74	25.50
Fe_2O_3	21.98		19.16	27.80	19.99	6.67
FeO		10.90				
MnO	0.24	0.11	0.24	0.31	0.30	0.04
MgO	15.46	5.23	8.69	12.73	8.90	2.78
CaO	5.96	10.56	8.62	6.54	8.83	11.52
Na_2O	1.14	3.23	1.88	0.64	1.62	3.95
K_2O	0.13	0.31	0.25	0.15	0.20	0.33
P_2O_5	0.04	0.78	1.09	1.58	1.19	0.53
Cr_2O_3	0.03		0.01	0.01	0.01	0.00
NiO	0.01		<dl	0.01	0.01	0.01
LOI	0.45	-0.09	-0.54	-0.73	-1.00	0.08
Sum	100.68	100.09	100.24	100.40	99.89	100.01
SO_3		>/= 0.108				
Cl		>/= 0.005				
Sc (µg/g)	12.8	7.3	14.7	16.5	12.6	4.8
V	484.2		349.5	428.0	356.1	141.6
Co	109.0		61.7	90.2	51.4	20.5
Ni	77.6		44.4	55.3	44.1	22.9
Cu	29.4		33.0	44.9	28.0	10.6
Zn	228		248	141	83	51
Rb	0.8	1.3	2.1	0.7	0.5	1.3
Sr	370	617	509	296	479	738
Y	1.5	8.9	11.9	14.9	12.2	5.7
Zr	32.6	35.2	67.8	73.3	48.0	25.4
Nb	3.2	3.7	6.1	9.1	5.4	2.2
Cs	0.0	0.0	0.1	0.0	0.0	0.0
Ba	132.9	291.2	230.0	133.5	210.3	340.3
La	2.5	16.1	18.7	20.7	18.1	13.1
Ce	4.3	34.3	41.7	51.7	42.8	27.2
Pr	0.5	4.6	5.7	7.4	5.9	3.5

Nd	2.0	21.5	27.1	34.7	27.7	15.3
Sm	0.38	3.71	4.87	6.08	4.77	2.56
Eu	0.85	3.19	3.00	3.02	3.13	3.00
Gd	0.32	3.13	4.07	5.24	4.54	2.09
Tb	0.05	0.38	0.46	0.60	0.52	0.23
Dy	0.29	1.86	2.40	3.15	2.54	1.18
Ho	0.06	0.34	0.45	0.55	0.45	0.20
Er	0.15	0.81	1.08	1.46	1.08	0.53
Tm	0.02	0.10	0.12	0.15	0.12	0.06
Yb	0.18	0.50	0.73	0.93	0.72	0.36
Lu	0.03	0.08	0.10	0.14	0.11	0.05
Hf	0.63	0.69	1.21	1.48	0.83	0.40
Ta	0.21	0.31	0.38	0.63	0.36	0.13
Pb	1.21	1.72	2.13	0.66	1.18	1.88
Th	0.072	0.279	0.254	0.466	0.275	0.206
U	0.044	0.089	0.114	0.178	0.102	0.061
Eu*	7.38	8.87	7.30	6.54	7.49	10.10

Grt-OG, garnet olivine gabbro; PX, orthopyroxenite. Oxides SiO_2 through Total are in wt.% as measured by XRF. Fe measured as Fe_2O_3 total, except for sample AM-IVZ-VM009, which was measured as FeO total at Washington State University. Trace elements Sc through U are in μg/g as measured by LA-ICP-MS.

Table 19: Normative mineralogy (CIPW norms) of Saliceto samples

	Units	AM_IVZ_VM008	MC_12_02_TAe	AM_IVZ_VM009	AM-VM22-14-D	AM-VM22-6f-D	AM-VM22-6f-L
SiO_2	wt.%	39.8	40.5	44.4	36.0	40.0	47.7
TiO_2	wt.%	3.4	3.7	2.2	5.7	3.6	1.3
Al_2O_3	wt.%	13.1	17.1	22.3	10.6	16.9	25.7
Fe_2O_3	wt.%						
FeO	wt.%	20.2	17.5	10.9	25.4	18.2	6.0
MnO	wt.%	0.2	0.2	0.1	0.3	0.3	0.0
MgO	wt.%	15.8	8.8	5.2	12.9	9.0	2.8
CaO	wt.%	6.1	8.8	10.6	6.6	8.9	11.6
Na_2O	wt.%	1.2	1.9	3.2	0.6	1.6	4.0
K_2O	wt.%	0.1	0.3	0.3	0.2	0.2	0.3
P_2O_5	wt.%	0.0	1.1	0.8	1.6	1.2	0.5
Sr	ppm	369.9	508.6	617.5	295.7	479.2	738.1
Ba	ppm	132.9	230.0	291.2	133.5	210.3	340.3
Ni	ppm	77.6	44.4	N/A	55.3	44.1	22.9
Cr	ppm	N/A	N/A	N/A	85.0	63.2	20.6
Zr	ppm	32.6	67.8	35.2	73.3	48.0	25.4
Output							
Quartz	%	0	0	0	0	0	0
Plagioclase	%	47.5	60.7	72.4	35.0	58.6	80.2
(Albite)	%	12.2	19.3	23.9	7.1	16.7	27.7
(Anorthite)	%	35.3	41.3	48.5	27.9	41.9	52.5
Orthoclase	%	1.1	2.0	2.2	1.3	1.6	2.4
Nepheline	%	0	0	3.8	0	0	4.9
Leucite	%	0	0	0.0	0	0	0
Corundum	%	0.02	0.26	0	0.9	0.5	0
Diopside	%	0	0	1.4	0	0	2.2
Hypersthene	%	7.0	4.4	0	19.9	7.1	0
Wollastonite	%	0	0	0	0	0	0
Olivine	%	37.5	23.5	14.7	27.9	22.8	7.1
Rutile	%	0	0	0	0	0	0
Ilmenite	%	4.4	4.7	2.5	7.7	4.5	1.5
Magnetite	%	2.4	2.0	1.2	3.2	2.1	0.6
Hematite	%	0	0	0	0	0	0
Apatite	%	0.1	2.6	1.7	4.0	2.8	1.1
Zircon	%	0.005	0.009	0.005	0.011	0.007	0.003
Perovskite	%	0	0	0	0	0	0
Chromite	%	0	0	0	0.012	0.008	0.002
Titanite	%	0	0	0	0	0	0
Total	%	100	100	100	100	100	100

Calculated using the spreadsheet of Hollocher (2022). Inputs of major elements (SiO_2 – P_2O_5) are on weight percent basis with total Fe calculated as FeO, and trace elements (Sr – Zr) are in ppm. A Fe^{+3}/(Fe total) ratio of 0.12 was used in normative mineralogy calculations. Output mineralogy is in volume percent. Minerals that bear no relevance to gabbroic rocks and had values of zero are not shown.

Table 20: Loadings of major elements, PCA of major elements. (a) Loadings of PCA of all Mafic Complex samples, (b) samples from the northern Mafic Complex (Val Sesia and Val Mastallone transect), and (c) of samples from the southern Mafic Complex (Val Sessera transect). Loadings that explain more variance than a single variable's worth are bolded.

(a)

	PC1	PC2	PC3	PC4
SiO_2	**0.433**	-0.090	0.058	-0.085
TiO_2	-0.224	**0.449**	0.246	-0.148
Al_2O_3	0.169	**0.495**	**-0.317**	-0.230
FeO	**-0.423**	0.135	0.174	-0.184
MnO	**-0.360**	0.107	0.236	**-0.484**
MgO	**-0.424**	-0.216	-0.043	0.058
CaO	-0.167	**0.406**	**-0.546**	0.072
Na_2O	**0.323**	**0.387**	-0.001	-0.036
K_2O	**0.335**	0.038	**0.436**	**-0.430**
P_2O_5	-0.025	**0.390**	**0.510**	**0.674**

(b)

	PC1	PC2	PC3	PC4
SiO_2	**0.418**	-0.165	0.062	-0.149
TiO_2	-0.196	**0.470**	0.264	-0.119
Al_2O_3	0.236	**0.461**	-0.277	-0.192
FeO	**-0.429**	0.150	0.149	-0.193
MnO	**-0.365**	0.122	0.153	**-0.554**
MgO	**-0.431**	-0.196	-0.058	0.076
CaO	-0.107	**0.417**	**-0.554**	0.024
Na_2O	**0.332**	**0.383**	-0.033	-0.018
K_2O	**0.325**	0.016	**0.469**	**-0.437**
P_2O_5	-0.029	**0.379**	**0.522**	**0.620**

(c)

	PC1	PC2	PC3	PC4
SiO_2	**0.449**	-0.013	0.060	-0.010
TiO_2	-0.243	**0.422**	0.153	0.220
Al_2O_3	0.095	**0.505**	-0.163	**0.368**
FeO	**-0.421**	0.137	0.270	0.009
MnO	**-0.336**	0.104	**0.587**	0.118
MgO	**-0.418**	-0.238	-0.046	-0.023
CaO	-0.197	**0.399**	**-0.519**	0.147
Na_2O	0.308	**0.390**	0.138	-0.060
K_2O	**0.364**	0.036	**0.476**	0.275
P_2O_5	-0.005	**0.410**	0.110	**-0.837**

Table 21: Loadings of PCA performed on trace elements. (a) PCA of all Mafic Complex samples. (b) PCA of trace elements from the northern Mafic Complex (Val Sesia and Val Mastallone). (c) PCA performed on trace elements from the southern Mafic Complex (Val Sessera).

(a)

	PC1	PC2	PC3	PC4
Sr	-0.061	0.280	**0.759**	**-0.355**
Ba	0.285	**-0.450**	0.206	**-0.344**
Rb	0.197	**-0.461**	**-0.318**	**-0.479**
Zr	**0.371**	0.021	0.017	0.022
Ni	-0.200	**0.404**	-0.242	**-0.715**
Nb	**0.359**	0.133	-0.161	0.040
Y	0.254	**0.463**	**-0.384**	-0.052
Nd	**0.386**	0.312	0.080	0.081
La	**0.420**	-0.050	0.154	-0.052
Ce	**0.425**	0.104	0.131	0.022

(b)

	PC1	PC2	PC3	PC4
Sr	-0.061	**0.566**	**-0.501**	0.293
Ba	0.239	**0.595**	0.015	-0.302
Rb	**0.322**	0.192	**0.546**	-0.174
Zr	0.310	-0.107	-0.106	**-0.619**
Ni	-0.248	-0.166	**-0.491**	**-0.561**
Nb	0.303	-0.087	0.051	0.150
Y	0.299	**-0.440**	-0.087	0.128
Nd	**0.392**	-0.171	**-0.326**	0.217
La	**0.416**	0.137	-0.139	-0.021
Ce	**0.412**	-0.025	-0.250	0.095

(c)

	PC1	PC2	PC3	PC4
Sr	-0.072	**0.517**	**-0.417**	**-0.485**
Ba	**0.335**	**-0.365**	-0.063	0.100
Rb	0.151	**-0.378**	**0.534**	**-0.585**
Zr	**0.391**	0.015	-0.153	0.215
Ni	-0.159	**0.364**	**0.557**	-0.083
Nb	**0.395**	0.085	0.103	**0.351**
Y	0.205	**0.446**	**0.422**	0.274
Nd	**0.363**	**0.327**	0.000	-0.136
La	**0.414**	-0.040	-0.100	-0.271
Ce	**0.424**	0.097	-0.064	-0.261

Table 22: Loadings of PCA performed on both major and trace elements for (a) the entire Mafic Complex, (b) the northern Mafic Complex (Val Sesia and Val Mastallone transects).

(a)

	PC1	PC2	PC3	PC4
SiO_2	**0.321**	-0.182	0.019	0.164
TiO_2	-0.175	**0.328**	-0.066	-0.178
Al_2O_3	-0.099	0.109	**0.411**	0.023
FeO	**-0.258**	**0.288**	-0.112	-0.056
MnO	-0.207	**0.246**	**-0.224**	-0.067
MgO	**-0.327**	0.097	-0.166	-0.132
CaO	**-0.293**	0.103	0.218	-0.060
Na_2O	**0.249**	0.082	**0.367**	0.105
K_2O	**0.300**	-0.031	-0.203	**-0.324**
P_2O_5	0.008	**0.292**	0.206	**-0.241**
Sr	-0.148	0.139	**0.469**	**-0.262**
Ba	**0.251**	0.092	0.070	**-0.494**
Rb	0.210	-0.021	**-0.311**	**-0.503**
Zr	0.191	**0.277**	-0.050	0.042
Ni	**-0.240**	0.027	**-0.224**	0.012
Nb	0.174	**0.292**	-0.106	0.166
Y	0.031	**0.315**	**-0.283**	**0.316**
Nd	0.141	**0.374**	-0.001	0.179
La	**0.273**	**0.254**	0.064	0.003
Ce	**0.232**	**0.312**	0.035	0.104

(b)

	PC1	PC2	PC3	PC4
SiO_2	**0.315**	-0.205	0.095	-0.112
TiO_2	-0.156	**0.360**	-0.111	0.020
Al_2O_3	-0.061	-0.120	**-0.428**	**0.290**
FeO	**-0.283**	**0.283**	0.009	0.093
MnO	**-0.250**	**0.238**	0.131	0.101
MgO	**-0.308**	0.156	0.106	0.158
CaO	**-0.307**	0.080	-0.180	0.076
Na_2O	0.188	-0.015	**-0.397**	**-0.269**
K_2O	**0.320**	0.010	0.050	**0.342**
P_2O_5	-0.005	**0.310**	**-0.237**	**-0.309**
Sr	-0.081	0.035	**-0.557**	0.015
Ba	0.204	0.077	**-0.347**	**0.347**
Rb	**0.301**	0.033	0.055	**0.379**
Zr	0.135	**0.278**	0.102	**0.374**
Ni	**-0.259**	0.019	0.029	0.164
Nb	0.147	**0.261**	0.038	0.183
Y	0.105	**0.307**	**0.240**	-0.088
Nd	0.169	**0.364**	0.026	**-0.256**
La	**0.262**	**0.265**	-0.109	-0.028
Ce	0.223	**0.313**	-0.031	-0.176

Figure 1: Generalized model of transcrustal magmatic systems. Adapted from Cashman *et al.* (2017).

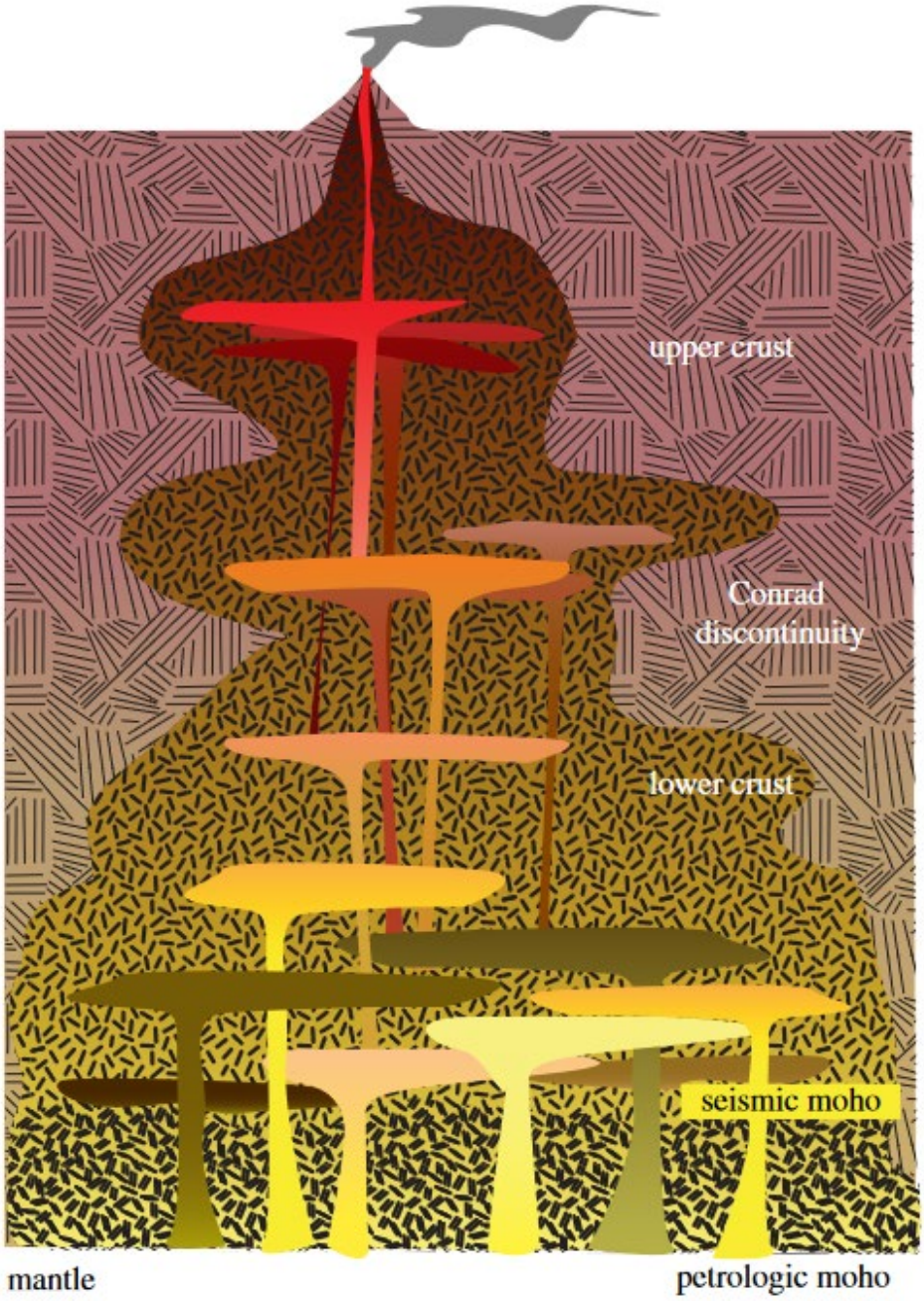
upper crust
Conrad discontinuity
lower crust
seismic moho
mantle
petrologic moho

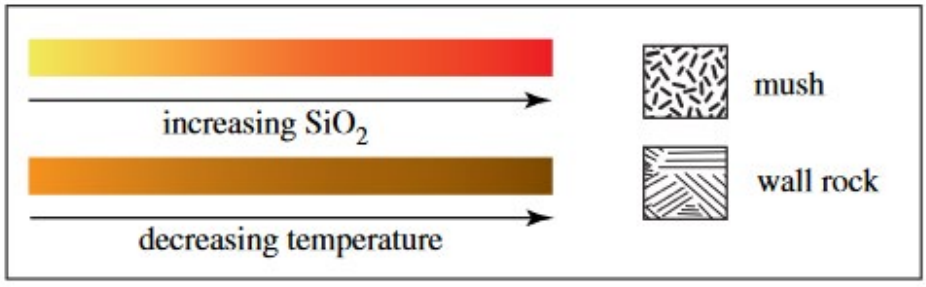
increasing SiO_2
decreasing temperature
mush
wall rock

Figure 2: conceptual model depicting the combined processes of compaction and reactive melt flow from Sparks *et al.* (2019).

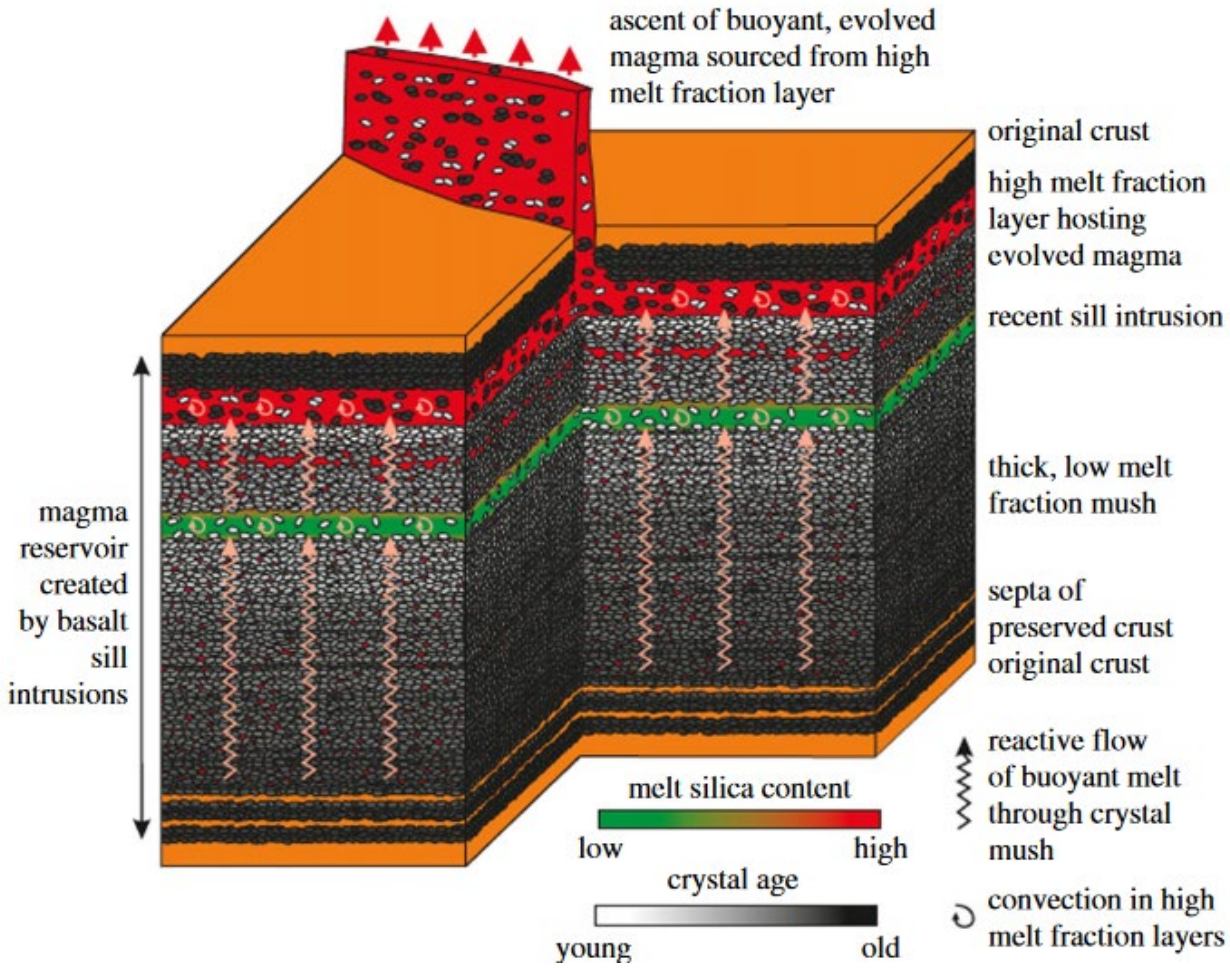
ascent of buoyant, evolved magma sourced from high melt fraction layer
original crust
high melt fraction layer hosting evolved magma
recent sill intrusion
thick, low melt fraction mush
septa of preserved crust original crust
magma reservoir created by basalt sill intrusions
reactive flow of buoyant melt through crystal mush
convection in high melt fraction layers
melt silica content
low
high
crystal age
young
old

Figure 3: model of melt fraction and temperature over the duration of the emplacement of a large intrusion in the lower crust from Jackson *et al.* (2018). (a) shows the melt fraction before, during, and after the emplacement of a single sill as predicted by the model. (b) the temperature changes as a function of time at the top of the large intrusion, encompassing the lifespan of the magmatic activity and (c) deeper down in the intrusion.

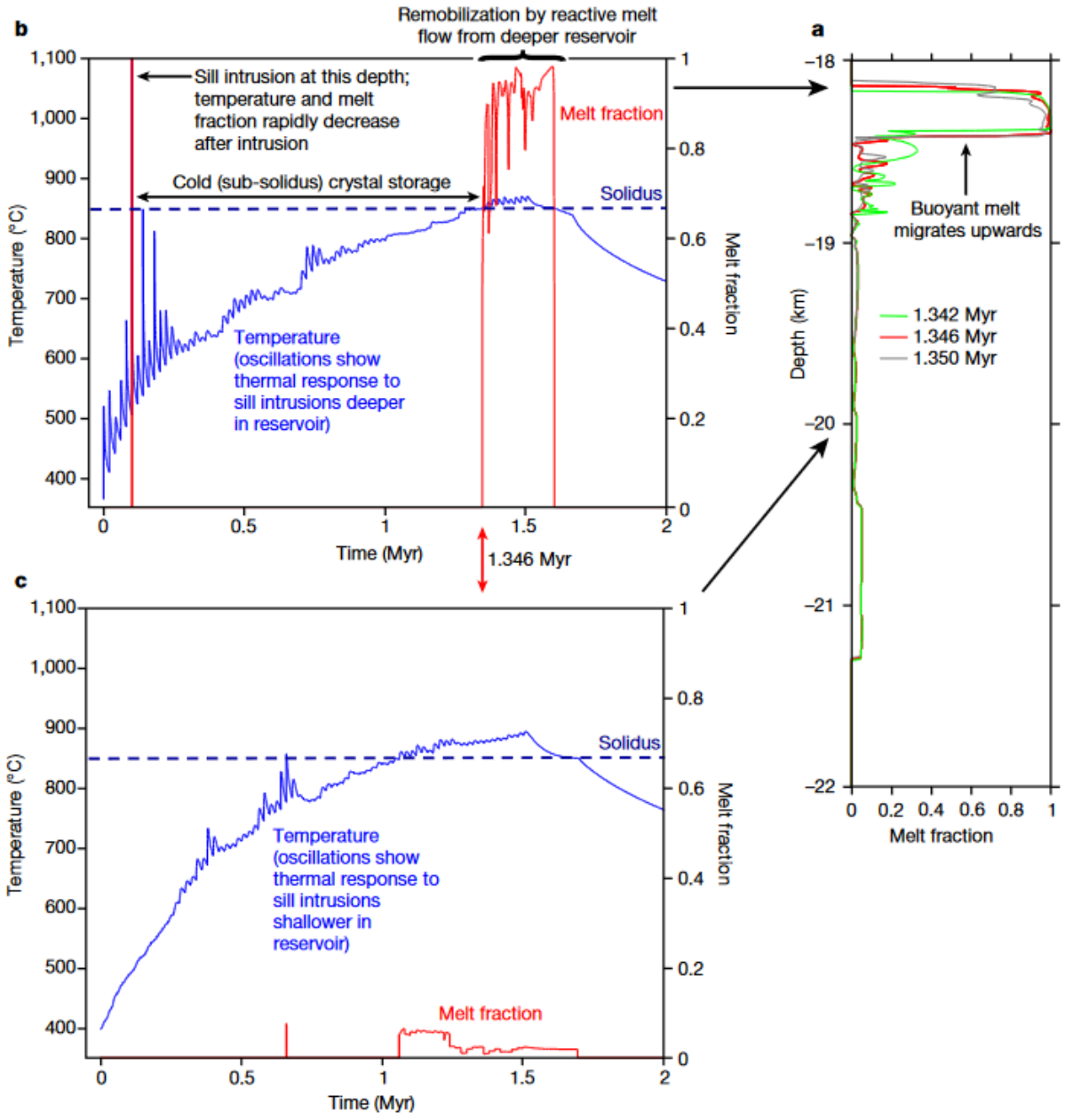
b
Remobilization by reactive melt flow from deeper reservoir
Sill intrusion at this depth; temperature and melt fraction rapidly decrease after intrusion
Melt fraction
Cold (sub-solidus) crystal storage
Solidus
Temperature (°C)
Temperature (oscillations show thermal response to sill intrusions deeper in reservoir)
Melt fraction
Time (Myr)
1.346 Myr
a
Buoyant melt migrates upwards
1.342 Myr
1.346 Myr
1.350 Myr
Depth (km)
Melt fraction
c
Solidus
Temperature (°C)
Temperature (oscillations show thermal response to sill intrusions shallower in reservoir)
Melt fraction
Melt fraction
Time (Myr)

Figure 4: The IVZ geology (after James, 2001; Brack *et al.*, 2010) with the Insubric Line (brown line) dividing the Adriatic from the Eurasian plate. The inset figure shows the location of the IVZ in Italy (Rutter *et al.*, 2003). The blue circles indicate the drill sites in Val d'Ossola within the Phase 1 of the DIVE (Drilling the Ivrea-Verbano Zone) project, sponsored by the International Continental Scientific Drilling Program. CMB = Cossato–Mergozzo–Brissago. Figure modified after Pistone *et al.* (2017).

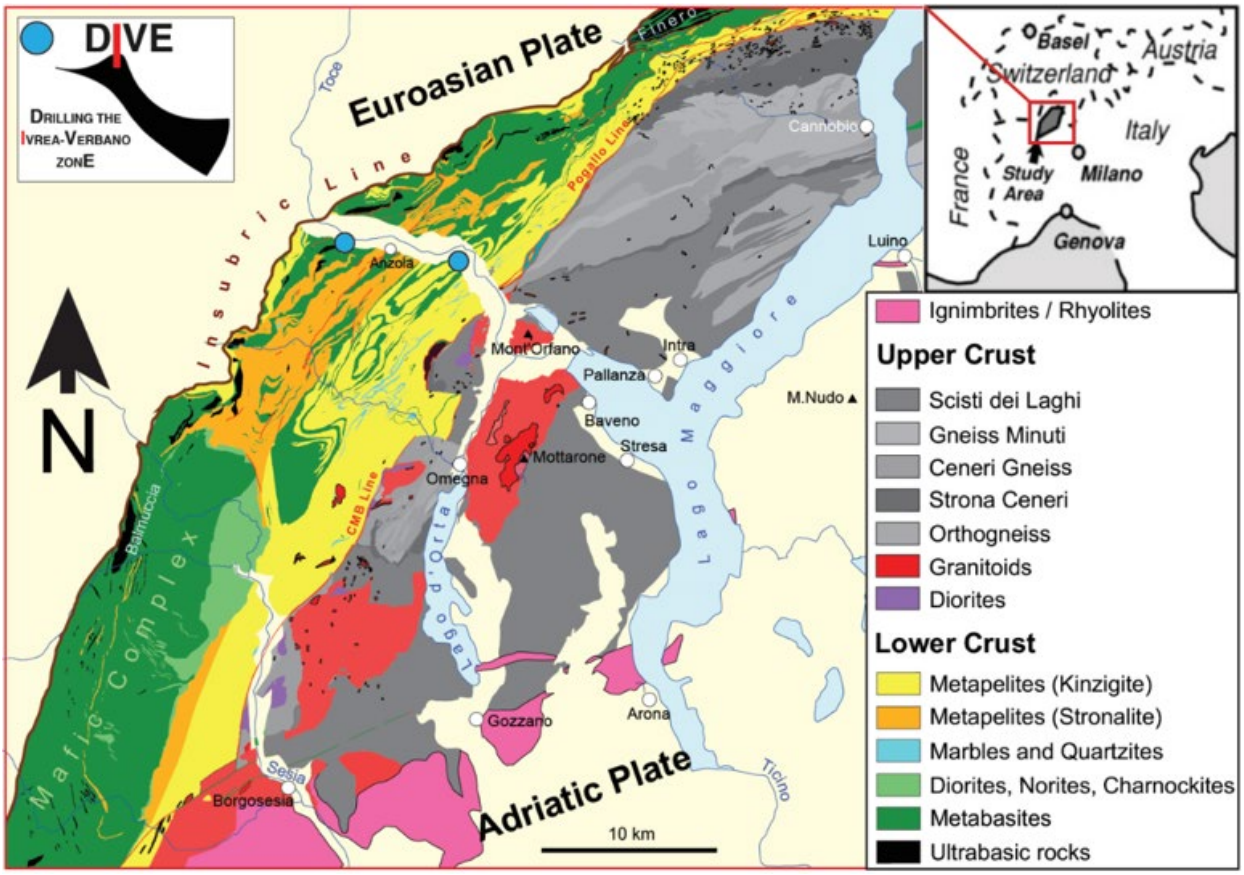
DIVE
Drilling the Ivrea-Verbano zone
Euroasian Plate
Adriatic Plate
Insubric Line
Pogallo Line
CMB Line
Finero
Toce
Cannobio
Luino
Anzola
Mont'Orfano
Intra
Pallanza
Baveno
Stresa
Mottarone
Omegna
M.Nudo
Lago Maggiore
Lago d'Orta
Arona
Gozzano
Sesia
Borgosesia
Ticino
Mafic Complex
Balmuccia
N
10 km
Basel
Austria
Switzerland
Italy
France
Study Area
Milano
Genova
Ignimbrites / Rhyolites
Upper Crust
Scisti dei Laghi
Gneiss Minuti
Ceneri Gneiss
Strona Ceneri
Orthogneiss
Granitoids
Diorites
Lower Crust
Metapelites (Kinzigite)
Metapelites (Stronalite)
Marbles and Quartzites
Diorites, Norites, Charnockites
Metabasites
Ultrabasic rocks

Figure 5: Geologic map of the Sesia Magmatic System adapted from Quick *et al.* (2009). Orientation is rotated to emphasize the continental cross-section aspect of the Ivrea-Verbano Zone. Saliceto is marked with a star.

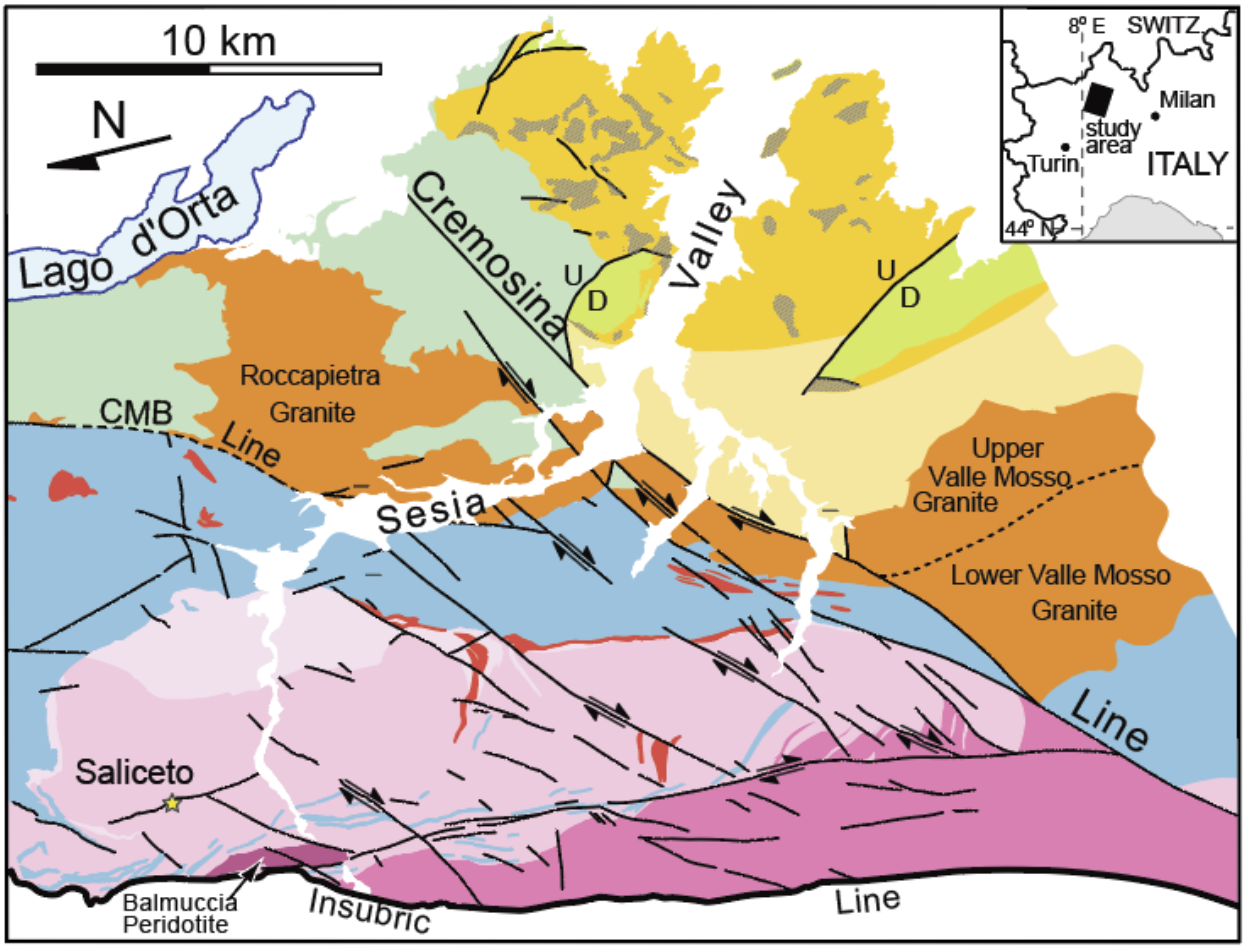

Sesia Valley volcanic and sedimentary rocks
- Limestone
- Caldera fill with megabreccia
- Volcanic rocks, undivided

Serie dei Laghi
- Graniti dei Laghi
- Schist and gneiss

Ivrea-Verbano Zone
- Granitic rocks
- Diorite
- Gabbronorite
  - Upper Mafic Complex
- Amphibole gabbro
  - Lower Mafic Complex
- Kinzigite Formation
- Balmuccia Peridotite
- Fault

Figure 6: Map of Mafic Complex showing sampling location of new bulk rock data from this study, sampled by Mattia Pistone and Benoît Petri in 2017. Map adapted from Sinigoi *et al.* (2016) and shows the most current nomenclature to describe the stratigraphy of the entire Mafic Complex as introduced by Sinigoi *et al.* (1996). This study discriminates the "Diorites" from the remainder of the Mafic Complex. Saliceto outcrop is marked with a star.

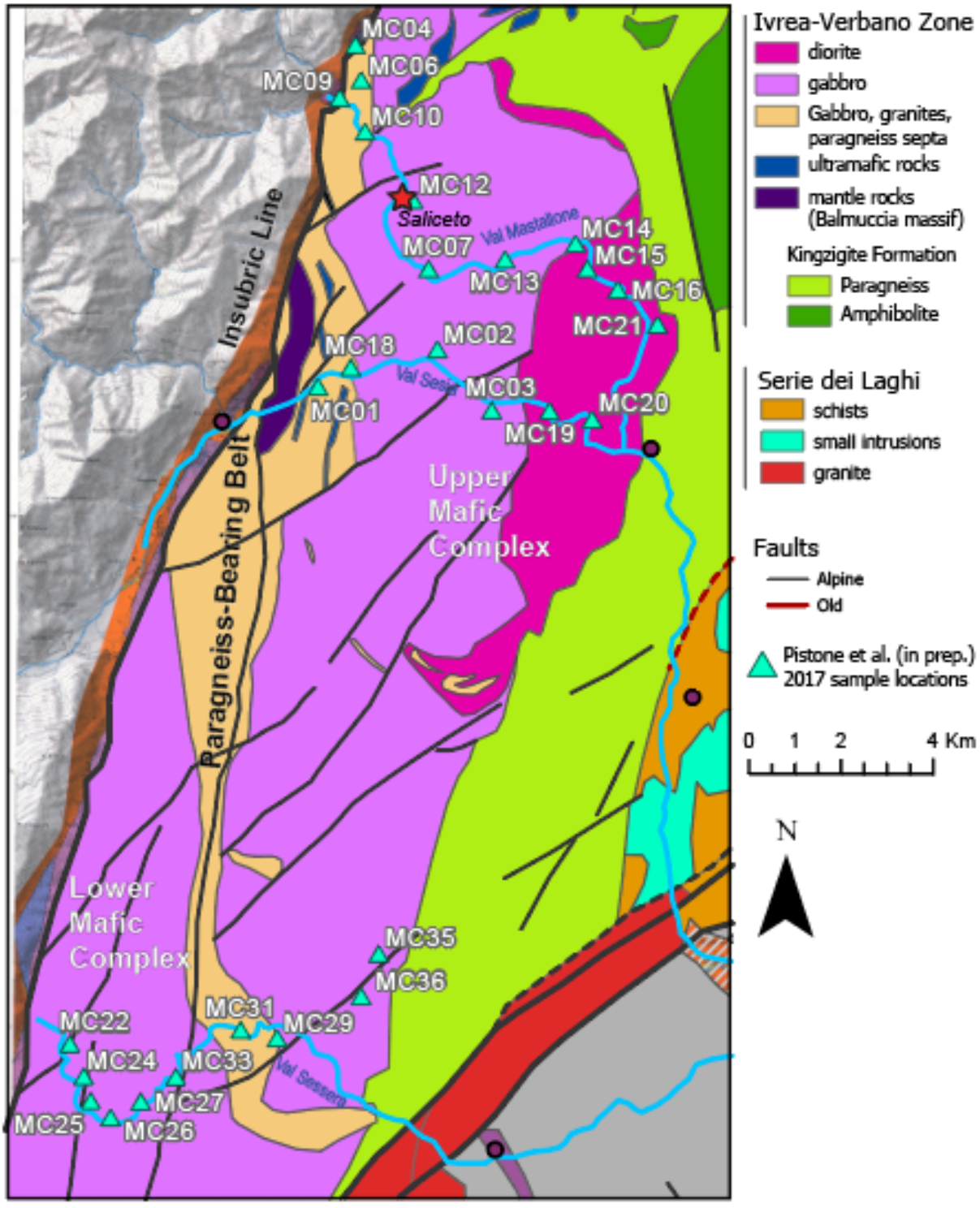
MC04
MC06
MC09
MC10
MC12
Saliceto
Val Mastallone
MC14
MC15
MC07
MC13
MC16
MC21
MC02
MC18
Val Sesia
MC03
MC20
MC01
MC19
Insubric Line
Paragneiss-Beating Belt
Upper Mafic Complex
Lower Mafic Complex
MC35
MC36
MC31
MC29
MC22
MC24
MC33
Val Sessera
MC27
MC25
MC26
Ivrea-Verbano Zone
diorite
gabbro
Gabbro, granites, paragneiss septa
ultramafic rocks
mantle rocks (Balmuccia massif)
Kingzigite Formation
Paragneiss
Amphibolite
Serie dei Laghi
schists
small intrusions
granite
Faults
Alpine
Old
Pistone et al. (in prep.) 2017 sample locations
0 1 2 4 Km
N

Figure 7: Low altitude aerial image of Saliceto area and Saliceto sample locations. Callout label colors as used for in-situ geochemical analysis plotting. Aerial imagery is not perfectly georeferenced due to low altitude perspective of camera. UAV imagery courtesy of Roger Maendel.

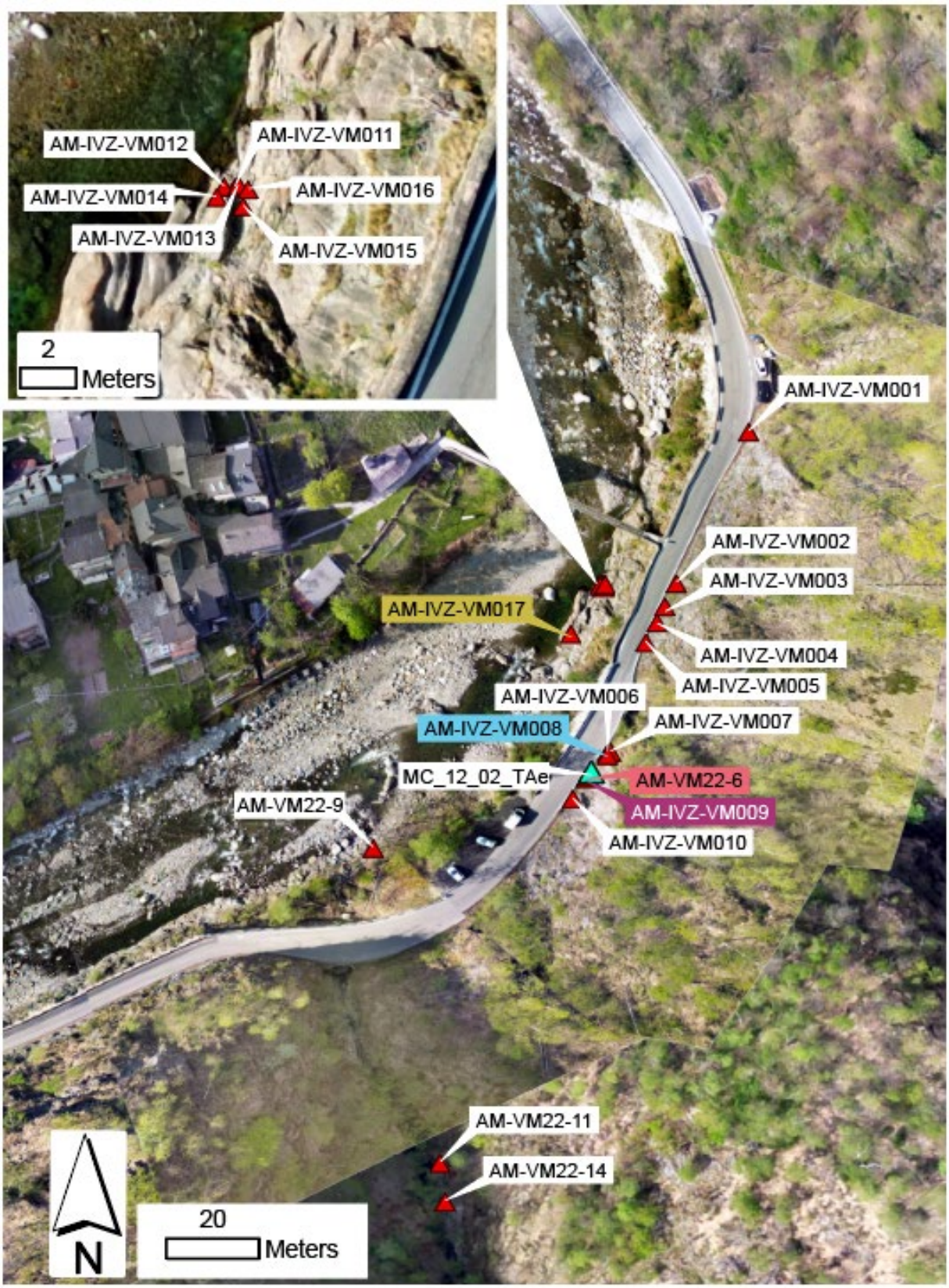
AM-IVZ-VM012
AM-IVZ-VM011
AM-IVZ-VM014
AM-IVZ-VM016
AM-IVZ-VM013
AM-IVZ-VM015
2
Meters
AM-IVZ-VM001
AM-IVZ-VM002
AM-IVZ-VM003
AM-IVZ-VM017
AM-IVZ-VM004
AM-IVZ-VM005
AM-IVZ-VM006
AM-IVZ-VM008
AM-IVZ-VM007
MC_12_02_TAe
AM-VM22-6
AM-VM22-9
AM-IVZ-VM009
AM-IVZ-VM010
AM-VM22-11
AM-VM22-14
N
20
Meters

Figure 8: Saliceto outcrop photos. (a) plants and steel mesh cover portions of the road outcrop. Author for scale. (b) view of Mastallone river and outcrops at river and road level (Torrente Mastallone), looking southward downstream with view of the Saliceto bridge. River outcrops sampled in detail appear in the center of the photo.


(a)


(b)

Figure 9: EPMA data and BSE/element map images plotted on a full thin section scan in ArcGIS Pro software (thin section A9, sample AM-IVZ-VM009). EPMA data points are from LSU session and the BSE images and element maps are from SEM at UGA GEM (see Methods). Note the 1-m scale bar; distances are scaled by 10^3, so this bar represents 1 mm at the true scale.

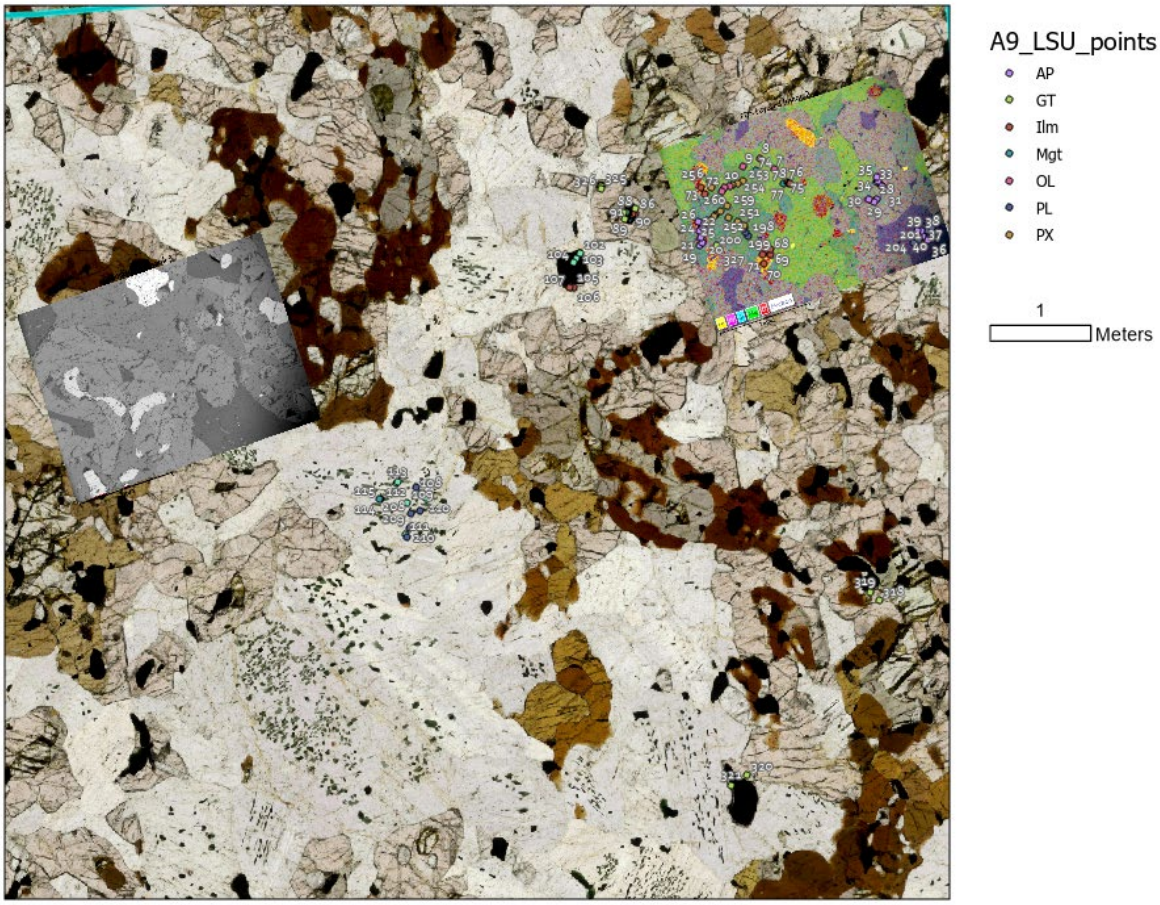
A9_LSU_points
AP
GT
Ilm
Mgt
OL
PL
PX
1
Meters

Figure 10: Geologic map of Mafic Complex sample locations (where determined) from the literature. Quadrangle map of Quick *et al.* (2003) digitized, with simplifications shown for rock types. Background is a hillshade surface model showing the high-relief topography of the region.

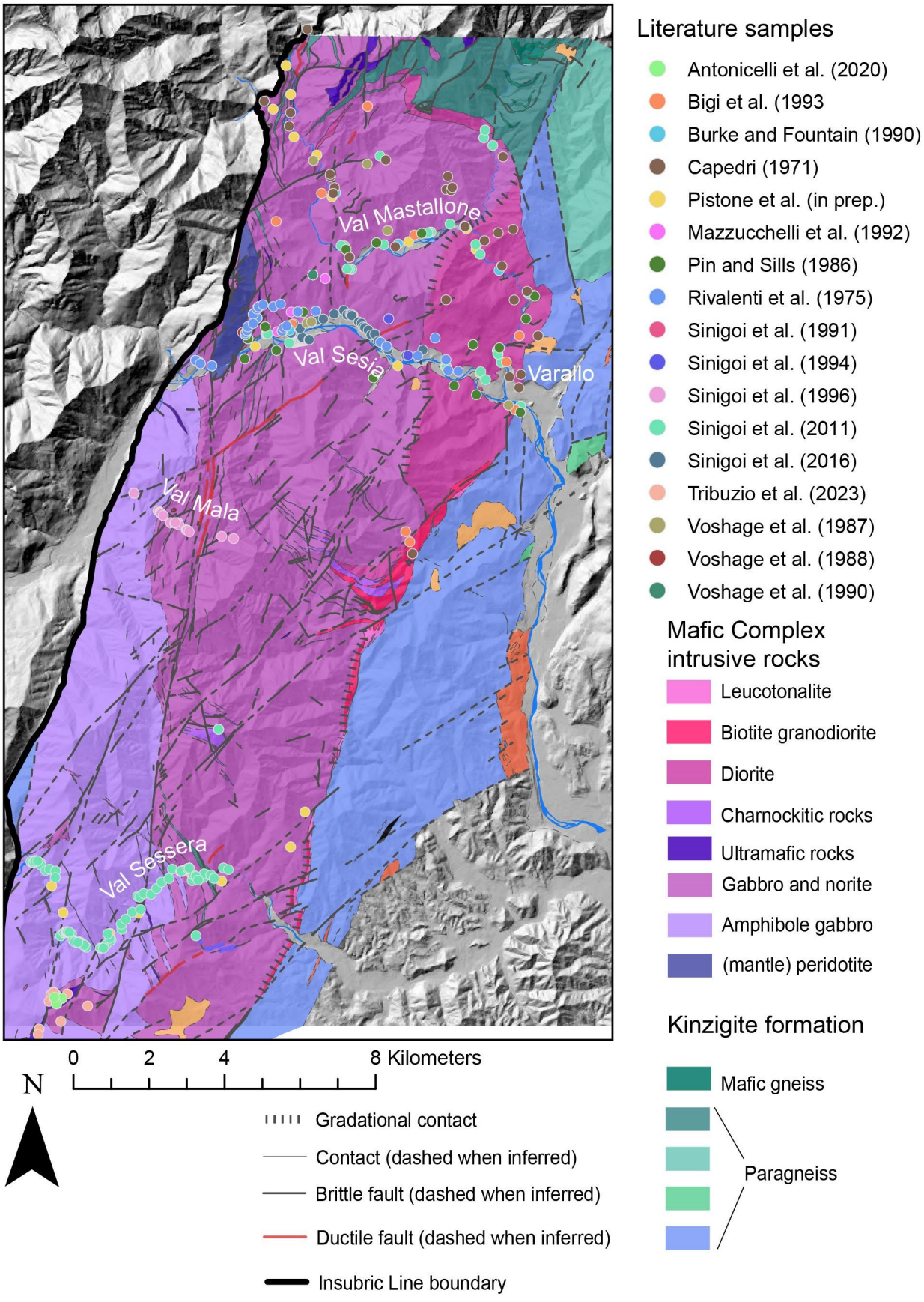
Val Mastallone
Val Sesia
Varallo
Val Mala
Val Sessera
0
2
4
8 Kilometers
N
Gradational contact
Contact (dashed when inferred)
Brittle fault (dashed when inferred)
Ductile fault (dashed when inferred)
Insubric Line boundary
Literature samples
Antonicelli et al. (2020)
Bigi et al. (1993
Burke and Fountain (1990)
Capedri (1971)
Pistone et al. (in prep.)
Mazzucchelli et al. (1992)
Pin and Sills (1986)
Rivalenti et al. (1975)
Sinigoi et al. (1991)
Sinigoi et al. (1994)
Sinigoi et al. (1996)
Sinigoi et al. (2011)
Sinigoi et al. (2016)
Tribuzio et al. (2023)
Voshage et al. (1987)
Voshage et al. (1988)
Voshage et al. (1990)
Mafic Complex intrusive rocks
Leucotonalite
Biotite granodiorite
Diorite
Charnockitic rocks
Ultramafic rocks
Gabbro and norite
Amphibole gabbro
(mantle) peridotite
Kinzigite formation
Mafic gneiss
Paragneiss

Figure 11: Stratigraphy of the northern Mafic Complex (Val Sesia and Val Mastallone) as a function of distance to the Insubric Line, west to east. Histograms of number of samples containing major element data from the literature as a function of distance to the Insubric Line for Val Mastallone and Val Sesia, which are shown above and below, respectively, the stratigraphic profiles. Samples are separated by watershed (Sesia and Mastallone rivers). In the Mastallone transect, boundaries between zones do not perfectly parallel the Insubric Line or are not as well-defined in the literature. Samples from Val Duggia, south of the Sesia transect, were included in the Sesia transect histogram. The stratigraphic position of Saliceto samples is marked with a star.

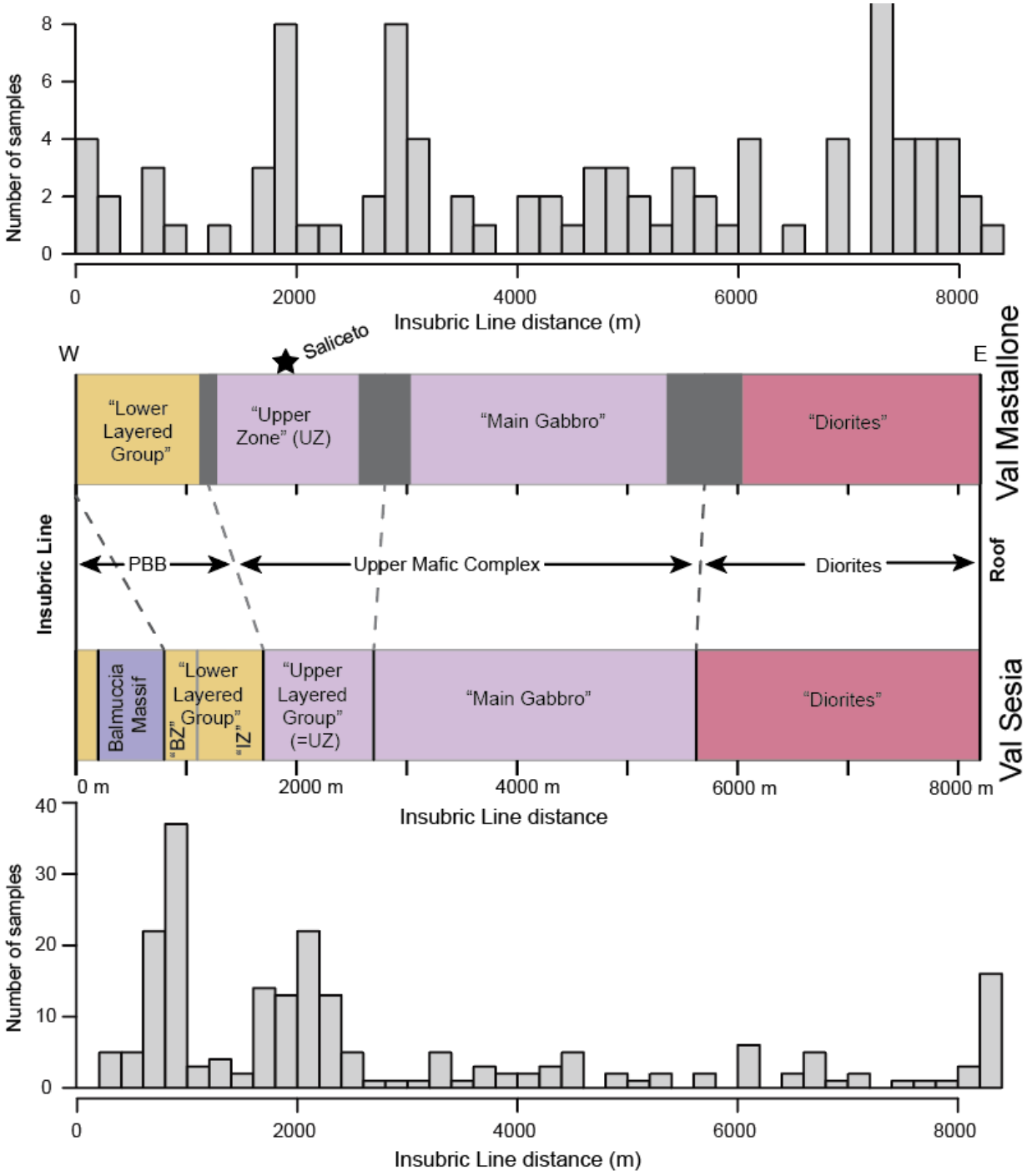
Number of samples
Insubric Line distance (m)
W
E
Saliceto
"Lower Layered Group"
"Upper Zone" (UZ)
"Main Gabbro"
"Diorites"
Val Mastallone
Insubric Line
PBB
Upper Mafic Complex
Diorites
Roof
Balmuccia Massif
"BZ"
"IZ"
"Lower Layered Group"
"Upper Layered Group" (=UZ)
"Main Gabbro"
"Diorites"
Val Sesia
0 m
2000 m
4000 m
6000 m
8000 m
Insubric Line distance
Number of samples
Insubric Line distance (m)

Figure 12: Brittle features at Saliceto. (a) Fault in the ravine of Rio della Scaravina. Rocks to the left are dark and garnet-bearing, whereas leucogabbros are exposed to the right (southwest) of the fault zone. (b) Fractures cross-cutting contact of garnet-dominant gabbro and gabbro-norite on the Mastallone river bank, 8 meters south of the Saliceto bridge.


(a)
garnet-free
leucogabbro
fault zone
garnet-bearing
gabbro


(b)
garnetiferous
melagabbro
leuco-gabbro

Figure 13: (a) Fine- to coarse grained banding in gabbro-norite (sample AM-VM22-9) at the base of the stratigraphic section studied. Cold chisel for scale is ~25 cm in length. (b) “Whisps” of garnet gabbro (dark colored rock) mantled by gabbro-norite (light colored rock) along Mastallone riverbank at Saliceto.


(a)
coarse-grained leucogabbro-norite
fine-grained gabbro-norite


(b)
leucogabbro-norite
garnetiferous melagabbro
leucogabbro-norite

Figure 14: Hand rock specimens and representative sampling location. (a) AM-IVZ-VM010 is a garnet amphibole olivine gabbro with (b) a 5.4 cm poikilitic amphibole crystal and (c) platy biotite. (d) AM-IVZ-VM009 is a garnet amphibole olivine gabbro with (e) compositional banding made of dark (olivine, amphibole and garnet) and light color minerals (plagioclase). (f) AM-VM22-6 sampling location showing banded gabbros. (g) Samples AM-VM22-6c (right) and AM-VM226f (left), both showing permanent marker rectangles indicating the locations of extracted rock billets for thin section preparation. Ruler is 10 cm long. Bulk rock analyses AM-VM22-6fL and AM-VM22-6fD were of the lightest and darkest portions of this sample, respectively. (h) AM-VM22-6c is intermediate in modal abundance of mafic minerals and plagioclase between samples AM-VM22-6fL and AM-VM22-6fD.

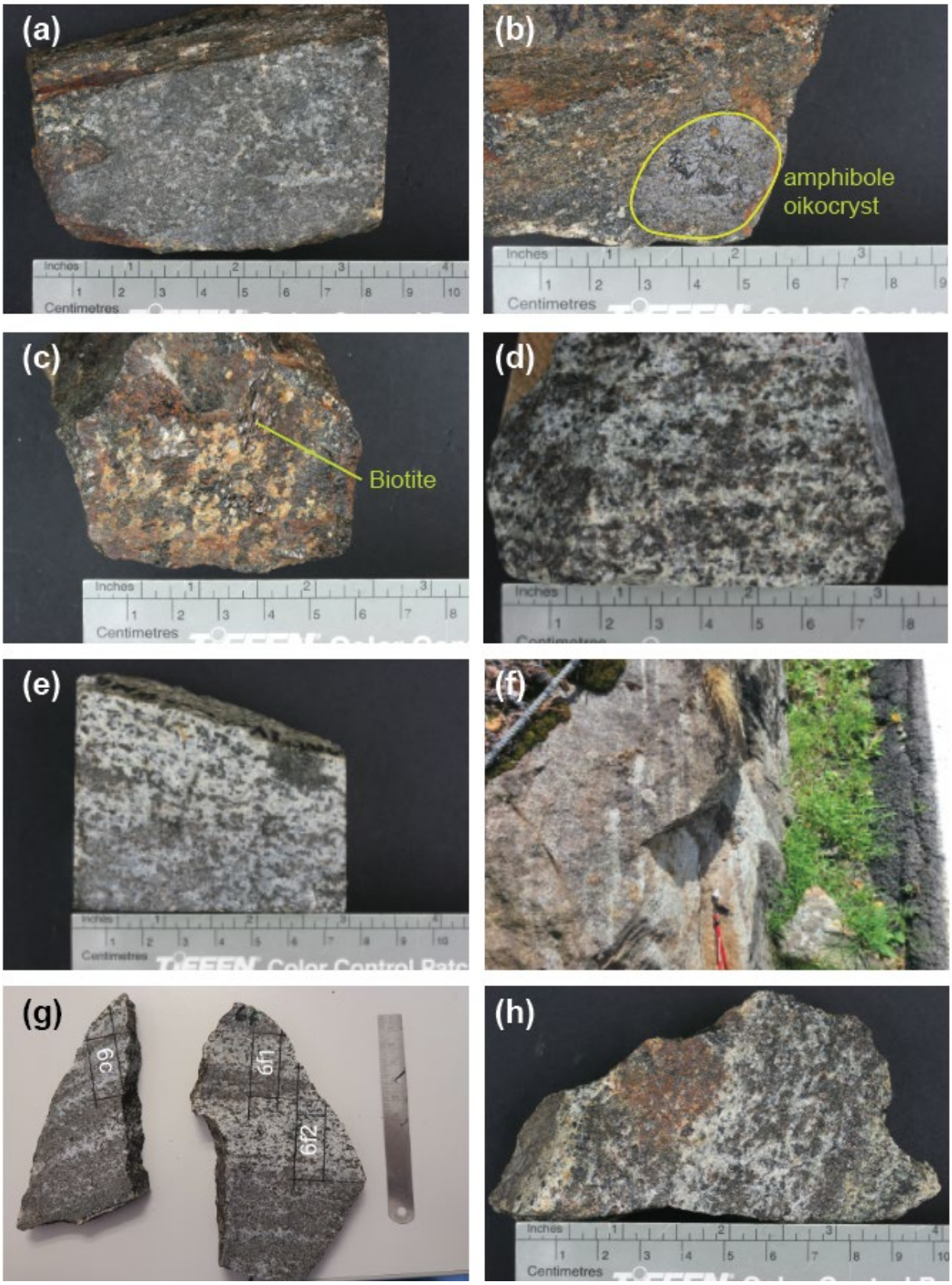
(a)
(b)
amphibole
oikocryst
(c)
Biotite
(d)
(e)
(f)
(g)
6c
6f1
6f2
(h)

Figure 15: Saliceto road cut hand samples. (a) – (b) AM-IVZ-VM007 is a garnet amphibole olivine gabbro with a mesocratic color index. (c) Billets prepared for thin sections of sample AM-IVZ-VM006, which is a mesocratic garnet amphibole olivine gabbro. (d) – (f) AM-IVZ-VM008 is a plagioclase-bearing amphibole pyroxenite with a holomelanocratic color index. It is garnet-free and contains (e) singular clumps of white plagioclase in an oxide/pyroxene matrix, as well as (f) light-colored veins of plagioclase that appear to cross-cut the ultramafic rock.

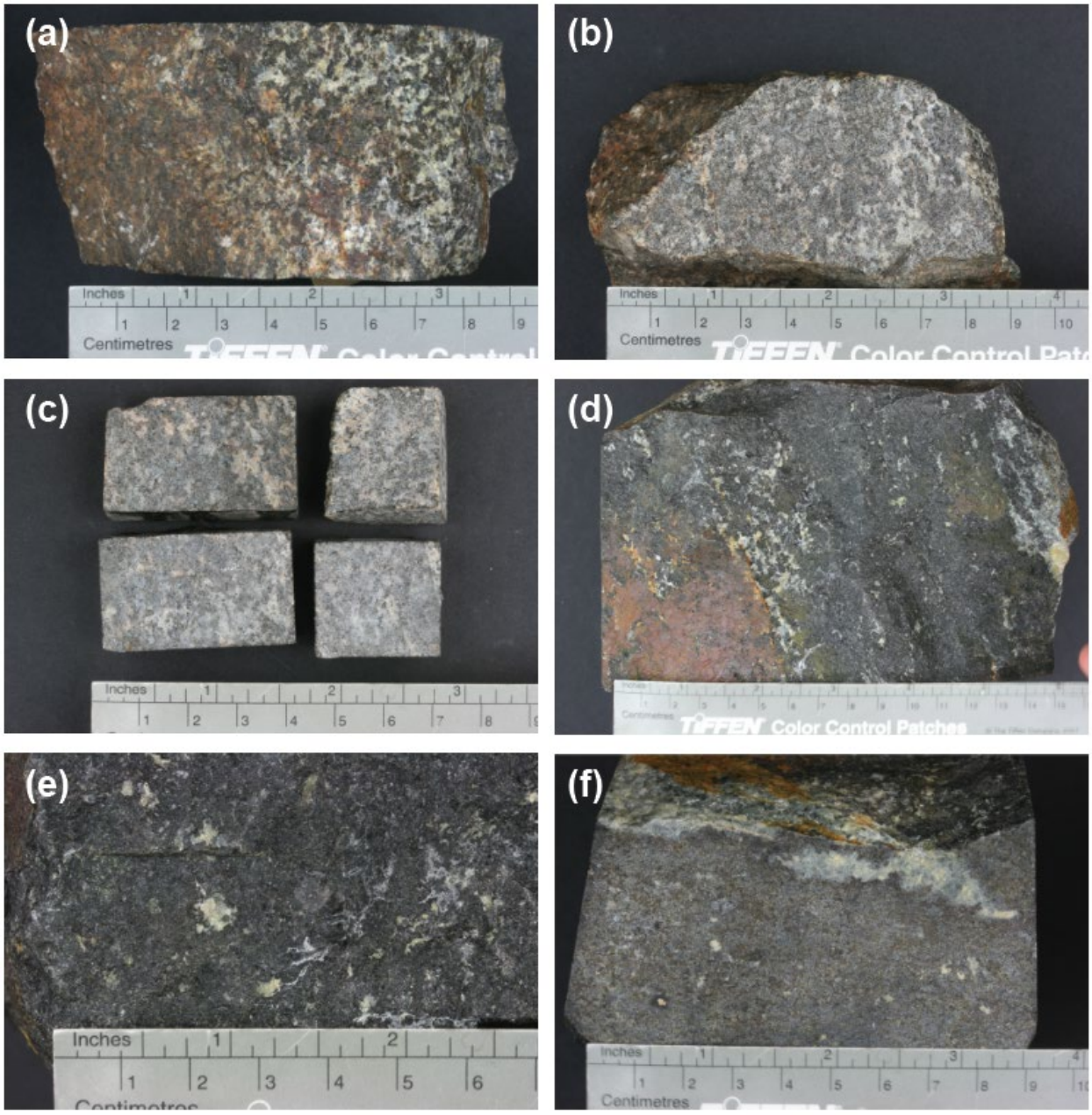
(a)
(b)
(c)
(d)
(e)
(f)
Inches
Centimetres
Color Control Patches

Figure 16: Saliceto road outcrop hand samples. (a) – (b) AM-IVZ-VM005 is a garnet-free amphibole gabbro-norite. (c) – (d) AM-IVZ-VM004 is a garnet amphibole norite. (e) – (f) AM-IVZ-VM003 is an amphibole gabbro-norite containing bands of poikilitic amphibole. (g) AM-IVZ-VM002 is a garnet amphibole gabbro-norite. (h) AM-IVZ-VM001 is a garnet-free amphibole-free gabbro-norite that contains trace biotite.

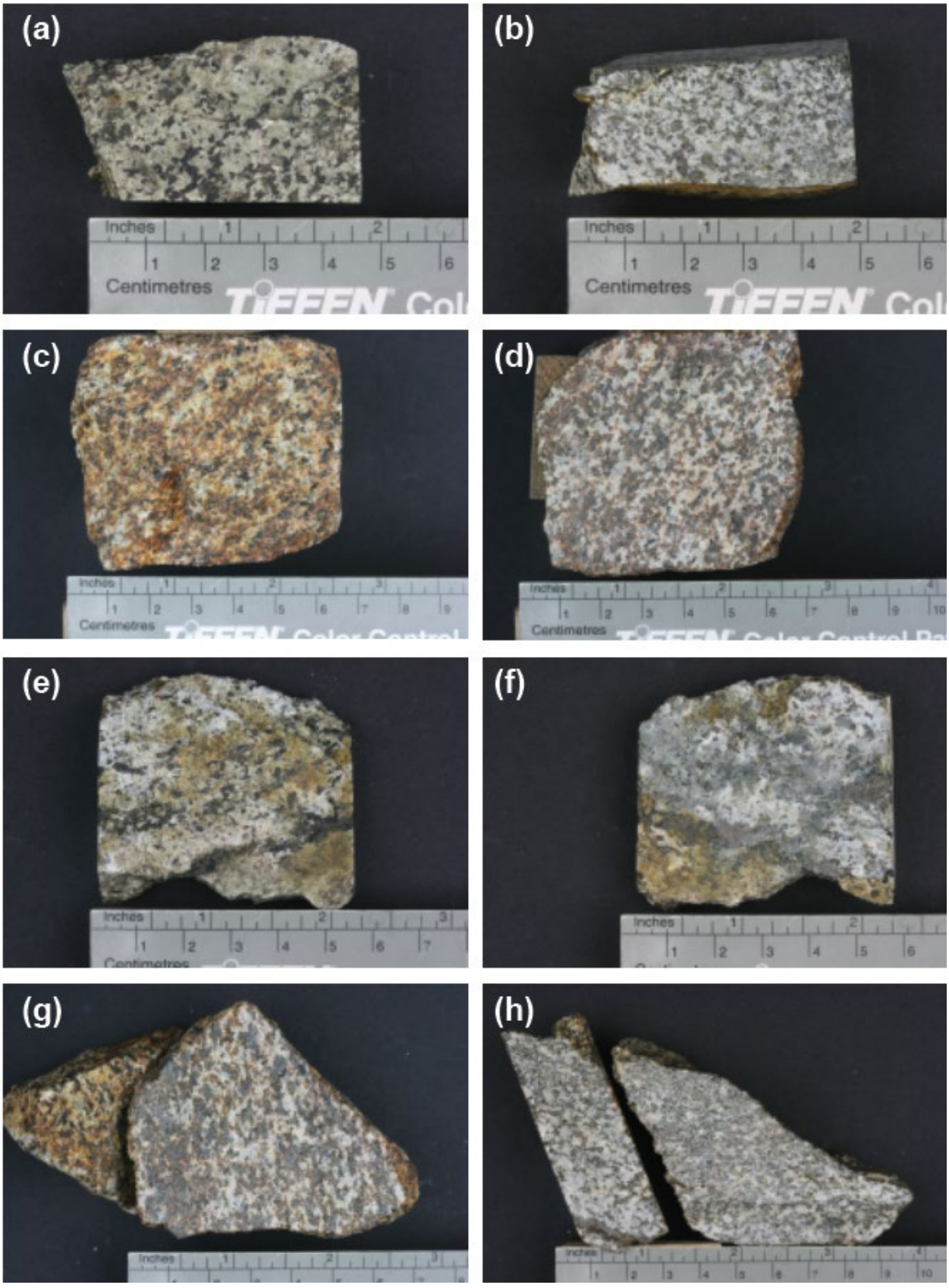
(a)
(b)
(c)
(d)
(e)
(f)
(g)
(h)
Inches
Centimetres

Figure 17: Hand samples from the Saliceto river outcrop (a). Dark, garnetiferous band appears vertically in the photo with irregular, wispy contact with light colored amphibole norites and gabbro-norites on both sides (right and left in photo). AM-IVZ-VM017 location is 5 m southward along the river bank (see Figure 7). Hammer for scale is ~30 cm in length. (b) AM-IVZ-VM014 is a garnet amphibole gabbro. (c) AM-IVZ-VM012 captures the wispy contact between the holomelanocratic, garnet-dominant gabbro and the amphibole gabbro. (d) AM-IVZ-VM011 is a holomelanocratic garnet- and amphibole-dominant gabbro. (e) AM-IVZ-VM013 is an amphibole norite with trace garnet. Samples AM-IVZ-VM015 (f) and AM-IVZ-VM016 (g) are both amphibole gabbro-norites.

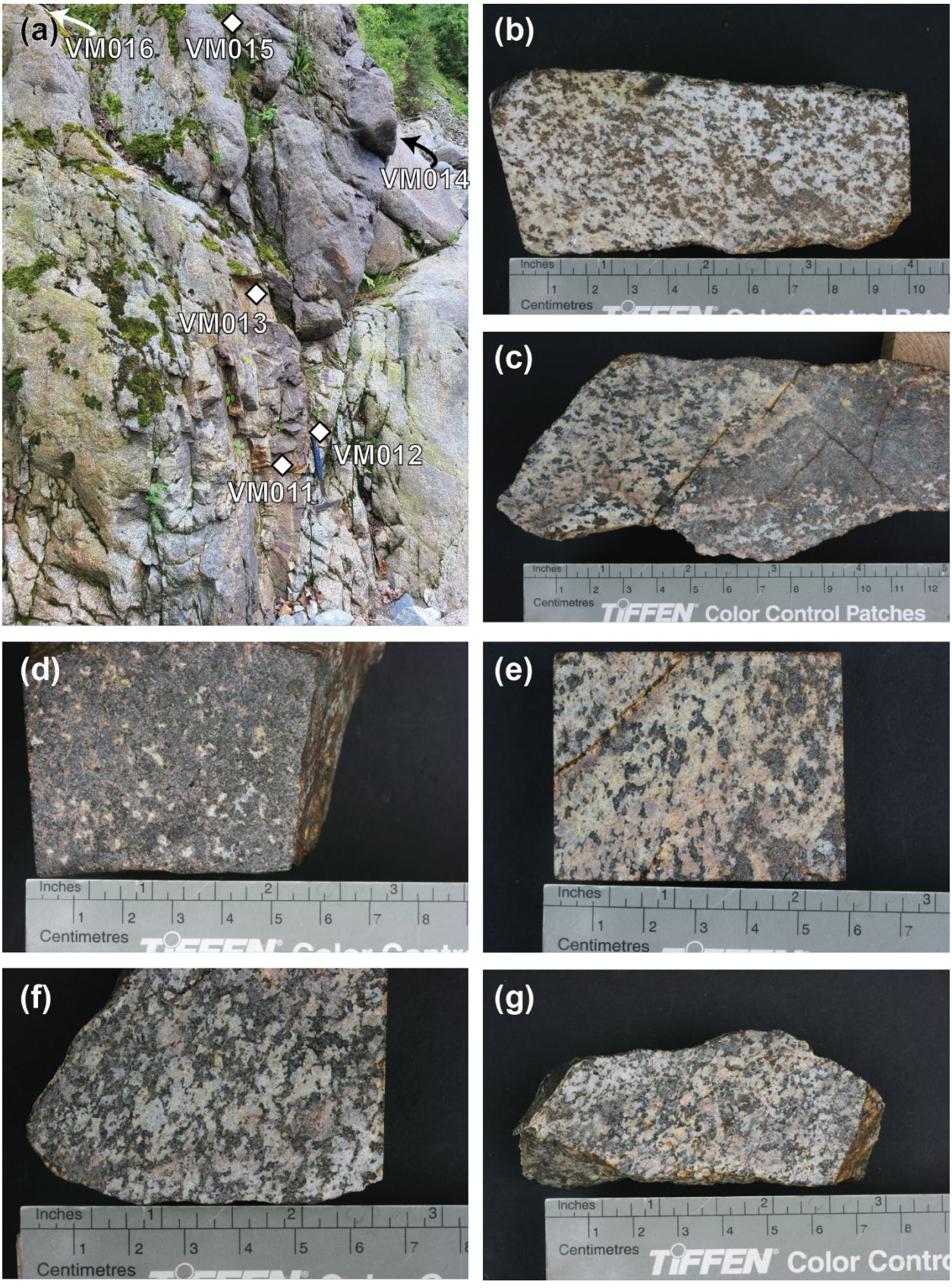
(a)
VM016
VM015
VM014
VM013
VM012
VM011
(b)
(c)
(d)
(e)
(f)
(g)
Inches
Centimetres
TIFFEN Color Control Patches

Figure 18: Hand samples from along the river outcrops and from the Rio della Scaravina ravine. (a) – (b) AM-IVZ-VM017 is a gabbro-norite containing a band of poikilitic amphibole grains. (c) AM-VM22-9a is a banded gabbro-norite from the river outcrop in the southern portion of the study area. It contains banding with darker bands composed of finer grained (~0.5 mm) pyroxene-dominant and lighter bands of coarser grain size (~1.5 mm) plagioclase-dominant. Similar banding and rock type was found in Rio della Scaravina near the road level, but it is unclear if these rocks were from the same stratigraphic band. Permanent marker rectangle depicts the area of thin section VM22-9a. (d) AM-VM22-13 is a garnet-bearing gabbro from near the fault zone in Rio della Scaravina. The pseudotachylite divides two rock domains in which one is garnet-bearing (right) and the other is garnet-free (left). (e) AM-VM22-12 is a melanocratic garnet amphibole olivine gabbro. (f) AM-VM22-13 appears to be a garnet-free pyroxenite in hand. (g) AM-VM22-14 captures the contact between the dark olivine- and garnet-rich band and plagioclase-dominant band. Permanent marker rectangles indicate part of rock where billets were extracted for thin section making. The dark portion of this sample is where bulk rock analysis AM-VM22-14D was applied.

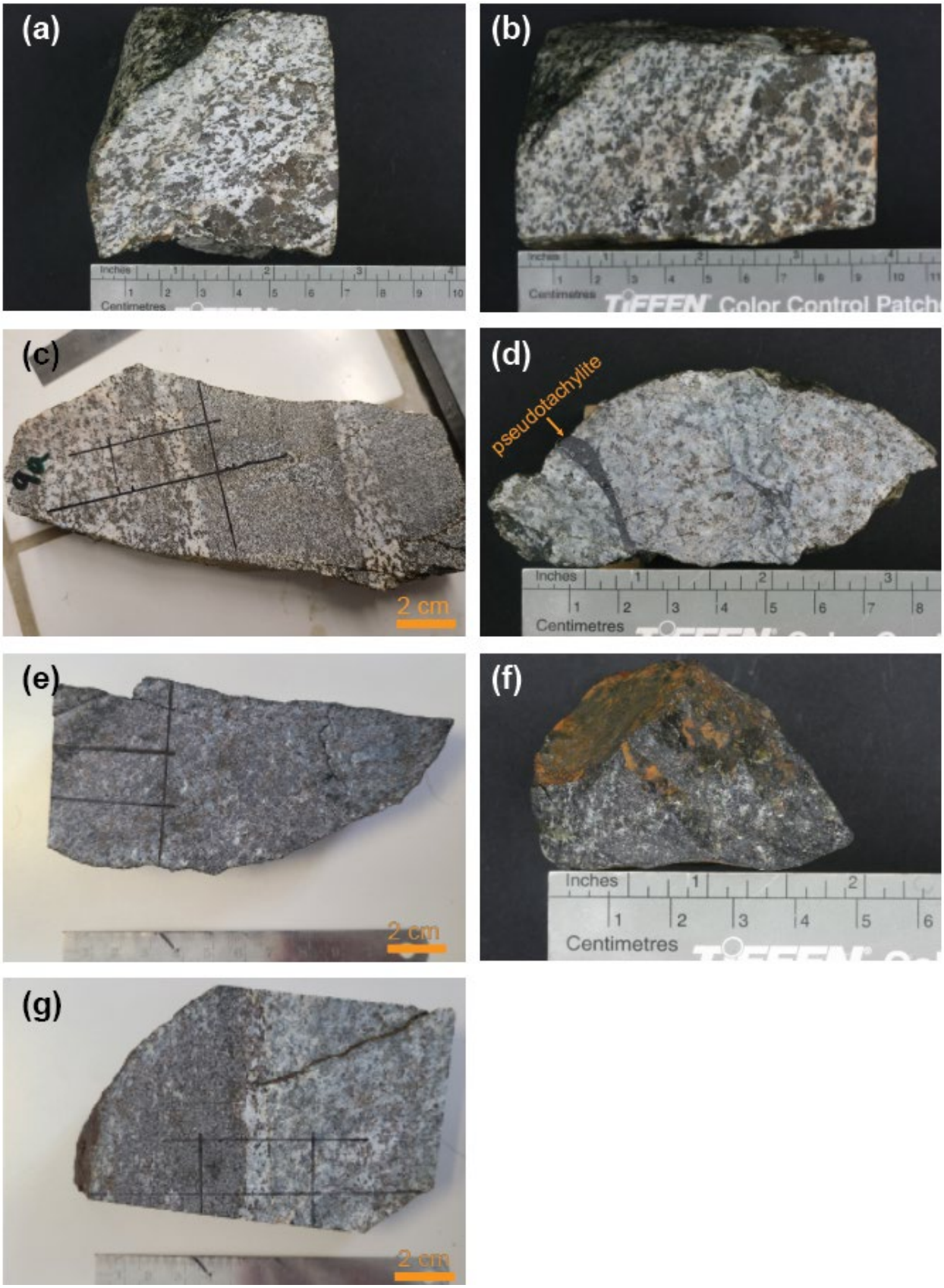
(a)
(b)
(c)
2 cm
(d)
pseudotachylite
(e)
2 cm
(f)
(g)
2 cm

Figure 19: Gabbroic rock ternary diagrams after Streckeisen (1976) for Saliceto olivine gabbros and pyroxenite. (a) Pyroxene-plagioclase-olivine ternary diagram showing normalized point counting values as red diamonds and the results of CIPW norm calculations as green triangles for each sample. Tie lines connect point counted and CIPW norm calculated points of each sample. (b) Modal mineralogy of Saliceto olivine gabbros and orthopyroxenite (AM-IVZ-VM008) plotted on pyroxene-plagioclase-amphibole (hornblende) ternary diagram. Px = pyroxenes; Ol = olivine; Pl = plagioclase; Hbl = hornblende.

(a)

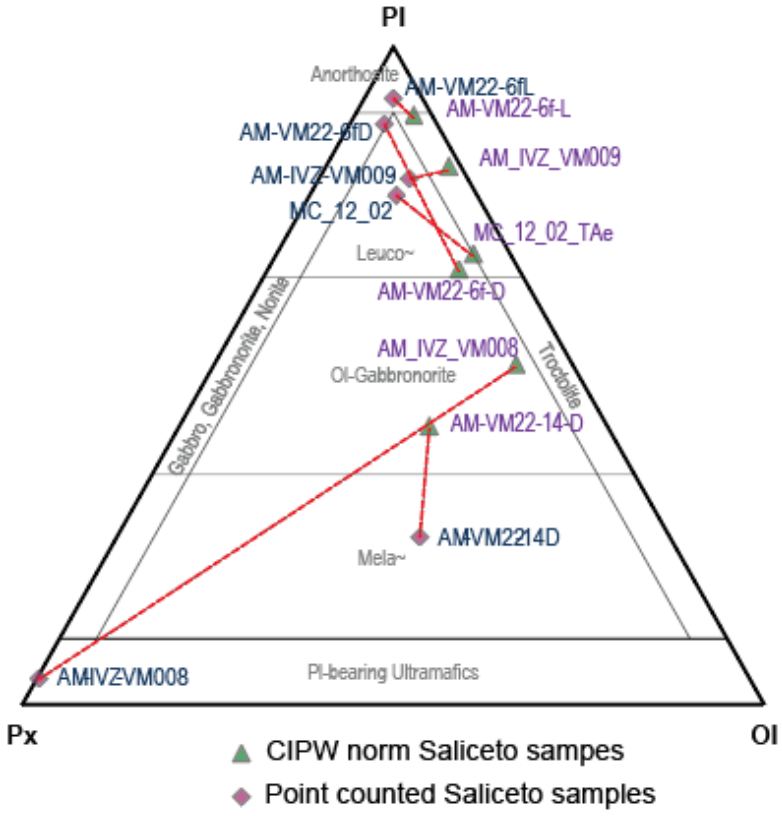
Pl
Anorthosite
AM-VM22-6fL
AM-VM22-6f-L
AM-VM22-6fD
AM_IVZ_VM009
AM-IVZ-VM009
MC_12_02
MC_12_02_TAe
Leuco~
AM-VM22-6f-D
AM_IVZ_VM008
Ol-Gabbronorite
Gabbro, Gabbronorite, Norite
Troctolite
AM-VM22-14-D
AM-VM2214D
Mela~
AM-IVZ-VM008
Pl-bearing Ultramafics
Px
Ol
CIPW norm Saliceto sampes
Point counted Saliceto samples

(b)

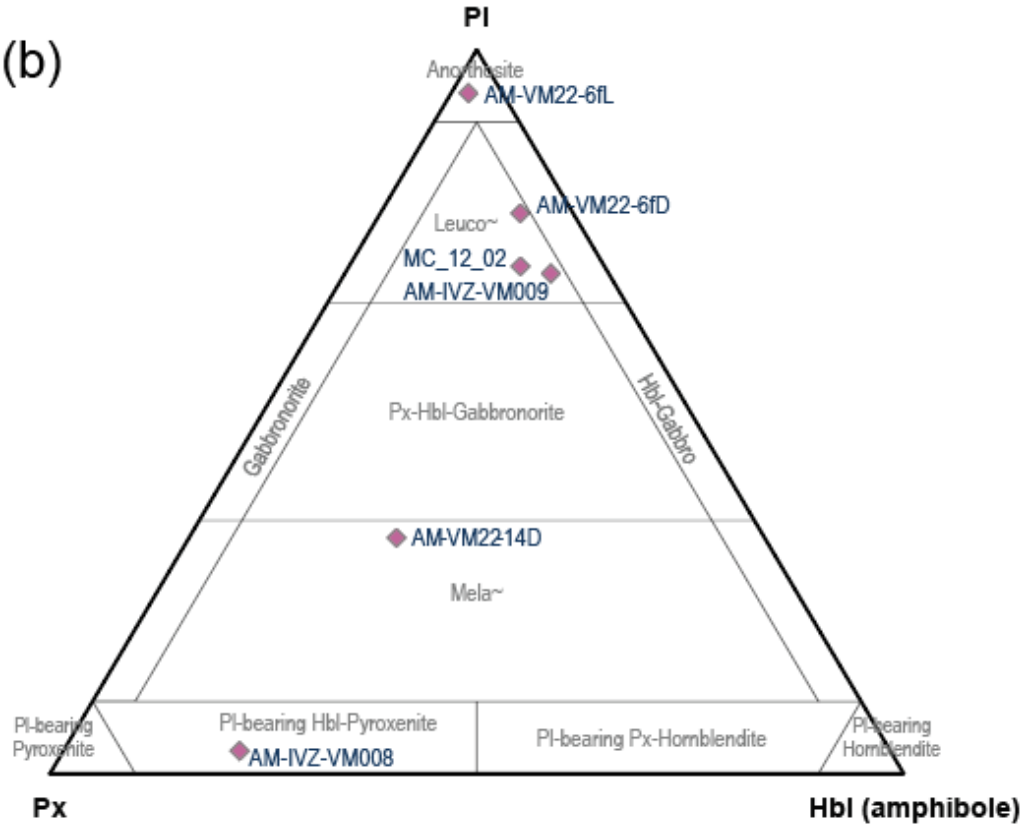
Pl
Anorthosite
AM-VM22-6fL
AM-VM22-6fD
Leuco~
MC_12_02
AM-IVZ-VM009
Gabbronorite
Px-Hbl-Gabbronorite
Hbl-Gabbro
AM-VM2214D
Mela~
Pl-bearing Pyroxenite
Pl-bearing Hbl-Pyroxenite
AM-IVZ-VM008
Pl-bearing Px-Hornblendite
Pl-bearing Hornblendite
Px
Hbl (amphibole)

Figure 20: Fine grained and coarse-grained banded gabbro-norite (AM-VM22-9a, 9a full thin section scan). Thin 30-µm thick section is not polished. Red scale bar is 0.5 mm in length. Note the increase in grain size and increase in plagioclase content in light bands. Oxides or opaque minerals (Opq) are abundant. The sample is from the base of the stratigraphic section at Saliceto outcrop (Figure 7).

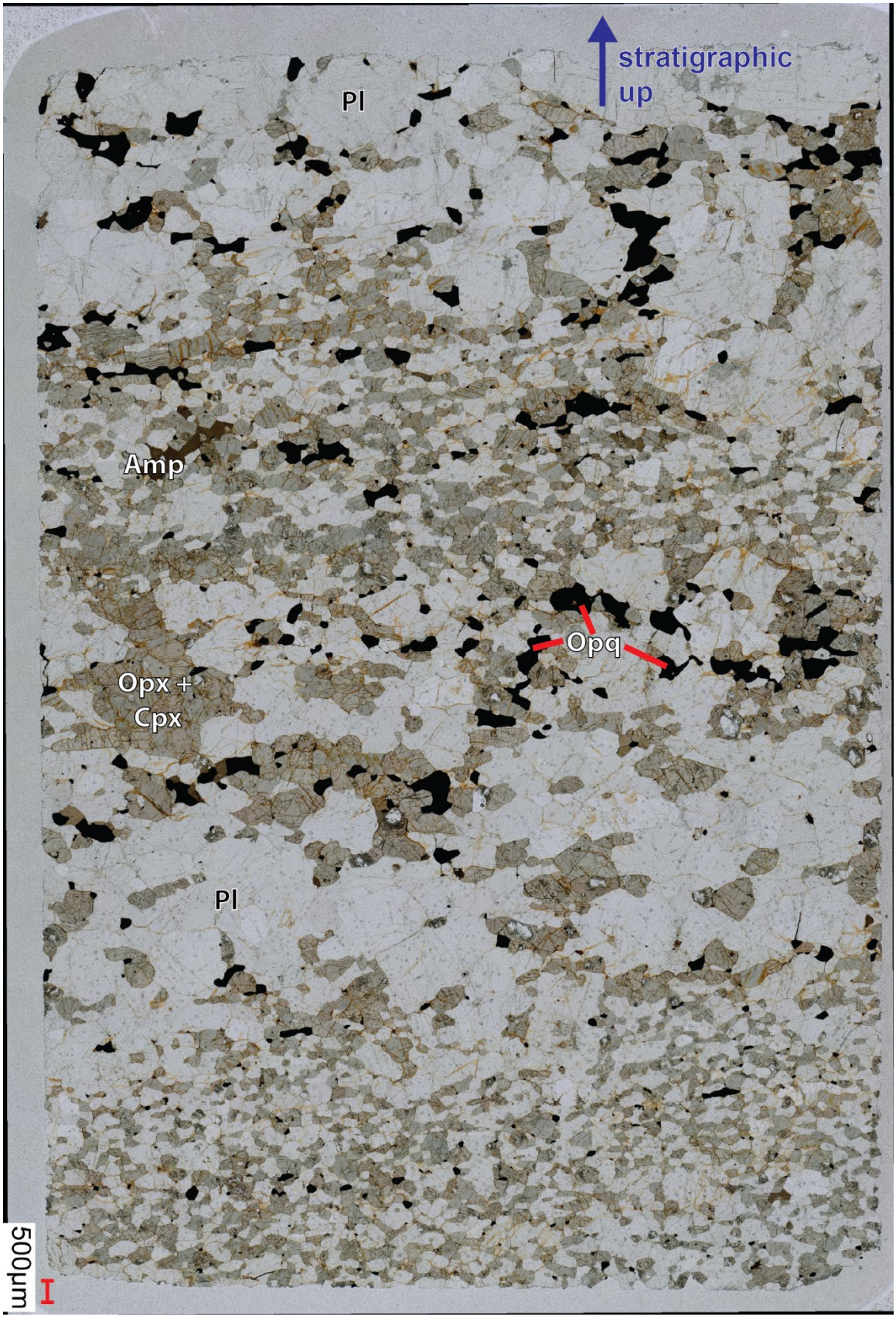
stratigraphic up
Pl
Amp
Opq
Opx + Cpx
Pl
500µm

Figure 21: Full thin section scan of gabbro-norite (AM-IVZ-VM001, thin section A1). The 50-μm thick and polished thin section contains plagioclase, orthopyroxene, clinopyroxene, and accessory minerals including biotite. Neither ilmenite nor apatite were seen in this thin section.

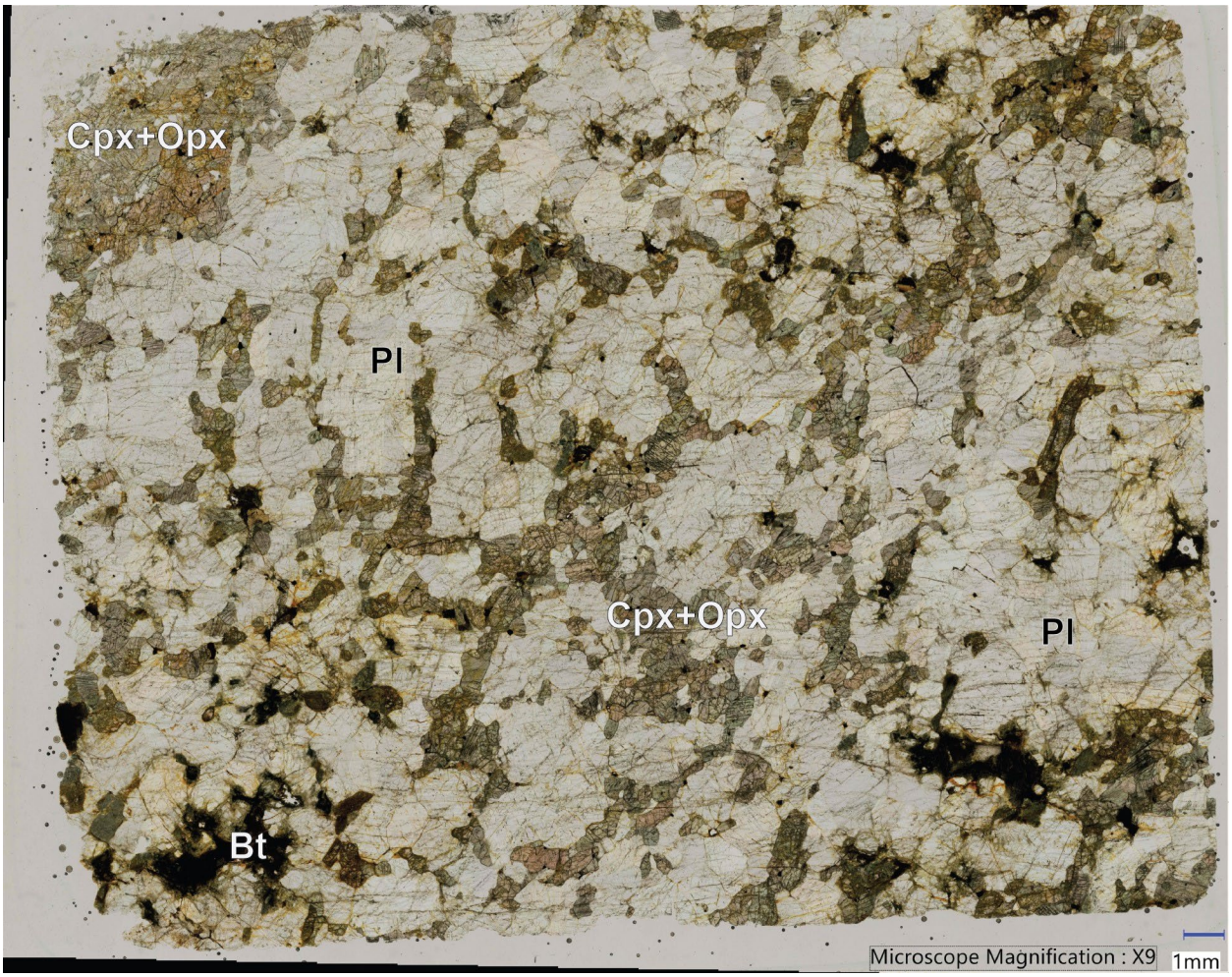
Cpx+Opx
Pl
Cpx+Opx
Pl
Bt
Microscope Magnification : X9
1mm

Figure 22: Fe-Ti oxide-bearing gabbro-norite (AM-IVZ-VM017, thin section A17). (a) Full thin section scan captures vein of amphibole. Note the overall banding and containment of amphibole to the band only. b) Closer view of large, poikilitic subhedral amphibole grain. Prg = pargasite.

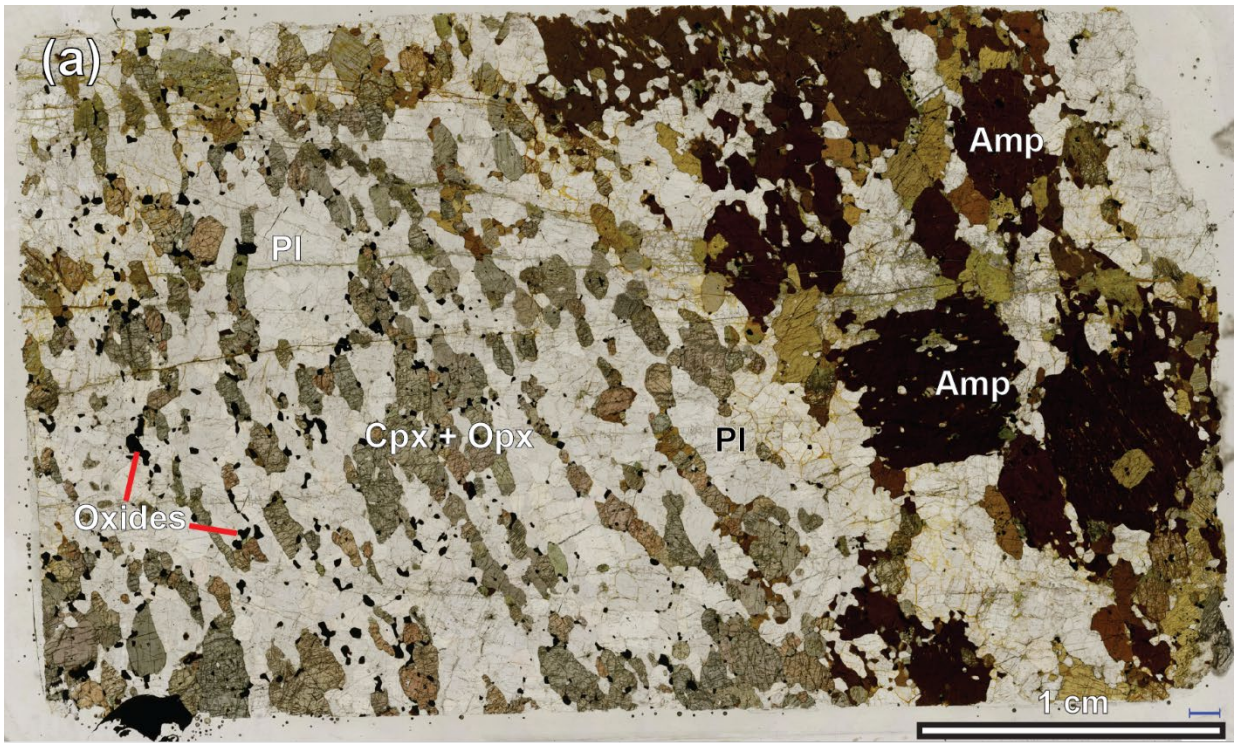
(a)
Amp
Pl
Amp
Cpx + Opx
Pl
Oxides
1 cm

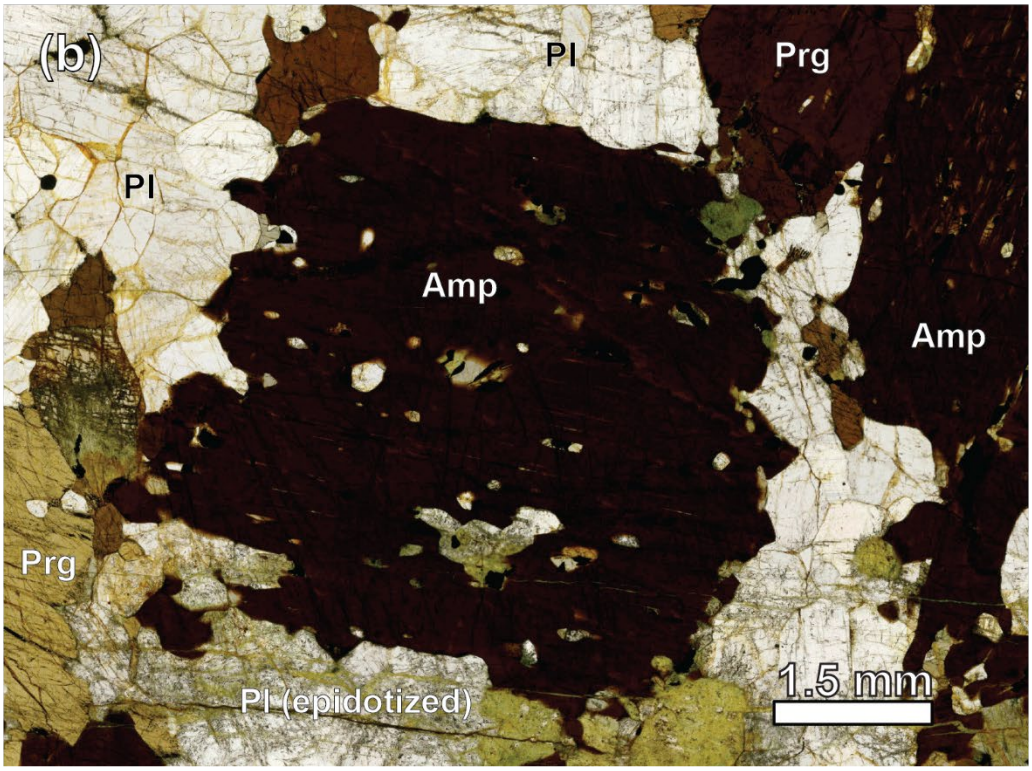
(b)
Pl
Prg
Pl
Amp
Amp
Prg
Pl (epidotized)
1.5 mm

Figure 23: Full thin section scans of (a) amphibole norite (AM-IVZ-VM013, thin section A13) and (b) garnet amphibole gabbro-norite (AM-IVZ-VM004, thin section A4). Minerals in the amphibole norite appear black are amphibole and minor oxide minerals. Plagioclase is dominant in the garnet amphibole gabbro-norite. Cumulus orthopyroxene is commonly separated from plagioclase by clinopyroxene coronas, amphibole coronas and lastly garnet coronas, but orthopyroxene – plagioclase boundaries with no corona are present. Note the greenish band of chlorite minerals in a fracture.

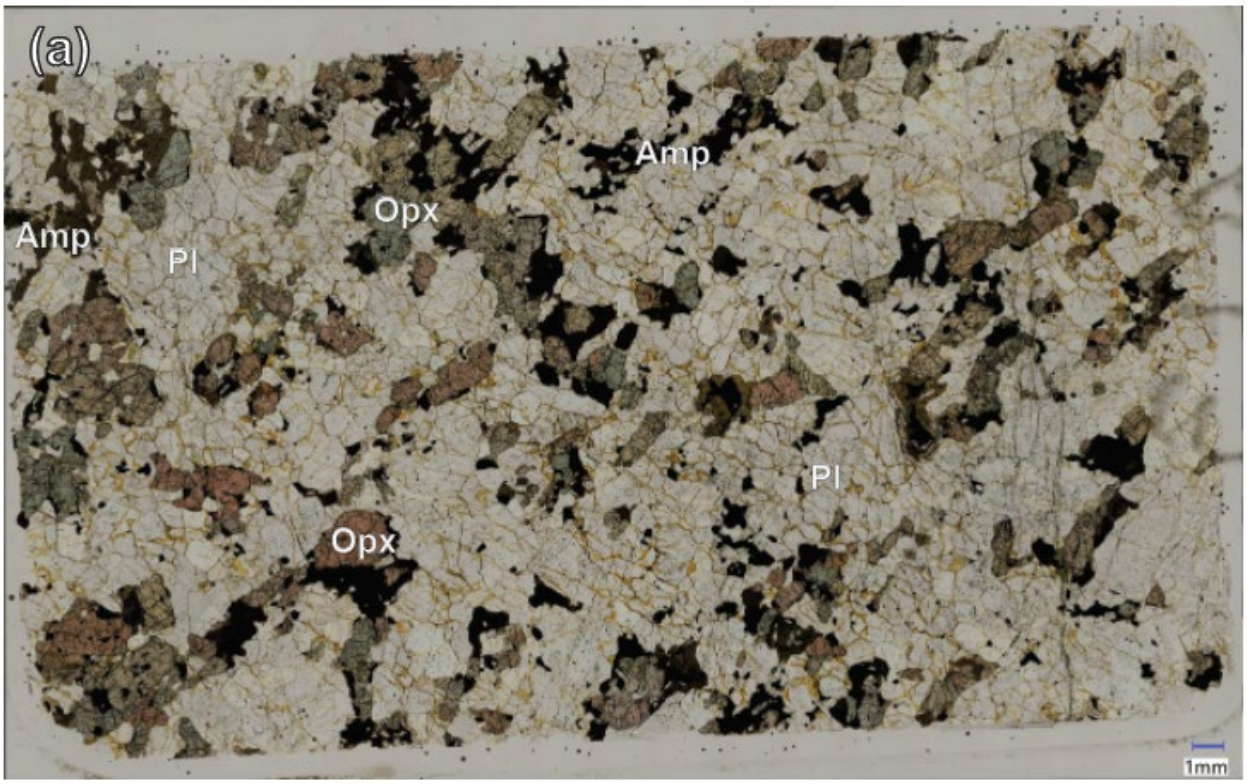
(a)
Amp
Pl
Opx
Amp
Pl
Opx
1mm

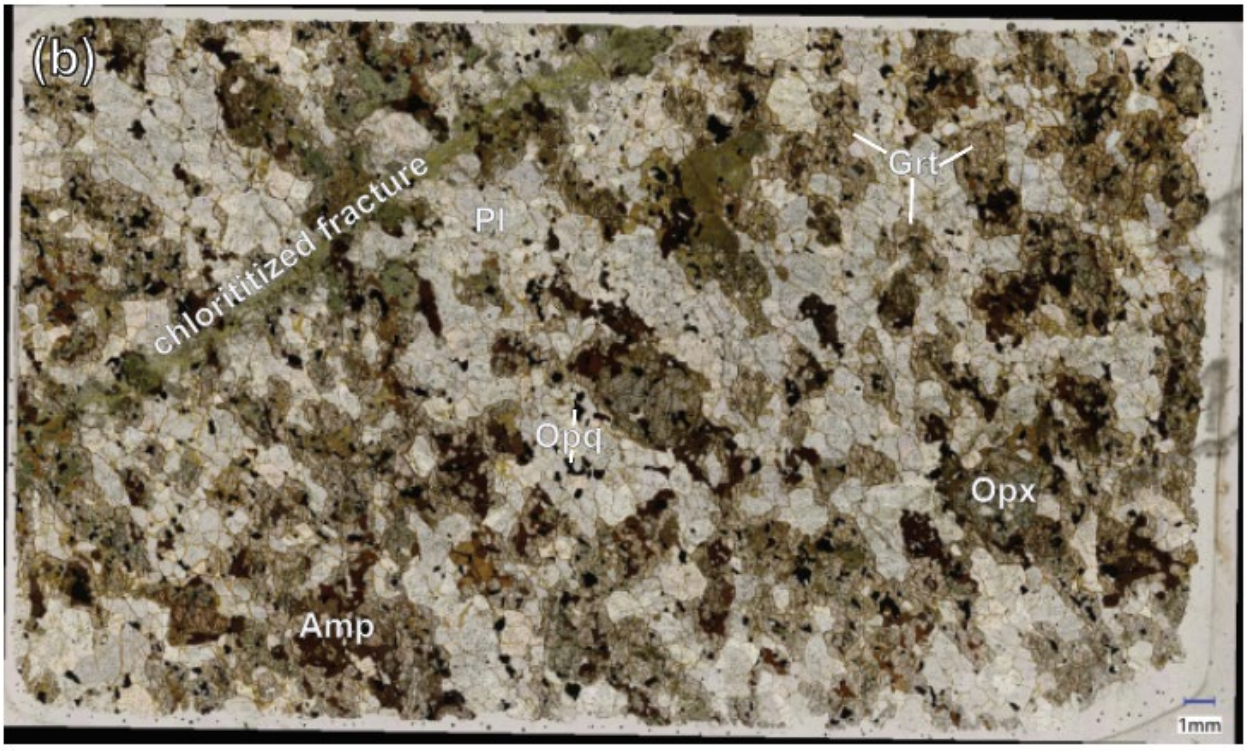
(b)
chlorititized fracture
Pl
Grt
Opq
Opx
Amp
1mm

Figure 24: Garnet amphibole mela-norite (AM-IVZ-VM011 full thin section scan) containing 6 vol.% plagioclase, 26 vol.% garnet, 26 vol.% pyroxene, 25 vol.% amphibole, 12 vol.% opaque minerals, and 5 vol.% apatite. Coronitic reactions have replaced much of the primary magmatic mineralogy (plagioclase + orthopyroxene). Pervasive orthopyroxene + vemicular magnetite intergrowths are surrounded or replaced by amphibole and garnet. This rock displays the most extensive growth of garnet and symplectites.

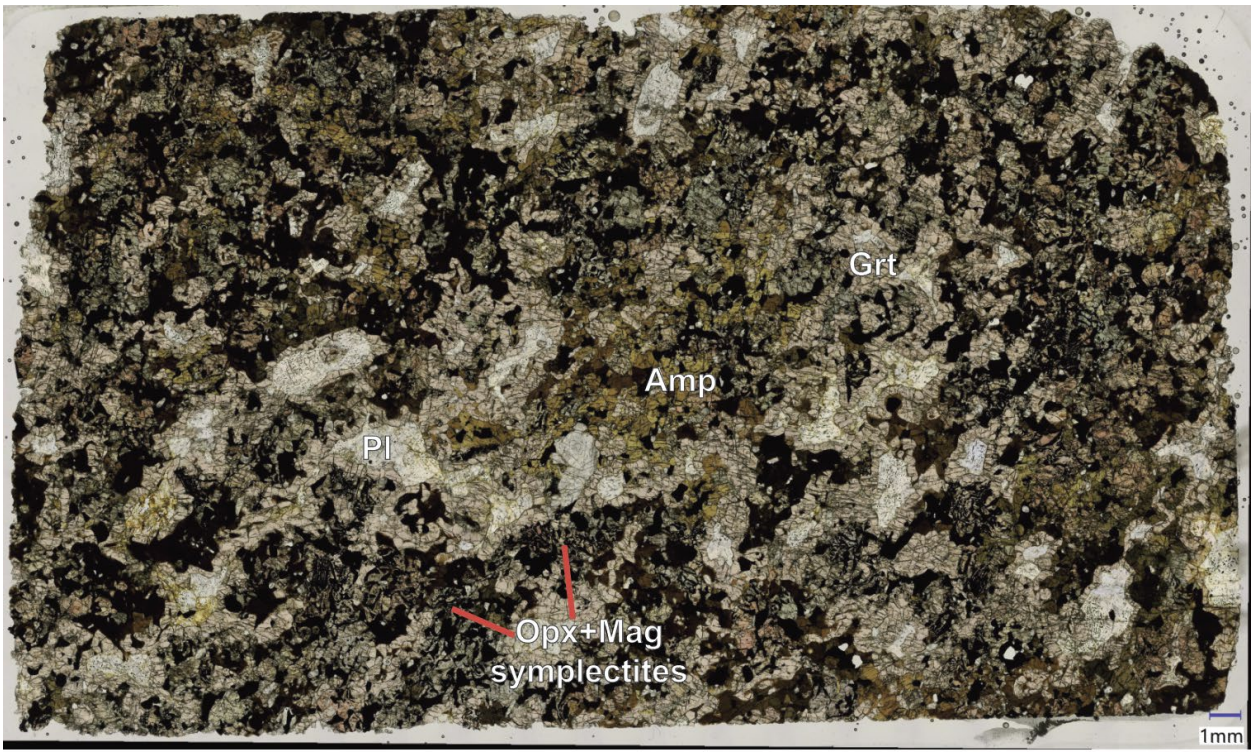
Grt
Amp
Pl
Opx+Mag
symplectites
1mm

Figure 25: General petrographic characteristics of garnet-free gabbronorite (AM-IVZ-VM016, thin section A16) and gabbro-norite (AM-IVZ-VM017, thin section A17). (a) Plane-polarized photomicrograph of subhedral orthopyroxene and clinopyroxene, and in places, clinopyroxene forming a corona around orthopyroxene. Note the brown ilmenite exsolutions in orthopyroxene (white ellipse). (b) Photomicrograph in cross-polarized light showing subhedral pyroxenes, plagioclase and minor oxides, apatite, and sulfides, amphibole in gabbro-norite. Note evidence of recrystallization shown best by plagioclase and apatite. Orthopyroxene in top right of photomicrograph shows kink deformation. Here the “Oxides” label indicates a complex oxyexsolution of ilmenite, magnetite, and Fe-Mg-spinel. Pyrrhotite and pentlandite are contained in the same rounded grain.

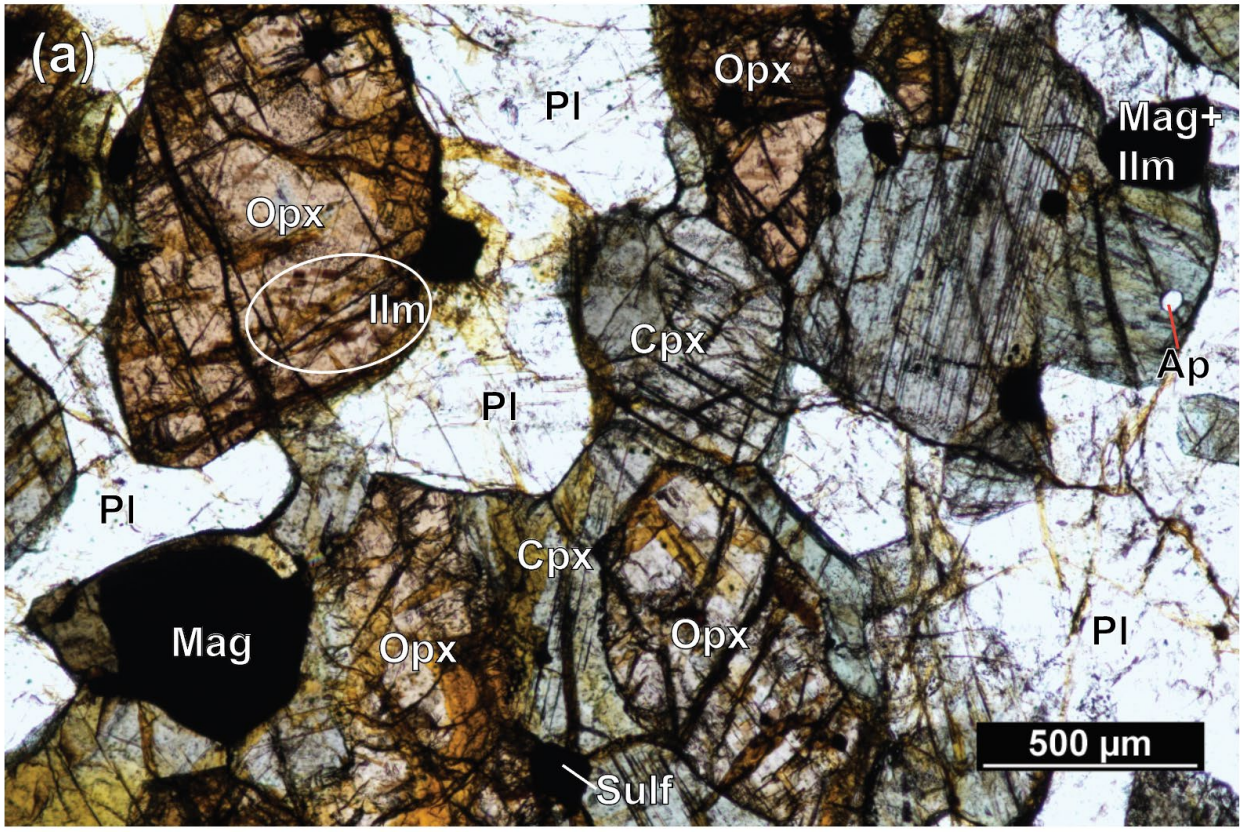
(a)
Opx
Pl
Mag+
Ilm
Opx
Ilm
Cpx
Ap
Pl
Pl
Cpx
Mag
Opx
Opx
Pl
500 µm
Sulf

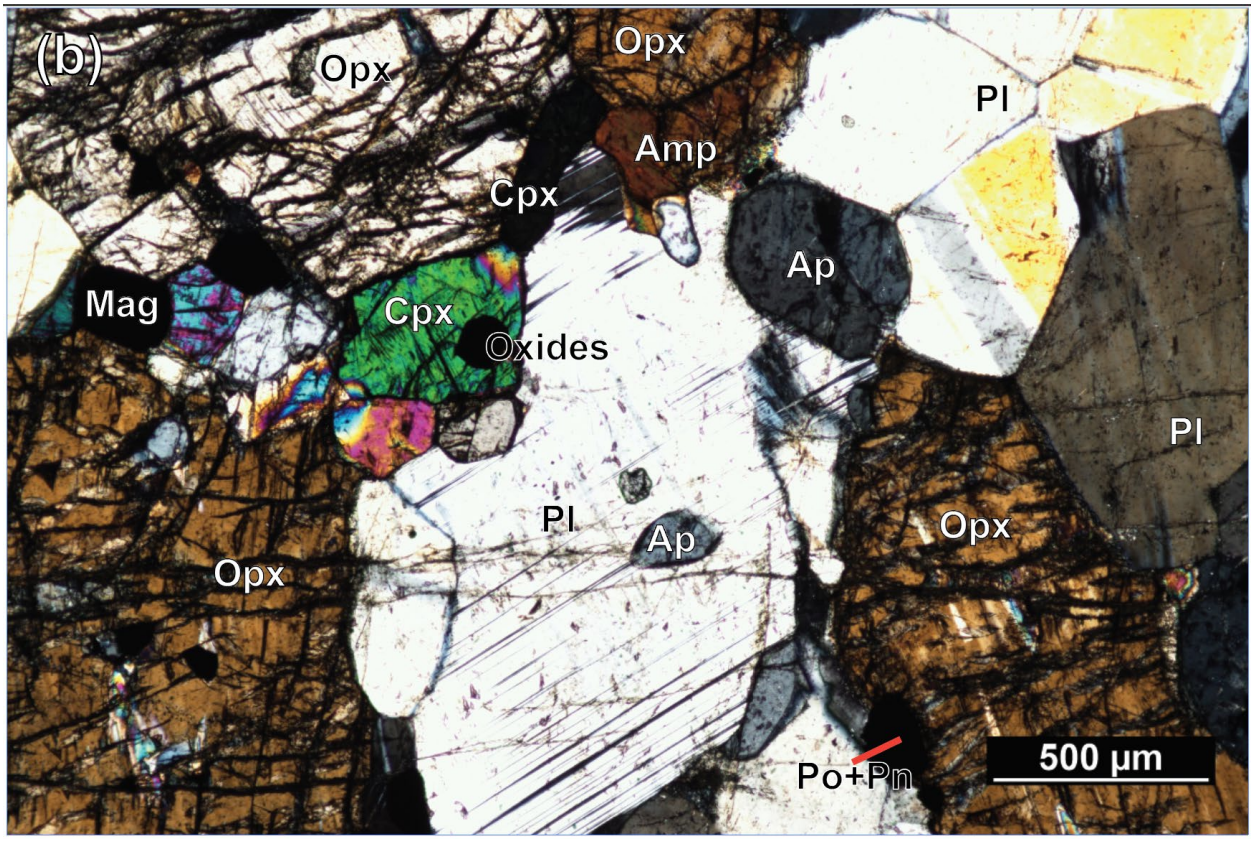
(b)
Opx
Opx
Pl
Amp
Cpx
Ap
Mag
Cpx
Oxides
Pl
Pl
Ap
Opx
Opx
Po+Pn
500 µm

Figure 26: Full thin section scans of garnet amphibole olivine gabbro (AM-IVZ-VM009, thin section A9) and garnet olivine gabbro from the Rio della Scaravina gully outcrop (AM-VM22-14, thin section 14a1[D]). (a) Note the mineralogical banding of mafic-dominated to plagioclase-dominant zones. Olivine is separated by coronas of orthopyroxene, clinopyroxene, amphibole, and garnet. Plagioclase contains green spinel (hercynite) inclusions. (b) Contact of melanocratic and mesocratic portions as shown in Figure 18g, but the adjacent thin section (14a2) does contain the same mineralogy yet higher plagioclase abundance. Note the extensive pyroxene and garnet coronas and the high modal abundance of olivine, and the relatively lower amphibole abundance compared to the scan of the previous sample.

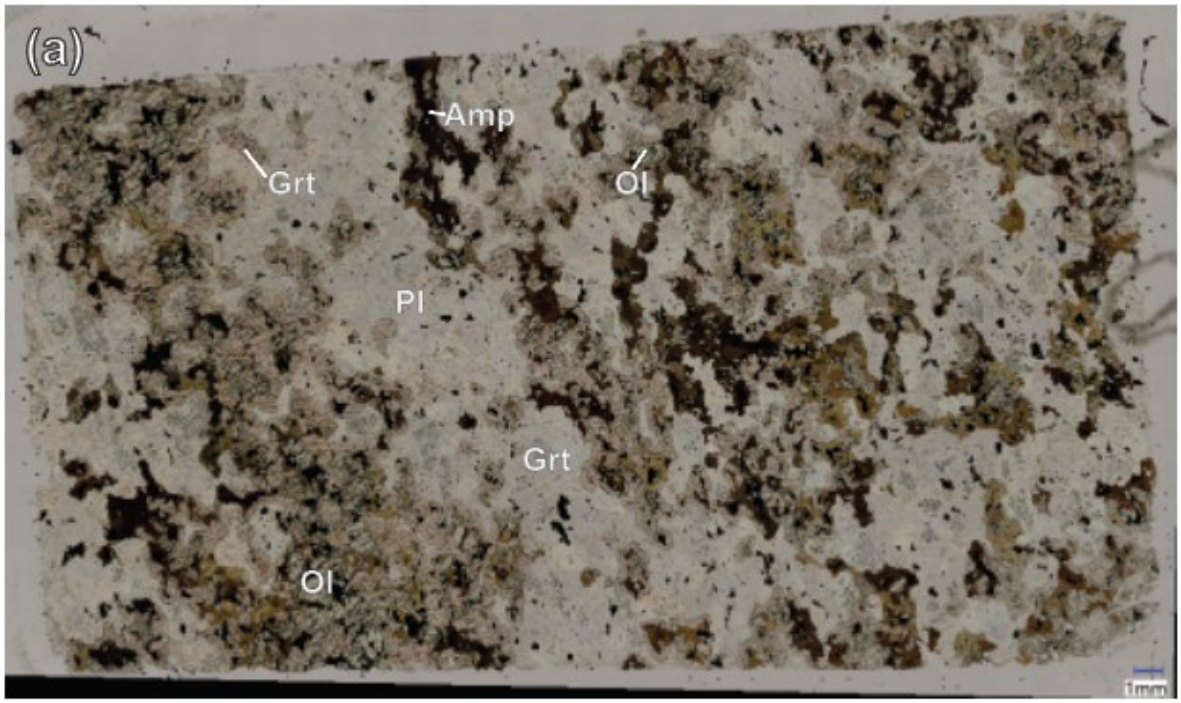
(a)
Amp
Grt
Ol
Pl
Grt
Ol
1mm

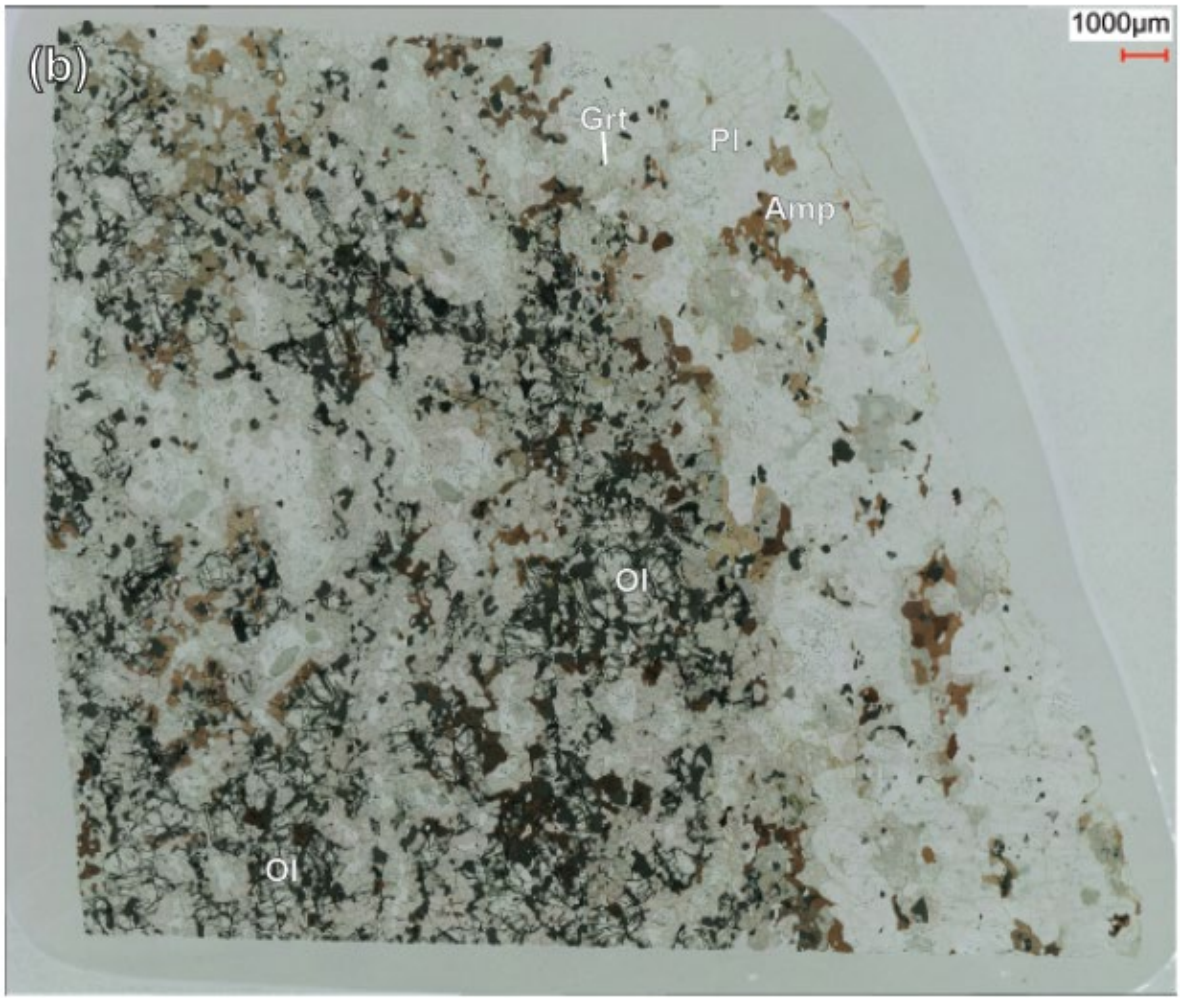
(b)
1000μm
Grt
Pl
Amp
Ol
Ol

Figure 27: General petrographic characteristics of olivine gabbros (AM-IVZ-VM009, thin section A9; and thin section A14, sample Sal-L). (a) Olivine with pyroxene and garnet coronas. Note the corona of clinopyroxene surrounding orthopyroxene. (b) Skeletal olivine with coronas of clinopyroxene and amphibole (Prg = pargasite).

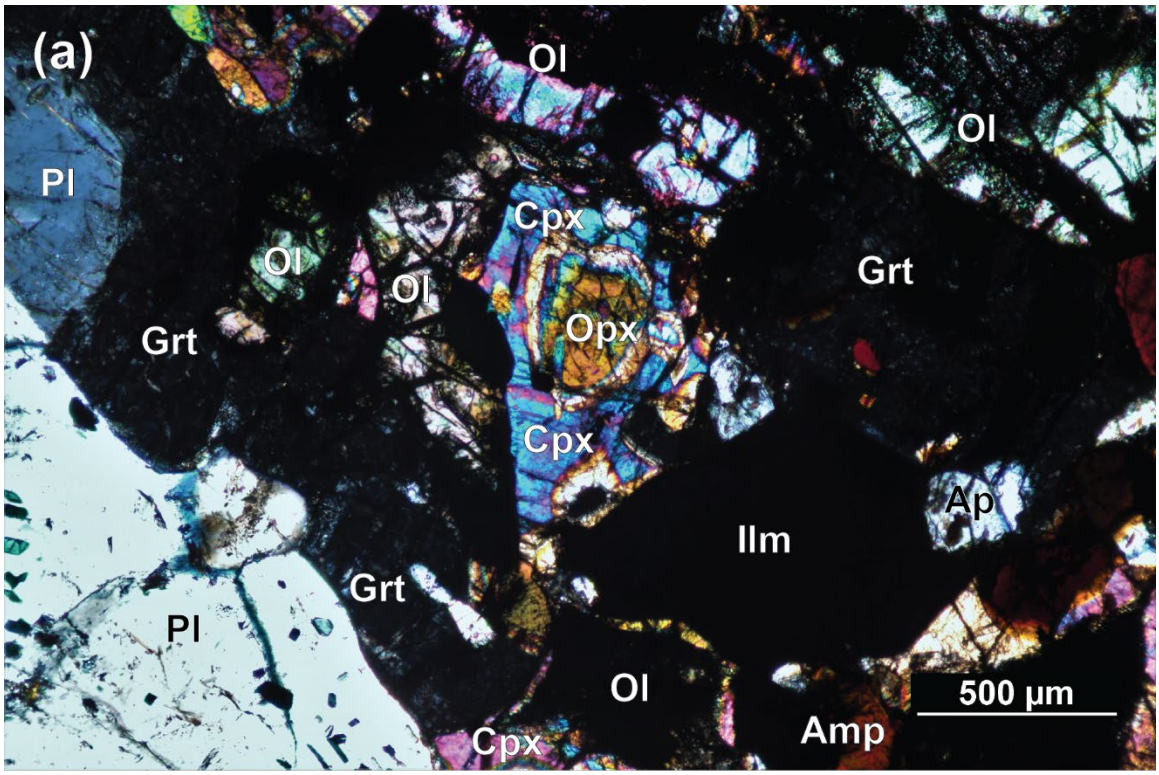
(a)
Ol
Ol
Pl
Cpx
Ol
Grt
Ol
Grt
Opx
Cpx
Ap
Ilm
Grt
Pl
Ol
500 µm
Cpx
Amp

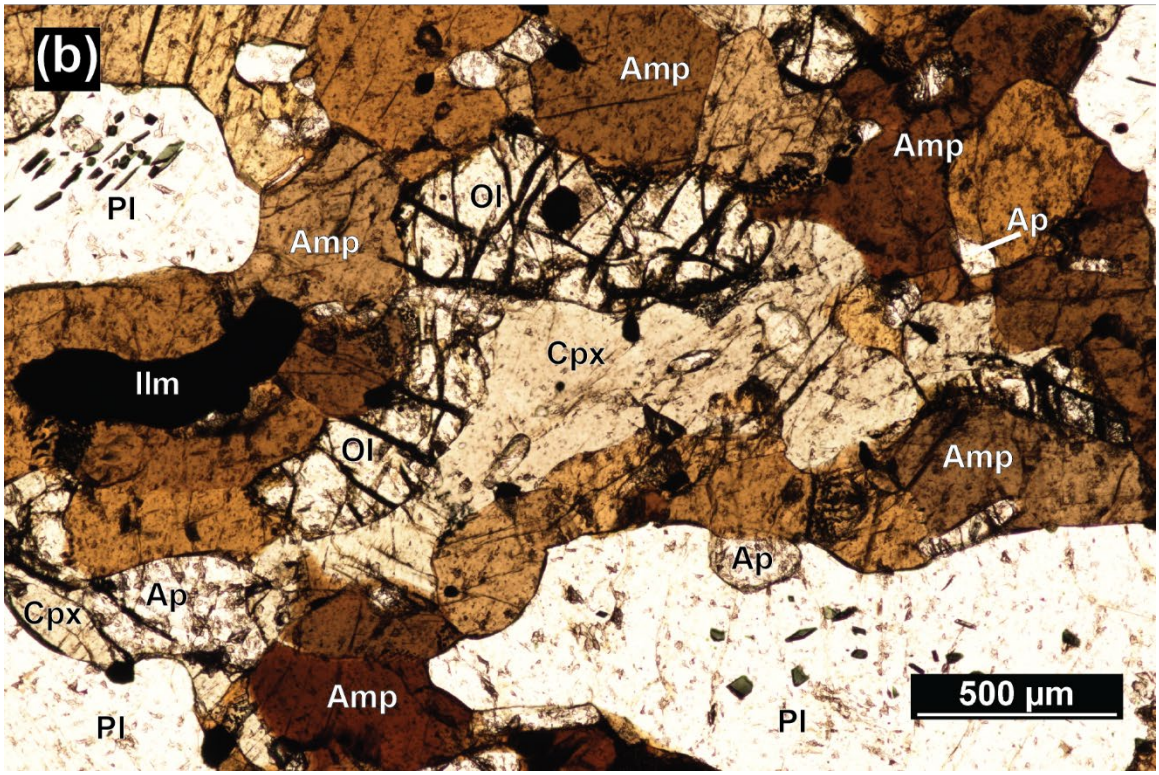
(b)
Amp
Amp
Pl
Ol
Ap
Amp
Cpx
Ilm
Ol
Amp
Ap
Cpx
Ap
Amp
500 µm
Pl
Pl

Figure 28: Pyroxenite thin section scan in plane-polarized light (AM-IVZ-VM008, thin section B3) composed primarily of anhedral embayed orthopyroxene. Amphibole that appears dark to brown appears to be a single oikocryst based on optical continuity. Inset is the same thin section scanned in cross-polarized light, highlighting the optical continuity of the large orthopyroxene grains.

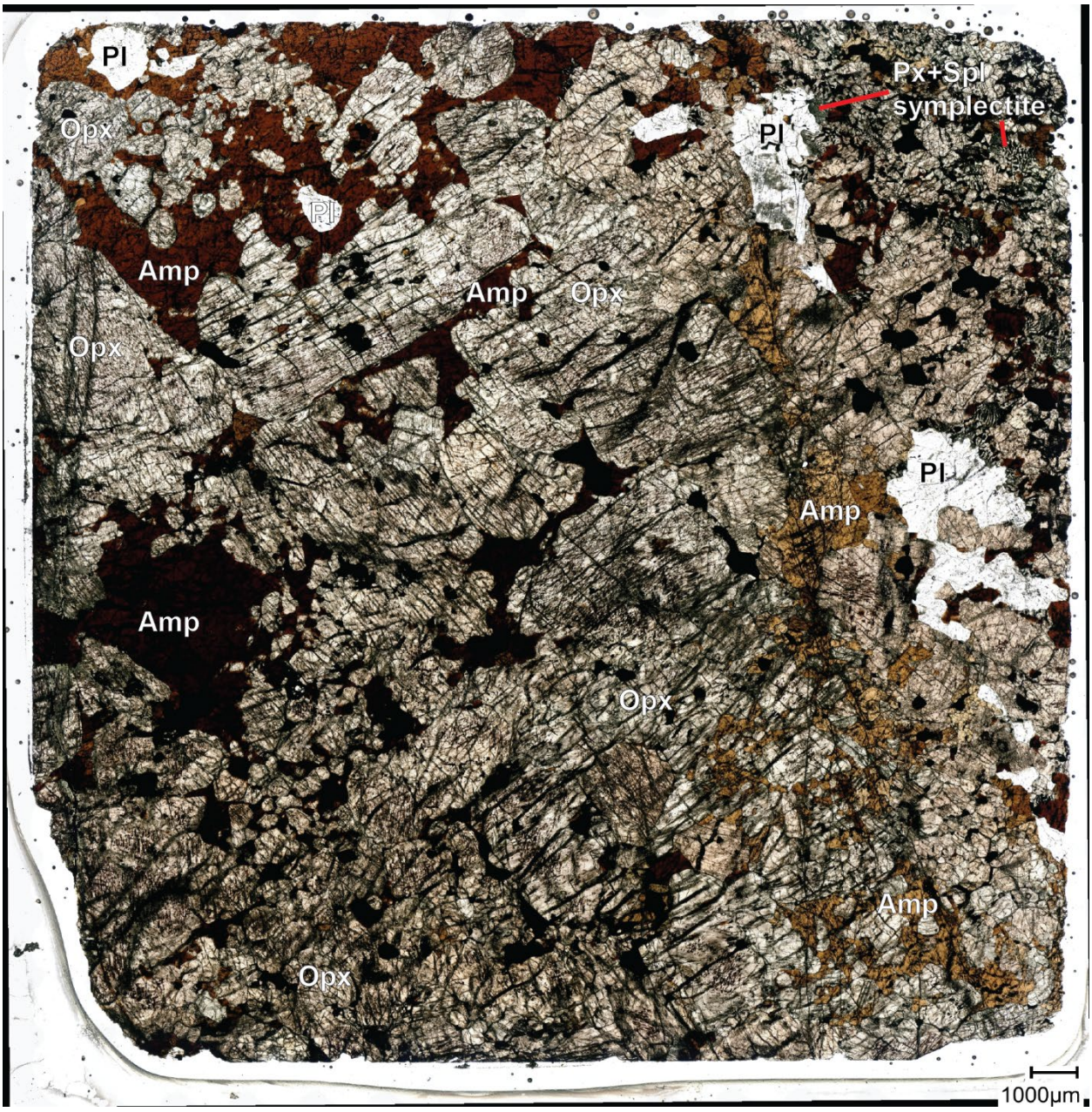
Pl
Opx
Pl
Amp
Amp
Opx
Opx
Px+Spl
symplectite
Pl
Pl
Amp
Amp
Opx
Amp
Opx
1000μm

Figure 29: Full thin section scan of pyroxenite (AM-IVZ-VM008, thin section B5) capturing plagioclase vein cross-cutting the pyroxenite as seen in hand sample (Figure 15f). Note the epidotization of plagioclase and Al-spinel clouded plagioclase. In this portion of this pyroxenite sample, medium-grained olivine and Fe-Ti oxides are abundant.


Pl
Opx+Spl symplectite
Cpx
Pl
Ep
Opx
Ol
Amp
1000um

Figure 30: Plagioclase orientation fabric in olivine gabbro. Full thin section scan in XPL of thin section 6c, sample AM-VM22-6c. Yellow bars indicate the orientation of twinning in plagioclase grains and the length of these twins, the (010) crystallographic plane, as intersected by the thin section.

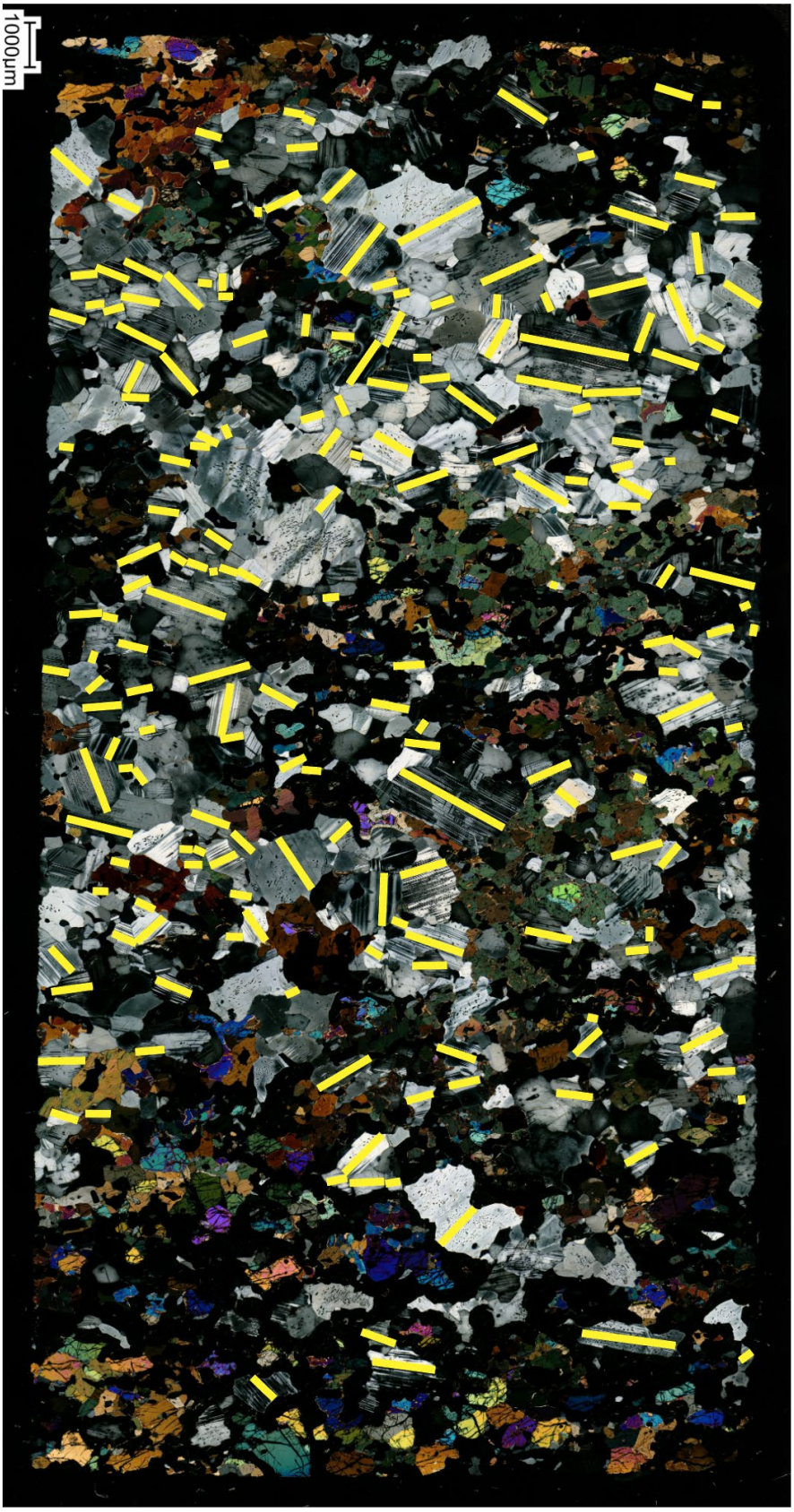
1000µm

Figure 31: Euhedral apatite inclusions in ilmenite in pyroxenite, thin section B21. Reflected light photomicrograph.

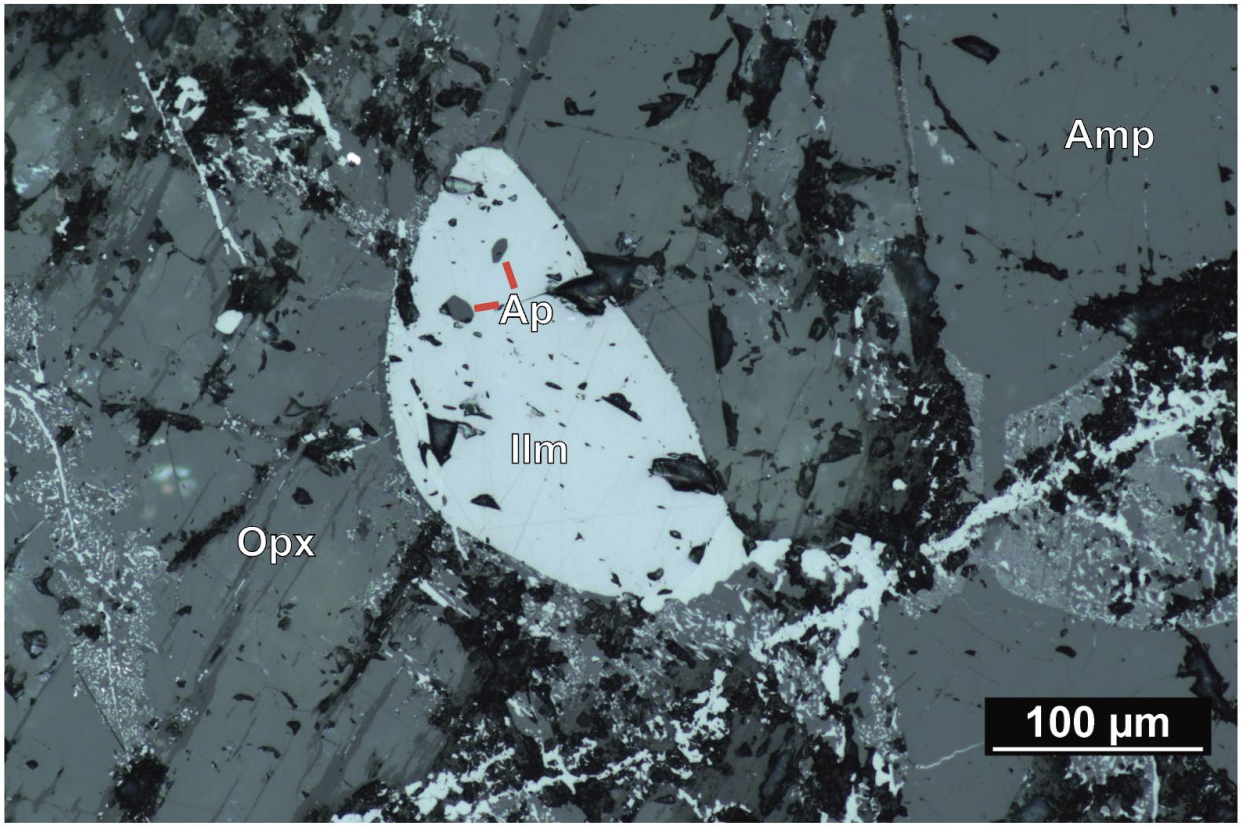
Amp
Ap
Ilm
Opx
100 µm

Figure 32: Oxide mineral microstructures. (a) Complex oxy-exsolution in gabbro-norite (AM-IVZ-VM017, thin section A17). Note the domains of magnetite at the exterior of the grain and ilmenite with hercynite and corundum exsolutions. Hercynite and corundum exsolutions appear to form in planes, some of which parallel the ilmenite-magnetite boundaries. Pyrite is irregular and altered. (b) Oxy-exsolution in of ilmenite, magnetite, Al-spinel (Hc) with an orthopyroxene corona in pyroxenite (sample AM-IVZ-VM008, thin section B5). The two primary domains appear to be ilmenite and magnetite. Aluminum spinel is found as exsolutions in the ilmenite near the ilmenite-magnetite boundary, but it is also found as a line that is in line with brittle fractures that crosscut both the ilmenite and magnetite domains.

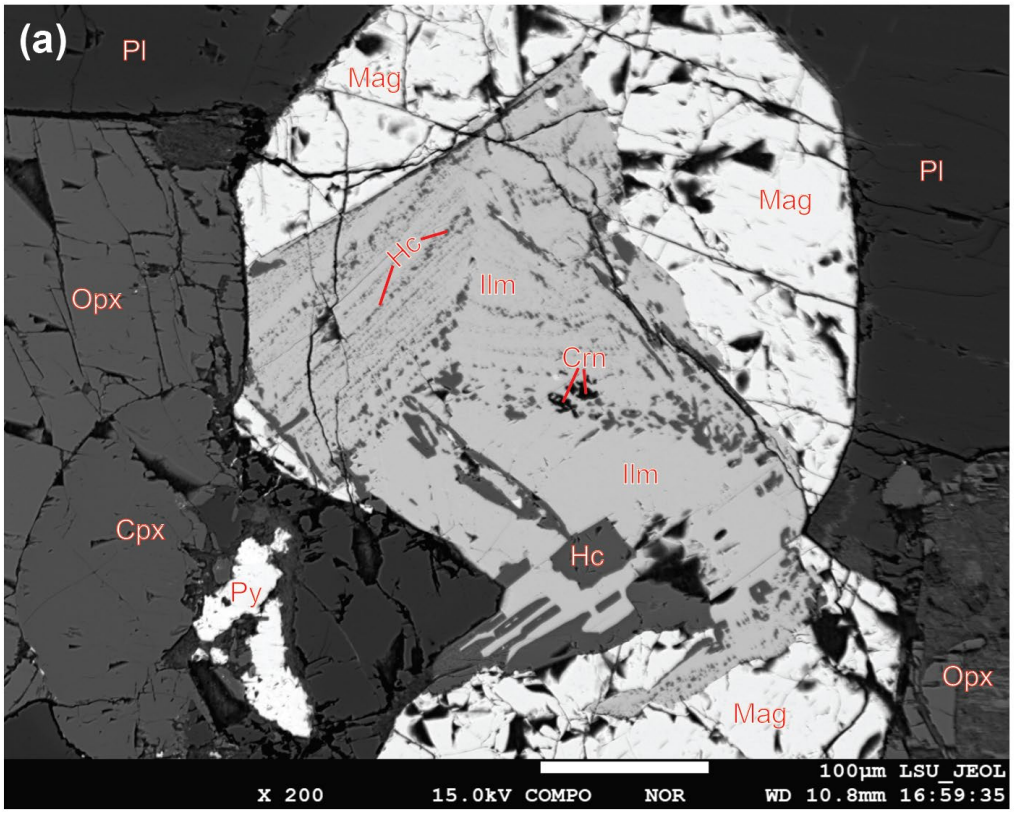
(a)
Pl
Mag
Pl
Mag
Hc
Ilm
Opx
Crn
Ilm
Cpx
Hc
Py
Opx
Mag
100µm LSU_JEOL
X 200
15.0kV COMPO
NOR
WD 10.8mm 16:59:35

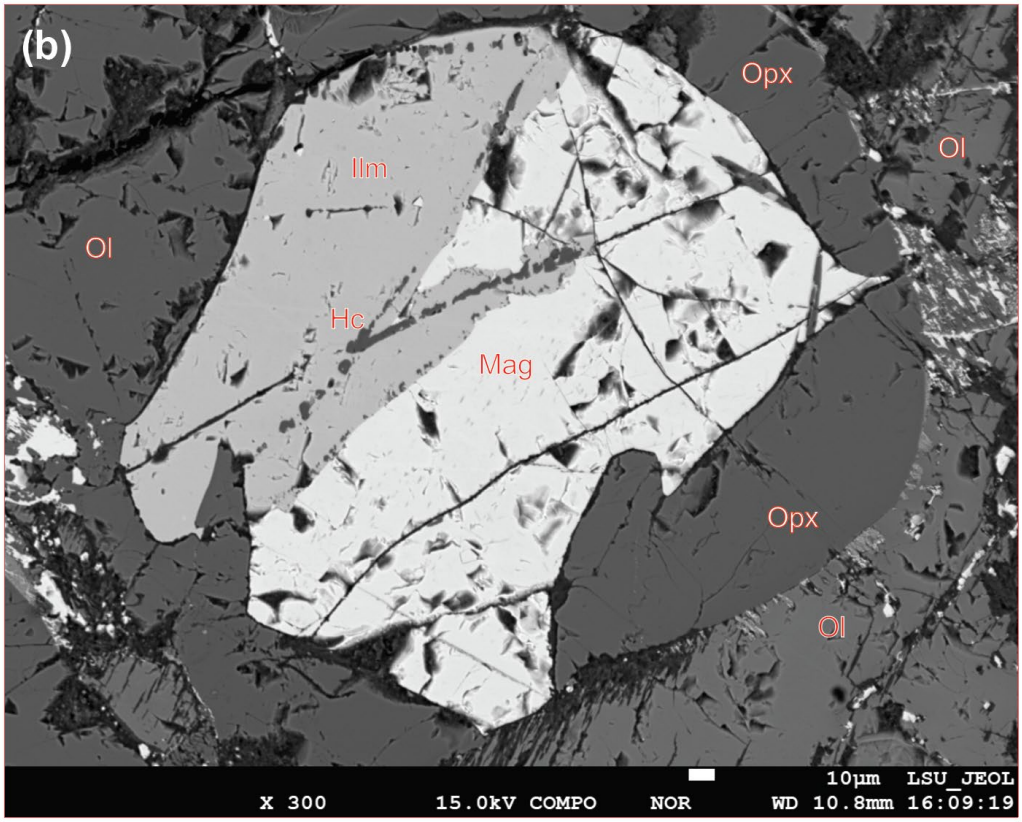
(b)
Opx
Ol
Ilm
Ol
Hc
Mag
Opx
Ol
10µm LSU_JEOL
X 300
15.0kV COMPO
NOR
WD 10.8mm 16:09:19

Figure 33: Microstructural characteristics of amphibole oikocrysts in gabbro-norite (AM-IVZ-VM017, thin section A17). Euhedral amphibole grain (chadacryst or “guest”) is fully enclosed in poikilitic amphibole in the rock. (a) Plane-polarized microphotograph showing that the two pargasites are not in optical continuity, and both contain annealed microfractures with opaque (oxide) infilling. (b) BSE image of same location as previous photomicrograph but different orientation. Exsolutions of clinopyroxene are pervasive throughout the poikilitic pargasite. Note the variety of chadacrysts and exsolutions in both grains. Note the thin line of oxide minerals at the contact of the central pargasite grain and the enclosing (oikocryst) amphibole grain.

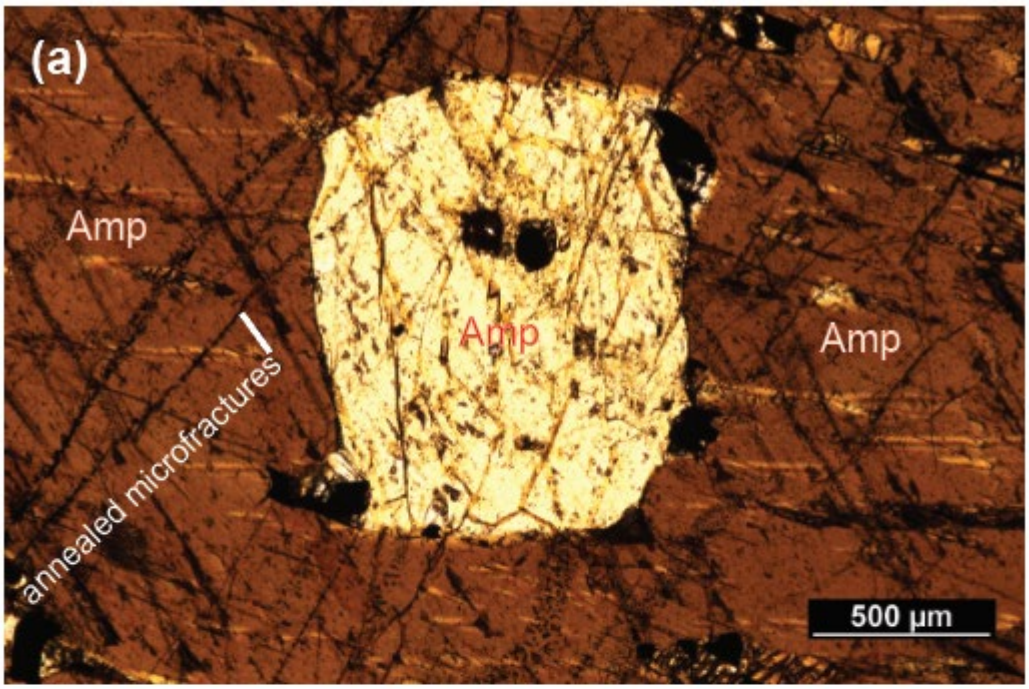
(a)
Amp
Amp
Amp
annealed microfractures
500 µm

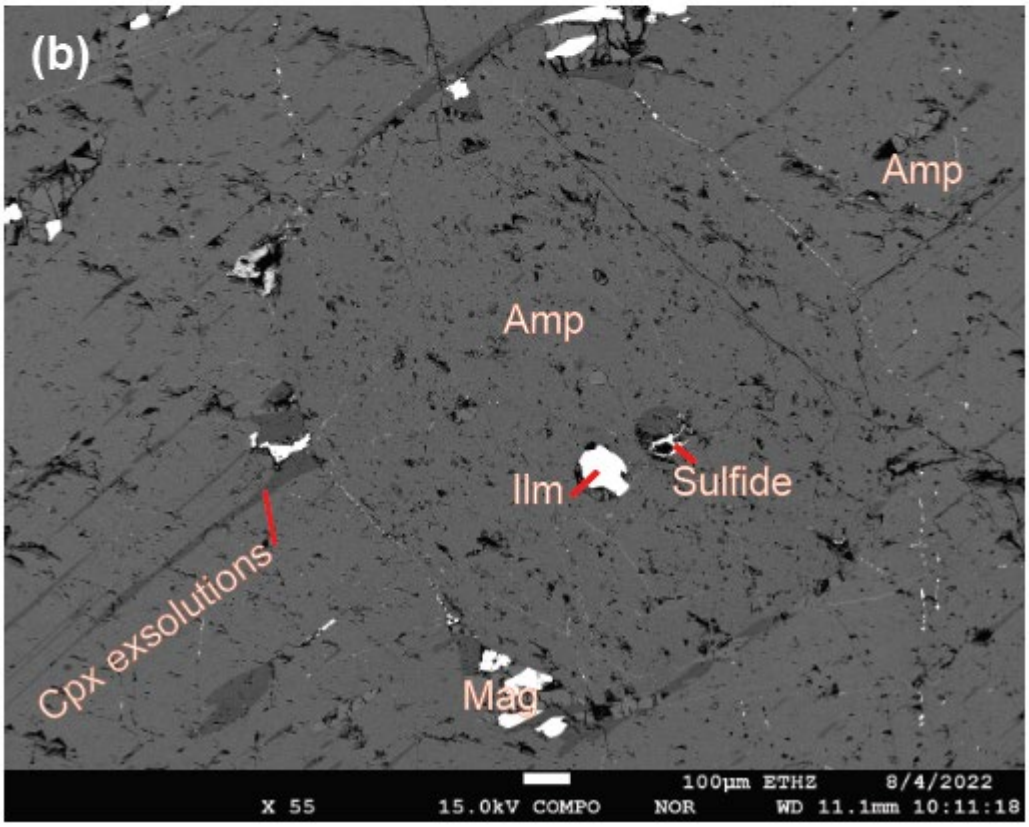
(b)
Amp
Amp
Ilm
Sulfide
Cpx exsolutions
Mag
100µm ETHZ
8/4/2022
X 55
15.0kV COMPO
NOR
WD 11.1mm 10:11:18

Figure 34: Magmatic, peritectic reactions in pyroxenite. Subhedral, rounded olivine is surrounded by magnetite, ilmenite, and orthopyroxene in pyroxenite (sample AM-IVZ-VM008, thin section B20) observed under reflected light. Olivine is altered, as shown by the darker mottling. Magnetite has trellis-like ilmenite exsolutions. Olivine grain in center has a magnetite-filled fracture.

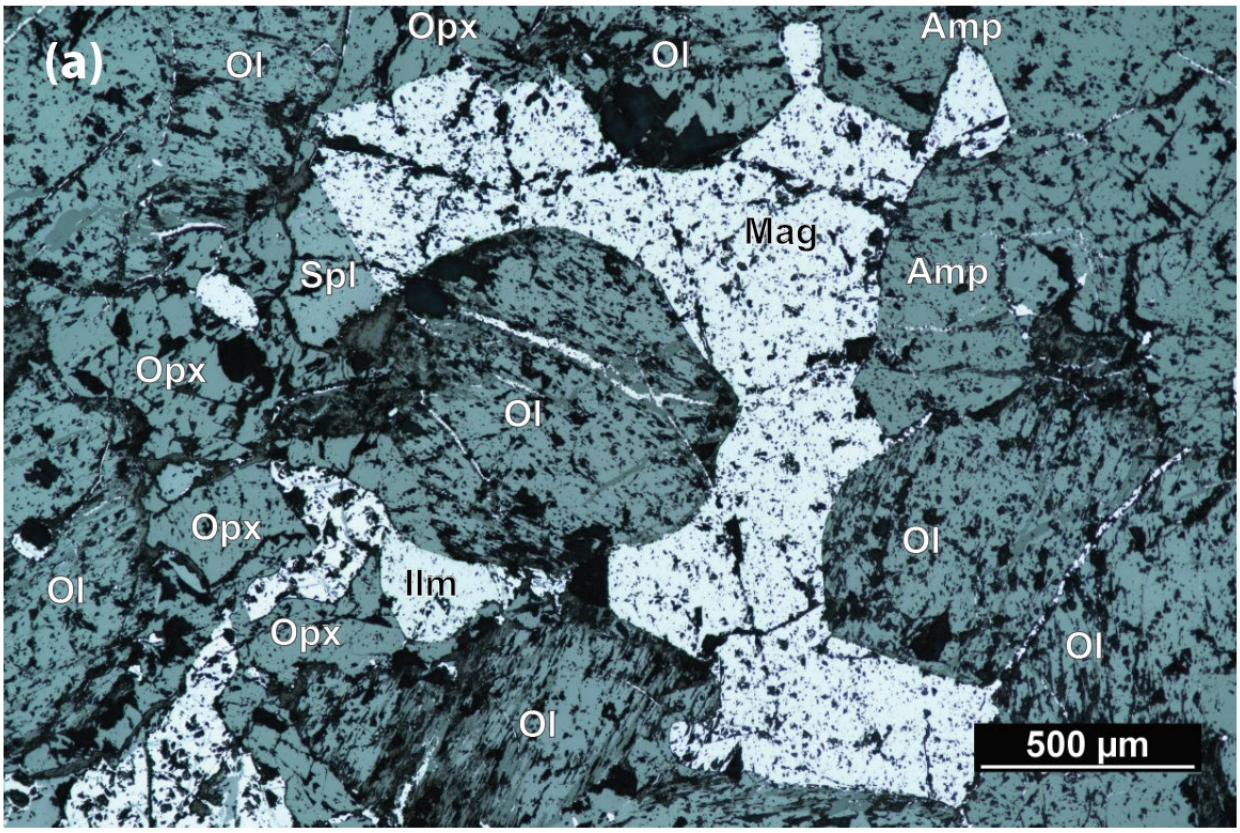
(a)
Ol
Opx
Ol
Amp
Mag
Spl
Amp
Opx
Ol
Opx
Ol
Ilm
Opx
Ol
Ol
Ol
500 µm

Figure 35: Pyroxenite petrography. (a) rounded orthopyroxene grains are surrounded by coronitic to poikilitic amphibole. Note the brownish rutile (Rt) exsolutions found at the cores of some orthopyroxene grains. (b) symplectites of clinopyroxene + Al spinel (Hc) and orthopyroxene + spinel. Note that the vermicular spinel becomes finer towards the plagioclase and thicker towards the clinopyroxene. Plagioclase contains oriented exsolutions of Al spinel (Hc). Symplectites appear to have formed after amphibole.

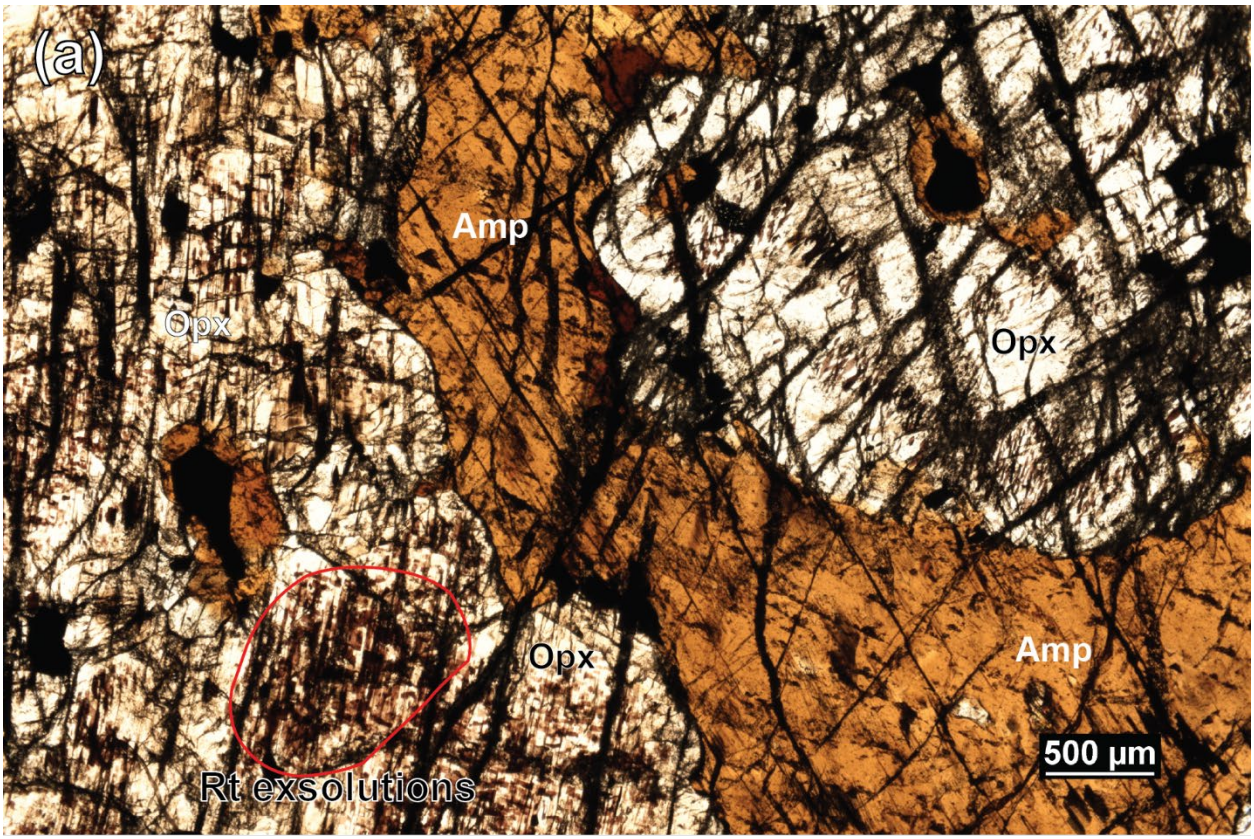
(a)
Amp
Opx
Opx
Opx
Amp
Rt exsolutions
500 µm

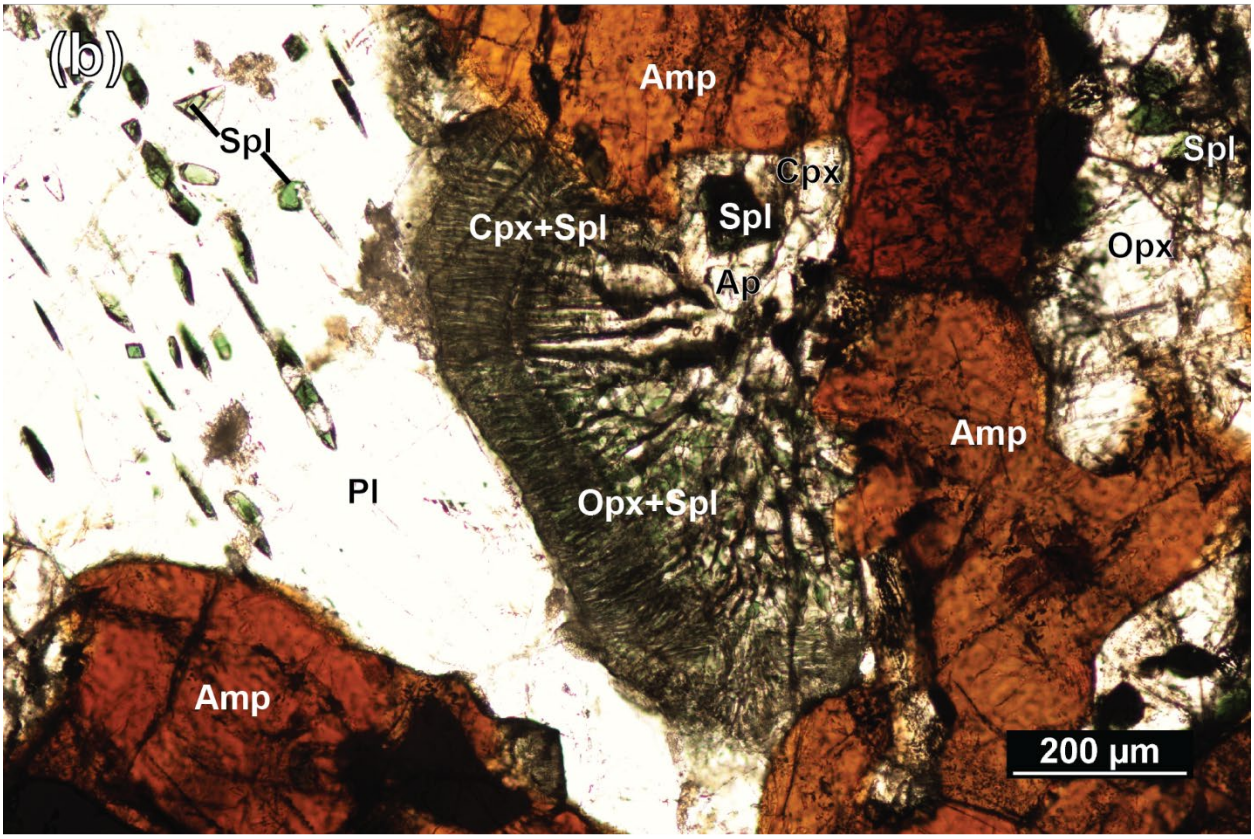
(b)
Spl
Amp
Cpx
Spl
Cpx+Spl
Ap
Spl
Opx
Amp
Pl
Opx+Spl
Amp
200 µm

Figure 36: Al spinel + pyroxene symplectites in pyroxenite (sample AM-IVZ-VM008, thin section A25). (a) reflected light image of plagioclase and symplectites of spinel + pyroxene in pyroxenite. Spinel is highlighted in red using JMicrovision software. Exsolutions of spinel create clouds in spinel, and these exsolutions appear to continue into both fine-grained clinopyroxene + vermicular spinel symplectites and farther into coarse-grained orthopyroxene. (b) Same location as (a) but at a higher magnification, highlighting the continuation of spinel exsolutions into pyroxene symplectites. The vermicular spinel in the clinopyroxene + spinel symplectites appears to be growing around the larger spinel exsolutions, appearing as though the vermicular spinel symplectites grew after the development of the symplectites. As also observed elsewhere, the relict spinel exsolutions appear thicker within the pyroxenes, further pointing to high Al activity during the development of symplectites.

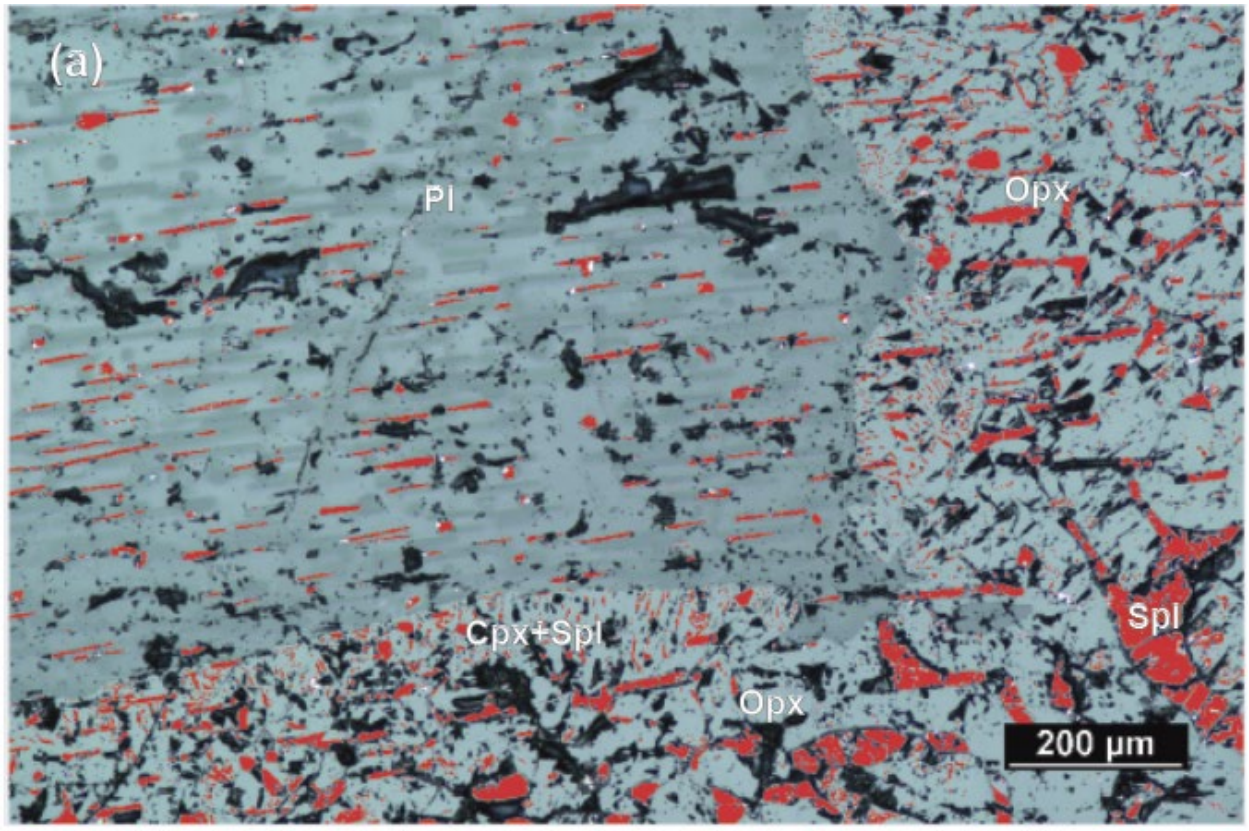
(a)
Pl
Opx
Cpx+Spl
Spl
Opx
200 µm

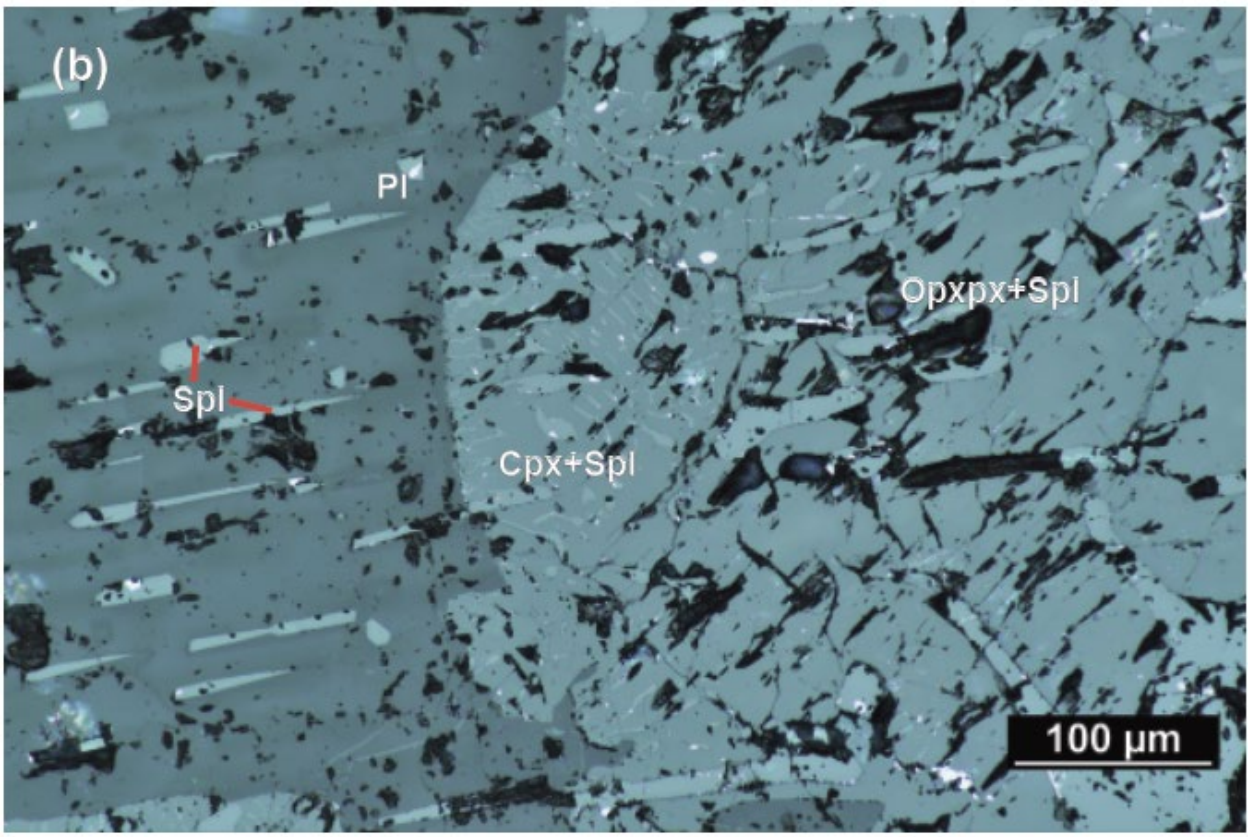
(b)
Pl
Opxpx+Spl
Spl
Cpx+Spl
100 µm

Figure 37: Multiple coronas surrounding skeletal olivine in olivine gabbro (thin section A9, sample AM-IVZ-VM009). Clinopyroxene + orthopyroxene coronas, amphibole coronas, and garnet coronas. False-color element map acquired with SEM-based EDS. Labeled apatite grain analyzed with EDS is shown; see section Apatite.

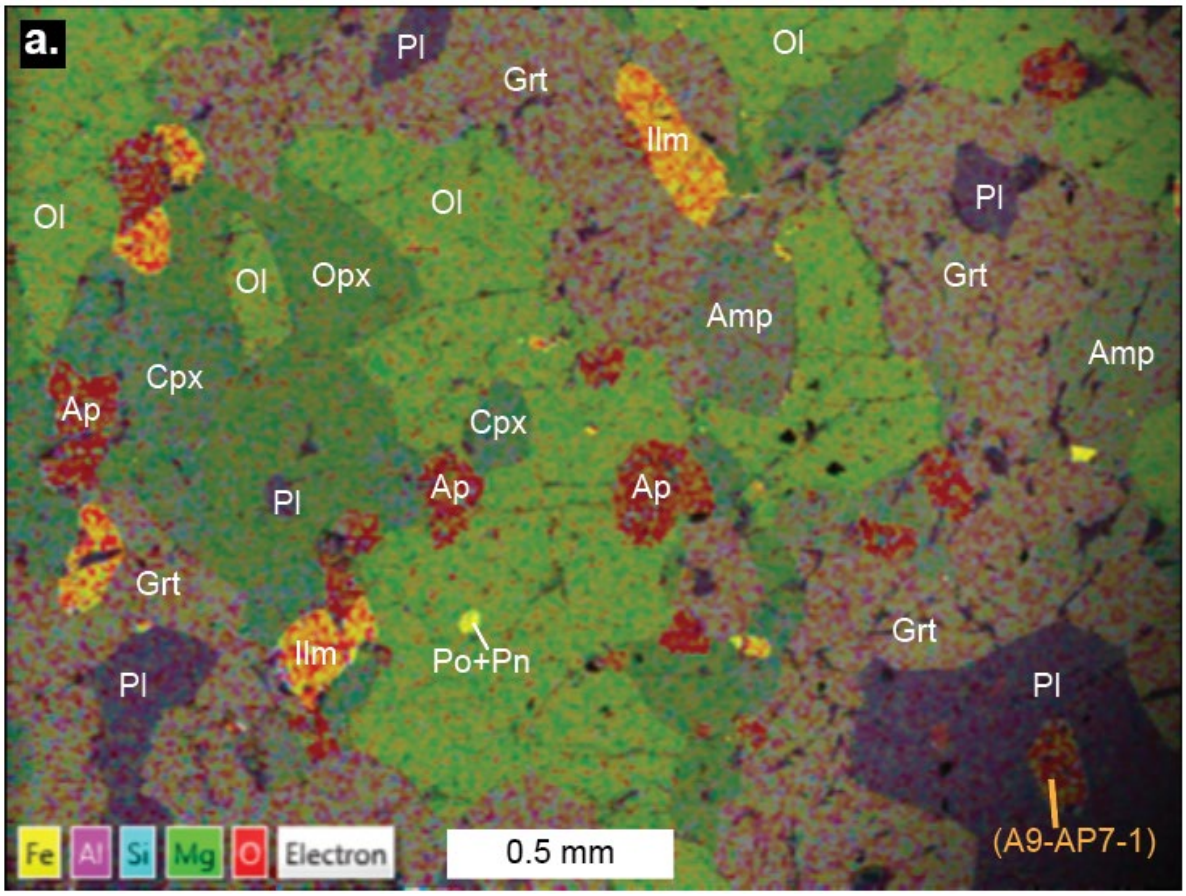
a.
Pl
Grt
Ol
Ilm
Ol
Ol
Opx
Ol
Pl
Grt
Amp
Amp
Cpx
Ap
Cpx
Ap
Ap
Pl
Grt
Ilm
Po+Pn
Grt
Pl
Pl
Fe
Al
Si
Mg
O
Electron
0.5 mm
(A9-AP7-1)

Figure 38: Recalculated compositions of olivine plotted as forsterite mol.%. Note that samples AM-VM22-6f and AM-IVZ-VM009 were collected within the same lithology, approximately 40 cm apart.

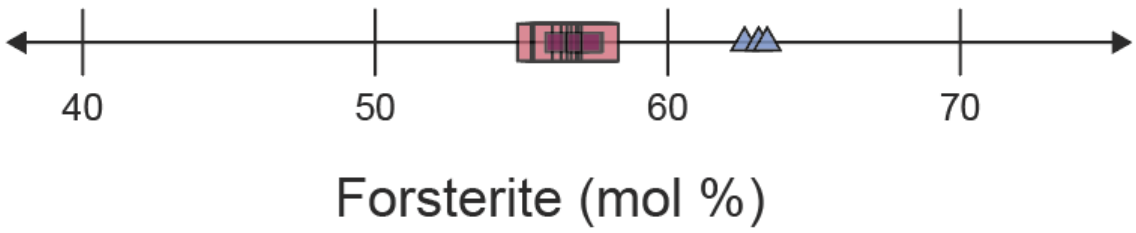

Forsterite (mol %)

pyroxenite, Sample AM-IVZ-VM008 (thin section B5)

olivine-gabbro, Sample AM-VM22-6c

olivine-gabbro, Sample AM-IVZ-VM009

Figure 39: Recalculated EPMA Saliceto orthopyroxene (enstatite) and clinopyroxene (diopside – augite) data plotted on a pyroxene ternary diagram using the MATLAB program of Walters (2022). En = enstatite; Wo = wollastonite; Fs = ferrosilite.

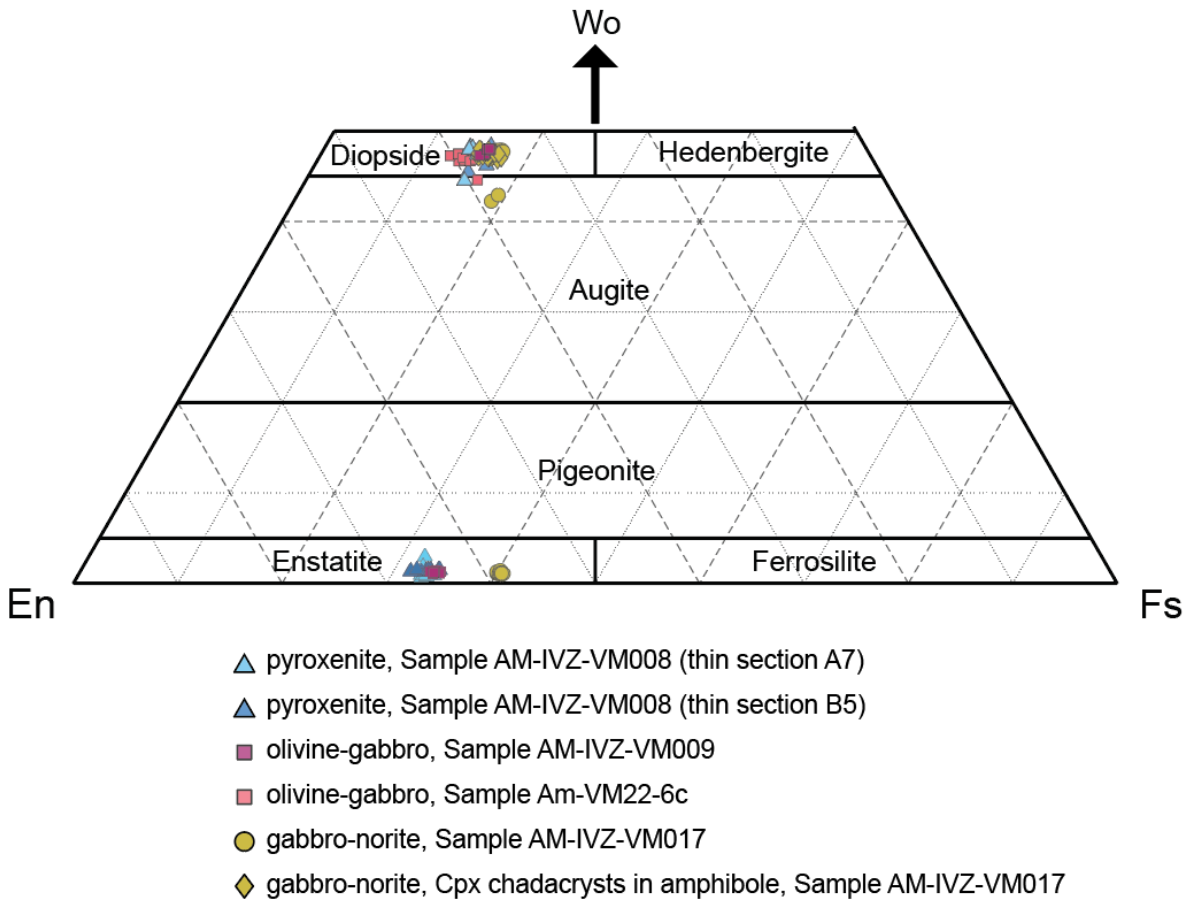
Wo
Diopside
Hedenbergite
Augite
Pigeonite
Enstatite
Ferrosilite
En
Fs
pyroxenite, Sample AM-IVZ-VM008 (thin section A7)
pyroxenite, Sample AM-IVZ-VM008 (thin section B5)
olivine-gabbro, Sample AM-IVZ-VM009
olivine-gabbro, Sample Am-VM22-6c
gabbro-norite, Sample AM-IVZ-VM017
gabbro-norite, Cpx chadacrysts in amphibole, Sample AM-IVZ-VM017

Figure 40: Pyroxenes compositions plotted as TiO_2 versus Al_2O_3 wt.% and Mg# for orthopyroxenes (a) and (b), and TiO_2 vs. Al_2O_3 and molar Mg# (c) and (d) for clinopyroxenes. Symbols as in Figure 39.

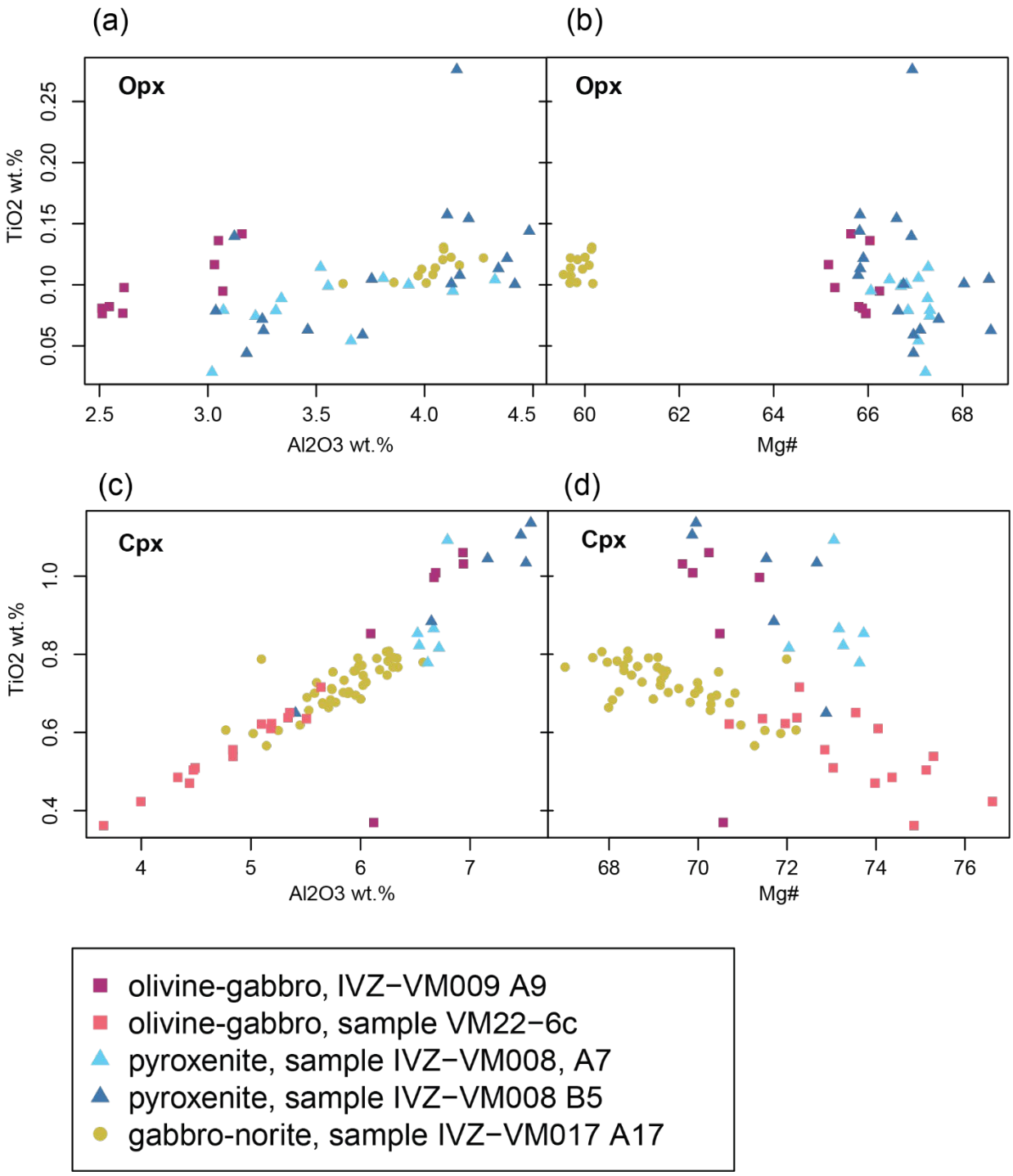
(a)
(b)
Opx
Opx
TiO2 wt.%
0.05
0.10
0.15
0.20
0.25
2.5
3.0
3.5
4.0
4.5
Al2O3 wt.%
60
62
64
66
68
Mg#
(c)
(d)
Cpx
Cpx
TiO2 wt.%
0.4
0.6
0.8
1.0
4
5
6
7
Al2O3 wt.%
68
70
72
74
76
Mg#
olivine-gabbro, IVZ−VM009 A9
olivine-gabbro, sample VM22−6c
pyroxenite, sample IVZ−VM008, A7
pyroxenite, sample IVZ−VM008 B5
gabbro-norite, sample IVZ−VM017 A17

Figure 41: Trace elements from in-situ LA-ICP-MS analyses of (a) orthopyroxene and (b) clinopyroxene from Saliceto samples normalized to primitive mantle concentrations from Hofmann (1988).

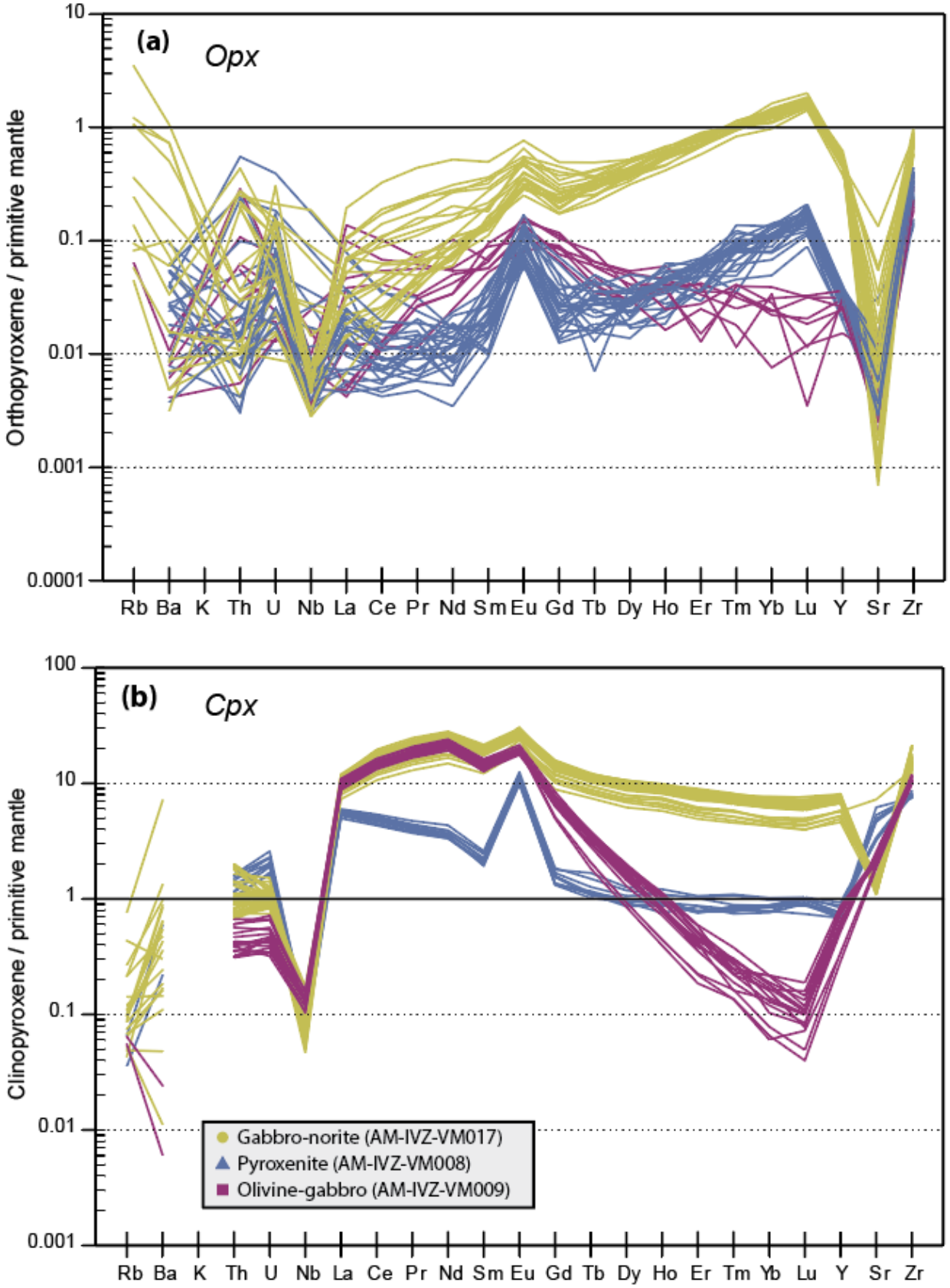
(a)
Opx
Orthopyroxene / primitive mantle
10
1
0.1
0.01
0.001
0.0001
Rb Ba K Th U Nb La Ce Pr Nd Sm Eu Gd Tb Dy Ho Er Tm Yb Lu Y Sr Zr
(b)
Cpx
Clinopyroxene / primitive mantle
100
10
1
0.1
0.01
0.001
Gabbro-norite (AM-IVZ-VM017)
Pyroxenite (AM-IVZ-VM008)
Olivine-gabbro (AM-IVZ-VM009)
Rb Ba K Th U Nb La Ce Pr Nd Sm Eu Gd Tb Dy Ho Er Tm Yb Lu Y Sr Zr

Figure 42: Recalculated EPMA plagioclase data of Saliceto samples plotted in (a) the Ab-An-Or ternary diagram, and (b) in the Ab versus An content plot.

(a)

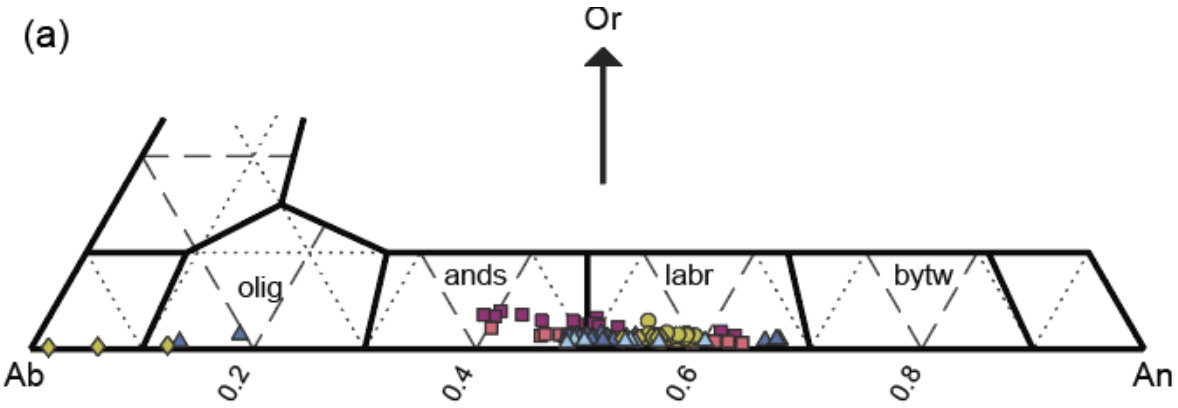

pyroxenite, Sample AM-IVZ-VM008 (thin section A7)
pyroxenite, Sample AM-IVZ-VM008 (thin section B5)
olivine-gabbro, Sample AM-VM22-6c
olivine-gabbro, Sample AM-IVZ-VM009
gabbronorite, Sample AM-IVZ-VM017
gabbronorite, plagioclase chadacrysts in amphibole, Sample AM-IVZ-VM017

(b)

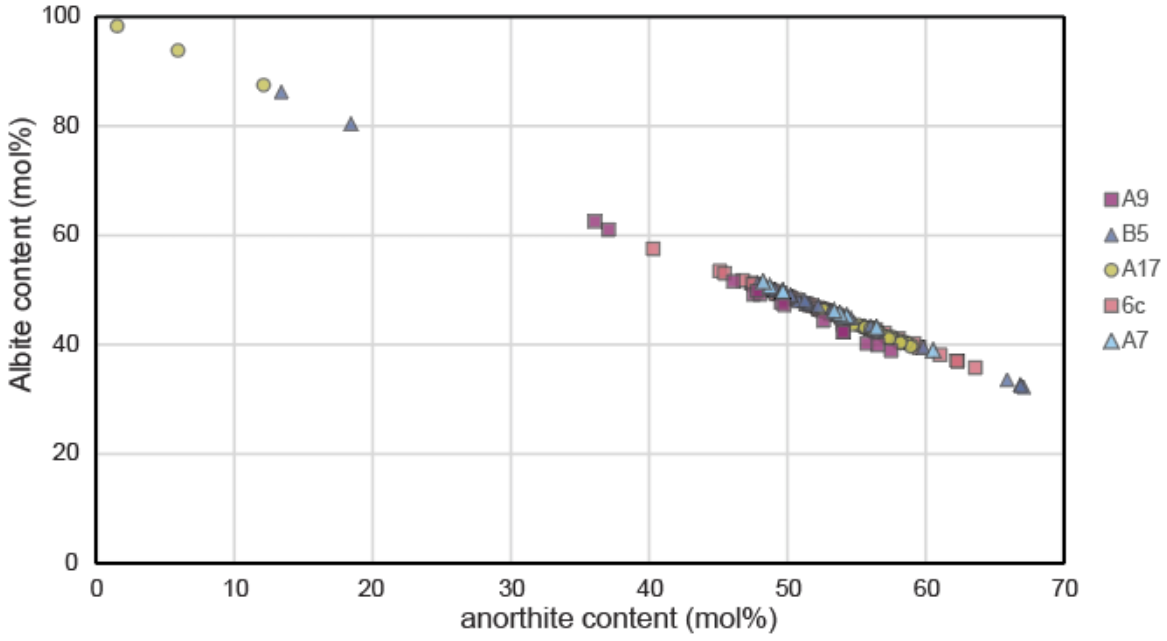

Figure 43: In-situ LA-ICP-MS analyses of (a) plagioclase and (b) amphibole from Saliceto samples normalized to primitive mantle concentrations from Hofmann (1988). Note the strong Ba, La, Eu and Sr anomalies present in all samples. Plagioclase is enriched in LREE with a decreasing trend and strongly depleted in HREE for all samples.

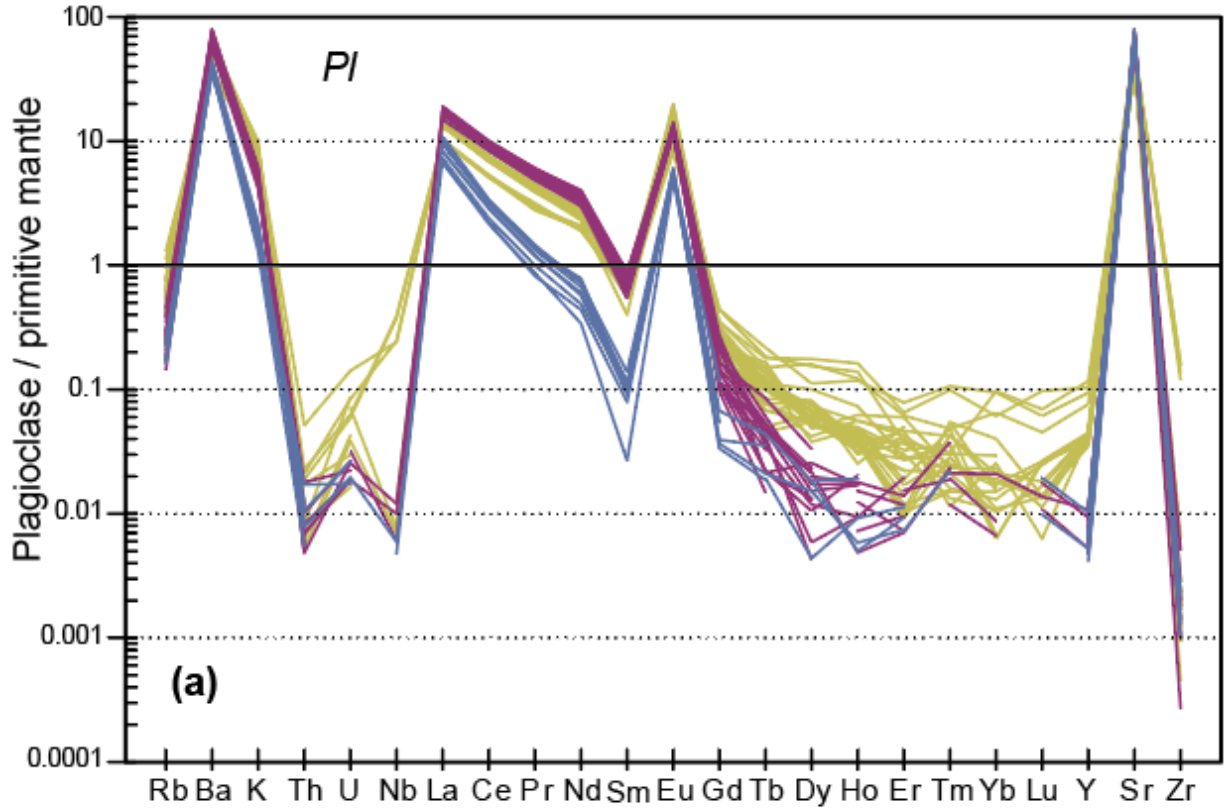
Pl
Plagioclase / primitive mantle
100
10
1
0.1
0.01
0.001
0.0001
(a)
Rb Ba K Th U Nb La Ce Pr Nd Sm Eu Gd Tb Dy Ho Er Tm Yb Lu Y Sr Zr

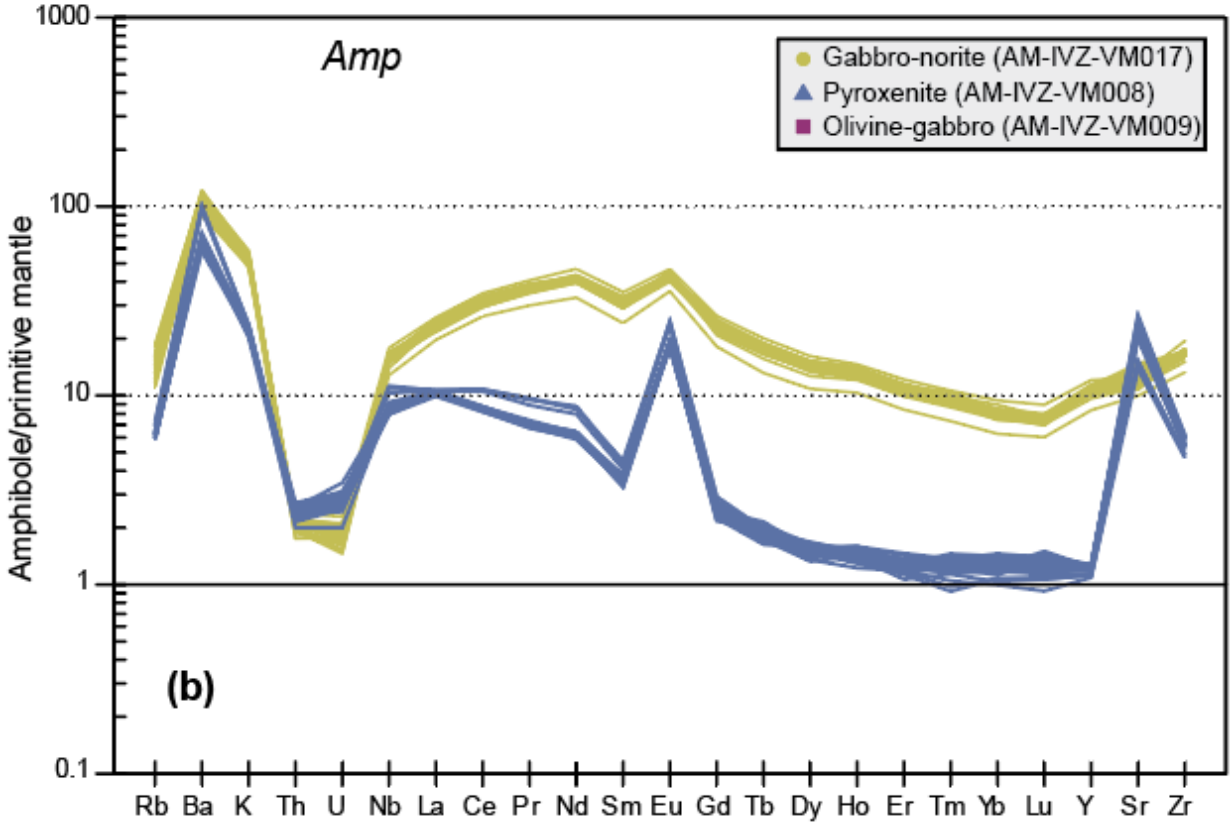
Amp
Gabbro-norite (AM-IVZ-VM017)
Pyroxenite (AM-IVZ-VM008)
Olivine-gabbro (AM-IVZ-VM009)
Amphibole/primitive mantle
1000
100
10
1
0.1
(b)
Rb Ba K Th U Nb La Ce Pr Nd Sm Eu Gd Tb Dy Ho Er Tm Yb Lu Y Sr Zr

Figure 44: Amphibole compositions plotted according to (a) the nomenclature of Hawthorne *et al.* (2012) and (b) Leake *et al.* (1997). Note the variance within rock samples (squares and circles) and within individual grains in orthopyroxenite (triangles).

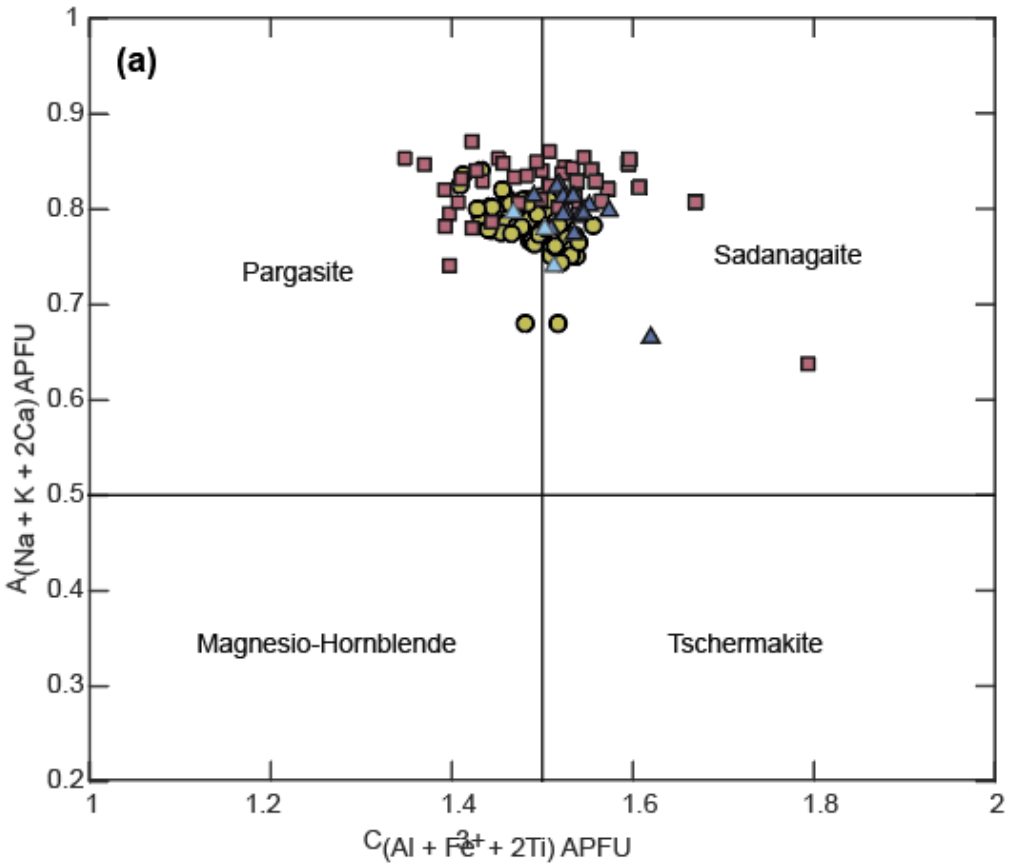

△ pyroxenite, Sample AM-IVZ-VM008 (thin section A7)

▲ pyroxenite, Sample AM-IVZ-VM008 (thin section B5)

■ olivine-gabbro, Sample AM-VM22-6c

● gabbronorite, Sample AM-IVZ-VM017

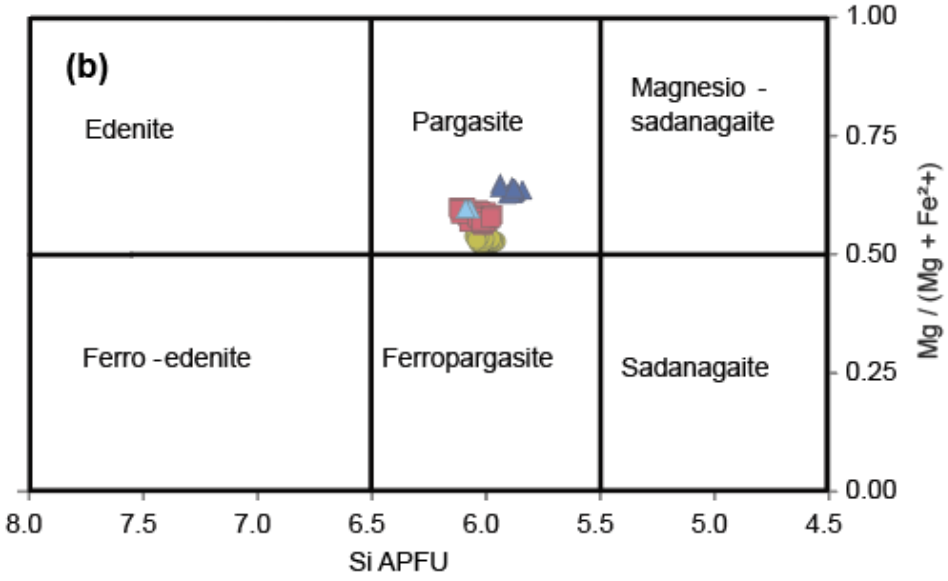

Figure 45: Transects of Na_2O and K_2O across two poikilitic amphibole grains, (a) and (b), in gabbronorite, thin section A17, sample AM-IVZ-VM017 (Figure 22). At the beginnings and ends of both transects, the amphibole is in contact with plagioclase.

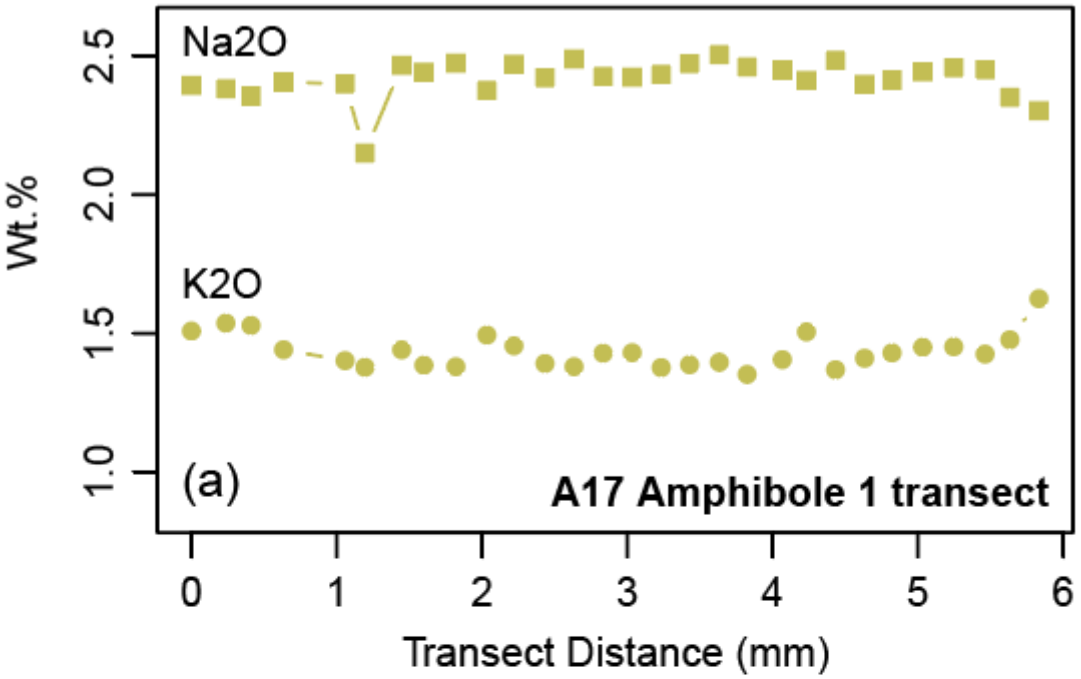
Na2O
K2O
Wt.%
1.0
1.5
2.0
2.5
(a)
A17 Amphibole 1 transect
0
1
2
3
4
5
6
Transect Distance (mm)

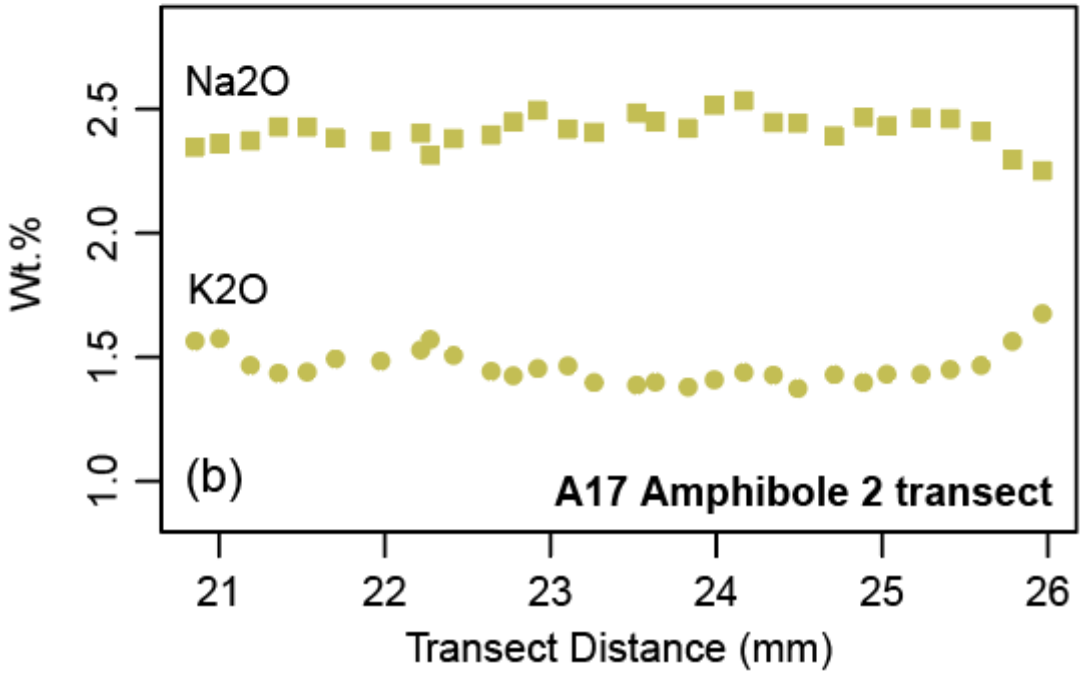
Na2O
K2O
Wt.%
1.0
1.5
2.0
2.5
(b)
A17 Amphibole 2 transect
21
22
23
24
25
26
Transect Distance (mm)

Figure 46: Garnet ternary diagram with Grs (grossular), Prp (pyrope), and Alm + Sps (almandine + spessartine) components of garnet in olivine gabbro calculated with the MATLAB scripts of Walters (2022). Note the little variation of all 43 analyses between analyses within and between the olivine gabbro samples.

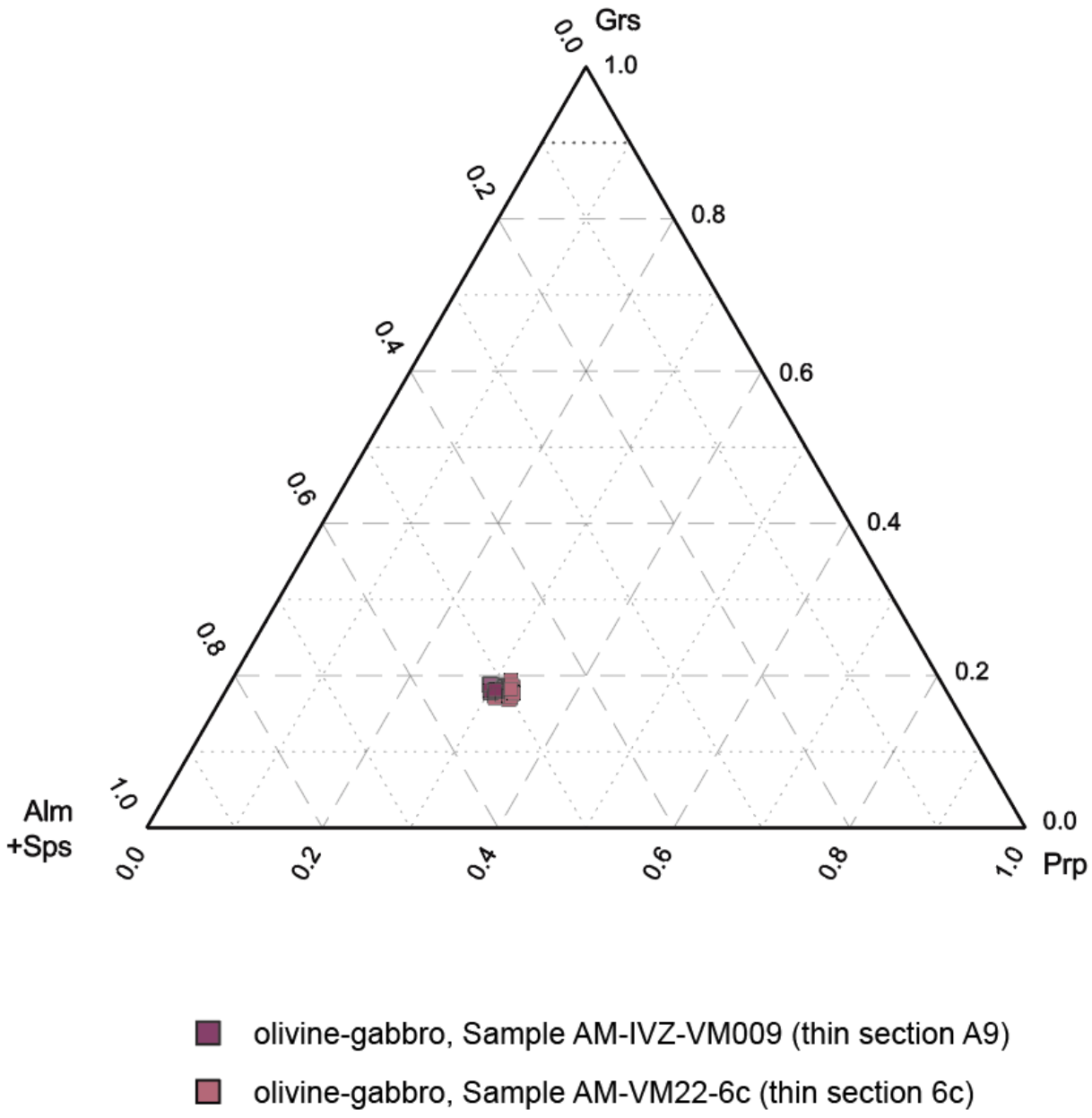
Grs
0.0
1.0
0.2
0.8
0.4
0.6
0.6
0.4
0.8
0.2
1.0
0.0
Alm
+Sps
0.0
0.2
0.4
0.6
0.8
1.0
Prp
olivine-gabbro, Sample AM-IVZ-VM009 (thin section A9)
olivine-gabbro, Sample AM-VM22-6c (thin section 6c)

Figure 47: Diagram showing trace elements of (a) apatite and (b) garnet normalized to primitive mantle (Hofmann, 1988).

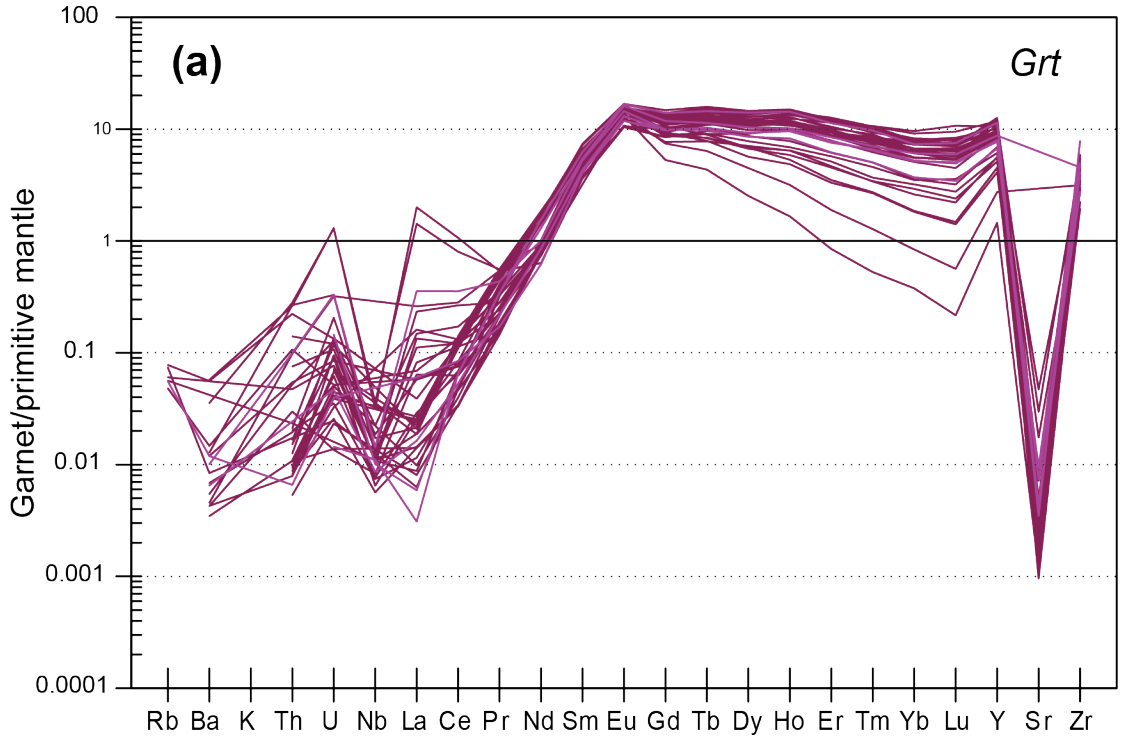
(a)
Grt
Garnet/primitive mantle
100
10
1
0.1
0.01
0.001
0.0001
Rb Ba K Th U Nb La Ce Pr Nd Sm Eu Gd Tb Dy Ho Er Tm Yb Lu Y Sr Zr

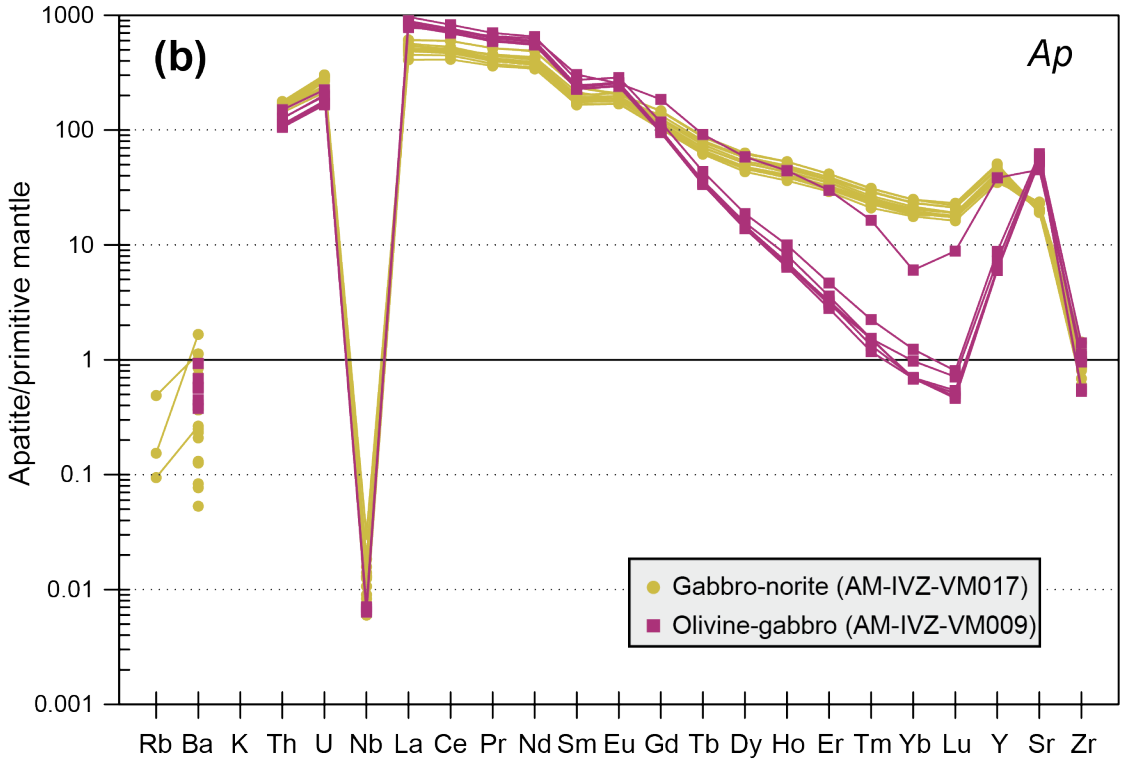
(b)
Ap
Apatite/primitive mantle
1000
100
10
1
0.1
0.01
0.001
Rb Ba K Th U Nb La Ce Pr Nd Sm Eu Gd Tb Dy Ho Er Tm Yb Lu Y Sr Zr
Gabbro-norite (AM-IVZ-VM017)
Olivine-gabbro (AM-IVZ-VM009)

Figure 48: Spinel group minerals (aluminum subgroup and iron subgroup according to Gaines *et al.*, 1997) plotted in spinel – hercynite – magnetite/ülvospinel – magnesioferrite/quandilite space as (a) by sample and (b) by texture. Exsolutions of spinel minerals in plagioclase are those shown in Figure 36. Mag-Ilm-Sp exsolutions are shown in Figure 32, and these are found in all rock types. Vermicular spinel found in orthopyroxenite is intergrown with clinopyroxene and orthopyroxene as shown in Figure 36b. Blobby spinel is Al subgroup spinel that is not clearly intergrown with other minerals and up to <1 mm in size.

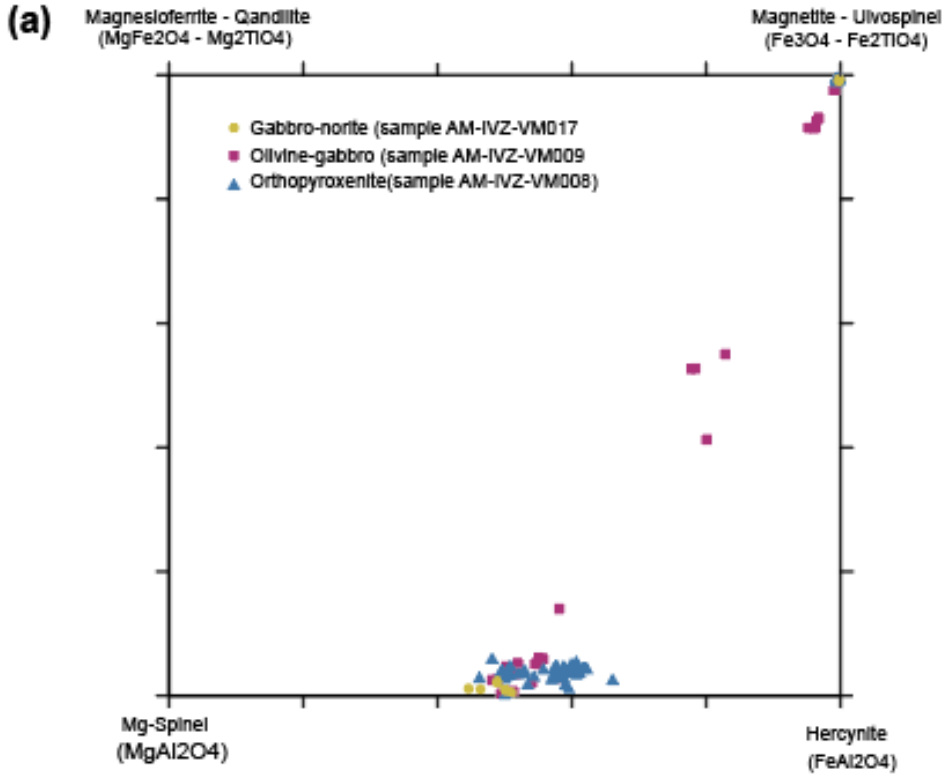
(a)
Magnesioferrite - Qandilite
(MgFe2O4 - Mg2TiO4)
Magnetite - Ulvospinel
(Fe3O4 - Fe2TiO4)
Gabbro-norite (sample AM-IVZ-VM017
Olivine-gabbro (sample AM-IVZ-VM009
Orthopyroxenite(sample AM-IVZ-VM008)
Mg-Spinel
(MgAl2O4)
Hercynite
(FeAl2O4)

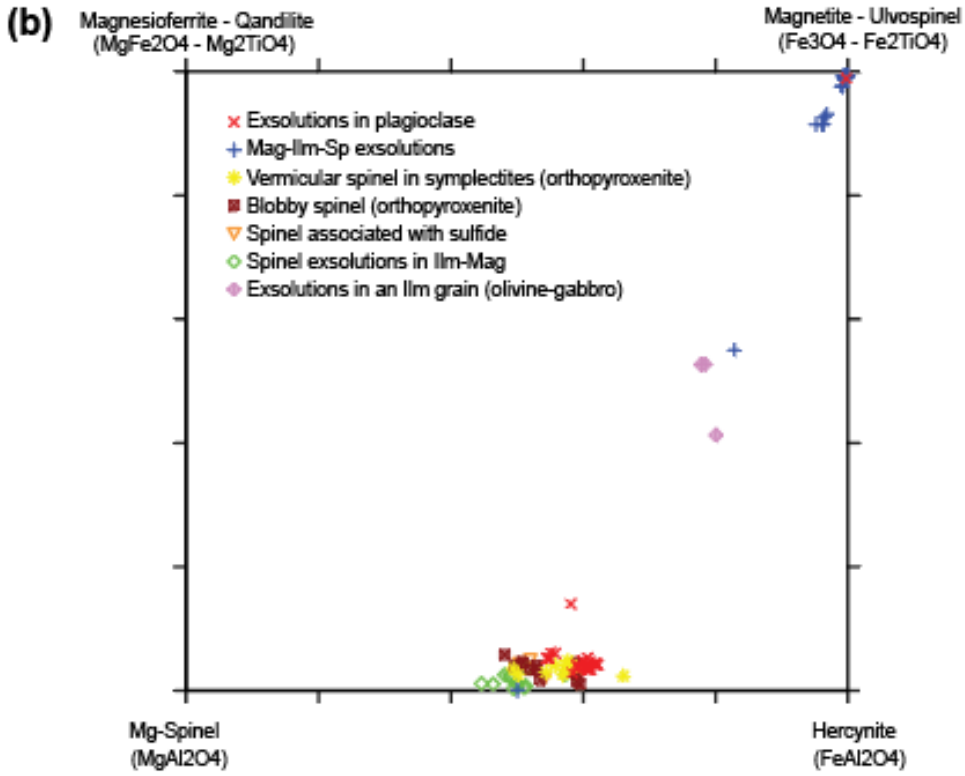
(b)
Magnesioferrite - Qandilite
(MgFe2O4 - Mg2TiO4)
Magnetite - Ulvospinel
(Fe3O4 - Fe2TiO4)
Exsolutions in plagioclase
Mag-Ilm-Sp exsolutions
Vermicular spinel in symplectites (orthopyroxenite)
Blobby spinel (orthopyroxenite)
Spinel associated with sulfide
Spinel exsolutions in Ilm-Mag
Exsolutions in an Ilm grain (olivine-gabbro)
Mg-Spinel
(MgAl2O4)
Hercynite
(FeAl2O4)

Figure 49: Multi element diagrams of oxides versus SiO_2 reporting all new bulk rock data from this study. Oxides are normalized to 100% and FeO is total iron oxide. LMC = Lower Mafic Complex; PBB = Paragneiss-Bearing Belt; UMC = Upper Mafic Complex.

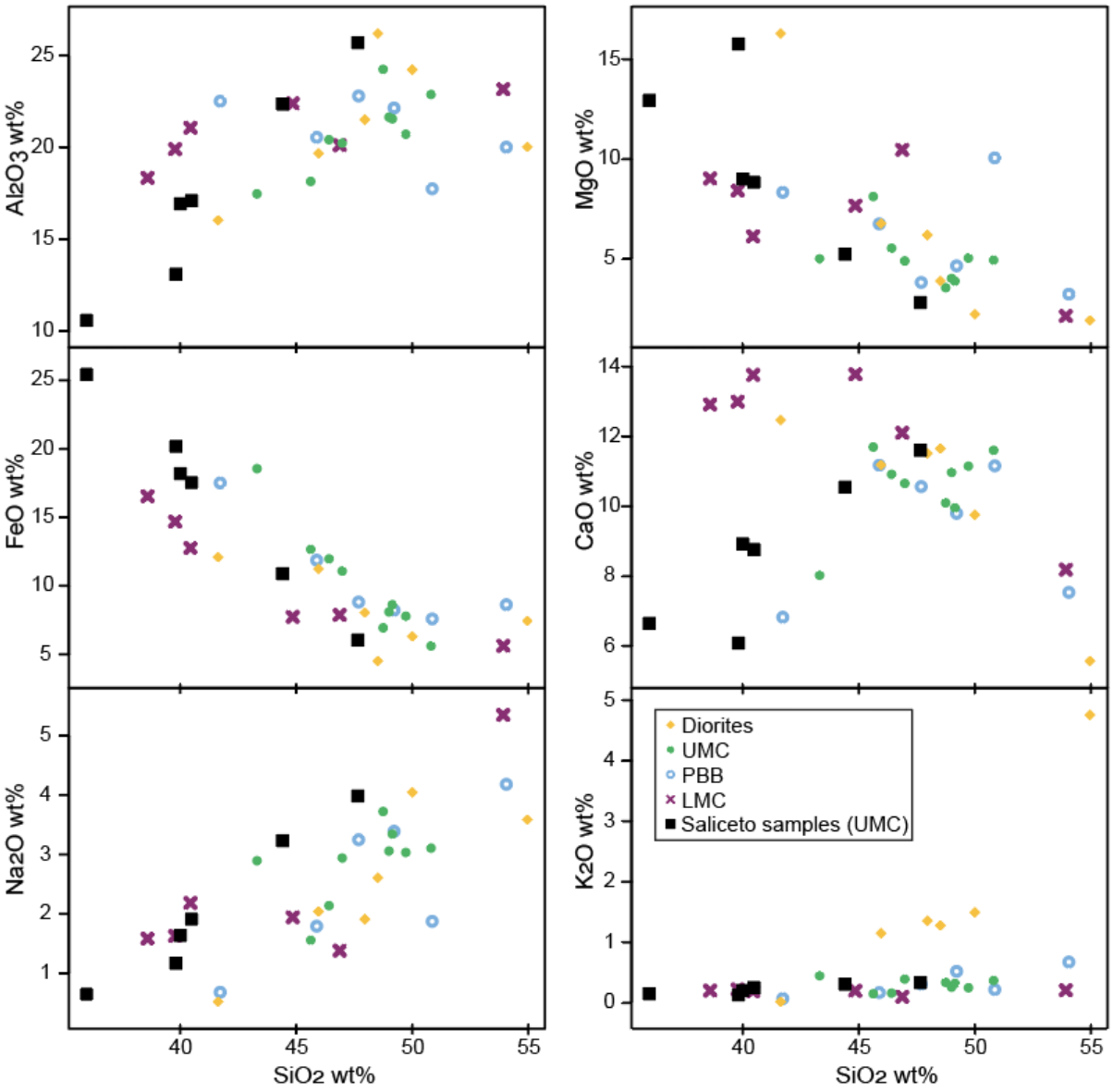
Al2O3 wt%
FeO wt%
Na2O wt%
MgO wt%
CaO wt%
K2O wt%
SiO2 wt%
SiO2 wt%
Diorites
UMC
PBB
LMC
Saliceto samples (UMC)

Figure 50: Multi element diagrams of oxides versus SiO_2 of literature data and new bulk rock data from the Mafic Complex, including leucosomes and paragneiss, plotted by the stratigraphic units of Sinigoi *et al.* (1996). Oxides normalized to 100% and FeO is calculated as total iron oxide. Magnesium number is reported as Mg# = 100*molar Mg/(Fe + Mg).

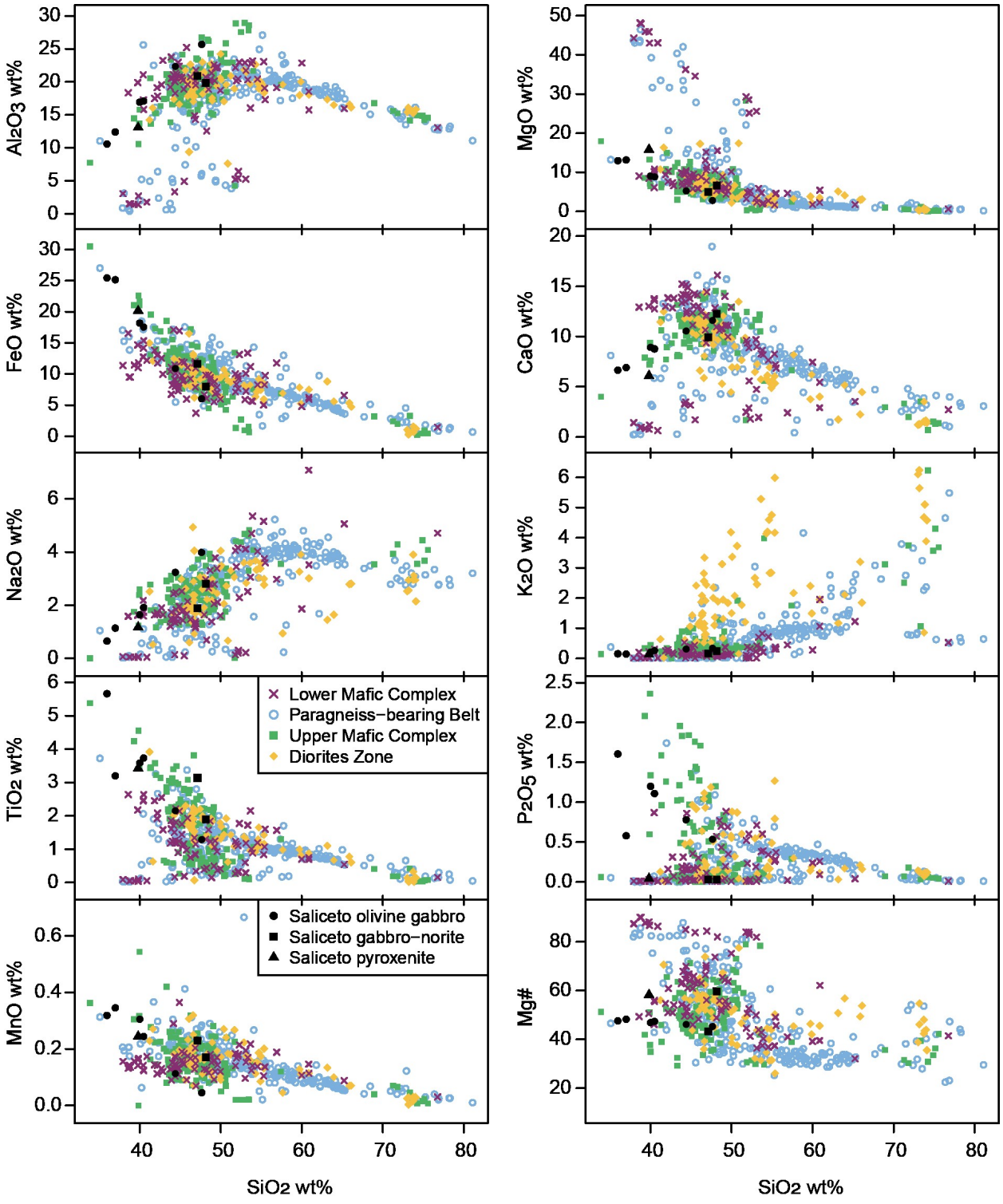
Al2O3 wt%
FeO wt%
Na2O wt%
TiO2 wt%
MnO wt%
MgO wt%
CaO wt%
K2O wt%
P2O5 wt%
Mg#
SiO2 wt%
SiO2 wt%
Lower Mafic Complex
Paragneiss−bearing Belt
Upper Mafic Complex
Diorites Zone
Saliceto olivine gabbro
Saliceto gabbro−norite
Saliceto pyroxenite

Figure 51: Multi element diagrams of oxides versus SiO_2 of literature data and new bulk rock data from the Mafic Complex, including leucosomes and paragneiss, plotted by rock type. Major oxides normalized to 100% and FeO is calculated as total iron oxide. Mg# = molar Mg/(Fe + Mg).

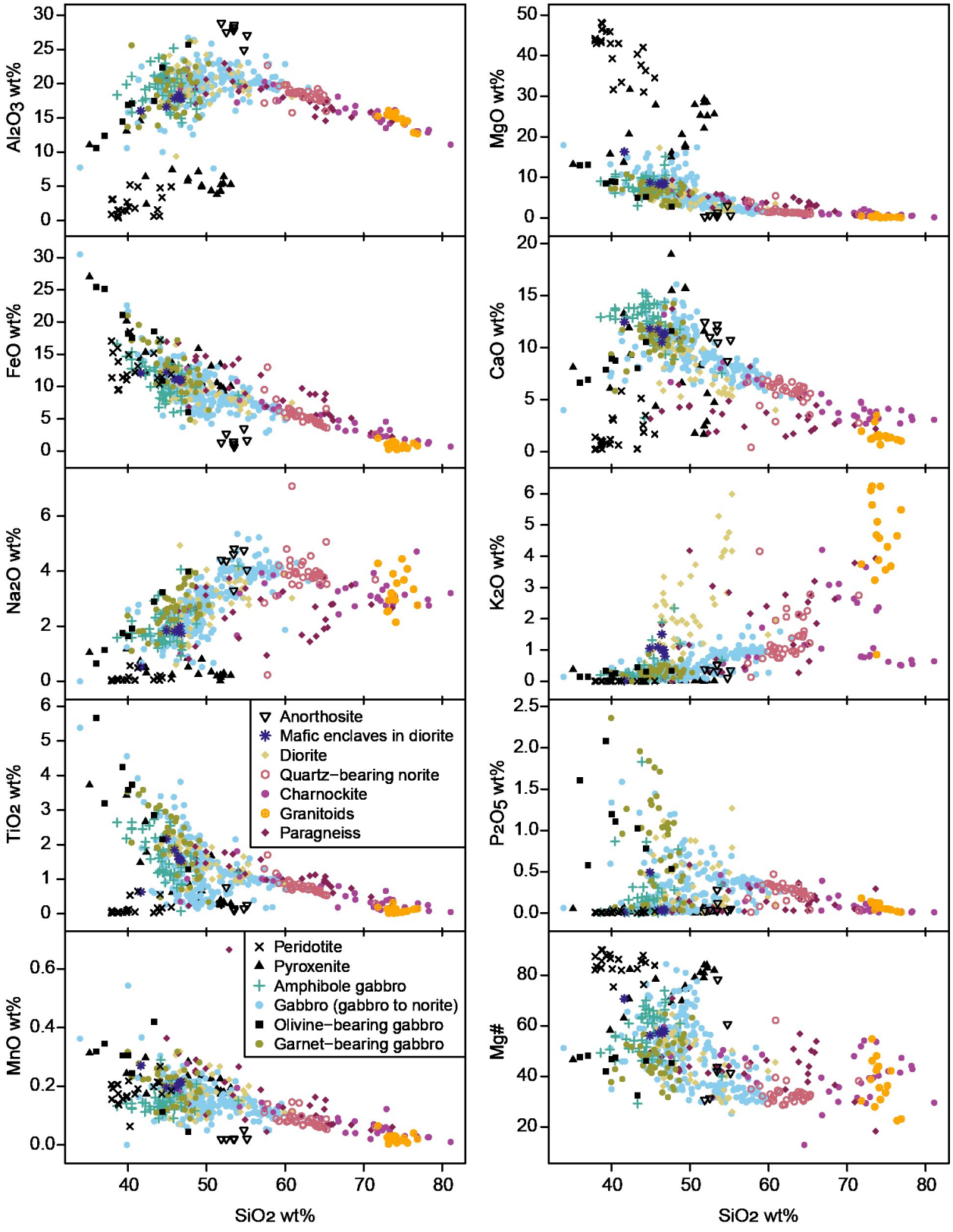
Al2O3 wt%
MgO wt%
FeO wt%
CaO wt%
Na2O wt%
K2O wt%
TiO2 wt%
P2O5 wt%
MnO wt%
Mg#
SiO2 wt%
SiO2 wt%
Anorthosite
Mafic enclaves in diorite
Diorite
Quartz-bearing norite
Charnockite
Granitoids
Paragneiss
Peridotite
Pyroxenite
Amphibole gabbro
Gabbro (gabbro to norite)
Olivine-bearing gabbro
Garnet-bearing gabbro

Figure 52: Major element bulk rock data of all rocks from new and literature data, plotted as major elements versus molar MgO/(FeO + MgO). Symbols as in Figure 51.

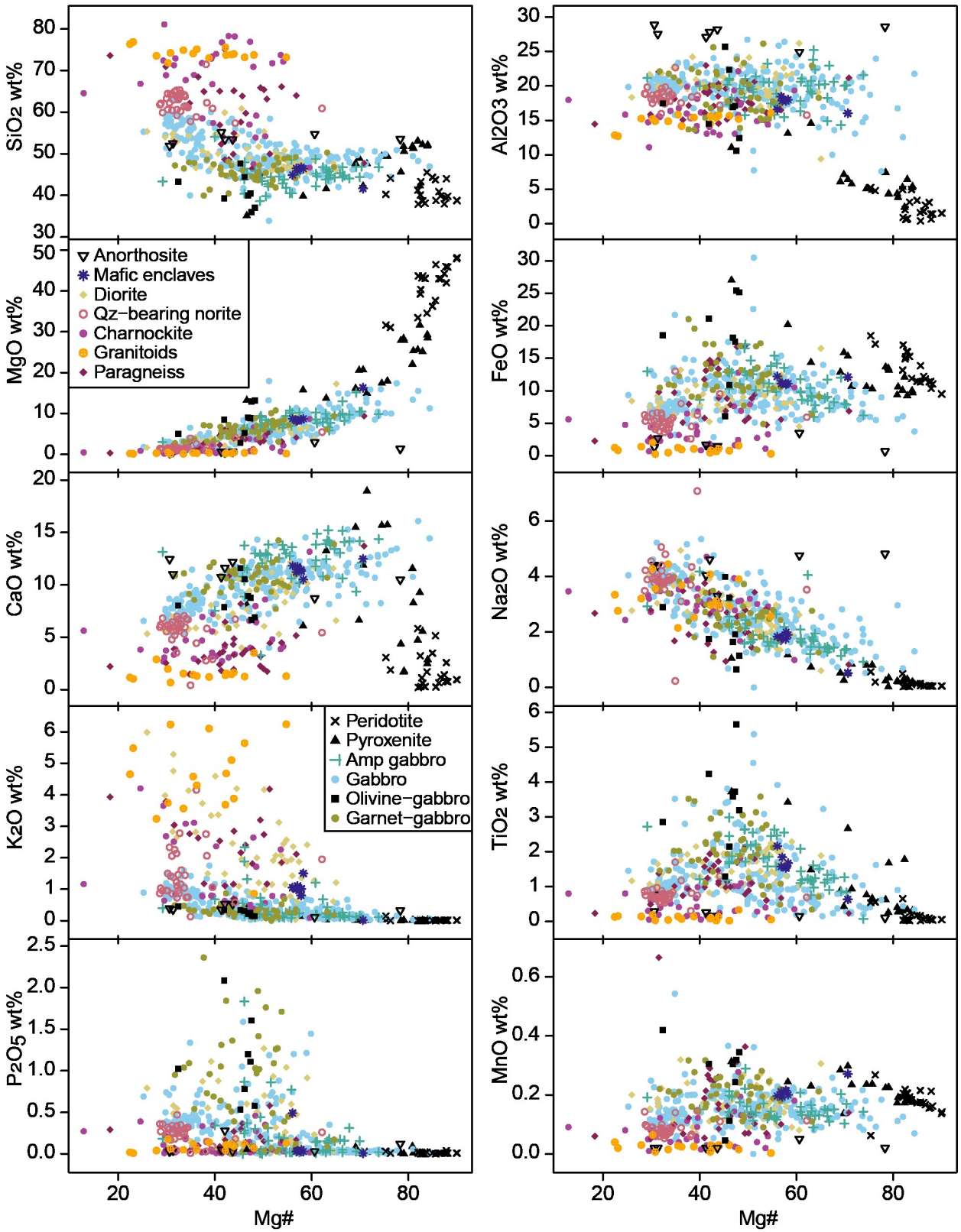
SiO2 wt%
Al2O3 wt%
MgO wt%
FeO wt%
CaO wt%
Na2O wt%
K2O wt%
TiO2 wt%
P2O5 wt%
MnO wt%
Mg#
Mg#
Anorthosite
Mafic enclaves
Diorite
Qz−bearing norite
Charnockite
Granitoids
Paragneiss
Peridotite
Pyroxenite
Amp gabbro
Gabbro
Olivine−gabbro
Garnet−gabbro

Figure 53: (a) AFM (A=Na_2O+K_2O, F=FeOt, M=MgO on a wt.% basis) ternary diagram showing a selection of literature data of igneous rocks from the Mafic Complex. (b) P_2O_5 vs. TiO_2 in bulk rock data from Mafic Complex. Symbols as in Figure 50.

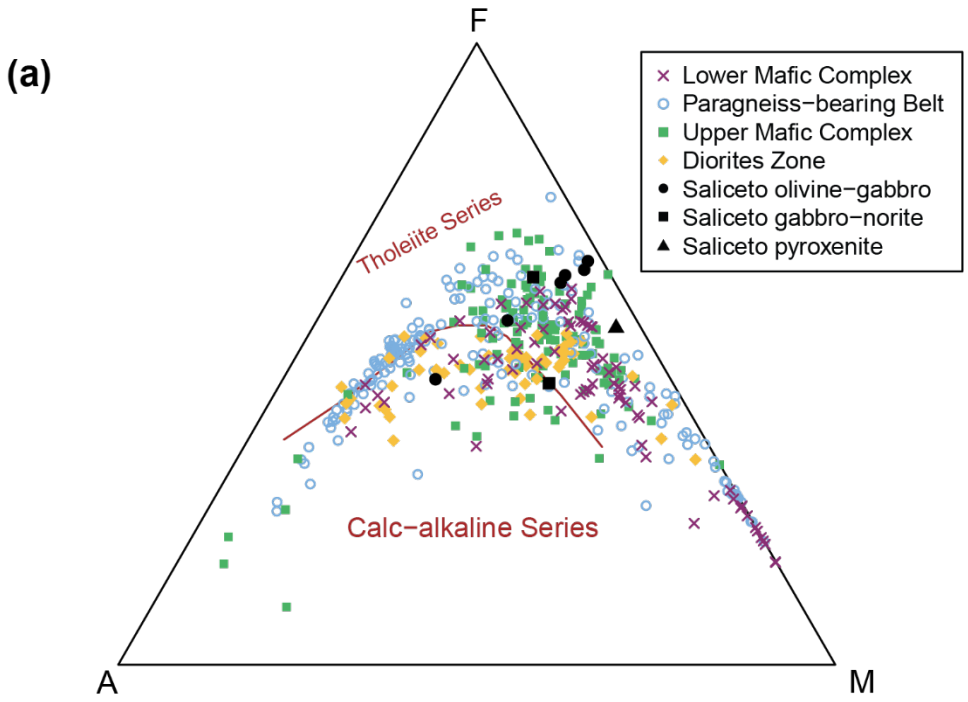
(a)
F
A
M
Tholeiite Series
Calc−alkaline Series
Lower Mafic Complex
Paragneiss−bearing Belt
Upper Mafic Complex
Diorites Zone
Saliceto olivine−gabbro
Saliceto gabbro−norite
Saliceto pyroxenite

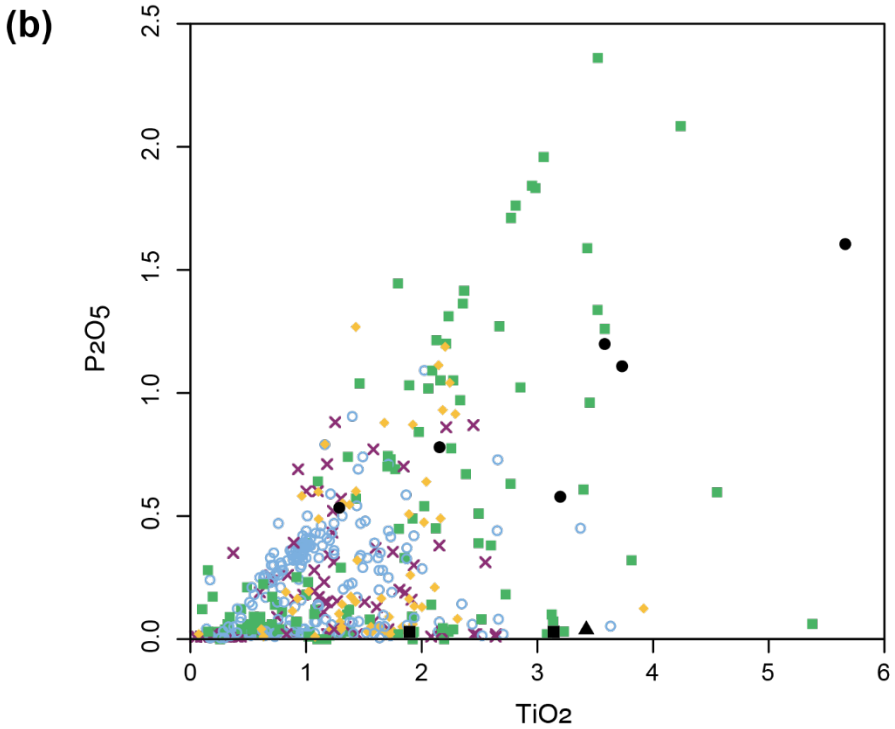
(b)
P2O5
TiO2
0.0
0.5
1.0
1.5
2.0
2.5
0
1
2
3
4
5
6

Figure 54: Bulk rock major elements plotted by rock type as a function of distance to the Insubric Line for the northern Mafic Complex, which approximates the base of the Mafic Complex. Data from literature and new bulk rock data. Paragneiss and charnockites data with no approximate location (Rivalenti *et al.*, 1975) is plotted to the left of zero. Mg# = molar Mg/(Fe + Mg). Symbols as in Figure 51.

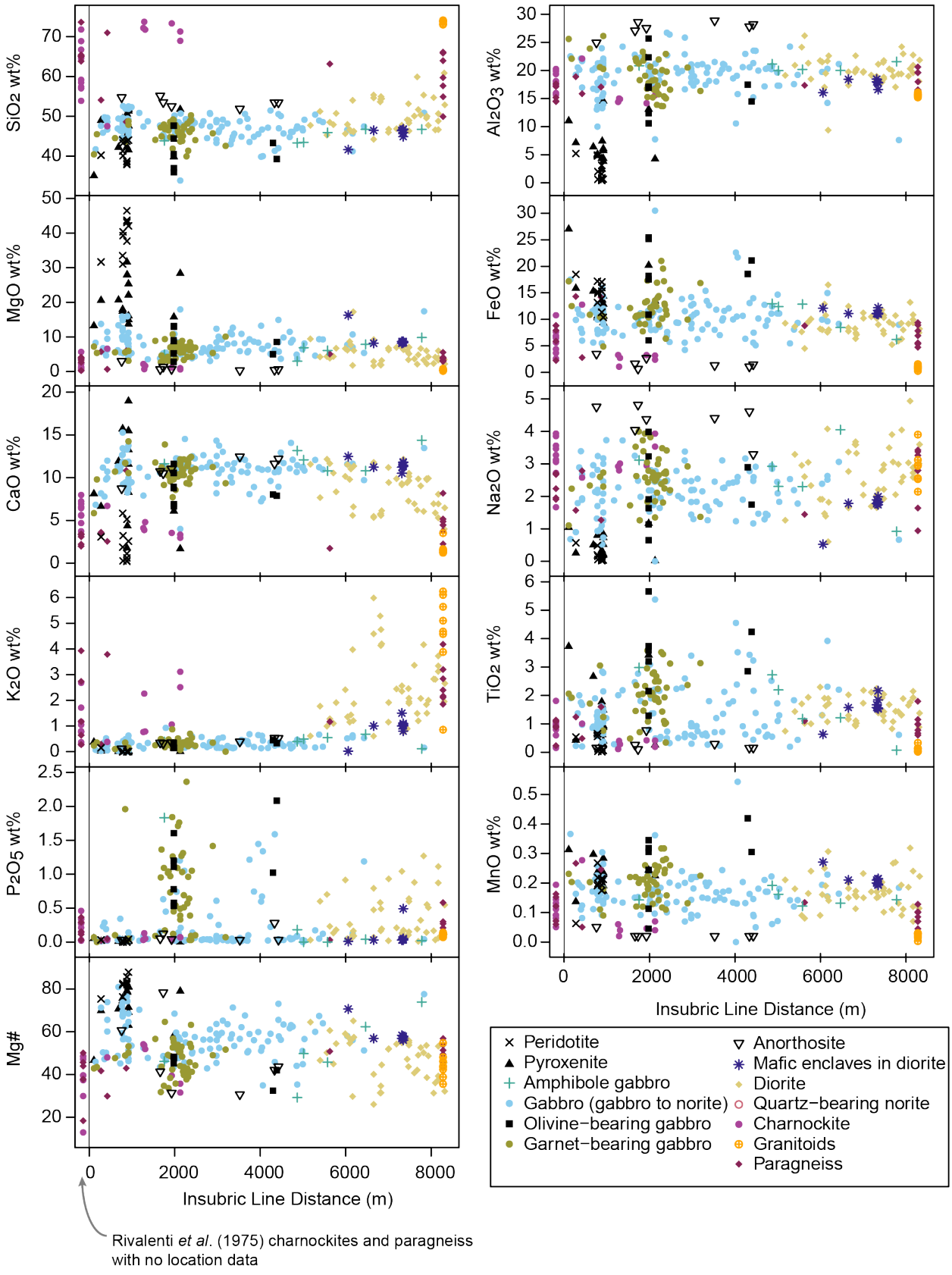
SiO2 wt%
MgO wt%
CaO wt%
K2O wt%
P2O5 wt%
Mg#
Al2O3 wt%
FeO wt%
Na2O wt%
TiO2 wt%
MnO wt%
Insubric Line Distance (m)
Peridotite
Pyroxenite
Amphibole gabbro
Gabbro (gabbro to norite)
Olivine−bearing gabbro
Garnet−bearing gabbro
Anorthosite
Mafic enclaves in diorite
Diorite
Quartz−bearing norite
Charnockite
Granitoids
Paragneiss
Rivalenti et al. (1975) charnockites and paragneiss with no location data

Figure 55: Lower Mafic Complex (LMC) samples bulk rock trace elements normalized to primitive mantle (Hofmann, 1988) highlighted, compared with all other literature bulk rock data of the Mafic Complex in gray.

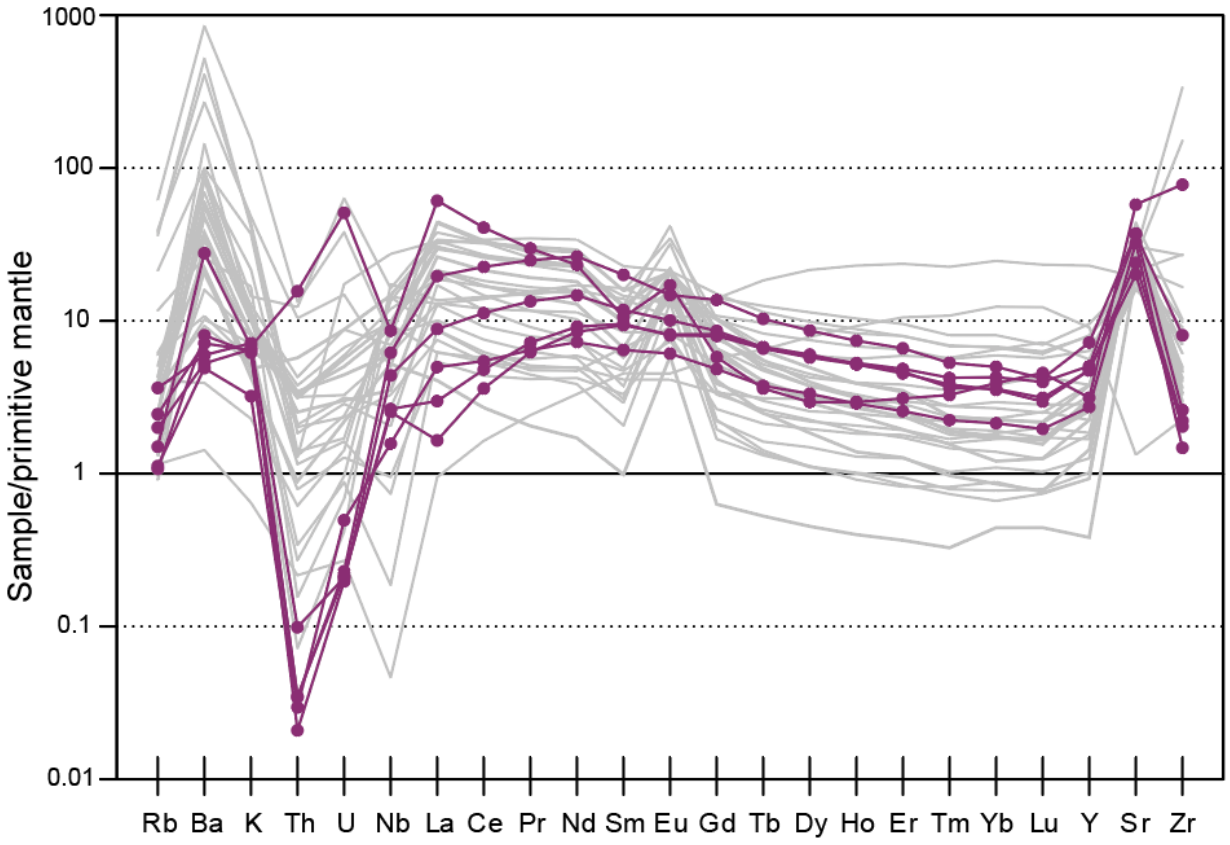
1000
100
10
1
0.1
0.01
Sample/primitive mantle
Rb Ba K Th U Nb La Ce Pr Nd Sm Eu Gd Tb Dy Ho Er Tm Yb Lu Y Sr Zr

Figure 56: Paragneiss-bearing belt (PBB) samples bulk rock trace elements normalized to primitive mantle (Hofmann, 1988) highlighted, compared with all other literature bulk rock data of the Mafic Complex in gray.

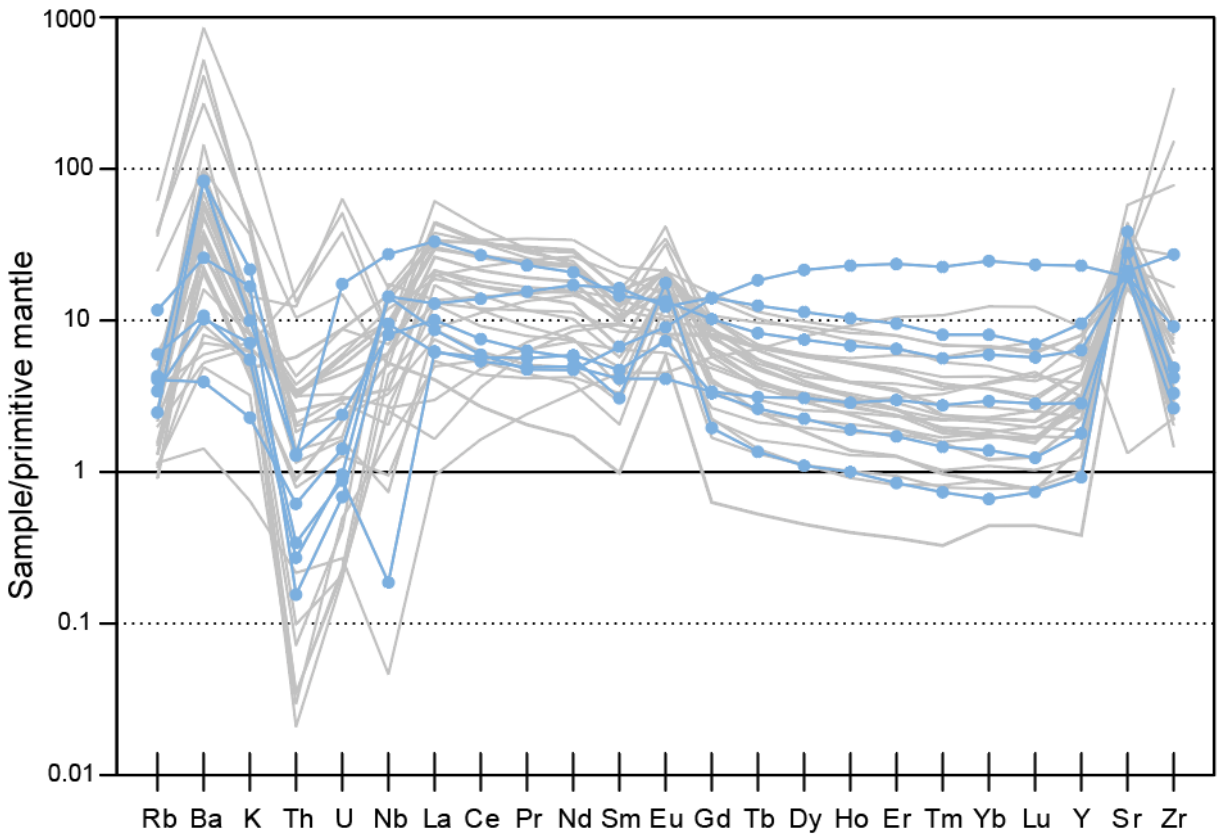
1000
100
10
1
0.1
0.01
Sample/primitive mantle
Rb Ba K Th U Nb La Ce Pr Nd Sm Eu Gd Tb Dy Ho Er Tm Yb Lu Y Sr Zr

Figure 57: Upper Mafic Complex (UMC) samples bulk rock trace elements normalized to primitive mantle (Hofmann, 1988) highlighted, compared with all other literature bulk rock data of the Mafic Complex in gray.

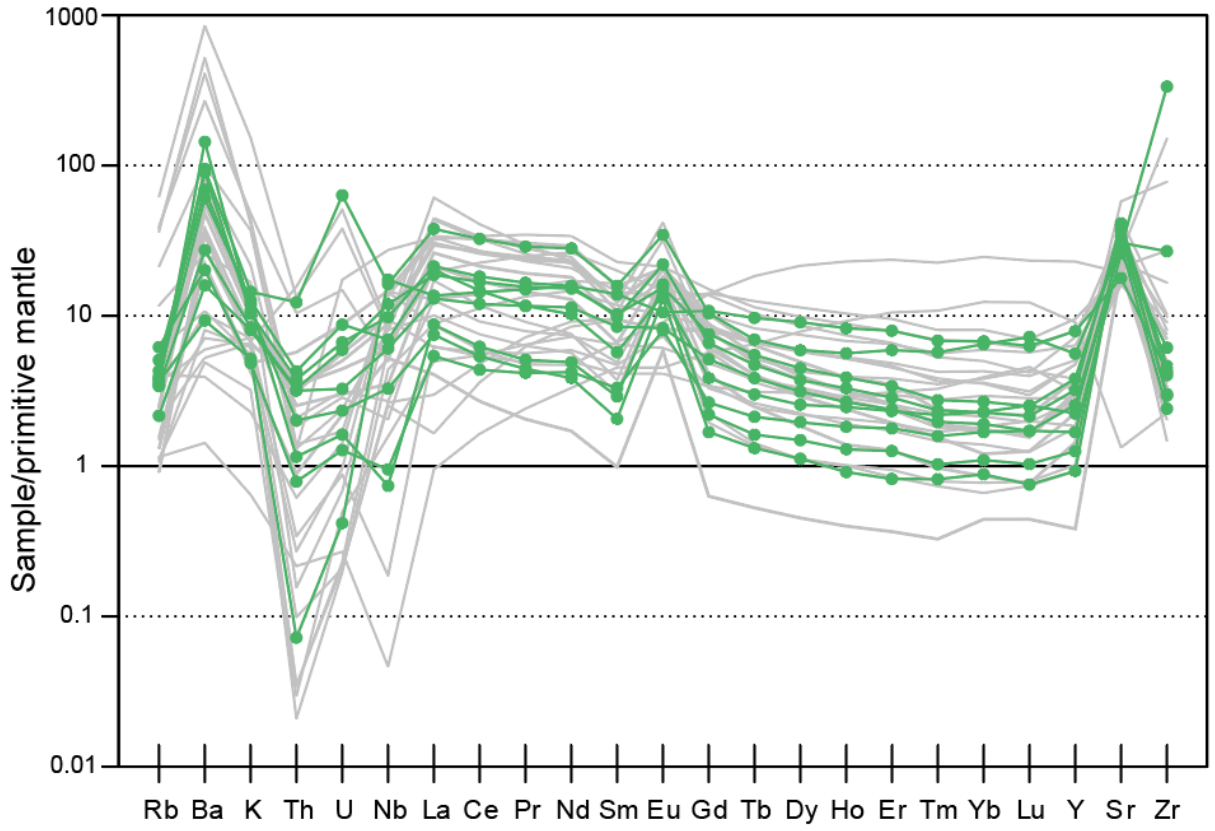
1000
100
10
1
0.1
0.01
Sample/primitive mantle
Rb Ba K Th U Nb La Ce Pr Nd Sm Eu Gd Tb Dy Ho Er Tm Yb Lu Y Sr Zr

Figure 58: “Diorite” group samples bulk rock trace elements normalized to primitive mantle (Hofmann, 1988) highlighted, compared with all other literature bulk rock data of the Mafic Complex in gray.

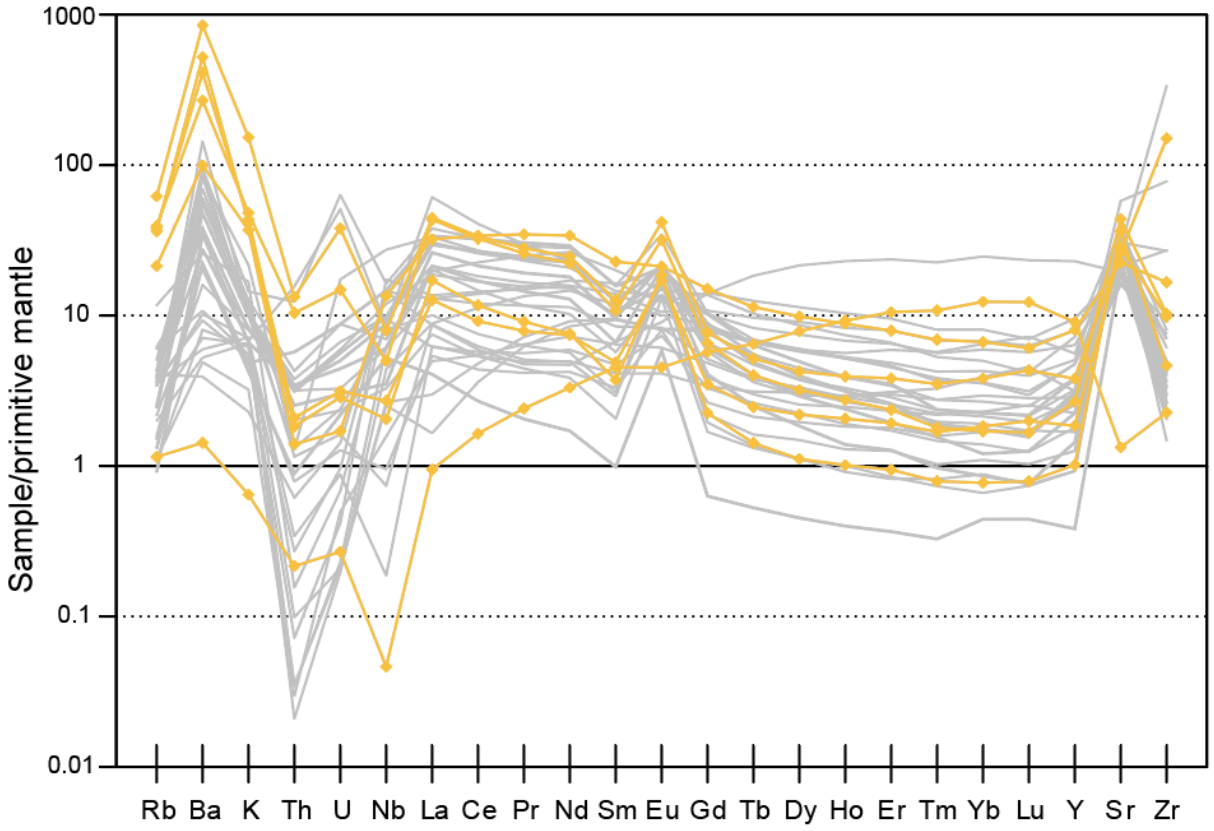
1000
100
10
1
0.1
0.01
Sample/primitive mantle
Rb Ba K Th U Nb La Ce Pr Nd Sm Eu Gd Tb Dy Ho Er Tm Yb Lu Y Sr Zr

Figure 59: Saliceto samples bulk rock trace elements normalized to primitive mantle (Hofmann, 1988) highlighted, with other Upper Mafic Complex bulk rock analyses in gray. Pyroxenite (AM-IVZ-VM008) is the most depleted in REE.

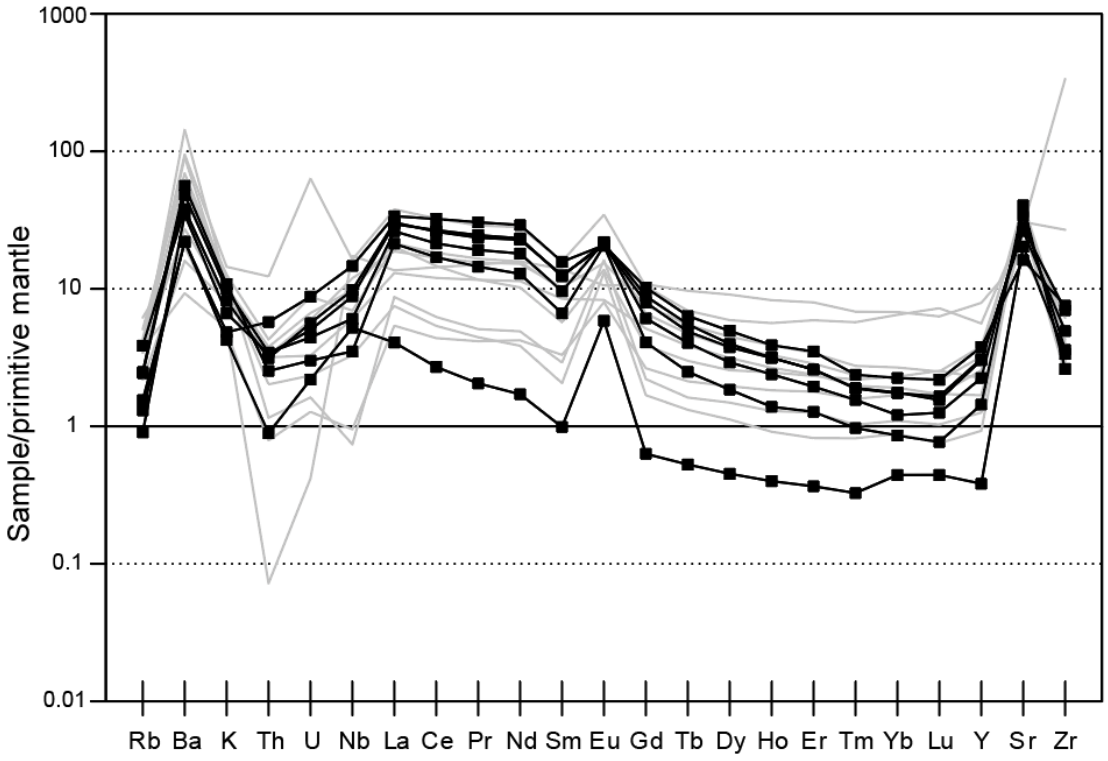
1000
100
10
1
0.1
0.01
Sample/primitive mantle
Rb Ba K Th U Nb La Ce Pr Nd Sm Eu Gd Tb Dy Ho Er Tm Yb Lu Y Sr Zr

Figure 60: Selected bulk rock trace elements plotted as a function of distance to the Insubric Line for the northern Mafic Complex (Val Sesia and Val Mastallone). Data from literature and new data. Symbols as in Figure 54.

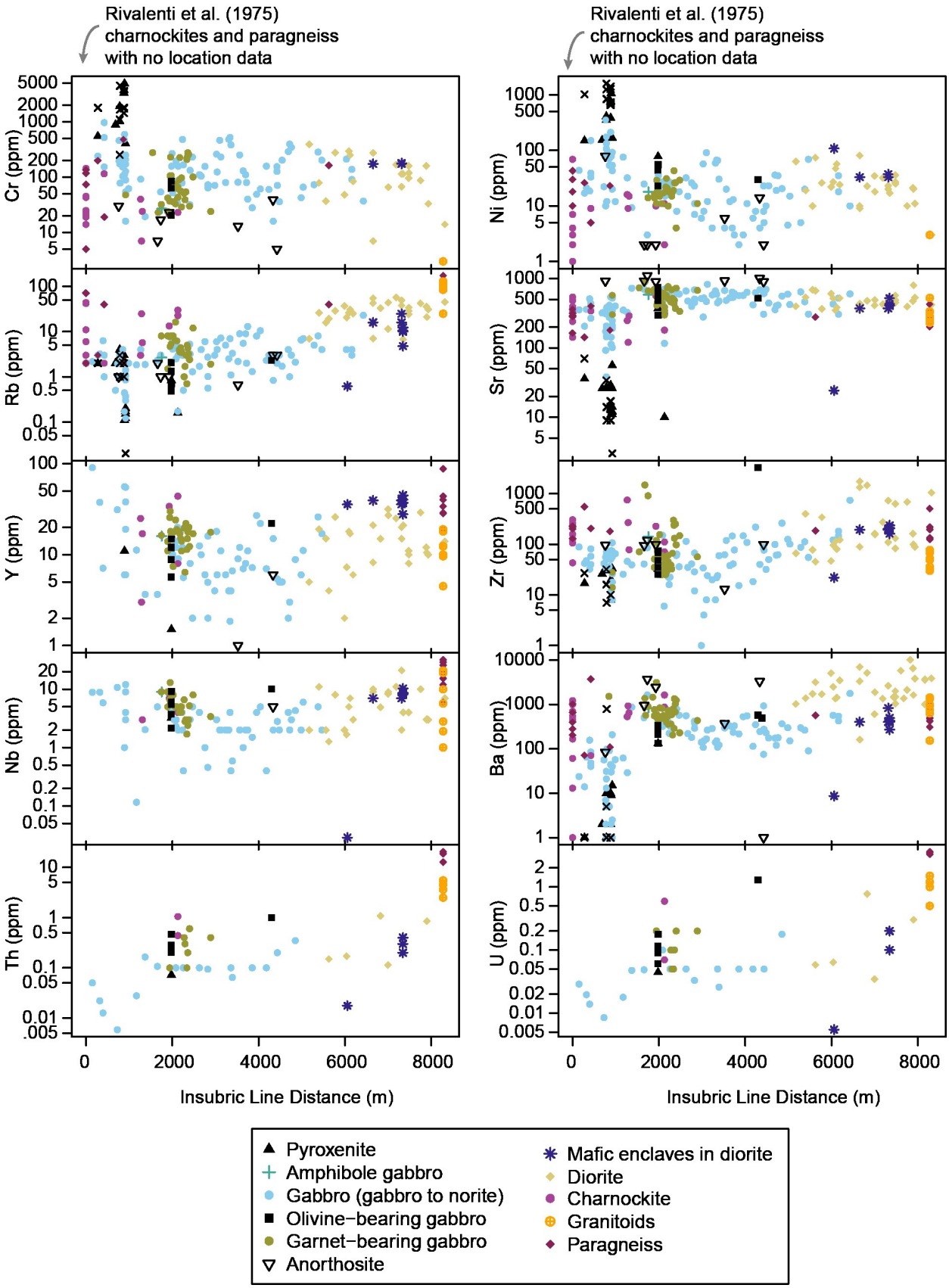
Rivalenti et al. (1975)
charnockites and paragneiss
with no location data
Rivalenti et al. (1975)
charnockites and paragneiss
with no location data
Cr (ppm)
Ni (ppm)
Rb (ppm)
Sr (ppm)
Y (ppm)
Zr (ppm)
Nb (ppm)
Ba (ppm)
Th (ppm)
U (ppm)
0
2000
4000
6000
8000
Insubric Line Distance (m)
Insubric Line Distance (m)
Pyroxenite
Amphibole gabbro
Gabbro (gabbro to norite)
Olivine−bearing gabbro
Garnet−bearing gabbro
Anorthosite
Mafic enclaves in diorite
Diorite
Charnockite
Granitoids
Paragneiss

Figure 61: Bulk rock REE normalized to primitive mantle values (Hoffman, 1988) plotted as a function of distance to the Insubric Line for the northern Mafic Complex (Val Sesia and Val Mastallone). Data from literature and new data. Symbols as in Figure 54.

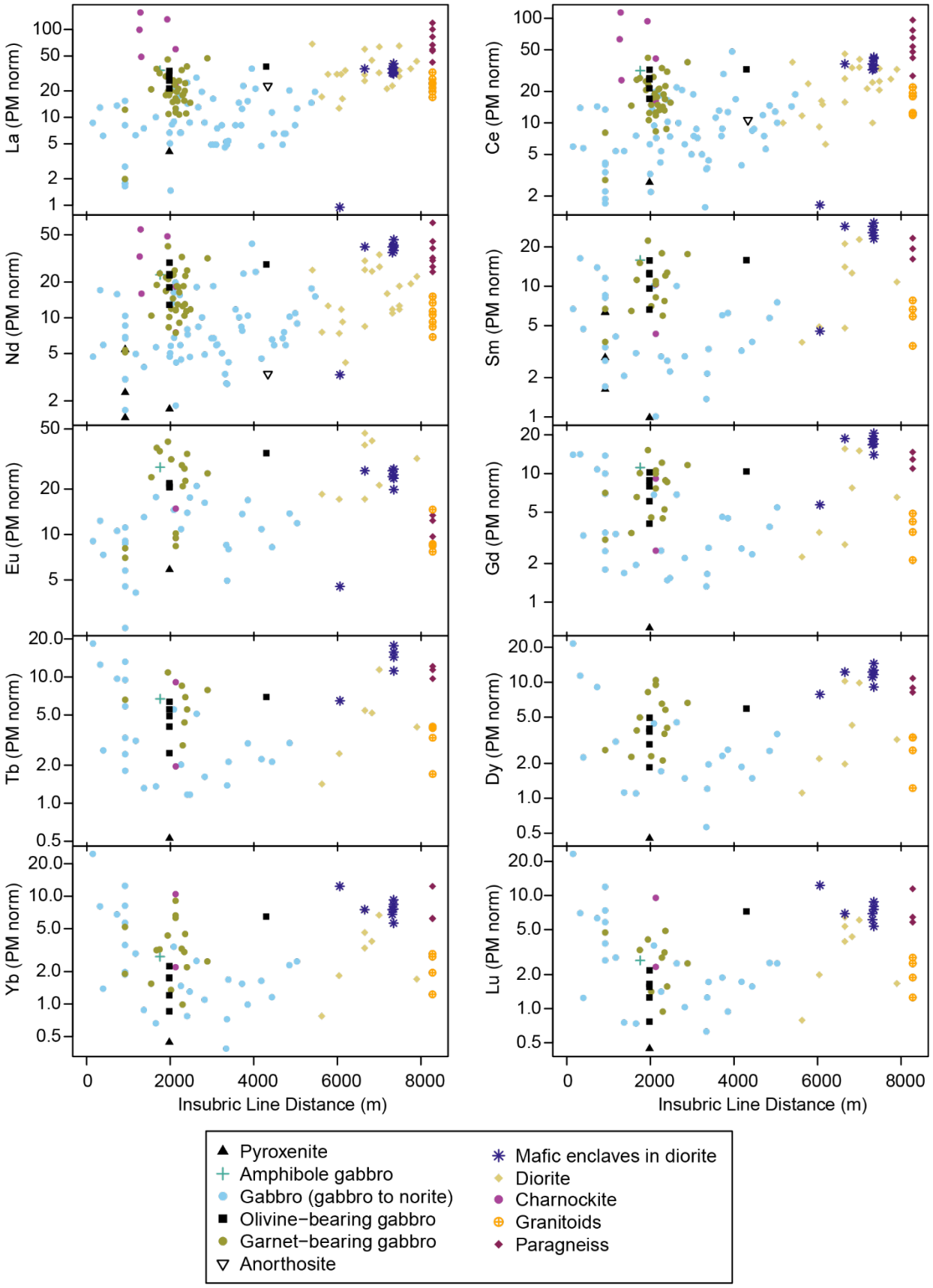
La (PM norm)
Ce (PM norm)
Nd (PM norm)
Sm (PM norm)
Eu (PM norm)
Gd (PM norm)
Tb (PM norm)
Dy (PM norm)
Yb (PM norm)
Lu (PM norm)
Insubric Line Distance (m)
Insubric Line Distance (m)
Pyroxenite
Amphibole gabbro
Gabbro (gabbro to norite)
Olivine−bearing gabbro
Garnet−bearing gabbro
Anorthosite
Mafic enclaves in diorite
Diorite
Charnockite
Granitoids
Paragneiss

Figure 62: Explained variance of each PC for PCA performed in this study. For PCA of major elements only: for all samples (a), for the northern Mafic Complex (b), for the Val Sessera transect (c). For PCA of trace elements only: for all samples from the Mafic Complex (d), for the northern Mafic Complex (e), and for the Val Sessera transect (f). For PCA of both major and trace elements: for all samples (g), for the northern Mafic Complex (h), and for the Val Sessera transect (i).

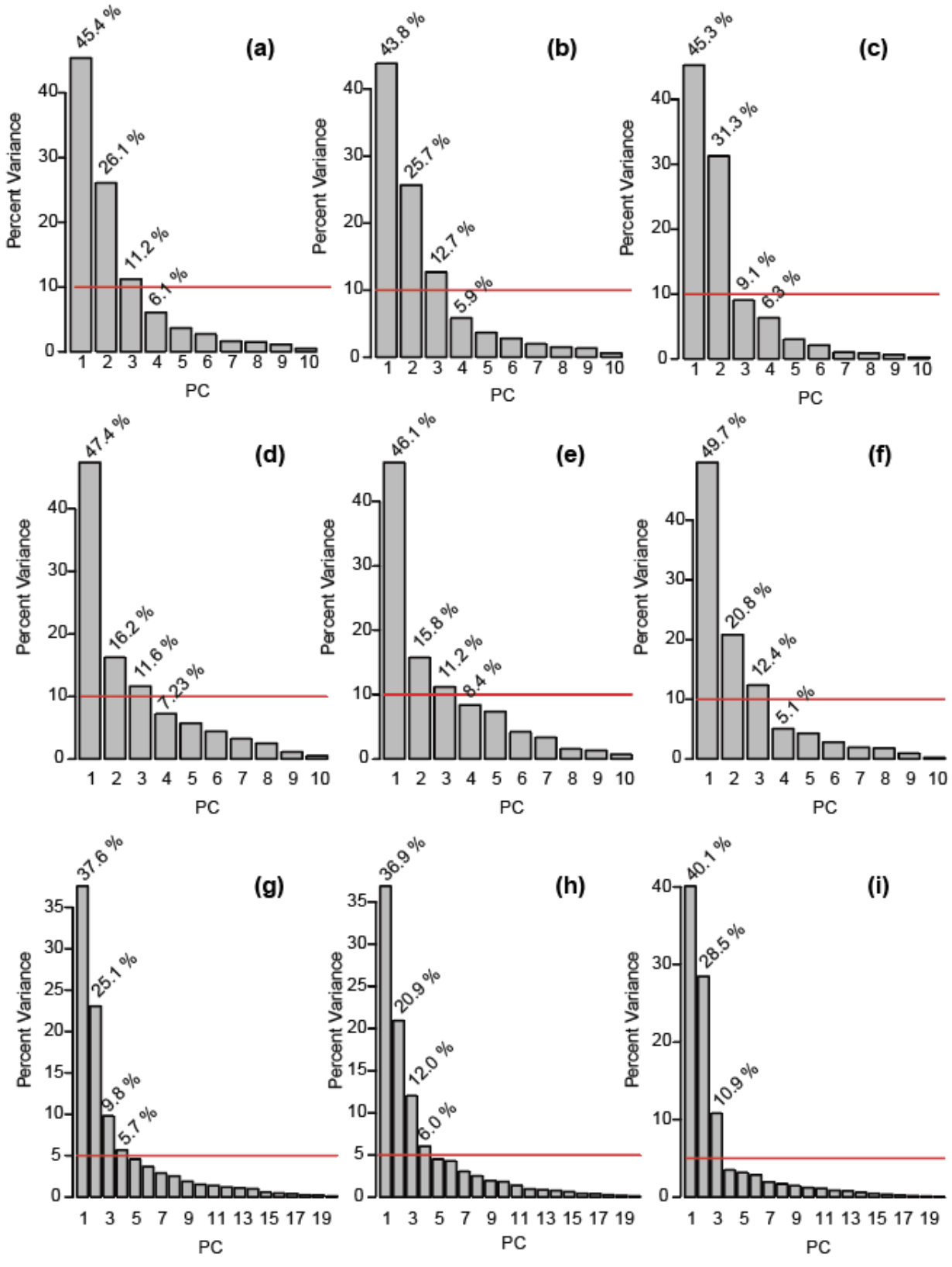
(a)
45.4 %
26.1 %
11.2 %
6.1 %
(b)
43.8 %
25.7 %
12.7 %
5.9 %
(c)
45.3 %
31.3 %
9.1 %
6.3 %
(d)
47.4 %
16.2 %
11.6 %
7.23 %
(e)
46.1 %
15.8 %
11.2 %
8.4 %
(f)
49.7 %
20.8 %
12.4 %
5.1 %
(g)
37.6 %
25.1 %
9.8 %
5.7 %
(h)
36.9 %
20.9 %
12.0 %
6.0 %
(i)
40.1 %
28.5 %
10.9 %
Percent Variance
PC

Figure 63: PCA of major elements from entire Mafic Complex, including paragneiss and charnockites, PC2 vs PC1 distance biplot by (a) zones of Sinigoi *et al.* (1996) and (b) by rock type. Symbols as in Figure 45 and 46, respectively. Loading vectors are not to scale. Symbols as in Figures 50 and 54 for (a) and (b), respectively.

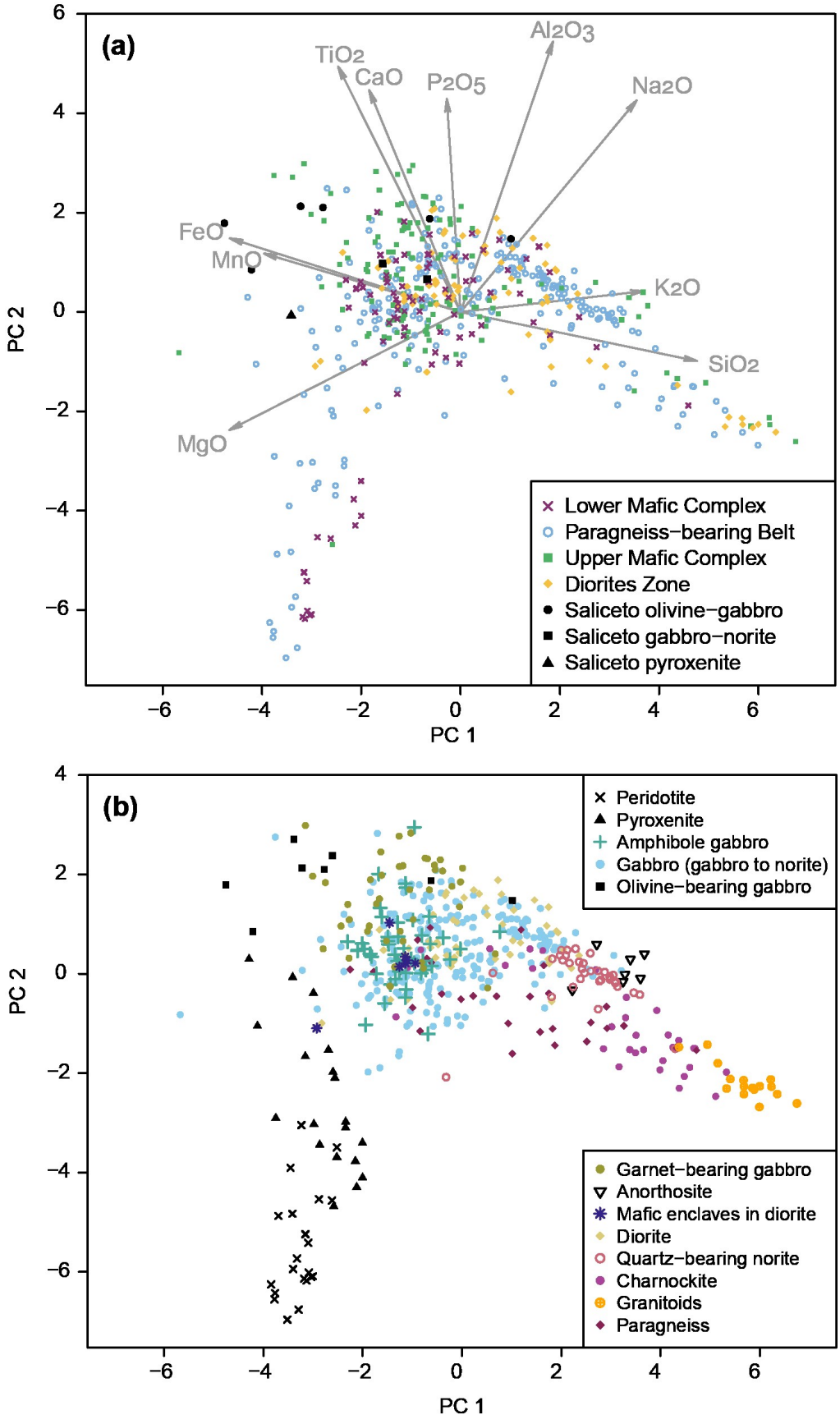
(a)
TiO2
CaO
P2O5
Al2O3
Na2O
FeO
MnO
K2O
SiO2
MgO
Lower Mafic Complex
Paragneiss−bearing Belt
Upper Mafic Complex
Diorites Zone
Saliceto olivine−gabbro
Saliceto gabbro−norite
Saliceto pyroxenite
PC 1
PC 2
(b)
Peridotite
Pyroxenite
Amphibole gabbro
Gabbro (gabbro to norite)
Olivine−bearing gabbro
Garnet−bearing gabbro
Anorthosite
Mafic enclaves in diorite
Diorite
Quartz−bearing norite
Charnockite
Granitoids
Paragneiss
PC 1
PC 2

Figure 64: PC2 vs PC1 distance biplot of PCA performed on major elements of entire Mafic Complex, with sample scores colored by Mg#.

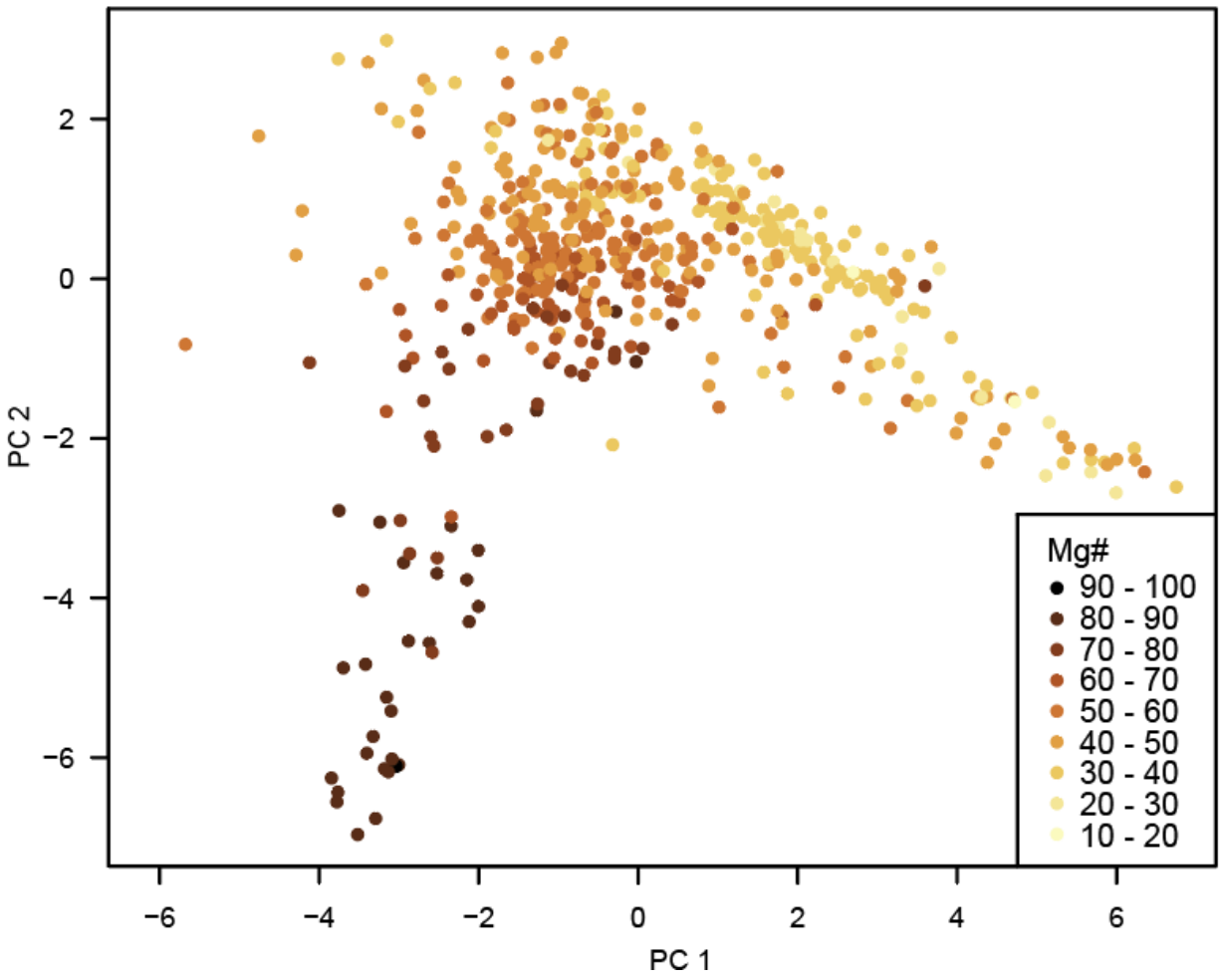
PC 2
PC 1
2
0
−2
−4
−6
−6
−4
−2
0
2
4
6
Mg#
90 - 100
80 - 90
70 - 80
60 - 70
50 - 60
40 - 50
30 - 40
20 - 30
10 - 20

Figure 65: PCA of major elements of all Mafic Complex samples, showing (a) $^{87}Sr/^{86}Sr$ and (b) $\delta^{18}O$ versus PC1 and (b) $^{87}Sr/^{86}Sr$ versus PC2. Isotopic data is only available for a limited number of analyses in the literature. The initial Sr isotopic ratios (Sr_i) are not calculated here.

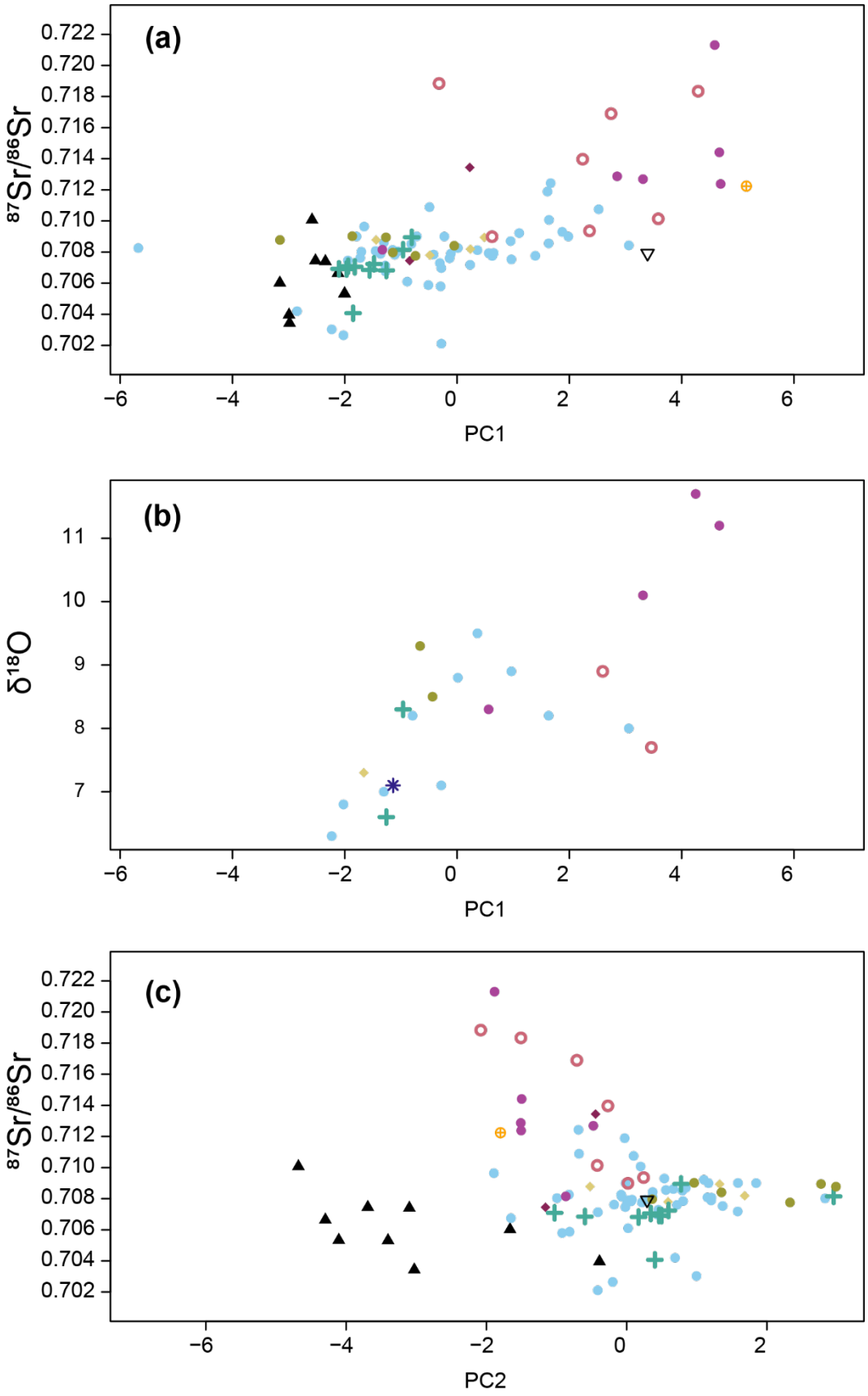
(a)
$^{87}Sr/^{86}Sr$
0.722
0.720
0.718
0.716
0.714
0.712
0.710
0.708
0.706
0.704
0.702
−6
−4
−2
0
2
4
6
PC1
(b)
$\delta^{18}O$
11
10
9
8
7
−6
−4
−2
0
2
4
6
PC1
(c)
$^{87}Sr/^{86}Sr$
0.722
0.720
0.718
0.716
0.714
0.712
0.710
0.708
0.706
0.704
0.702
−6
−4
−2
0
2
PC2

Figure 66: PCA of major elements of samples from the northern Mafic Complex (Val Sesia and Val Mastallone), PCs projected as distance to the Insubric Line. Symbols as in Figure 54. Loading vectors are not to scale.

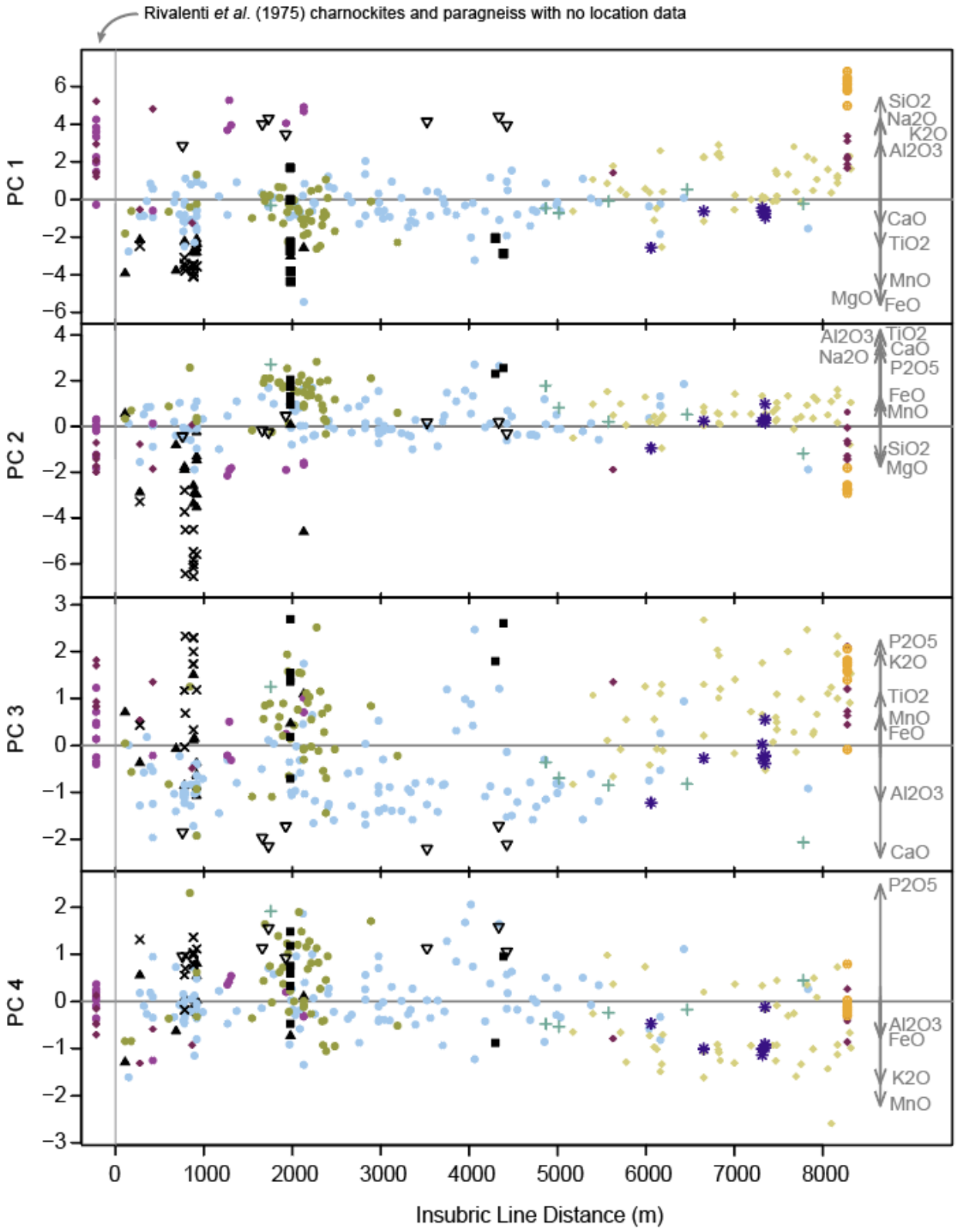
Rivalenti et al. (1975) charnockites and paragneiss with no location data
PC 1
SiO2
Na2O
K2O
Al2O3
CaO
TiO2
MnO
MgO
FeO
PC 2
Al2O3
Na2O
TiO2
CaO
P2O5
FeO
MnO
SiO2
MgO
PC 3
P2O5
K2O
TiO2
MnO
FeO
Al2O3
CaO
PC 4
P2O5
Al2O3
FeO
K2O
MnO
0
1000
2000
3000
4000
5000
6000
7000
8000
Insubric Line Distance (m)

Figure 67: PCA of major elements from entire Mafic Complex, including paragneiss and charnockites, PC4 vs PC3 distance biplot by (a) zones of Sinigoi *et al.* (1996) and (b) by rock type. Symbols as in Figures 50 and 54 for (a) and (b), respectively. Loading vectors are not to scale.

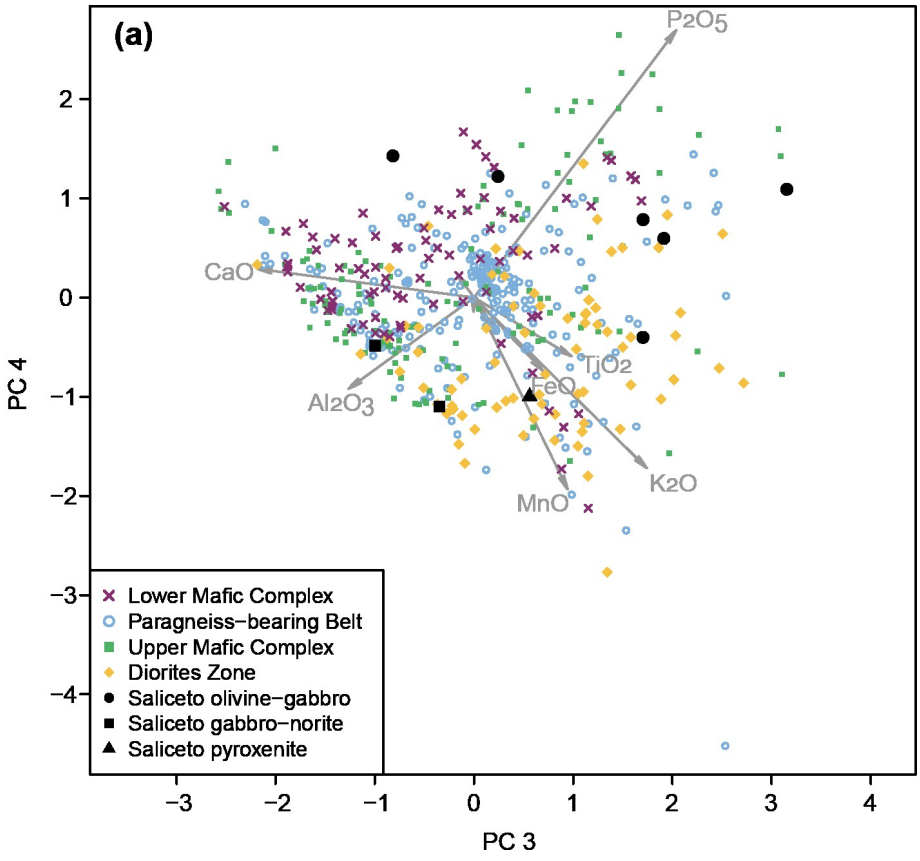
(a)
P2O5
CaO
TiO2
FeO
Al2O3
K2O
MnO
Lower Mafic Complex
Paragneiss−bearing Belt
Upper Mafic Complex
Diorites Zone
Saliceto olivine−gabbro
Saliceto gabbro−norite
Saliceto pyroxenite
PC 4
PC 3

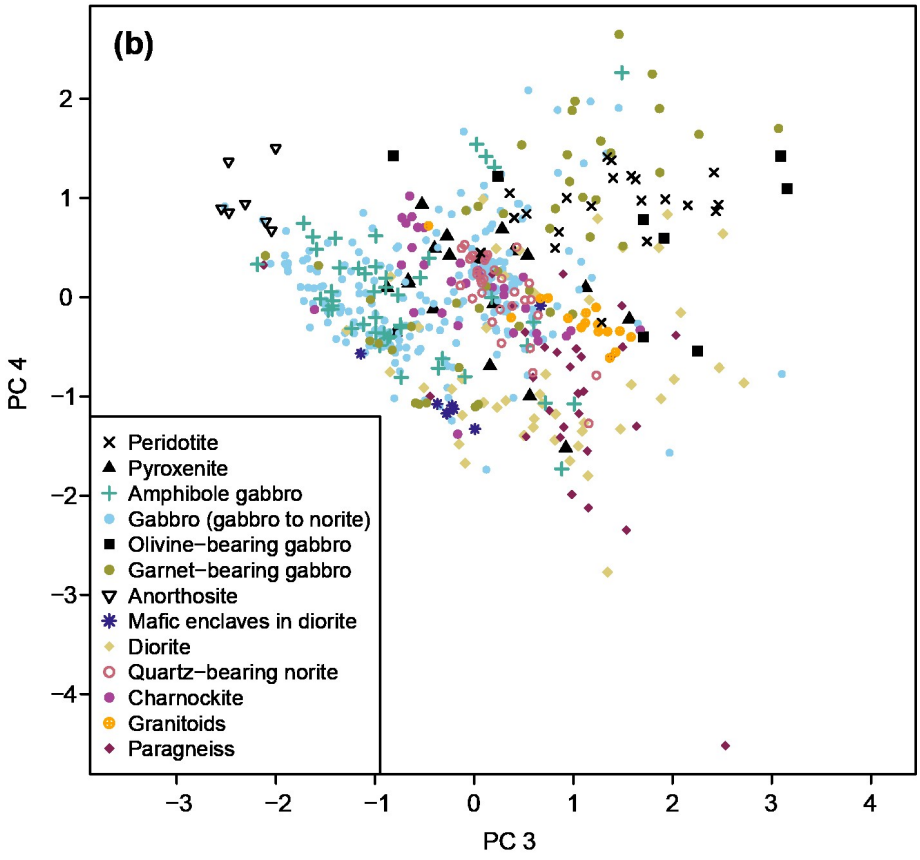
(b)
Peridotite
Pyroxenite
Amphibole gabbro
Gabbro (gabbro to norite)
Olivine−bearing gabbro
Garnet−bearing gabbro
Anorthosite
Mafic enclaves in diorite
Diorite
Quartz−bearing norite
Charnockite
Granitoids
Paragneiss
PC 4
PC 3

Figure 68: PCA of trace elements of samples from entire Mafic Complex, PC2 vs PC1. Loading vectors are not to scale. Symbols as in Figures 50 and 54 for (a) and (b), respectively.

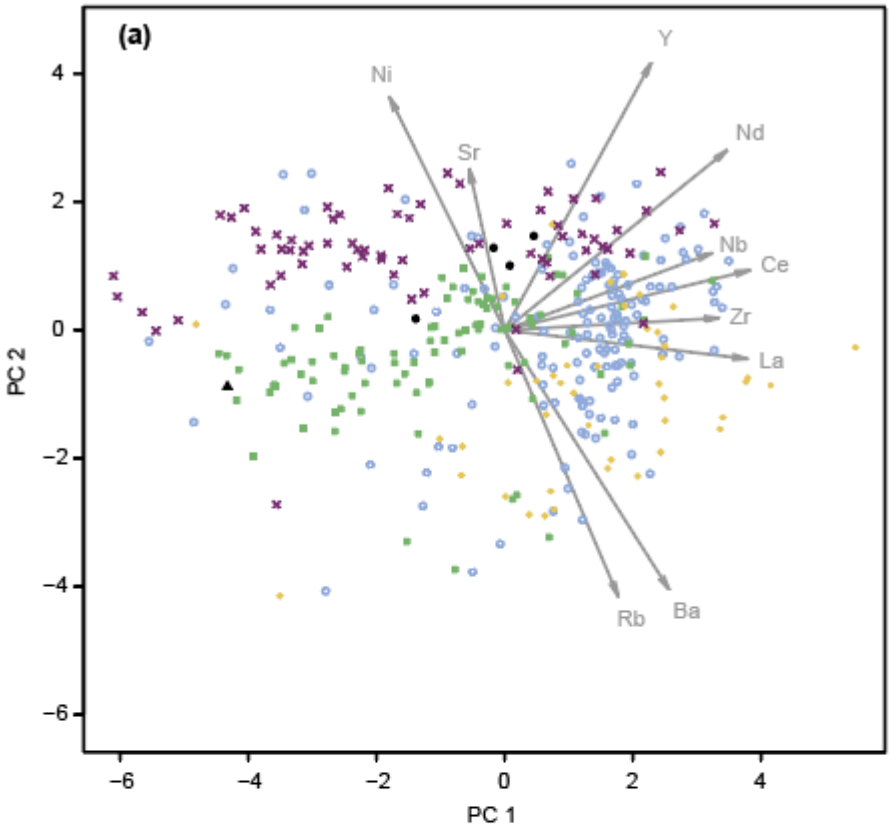
(a)
Y
Ni
Nd
Sr
Nb
Ce
Zr
La
Rb
Ba
PC 2
PC 1
4
2
0
−2
−4
−6
−6
−4
−2
0
2
4

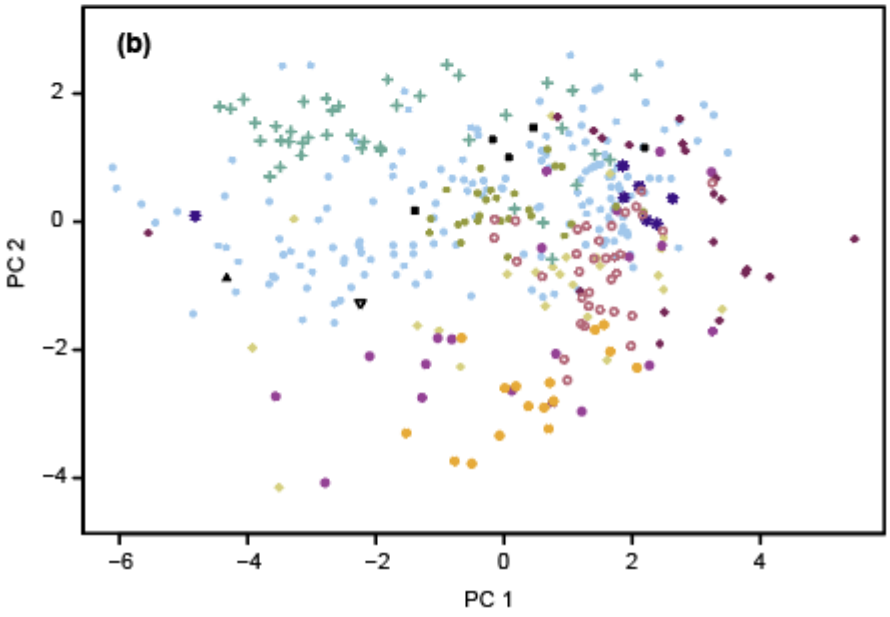
(b)
PC 2
PC 1
2
0
−2
−4
−6
−4
−2
0
2
4

Figure 69: PCA performed on major and trace elements of all lithologies in the Mafic Complex, PC2 vs PC1 distance biplots, by (a) zones within the Mafic Complex and (b) by lithology. Symbols as in Figures 50 and 54 for (a) and (b), respectively. The loading vectors of elements are not to scale.

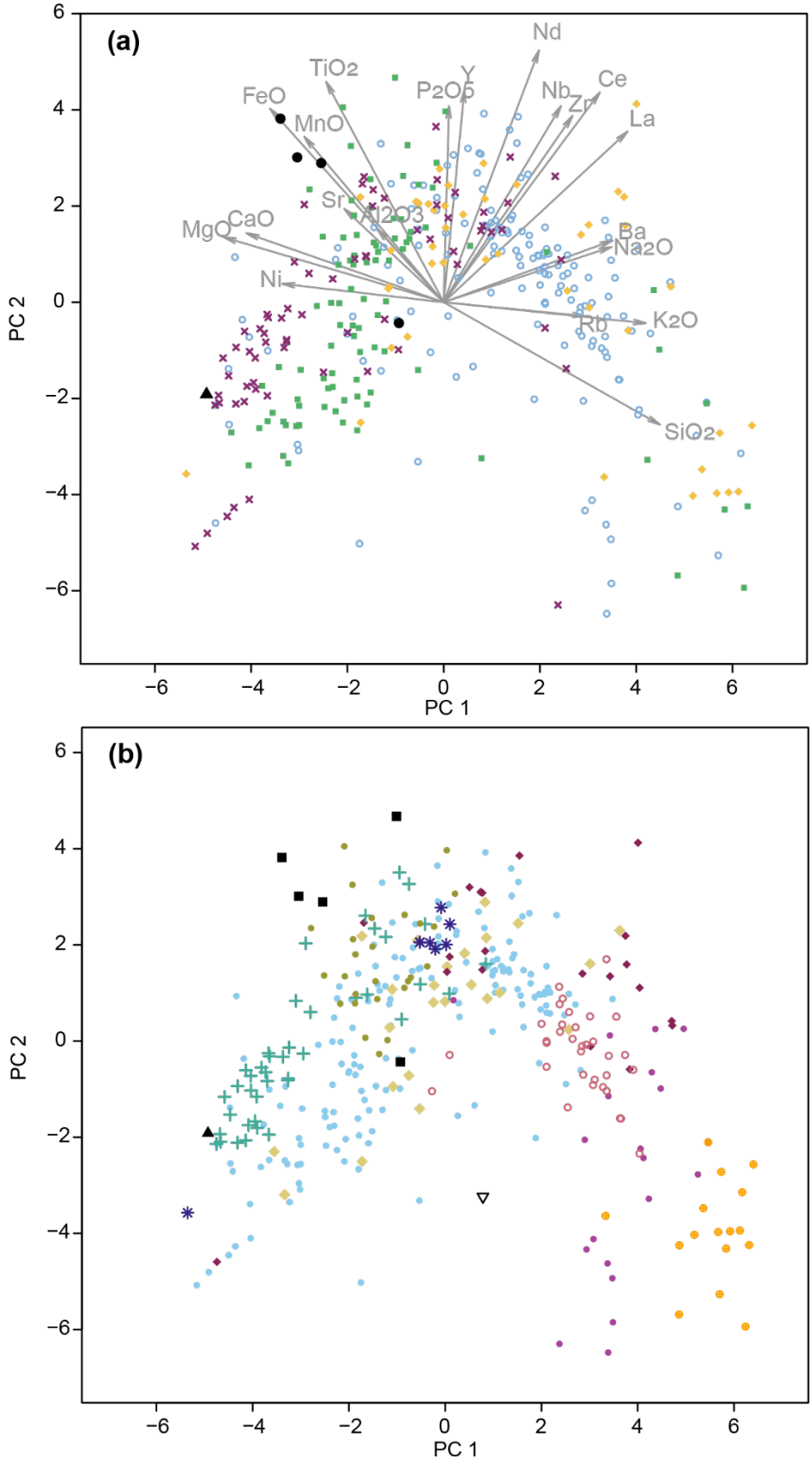
(a)
Nd
TiO2
Y
P2O5
Nb
Ce
FeO
Zr
MnO
La
Sr
Al2O3
MgO
CaO
Ba
Na2O
Ni
Rb
K2O
SiO2
PC 2
PC 1
(b)
PC 2
PC 1

Figure 70: PCA performed on major and trace elements of all lithologies in the Mafic Complex, PC4 vs PC3 distance biplots, by (a) zones within the Mafic Complex and (b) by lithology. Symbols as in Figures 50 and 54 for (a) and (b), respectively. The loading vectors of elements are not to scale.

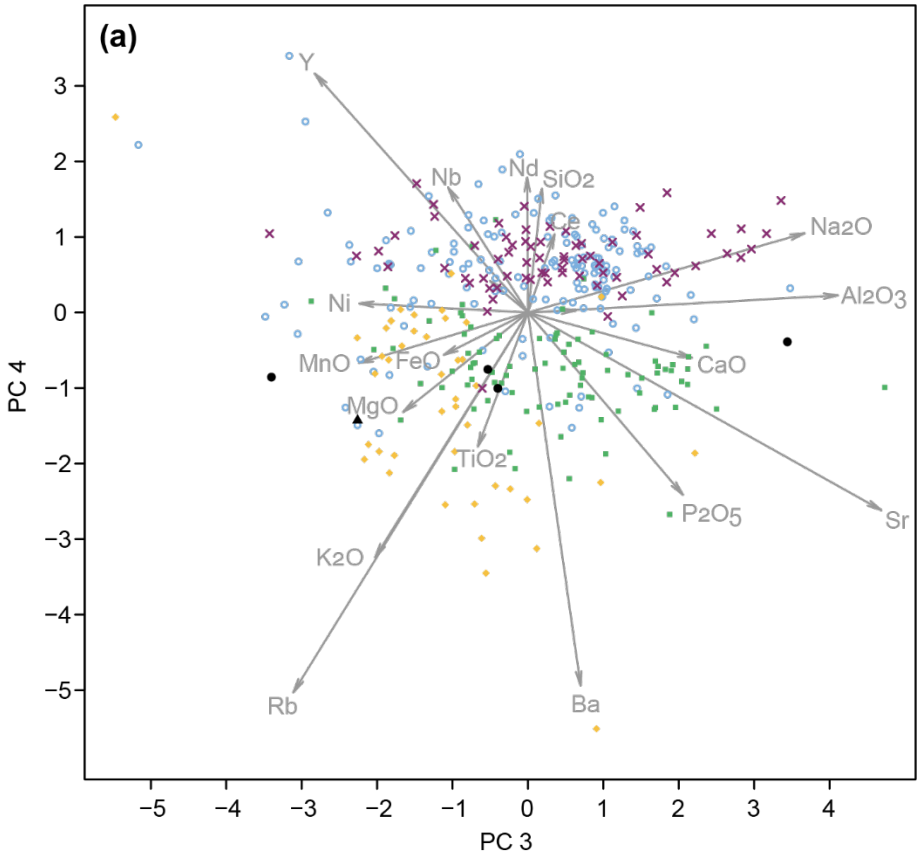
(a)
Y
Nb
Nd
SiO2
Ce
Na2O
Al2O3
Ni
MnO
FeO
CaO
MgO
TiO2
P2O5
Sr
K2O
Rb
Ba
PC 4
PC 3

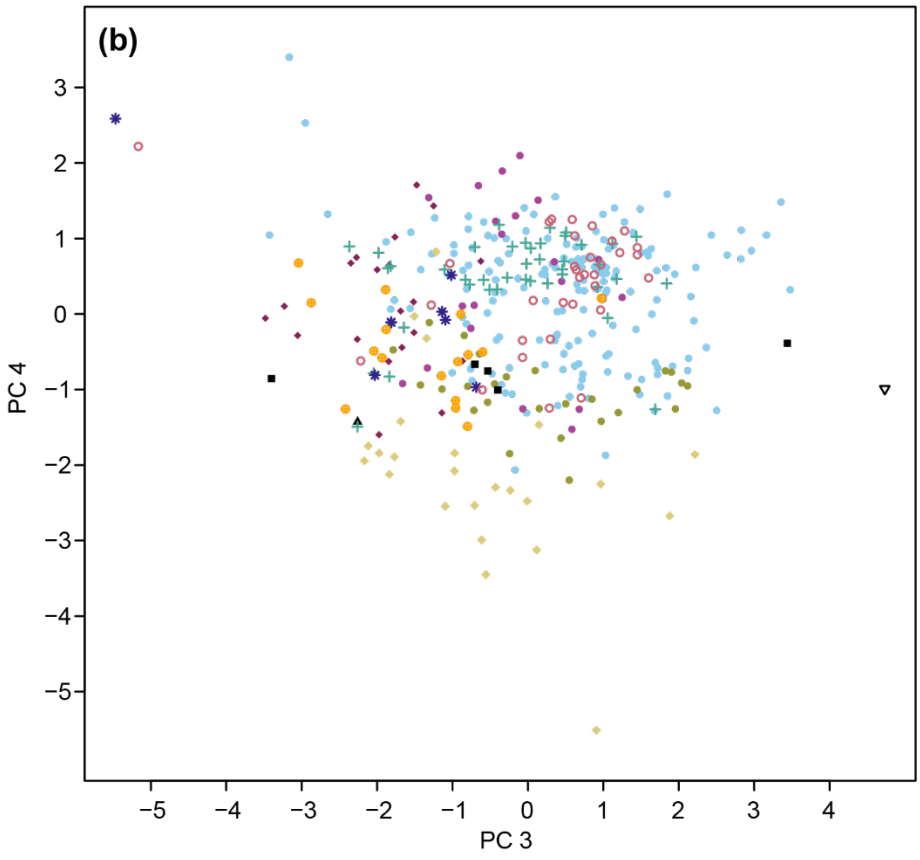
(b)
PC 4
PC 3

Figure 71: Principal components from PCA performed on major and trace elements from samples from the northern Mafic Complex (Val Sesia and Val Mastallone) plotted versus distance to the Insubric Line. Symbols as in Figure 54. Loading vectors in gray are not scaled.

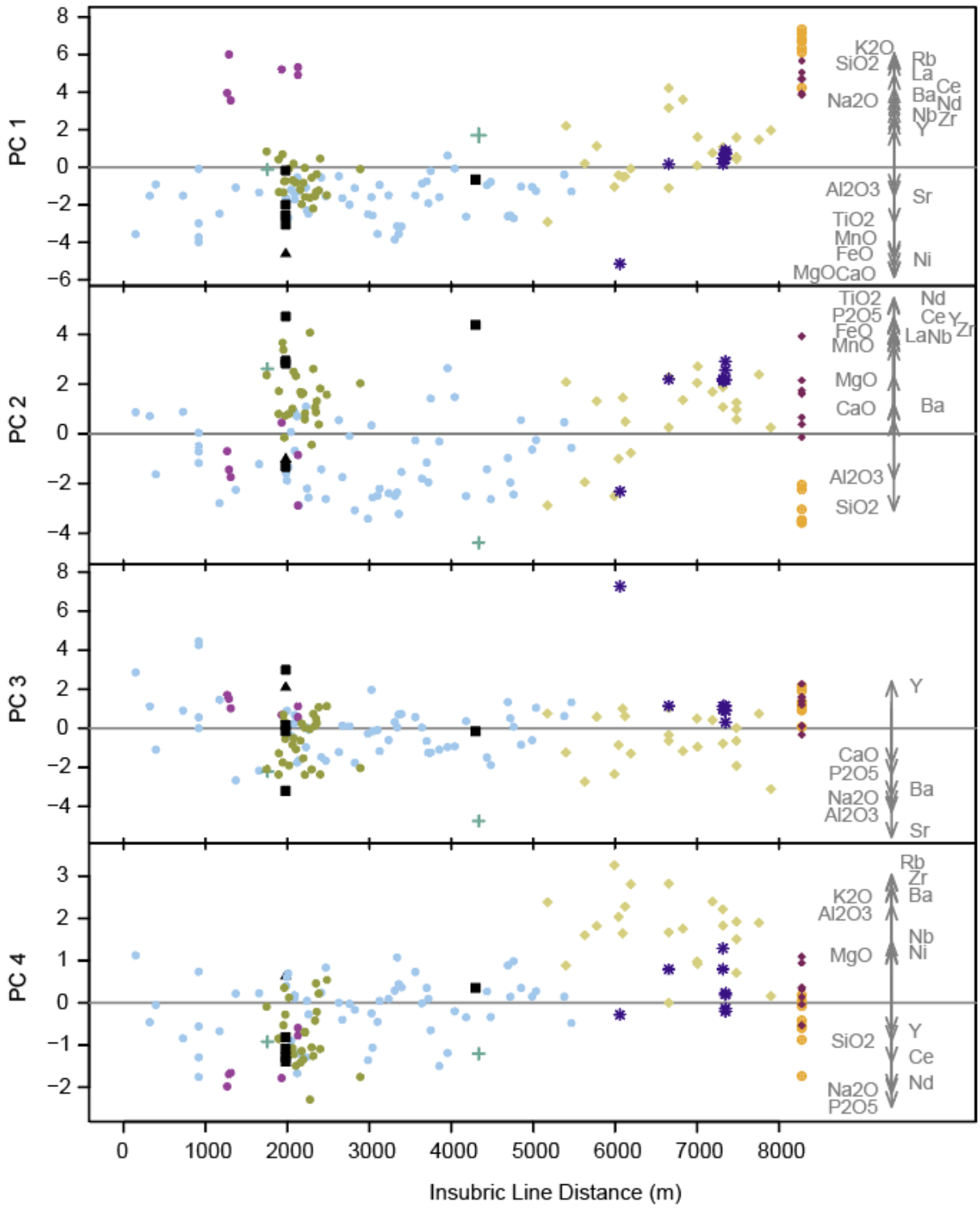
PC 1
PC 2
PC 3
PC 4
K2O
SiO2
Na2O
Rb
La
Ce
Ba
Nd
Nb
Zr
Y
Al2O3
Sr
TiO2
MnO
FeO
Ni
MgO
CaO
P2O5
Insubric Line Distance (m)
0
1000
2000
3000
4000
5000
6000
7000
8000